

QUANTIFICATION IN NUCLEAR MEDICINE IMAGING

EDITED BY: Ivo Rausch and Michel Koole

PUBLISHED IN: Frontiers in Physics and Frontiers in Physiology



frontiers

Frontiers eBook Copyright Statement

The copyright in the text of individual articles in this eBook is the property of their respective authors or their respective institutions or funders. The copyright in graphics and images within each article may be subject to copyright of other parties. In both cases this is subject to a license granted to Frontiers.

The compilation of articles constituting this eBook is the property of Frontiers.

Each article within this eBook, and the eBook itself, are published under the most recent version of the Creative Commons CC-BY licence.

The version current at the date of publication of this eBook is CC-BY 4.0. If the CC-BY licence is updated, the licence granted by Frontiers is automatically updated to the new version.

When exercising any right under the CC-BY licence, Frontiers must be attributed as the original publisher of the article or eBook, as applicable.

Authors have the responsibility of ensuring that any graphics or other materials which are the property of others may be included in the CC-BY licence, but this should be checked before relying on the CC-BY licence to reproduce those materials. Any copyright notices relating to those materials must be complied with.

Copyright and source acknowledgement notices may not be removed and must be displayed in any copy, derivative work or partial copy which includes the elements in question.

All copyright, and all rights therein, are protected by national and international copyright laws. The above represents a summary only. For further information please read Frontiers' Conditions for Website Use and Copyright Statement, and the applicable CC-BY licence.

ISSN 1664-8714

ISBN 978-2-88974-117-5

DOI 10.3389/978-2-88974-117-5

About Frontiers

Frontiers is more than just an open-access publisher of scholarly articles: it is a pioneering approach to the world of academia, radically improving the way scholarly research is managed. The grand vision of Frontiers is a world where all people have an equal opportunity to seek, share and generate knowledge. Frontiers provides immediate and permanent online open access to all its publications, but this alone is not enough to realize our grand goals.

Frontiers Journal Series

The Frontiers Journal Series is a multi-tier and interdisciplinary set of open-access, online journals, promising a paradigm shift from the current review, selection and dissemination processes in academic publishing. All Frontiers journals are driven by researchers for researchers; therefore, they constitute a service to the scholarly community. At the same time, the Frontiers Journal Series operates on a revolutionary invention, the tiered publishing system, initially addressing specific communities of scholars, and gradually climbing up to broader public understanding, thus serving the interests of the lay society, too.

Dedication to Quality

Each Frontiers article is a landmark of the highest quality, thanks to genuinely collaborative interactions between authors and review editors, who include some of the world's best academicians. Research must be certified by peers before entering a stream of knowledge that may eventually reach the public - and shape society; therefore, Frontiers only applies the most rigorous and unbiased reviews.

Frontiers revolutionizes research publishing by freely delivering the most outstanding research, evaluated with no bias from both the academic and social point of view. By applying the most advanced information technologies, Frontiers is catapulting scholarly publishing into a new generation.

What are Frontiers Research Topics?

Frontiers Research Topics are very popular trademarks of the Frontiers Journals Series: they are collections of at least ten articles, all centered on a particular subject. With their unique mix of varied contributions from Original Research to Review Articles, Frontiers Research Topics unify the most influential researchers, the latest key findings and historical advances in a hot research area! Find out more on how to host your own Frontiers Research Topic or contribute to one as an author by contacting the Frontiers Editorial Office: frontiersin.org/about/contact

QUANTIFICATION IN NUCLEAR MEDICINE IMAGING

Topic Editors:

Ivo Rausch, Medical University of Vienna, Austria

Michel Koole, KU Leuven, Belgium

Citation: Rausch, I., Koole, M., eds. (2022). Quantification in Nuclear Medicine Imaging. Lausanne: Frontiers Media. doi: 10.3389/978-2-88974-117-5

Table of Contents

- 05 Clinically Valuable Quality Control for PET/MRI Systems: Consensus Recommendation From the HYBRID Consortium**
Alejandra Valladares, Sahar Ahangari, Thomas Beyer, Ronald Boellaard, Zacharias Chalampalakis, Claude Comtat, Laura DalToso, Adam E. Hansen, Michel Koole, Jane Mackewn, Paul Marsden, Johan Nuyts, Francesco Padormo, Ronald Peeters, Sebastian Poth, Esteban Solari and Ivo Rausch
- 19 Attenuation Correction Approaches for Serotonin Transporter Quantification With PET/MRI**
Lucas Rischka, Gregor Gryglewski, Neydher Berroterán-Infante, Ivo Rausch, Gregory Miles James, Manfred Klöbl, Helen Sigurdardottir, Markus Hartenbach, Andreas Hahn, Wolfgang Wadsak, Markus Mitterhauser, Thomas Beyer, Siegfried Kasper, Daniela Prayer, Marcus Hacker and Rupert Lanzenberger
- 30 Regional Accuracy of ZTE-Based Attenuation Correction in Static [^{18}F]FDG and Dynamic [^{18}F]PE2I Brain PET/MR**
Georg Schramm, Michel Koole, Stefanie M. A. Willekens, Ahmadreza Rezaei, Donatienne Van Weehaeghe, Gaspar Delso, Ronald Peeters, Nathalie Mertens, Johan Nuyts and Koen Van Laere
- 41 Optimization of the κ'_2 Parameter Estimation for the Pharmacokinetic Modeling of Dynamic PIB PET Scans Using SRTM2**
Débora E. Peretti, Fransje E. Reesink, Janine Doorduyn, Bauke M. de Jong, Peter P. De Deyn, Rudi A. J. O. Dierckx, Ronald Boellaard and David Vázquez García
- 52 Magnetic Resonance-Based Attenuation Correction and Scatter Correction in Neurological Positron Emission Tomography/Magnetic Resonance Imaging—Current Status With Emerging Applications**
Jarmo Teuho, Angel Torrado-Carvajal, Hans Herzog, Udunna Anazodo, Riku Klén, Hidehiro Iida and Mika Teräs
- 70 Study of the Effect of Reconstruction Parameters for Myocardial Perfusion Imaging in PET With a Novel Flow Phantom**
Reetta Siekkinen, Jarmo Teuho, Nadia A. S. Smith, Andrew Fenwick, Anna K. Kirjavainen, Kalle Koskensalo, Antti Saraste and Mika Teräs
- 80 Bayesian Estimation of the ntPET Model in Single-Scan Competition PET Studies**
Zacharie Irace, Inés Mérida, Jérôme Redouté, Clara Fonteneau, Marie-Françoise Suaud-Chagny, Jérôme Brunelin, Benjamin Vidal, Luc Zimmer, Anthonin Reilhac and Nicolas Costes
- 99 First Phantom-Based Quantitative Assessment of Scandium-44 Using a Commercial PET Device**
Thiago V. M. Lima, Silvano Gnesin, Egbert Nitzsche, Pablo G. Ortega, Cristina Müller and Nicholas P. van der Meulen
- 109 Methods for Quantifying Neurotransmitter Dynamics in the Living Brain With PET Imaging**
Jenny Ceccarini, Heather Liu, Koen Van Laere, Evan D. Morris and Christin Y. Sander

117 Monte Carlo Simulations of the GE Signa PET/MR for Different Radioisotopes

Paulo R. R. V. Caribé, Stefaan Vandenberghe, André Diogo, David Pérez-Benito, Nikos Efthimiou, Charlotte Thyssen, Yves D'Asseler and Michel Koole

129 Influence of Multiple Animal Scanning on Image Quality for the Sedecal SuperArgus2R Preclinical PET Scanner

Nikos Efthimiou, John D. Wright, Luke Clayton, Isaline Renard, Federico Zagni, Paulo R.R.V. Caribé, Stephen J. Archibald and Christopher J. Cawthorne



Clinically Valuable Quality Control for PET/MRI Systems: Consensus Recommendation From the HYBRID Consortium

Alejandra Valladares¹, Sahar Ahangari², Thomas Beyer¹, Ronald Boellaard^{3,4}, Zacharias Chalampalakakis⁵, Claude Comtat⁵, Laura DalToso⁶, Adam E. Hansen², Michel Koole⁷, Jane Mackewn⁶, Paul Marsden⁶, Johan Nuyts⁷, Francesco Padormo⁸, Ronald Peeters⁹, Sebastian Poth¹⁰, Esteban Solari¹¹ and Ivo Rausch^{1*}

¹ Quantitative Imaging and Medical Physics Team, Center for Medical Physics and Biomedical Engineering, Medical University of Vienna, Vienna, Austria, ² Department of Clinical Physiology, Nuclear Medicine and Positron Emission Tomography, Rigshospitalet, University of Copenhagen, Copenhagen, Denmark, ³ Department of Radiology and Nuclear Medicine, Vrije Universiteit Medical Center, Amsterdam, Netherlands, ⁴ Department of Nuclear Medicine and Molecular Imaging, University Medical Center Groningen, Groningen, Netherlands, ⁵ Service Hospitalier Frédéric Joliot, IMIV, CEA, INSERM, CNRS, Université Paris-Sud, Orsay, France, ⁶ King's College London & Guy's and St. Thomas' Positron Emission Tomography Center, School of Biomedical Engineering and Imaging Sciences, King's College London, London, United Kingdom, ⁷ Nuclear Medicine and Molecular Imaging, University Hospitals Leuven, Katholieke Universiteit Leuven, Leuven, Belgium, ⁸ Medical Physics, Guy's and St. Thomas' National Health Service Foundation Trust, London, United Kingdom, ⁹ Department of Radiology, Universitair Ziekenhuis Gasthuisberg, Leuven, Belgium, ¹⁰ Department of Nuclear Medicine, University Hospital Tuebingen, Tuebingen, Germany, ¹¹ Department of Nuclear Medicine, Klinikum rechts der Isar, Munich, Germany

OPEN ACCESS

Edited by:

Claudia Kuntner,
Austrian Institute of Technology
(AIT), Austria

Reviewed by:

Michael D. Noseworthy,
McMaster University, Canada
Abass Nona Alavi,
University of Pennsylvania,
United States

*Correspondence:

Ivo Rausch
ivo.rausch@meduniwien.ac.at

Specialty section:

This article was submitted to
Medical Physics and Imaging,
a section of the journal
Frontiers in Physics

Received: 28 May 2019

Accepted: 05 September 2019

Published: 24 September 2019

Citation:

Valladares A, Ahangari S, Beyer T, Boellaard R, Chalampalakakis Z, Comtat C, DalToso L, Hansen AE, Koole M, Mackewn J, Marsden P, Nuyts J, Padormo F, Peeters R, Poth S, Solari E and Rausch I (2019) Clinically Valuable Quality Control for PET/MRI Systems: Consensus Recommendation From the HYBRID Consortium. *Front. Phys.* 7:136. doi: 10.3389/fphy.2019.00136

Quality control (QC) of medical imaging devices is essential to ensure their proper function and to gain accurate and quantitative results. Therefore, several international bodies have published QC guidelines and recommendations for a wide range of imaging modalities to ensure adequate performance of the systems. Hybrid imaging systems such as positron emission tomography/computed tomography (PET/CT) or PET/magnetic resonance imaging (PET/MRI), in particular, present additional challenges caused by differences between the combined modalities. However, despite the increasing use of this hybrid imaging modality in recent years, there are no dedicated QC recommendations for PET/MRI. Therefore, this work aims at collecting information on QC procedures across a European PET/MRI network, presenting quality assurance procedures implemented by PET/MRI vendors and achieving a consensus on PET/MRI QC procedures across imaging centers. Users of PET/MRI systems at partner sites involved in the HYBRID consortium were surveyed about local frequencies of QC procedures for PET/MRI. Although all sites indicated that they perform vendor-specific daily QC procedures, significant variations across the centers were observed for other QC tests and testing frequencies. Likewise, variations in available recommendations and guidelines and the QC procedures implemented by vendors were found. Based on the available information and our clinical expertise within this consortium, we were able to propose a minimum set of PET/MRI QC recommendations including the daily QC, cross-calibration tests, and an image quality (IQ) assessment for PET and coil checks and MR image quality tests for MRI. Together with regular checks of the PET-MRI alignment, proper PET/MRI performance can be ensured.

Keywords: hybrid imaging, consensus, recommendations, quality control, PET/MRI

INTRODUCTION

With the introduction of clinical PET/MRI systems in 2010 [1, 2], a novel hybrid PET system became available, in addition to PET/CT and SPECT/CT. The combination of PET with MRI has several advantages; it offers high soft tissue contrast by MRI, together with a reduced radiation burden compared to CT [3]. Moreover, the high-resolution anatomical images from MRI can be used for accurate partial volume correction (PVC) [4] and fast MRI sequences can be used to correct for motion in PET examinations [5]. Further, a broad spectrum of available MRI sequences offers a variety of multi-parametric information, which bears high potential to improve disease characterization through radiomics and machine learning (ML) approaches [6].

Nonetheless, the typically rather low number of available datasets for a specific disease from PET/MRI in a single-center renders a systematic evaluation of possible advantages over other modalities, and the use of PET/MRI data for ML approaches challenging. Therefore, pooling of PET/MRI data across multiple imaging centers is desirable.

However, comparability of imaging data from hybrid PET information is often hampered by differences in local imaging protocols and quality control standards [7–9]. In addition to variations in imaging protocols driven by local preferences of the physicians in charge, variations in QC procedures and imaging protocols, as demonstrated for PET/CT operations [7], can be widely attributed to differences in system design between vendors and system generations (mainly using different reconstruction algorithms or settings). However, in contrast to PET/CT, there are only three main PET/MRI systems on the market all introduced between 2010 and 2015. Thus, all systems have implemented state-of-the-art reconstruction algorithms as well as similar technological characteristics. Therefore, a smaller variation in QC procedures and IQ parameters of PET/MRI compared with PET/CT could be expected. However, first findings indicate that this is not the case. Boellaard et al. [10] reported high accuracy of phantom-based QC for three PET/MRI systems, but only when using dedicated phantom acquisition and processing protocols; when using clinical protocols, significant variances between the systems were reported. Further, in a previous multi-center trial, the inter-site variability of NEMA image quality evaluations was reported to be similar to previous reports for PET/CT systems [11]. These findings are an indication that similar variabilities in PET/MRI operation, including basic quality control standards, exist as it was shown for PET/CT.

Currently, there are several recommendations on quality assurance procedures for PET, PET/CT, and MRI systems [12–16] and guidelines for standardized imaging protocols [12, 13, 15, 17, 18]. For PET/MRI, one report exists describing the implementation of a simultaneous hybrid PET/MRI system in an integrated research and clinical setting [19]. Further, two guidelines for oncological whole-body [^{18}F]-FDG-PET/MRI [20, 21] have been published. However, there is currently no recommendation dedicated to QC procedures for PET/MRI systems.

This work aims at (a) summarizing relevant guidelines and recommendations by international bodies on PET and MRI quality control programs, (b) assessing variations of local QC procedures at European hybrid imaging sites, (c) summarizing PET/MRI QC procedures implemented by system's manufacturers, and (d) developing a consensus recommendation of a minimal set of QC measures for PET/MRI throughout the HYBRID (Healthcare Years for Bright Researchers for Imaging Data) consortium.

MATERIALS AND METHODS

HYBRID is an innovative training network project funded by the European Commission (MSCA No. 764458). It aims at promoting the field of non-invasive disease characterization in the light of personalized medicine by enhancing the information gained from molecular and hybrid imaging technologies. The HYBRID consortium brings together international academic, industrial and non-governmental partners in a cross-specialty network including eight partner sites with extensive clinical experience in PET/MRI as well as three vendors of currently available PET/MRI systems.

Summary of Existing Recommendations

To get an overview of the existing and recommended QC tests for PET and MRI systems, we summarized QC guidelines and recommendations published by all major international bodies related to the field of medical imaging. For PET and PET/CT these included suggestions by the American College of Radiology (ACR) [17], the Society of Nuclear Medicine and Molecular Imaging (SNMMI), and the European Association of Nuclear Medicine (EANM) through the EANM Research Ltd (EARL) initiative [15, 22], the International Atomic Energy Agency (IAEA) [16] and the Intersocietal Accreditation Commission (IAC) [23]. For MRI, we gathered information from the ACR [13] and the IAC [14]. All the information was grouped in a table to have a complete overview of the differences and similarities between different recommendations.

State of Implementation of QC Procedures

Based on international QC guidelines and recommendations, we designed a survey to collect information about the QC tests and testing frequencies from all eight users of PET/MRI systems within the HYBRID consortium.

The survey form itself contained two tables: one with the list of the QC tests for the PET part of the systems, and the second one with commonly used MRI QC tests. For each test, the eight participating sites were asked to report the testing frequency at which they perform these tests. Further, the form permitted the addition of information regarding phantoms and tools used or any other free-text comments regarding the implemented procedures.

To increase the response rate from the participants, the document included an introduction to the topic, the aim of the survey and contact details for support during the time of

evaluation. All documents, including the survey form, were sent by email to the imaging centers during summer-autumn 2018. Responses were grouped by PET/MRI system (one per center) in a single table and served as the basis for a consensus on PET/MRI QC.

QC Procedures Implemented by the Vendor

As supporting data for discussions on routine PET/MRI QC procedures, the quality control procedures implemented in three available PET/MRI systems (the Siemens Biograph mMR [2], the GE SIGNA PET/MR [24], and the Ingenuity TF PET/MR [1]) were summarized. These included daily quality assurance (DQA) procedures and additional regular tests. The information was collected from the user manuals of the systems and information provided directly by the vendors.

Consensus Recommendation on QC for PET/MR

Based on the available recommendations for stand-alone PET(/CT) and MRI systems, the responses to the survey on QC procedures and the vendor's implemented quality assurance measures, recommendations for PET/MRI QC were drafted. Findings were presented to and discussed with the participants of the survey, which included experienced clinical PET/MRI users, to achieve a consensus on a minimum set of PET/MRI QC procedures from the HYBRID consortium.

RESULTS

Existing Recommendations for PET and MRI Modalities

Recommended QC tests and testing frequencies for PET(/CT) and MRI reported by international organizations are summarized in **Tables 1, 2**, respectively. For PET, all guidelines included the Daily QC (as implemented by the vendor) and a test for image uniformity. However, other suggested tests and testing frequencies differ between the guidelines. For example, for the sensitivity, spatial resolution, and image uniformity a high variability of testing frequencies, tools, and calculation methods was observed. Likewise, for MRI systems, the testing frequencies for most of the tests such as image uniformity, linearity, spatial resolution, table positioning, slice thickness, and slice positioning were highly variable.

State of Implementation of QC Procedures

All of the eight participating centers completed the form for the available PET/MRI systems on-site resulting in reported QC procedures for five Siemens Biograph mMR PET/MR, two GE SIGNA PET/MR, and one Philips Ingenuity TF PET/MR. Of note, the GE and Philips systems have PET time-of-flight (TOF) capabilities. Survey forms were mainly completed by the on-site medical physics expert.

The DQA protocol provided by the vendors was indicated to be performed daily for all systems. However, the testing frequencies of other evaluated tests were highly variable (**Table 3**).

Tests and Testing Frequencies for the PET Component

DQA procedure

All PET/MRI centers indicated that they perform the DQA as implemented by the manufacturers, including the assessment of detector stability. It is performed automatically or semi-automatically with phantoms provided by vendors, after the routine system initialization or start-up. One of the GE sites (center 7) indicated they perform a daily check of the PET system readiness monitor and an additional monthly DQA, including a partial detector set-up with coincidence timing calibration (CTC).

Timing resolution

At 3/8 of the centers (two Siemens and one Philips), the test was indicated to be performed daily. Variations across the answers for other Siemens systems ranged from performing the test "by manufacturer's recommendations" to "not performed as part of the routine QC." Responses for the GE systems varied between monthly and quarterly.

Sensitivity

The testing frequency for this test presented a high variability across the centers. The answers were: daily, quarterly, annually, or at the commissioning of the system (during the acceptance test). One of the Siemens centers indicated not performing the test as part of the routine QC.

Spatial resolution

Two of the involved centers did not present any specific testing frequency for this test, Center 4 indicated to perform it daily, and the rest of the answers (62.5 % of the systems) ranged from yearly to once every 10 years.

Image uniformity

Three of the eight centers indicated a daily testing frequency; another three indicated they perform the test every 3 months, one center reported the test to be done annually, and one reported not to perform it as part of the routine QC.

Normalization

A daily testing frequency was reported for 4 Siemens PET/MRI systems. From three of the sites (GE and Philips systems), the test was indicated to be done every 3 months. Only one of the centers indicated to perform the normalization test every 6 months.

Image quality and attenuation accuracy. Scatter correction and quantitation

Three centers indicated to performing the test annually, one of them specified to use the NEMA IQ phantom. One center reported to perform it every 10 years, two at the acceptance testing and one reported not to perform it as part of the routine QC.

Tests and Testing Frequencies for the MRI Component

Responses on the QC tests and testing frequencies for the MRI component varied significantly across partner sites. A summary

TABLE 1 | QC tests for PET and PET/CT systems.

Test	ACR [17]	EANM/EARL [15]	IAC [23]	IAEA [16]
PET Part				
Daily system test (by manufacturer's recommendation)	Daily	Daily	Daily	Daily
Detector stability	N/A	Daily or when available	N/A	Daily
Coincidence timing resolution	N/A	N/A	N/A	Daily for TOF PETs
Clinical mode acquisition	N/A	N/A	N/A	Daily (optional procedure)
Sensitivity	Annually	Daily or when available	N/A	Whenever performance change is suspected
Spatial resolution	Quarterly	N/A	N/A	Quarterly or when available
Image uniformity	Quarterly	Daily or when available, by using $^{68}\text{Ge}/^{68}\text{Ga}$ cylindrical phantom.	By manufacturer's recommendation	Quarterly
Normalization	N/A	By manufacturer's recommendation	By manufacturer's recommendation and major hardware repair	By manufacturer's recommendation, after significant QC results variation or hardware repair ^a
Absolute calibration (also called cross-calibration, well-counter calibration, radioactivity calibration factors, radioactivity concentration calibration, or SUV calibration)	N/A	Quarterly Also, always after soft/hardware revisions/upgrades, and after new setups/normalizations	By manufacturer's recommendation or after a hardware change	Quarterly
Image quality and accuracy of attenuation, and scatter correction and quantitation	Annually	Annually Also, always after major changes in soft/hardware	By manufacturer's recommendation	Annually
Preventive maintenance	N/A	By manufacturer's recommendation As well as calibration of all the devices involved (well counters, clocks, etc.).	6-monthly	Regular basis
PET and CT images alignment check (offset calibration or co-registration check)	Periodically	By manufacturer's recommendation	N/A	Quarterly and after gantries are separated
CT Part				
CT laser alignment				Monthly and after laser's service ^b
Tabletop alignment and positional accuracy, and scout scan accuracy				Monthly also, after service ^b
CT number and uniformity, image noise and artifacts				Monthly ^c
High contrast spatial resolution (MTF or modulation)	For all the test, at least annually according to ACR guidelines [25]	Recommended tests by national or international guidelines on CT QC. Following national law's recommendations	Recommended tests by IAC guidelines for CT	Monthly or after service that can affect MTF
Scatter radiation and shielding verification according to local regulations				Annually
KVp-values and HVL to verify appropriated filtration between source and patient				Annually also, after major changes
Dosimetry				Annually
Electron density accuracy	N/A	N/A	N/A	Annually ^d

Recommended QC tests and testing frequencies by international guidelines. N/A, the test is not included in the guideline, or testing frequency is not specified.

^aWhen performing normalization monthly, it is recommended to perform a detector calibration every 3 months or prior to the normalization if there are noticeable changes in QC over the preceding month.

^bIf the PET/CT system is used for radiotherapy planning, the test should be performed daily or prior to the patient examination.

^cDaily, Water CT number; monthly, CT number of other materials.

^dThe test applied only if the PET/CT system is used for radiotherapy planning.

TABLE 2 | QC tests and testing frequencies for MRI systems.

Test	ACR [13]	IAC [14]
Resonance/center frequency	Weekly	Daily ^a
Low contrast detectability (e.g., SNR)	Weekly	Daily ^a
Image uniformity/magnetic field homogeneity	Quarterly	Daily ^a
Linearity (geometry accuracy)	Weekly	Acceptance testing
High-contrast spatial resolution	Weekly	Acceptance testing
Low-contrast spatial resolution	Weekly	Acceptance testing
Image artifacts (e.g., Ghosting, DC-offset)	Weekly	Daily or weekly
Table positioning	Weekly	N/A
Slice thickness accuracy	Quarterly	Acceptance testing
Slice position/separation error (also called slice position accuracy)	Quarterly	Acceptance testing
Radiofrequency coil checks	Annually	Annually
Preventive maintenance	Annually	Annually

This table summarizes the recommendations on QC for MRI systems given by international guidelines. All the tests should be included in the acceptance testing to establish references values for the routine QC results. In this table, N/A: the test or testing frequency is not specified in the guideline.

^a Depending on the stability of the system, the test can be performed weekly instead daily.

of all the results of the QC survey can be found in **Table 3**. Results can be summarized in two statements: (I) there are no standard QC procedures for MRI or (II) the QC procedures are done entirely by and with phantoms provided by the vendors. We obtained a different response, only for some specific tests. The resonance frequency test for one of Siemens Biograph mMR (center 3) is indicated to be performed daily. For the Philips Ingenuity TF PET/MR, four of the surveyed tests [resonance frequency, image uniformity, linearity, and radiofrequency (RF) coils check tests] are performed weekly.

Additional to the performance tests for the PET and the MRI component of the system, PET and MR images alignment was reported to be checked with varying frequencies between centers with answers ranging from: at acceptance test or after an engineering service and by manufacturer's recommendation to regular checks in intervals between 3 and 12 months.

The frequency of the preventive maintenance was reported to be every 3 months in most of the centers with just two centers indicating intervals of every 6 months and yearly.

QC Procedures Implemented by the Vendor

Tables 4–6 present tests and testing frequencies included in the DQA of the Siemens, GE and Philips PET/MRI systems. A detector stability test is included within all DQA procedures. However, other tests vary between vendors. For the PET component of GE and Siemens systems, the DQA by the vendors is based on a $^{68}\text{Ge}/^{68}\text{Ga}$ PET Annulus Phantom (a hollow cylinder with a thick radioactive wall) and a cylindrical $^{68}\text{Ge}/^{68}\text{Ga}$ phantom, respectively. The DQA by Siemens includes testing the correct function of the detectors and electric components of the system. It includes an assessment of block noise, block

efficiency, system efficiency, and image plane efficiency. Further, it includes a measurement of randoms and scatter ratio, a normalization check, an inspection of the sinograms, and it performs a partial detector setup. For the GE PET/MRI systems, the DQA includes an assessment of the collected coincidences and singles, an assessment of deadtime, energy peak, and gain changes. In contrast, the DQA of the Philips systems is based on a ^{22}Na point source. The DQA include the inspection of the sinograms and an assessment of the energy resolution. For SIGNA GE PET/MR and Philips Ingenuity TF PET/MR, systems with TOF capabilities, the DQA by vendors also includes a timing resolution check.

Differences across the QC protocols implemented by the vendor were found for the MRI part of the PET/MRI systems.

Within the Siemens DQA, a coil check is available. Further, the preventive maintenance usually includes an image quality test using the head and body spherical phantoms (180 and 300 mm outer diameter, respectively) provided by the vendor. This test allows an assessment of signal-to-noise ratio (SNR) and artifacts. Also, procedures to check each configured local coil individually based on evaluation of SNR and image intensity are available and done usually during preventive maintenance to verify satisfactory coil operation.

For GE systems, at least one specific phantom is provided to check the MRI component; the TLT spherical phantom is used to test geometry accuracy, ghosting level, and SNR. The test is available in the DQA implemented by the vendor, but the system's user can decide to perform it or not.

For Philips systems, the DQA does not include any test for the MRI component. However, Philips provides a 200 mm head phantom to check the MRI component of the Ingenuity TF PET/MRI through an MRI IQ evaluation. This procedure is recommended to be done weekly and can be performed automatically by the system. However, it is recommended to visually check the images for artifacts (e.g., ghosting and lines).

Consensus Recommendation on QC for PET/MRI

The minimum consensus on PET/MRI QC includes for all the systems the following tests: For the PET component, the DQA implemented by the vendor, a quarterly cross-calibration (CC) test and a yearly IQ test. For the MRI component, the consensus includes a monthly coil check and an MR image quality test to be performed at least quarterly. Further, the check of the PET-MRI alignment should be performed after mechanical manipulations on the PET/MRI gantry and after software updates. **Table 7** summarizes the proposed recommendations, including the purpose of the test, testing frequency, and additional comments for the implementation on three of the commercially available PET/MRI systems.

DISCUSSION

In this work, existing QC guidelines for PET and MRI systems were summarized, and the variability of implemented QC protocols for PET/MRI systems was assessed with the ultimate

TABLE 3 | Performed QC tests and testing frequencies for PET/MRI systems across the participant sites.

Test	Siemens					GE		Philips
	CENTER 1	CENTER 2	CENTER 3	CENTER 4	CENTER 5	CENTER 6	CENTER 7	CENTER 8
PET Part								
DQA	Daily	Daily	Daily	Daily, DQA-Phantom	Daily	Daily	Daily Also, an additional monthly DQA with partial detector set-up with time alignment (CTC)	Daily
Detector stability	Daily	Daily	Daily	Daily, DQA-Phantom, quarterly, with constancy test	Daily	Daily	Daily, and full detector calibration after every significant intervention	Daily
Coincidence timing resolution	By manufacturer's recommendation	N/P	N/A	Daily, DQA-Phantom, quarterly, with constancy test	Daily	Quarterly	Monthly Also crystal (update bias) and energy calibration	Daily
Sensitivity	Daily	N/P	At acceptance test. Measurement of the absolute sensitivity of the system	Daily, DQA-Phantom, quarterly, with constancy test	Annually	At acceptance test	At acceptance test	Quarterly
Spatial resolution	N/P	N/P	Annually Scan of a NEMA phantom- recovery curve measurements	Daily, DQA-Phantom, quarterly, with constancy test	Annually	At acceptance test	At acceptance test	Once every 10 years
Image uniformity	Daily	N/P	Daily Profile plot through the phantom	Daily, DQA-Phantom, the system decides automatically if the test has to be done quarterly, with constancy test	Annually	Quarterly	Quarterly, combined with the normalization	Quarterly
Normalization	Daily: check	6-monthly and when new phantoms are acquired	Daily	Daily, DQA-Phantom	Daily	Quarterly	Quarterly	Quarterly
Cross- calibration	6-monthly	6-monthly and when a new phantom is acquired	Quarterly	Yearly and after getting a new DQA cylindrical phantom performed by vendor's instructions	Every 2 weeks	Quarterly	Quarterly	Quarterly
High-contrast spatial resolution	By manufacturer's recommendation	Quarterly MRI Maintenance and QA is done entirely by the vendor	Not performed as routine QC6-monthly and after repairs Constancy test by Siemens-Service with Siemens recommended phantoms	6-monthly and after repairs Constancy test by Siemens-Service with Siemens recommended phantoms	Quarterly by vendor	N/P	No standard QC procedures for MRI	Once every 10 years

(Continued)

TABLE 3 | Continued

Test	Siemens					GE		Philips
	CENTER 1	CENTER 2	CENTER 3	CENTER 4	CENTER 5	CENTER 6	CENTER 7	CENTER 8
Low-contrast spatial resolution	By manufacturer's recommendation	Quarterly MRI Maintenance and QA is done entirely by the vendor	Not performed as routine QC	6-monthly and after repairs Constancy test by Siemens-Service with Siemens recommended phantoms	Quarterly by vendor	N/P	No standard QC procedures for MRI	N/A
Table positioning	By manufacturer's recommendation	Quarterly MRI Maintenance and QA is done entirely by the vendor	Not performed as routine QC	6-monthly and after repairs Constancy test by Siemens-Service with Siemens recommended phantoms	Quarterly by vendor	Quarterly	Quarterly. During maintenance	Once every 10 years
Slice thickness accuracy	By manufacturer's recommendation	Quarterly MRI Maintenance and QA is done entirely by the vendor	Not performed as routine QC	6-monthly and after repairs Constancy test by Siemens-Service with Siemens recommended phantoms	Quarterly by vendor	N/P	No standard QC procedures for MRI	Once every 10 years
Slice position/separation error	By manufacturer's specifications	Quarterly MRI Maintenance and QA is done entirely by the vendor	N/A	6-monthly and after repairs Constancy test by Siemens-Service with Siemens recommended phantoms	Quarterly by vendor	N/P	No standard QC procedures for MRI	Once every 10 years
Radio-frequency coil checks	Daily included in the DQA	Quarterly MRI Maintenance and QA is done entirely by the vendor	Daily See note above regarding cycling coils	6-monthly and after repairs Constancy test by Siemens-Service with Siemens recommended phantoms	Quarterly by vendor	N/P	Quarterly. During maintenance	Weekly
MRI preventive maintenance	Quarterly	Quarterly MRI Maintenance and QA is done entirely by the vendor	Quarterly	6-monthly and after repairs Constancy test by Siemens (Siemens recommended phantoms)	Quarterly by vendor	Quarterly	Quarterly	Quarterly

N/A, Not clear definition of the test; N/P, Not performed as part of the routine QC.

TABLE 4 | DQA tests for Siemens Biograph mMR PET/MR systems.

Imaging component	Test	Tool/calculation	Tolerance criteria
PET	Partial detector setup	PET 20 cm mMR ^{68}Ge Daily QC phantom (uniform) and the required holder Parts of the PET detector electronics are calibrated during this test.	Not apply
	Normalization	PET 20 cm mMR ^{68}Ge Daily QC phantom (uniform) and the required holder New normalization map is created. Further, it checks if a valid and successful normalization result is available in the system's database. Sinograms of the phantom scan are displayed, and visual assessment is required.	Normal looking sinogram is expected.
	Block noise	The system displays the number of blocks out of range.	0–3 crystals
	Block efficiency	Checks for a uniform detector response by comparing a block response to the average of all the block responses. The system displays the number of blocks out of range.	80–120%
	Measured randoms	Checks the capability of the system for measuring random events.	85–115%
	Scanner efficiency	Checks the counting rate produced by a known activity concentration.	33.6–62.4 (count/sec)/(Bq/cc)
	Scatter ratio	Checks the scatter fraction by a known activity concentration	31.5–38.5%
	Scanner efficiency correction factor (ECF)	Calculates the value of the scanner quantification factor to determine the ratio between the activity in the scanner and the detected counts.	1.8E007–2.8E007 (Bq*s)/(ECAT counts)
	Image plane efficiency	To determine hardware variances of line of response detection to getting a uniform image. The system displays the number of planes out of range.	0–5%

The daily procedure included by the vendor only checks the PET component of the PET/MRI systems. It aims to perform a PET setup and normalization. The reference values for these tests are established during acceptance testing and updated to the last calibration of the system. The boundaries shown in the table serve only as an example. No MRI-related tests are included in the DQA. The MRI component is checked during preventive maintenance/service. Ref: Biograph mMR. Function Description. System. Tune-Up/QA. © Siemens, 2011.

goal to reach a consensus on a minimum set of QC procedures. The results revealed quite significant variations between the existing recommendations and QC measures implemented in different centers. The reported variations of local PET and MRI QC procedures and testing frequencies are assumed to partly reflect the variations seen in the existing guidelines for the single modalities and the non-existence of specific recommendations for PET/MRI. However, in part, the variability in the reporting seems to be caused by differences in the definition of the specific tests between the centers and a lack of in-depth knowledge about the implemented QC measures included in the DQA and the tests performed by the vendor during the preventive maintenance. For example, the sensitivity of a PET system reflects how many events can be detected for a given activity within the field of view (FOV). A change in sensitivity can possibly be caused by malfunctioning detectors, changes in the energy resolution or the coincidence timing window. The NEMA NU2 protocols give clear testing procedures [26] to measure sensitivity in a reproducible and standardized way. However, to monitor sensitivity and to assess potential changes, multiple methods can be used. For example, the sensitivity can be monitored using the long half-life sources used for DQA (e.g., $^{68}\text{Ga}/^{68}\text{Ge}$). Therefore, these differences in methods to measure sensitivity can lead to differences in local definitions of this test, and thus, to differences in implementation and reporting. It can be seen in the results from the survey, where the answers indicate that some of the centers seem to refer to the specific NEMA NU2 protocol as the test for sensitivity, and thus, report this test to be done only during acceptance testing.

QC, as part of a quality assurance program, aims at monitoring if a system works as expected. For proper performance of the

PET part, the detectors and measurement electronics need to work correctly. Checking the detector stability and sensitivity allows early detection of any sudden changes (e.g., failures of detector modules). Normalization is needed to correct for variations of the efficiency of individual detectors and is essential for uniformity in reconstructed PET images. Further, the spatial resolution of a PET system, mainly dependent on the detector geometry and the set reconstruction protocol, is relevant for lesion detectability and quantitative readings of small structures. In TOF PET systems, the measurement of the timing resolution is needed to ensure TOF precision. Furthermore, the cross-calibration of the PET with the dose calibrators needs to be ensured for accurate quantitative measurements like SUVs. With the proposed recommendation, including the DQA, a quarterly cross-calibration test, and a yearly IQ assessment, proper PET performance can be ensured.

The DQA provided by the vendors covers most of the tests mentioned before. For all systems, the correct functionality of the detectors is checked, and the stability of sensitivity is assessed by the counts collected from a known activity source ($^{68}\text{Ge}/^{68}\text{Ga}$ cylinder phantom for Siemens, $^{68}\text{Ge}/^{68}\text{Ga}$ PET Annulus Phantom for GE and ^{22}Na point source for Philips). Further, for systems with TOF capabilities, a timing resolution test is included in the DQA, and for the Siemens PET/MRI system, the normalization map of the detectors is renewed. All these parameters are evaluated within the DQA compared to a baseline established at the commission of the system and updated during the last calibration or after replacement of the DQA source.

In addition to the DQA, cross-calibration is required to ensure proper quantification. The CC test is done using a

TABLE 5 | DQA tests for GE SIGNA PET/MR systems.

Imaging component	Test	Tool/calculation	Tolerance criteria
PET	Coincidence	PET annulus phantom Number of coincidence events associated with each crystal element. Coincidence counts or prompt rates with the DQA phantom are assessed by measuring the system mean, and the per block (4 × 9 crystals) mean against the expected values from a decay-corrected baseline. This test assesses system ability to produce coincidence events from detected singles and their timing values. Coincidence directly relates to sensitivity during patient acquisitions.	System mean change < ±9% of baseline Block mean change < ±18% of baseline
	Singles	PET annulus phantom Number of individual events detected in each crystal. Singles counts or singles rates with the DQA phantom are assessed by measuring the system mean, and the per block (4 × 9 crystals) mean against the expected value from a baseline after compensating for phantom activity decay. This test assesses system ability to detect and acquire singles events.	System mean change < ±9% of baseline Block mean change < ±27% of baseline
	Deadtime	PET annulus phantom The fraction of time that each detector block is busy. A high value may indicate noisy electronics or a light leak in the detector. A zero value indicates a loss of signal which should match low values in singles and coincidence.	System mean change ±0.002 Block change ±0.003
	Timing	PET annulus phantom Coincidence timing error for each crystal. Timing measurements indicate how many fractional bins of timing adjustment would be needed to calibrate timing. Timing bin size is 13.02 ps.	−1 to +1 System mean change < ±0.1 bins, < ±1.3 ps Block mean change < ±5 bins, < ±65 ps
	Energy peak	PET annulus phantom Peak energy spectrum of all crystals. Changes in position of the Energy Peak indicate that the current measured energy values, not including real-time gain stabilization (RTGS), have changed from their calibrated target positions. This can occur under conditions of thermal changes in the detection system and indicate a need to calibrate the gain.	System mean change < ±8%
	Gain changes	PET annulus phantom Gain assessment indicates the percentage change in gain that would be needed to adjust measured energies to their target values. Assessment is performed on each of 18 gain channels per detector block and on the mean value of change for the entire block.	Block mean change < ±6% Channel change < ±8%
MRI	Geometric accuracy	TLT spherical phantom. Calculation of the relative diameter of the phantom along the phase and frequency directions x, y, and z (e.g., $D_x = D_{\text{phase}}$, $x - D_{\text{freq}}$, x). Here, D is the ratio between the measured and known diameter of the phantom along x, y, and z-direction.	Not applicable
	Ghosting level	TLT spherical phantom. Average value of the signal reported in a square 25 pixel ROI (5 × 5 pixels) in the region beyond the phantom area in the phase-encoding direction.	Not applicable
	Signal to noise ratio	Ratio S/N calculated from one signal image and one noise image. Calculation of transmit gain (TG in 0.1 dB) and center frequency (CF in Hz). This test can be performed with different combinations of coil/phantoms/holders	Not applicable

The results obtained from the PET component are compared with a baseline established at the commissioning of the system and updated quarterly. Ref: SIGNA™ PET/MR. 26.0 Operator Manual English 5770625-1EN (2017/11) Rev.2. © General Electric Company, 2017.

homogeneously water filled cylinder usually provided by the vendor together with the respective attenuation correction protocol. A change in cross-calibration is unlikely to be caused by a change in PET system stability [27]. Therefore, changes are expected to be mostly related to replacement of the $^{68}\text{Ge}/^{68}\text{Ga}$ phantom (for GE and Siemens DQA) which are also used for PET calibration, changes in the calibration of the dose calibrators or modified cross-calibration factors after software updates. To covering all these potential influencing factors, an at

least quarterly cross-calibration check for ^{18}F is recommended. Furthermore, CC checks and eventually CC adjustments have to be performed after replacements of the DQA phantoms, software updates or changes in the dose calibrators used for patient injection dose measurements. In addition to the CC, the CC phantom measurements can be used for the evaluation of the axial and transaxial uniformity, e.g., using the method published by the IAEA [16], and it is used for the normalization of the Philips PET/MRI system.

TABLE 6 | DQA tests for Philips Ingenuity TF PET/MR systems.

Imaging component	Test	Tool/calculation	Tolerance criteria
PET	System initialization	Restarts the hardware and firmware on the system	If the system initialization fails, the program stops
	Hardware sensor test	Verifies that voltages and currents are correct for PET gantry electronics	Not specified
	Baseline collection	The system collects the analog offsets of all photomultiplier channels as baseline data. These baseline values are used by the scanner processing electronics as a reference in each data collection and after baseline collection.	The system displays a message indicating when a Baseline Collection is completed successfully. If the measured values are slightly outside the normal range, it is possible using the scanner. If the measured values are significantly outside the allowed range, the scanner should not be used.
	PMT gain calibration	Optimizes the electronic gain for each PMT channel. When the system cannot calibrate all the PMTs for the target gain value within the allowed number of tries, the system displays a failed status message.	Target gain value
	Energy	²² Na source centered in a 256 mm FOV. Collects list View data and calculates the energy centroids and FWHM.	Energy centroids should be ~100. FWHM Threshold.
	Timing	²² Na source centered in a 256 mm FOV. The Timing Test compares the system timing against the calibration settings.	Reference values from timing calibration.
	Emission sinogram	²² Na source centered in a 256 mm FOV. Collects data for the emission QC sinogram for 2 min. Alerts when the system drift affects image quality or if acquisition hardware is defective.	Visual assessment

Summary of the test, tools, and calculation methods for the daily QC of the PET component of the system. Also, a weekly test using a 200 mm head phantom is suggested for the IQ test of the MRI component. Ref, Information provided by the vendor.

In general, a PET system uses a single CC factor usually based on ¹⁸F. In theory, this should allow a correct quantification of any PET isotope, given the correct set of correction factors for differences in positron branching ratios and half-life in the PET software and, in case of non-pure positron emitters, a proper prompt gamma correction [28]. However, previous studies have reported deviations in CC for isotopes other than ¹⁸F [29]. These deviations were attributed to incorrect calibration factors within the dose calibrators [30] or effects resulting from the use of different isotope containers between calibration and clinical routine [31]. To account for these issues, a check of the CC for all PET isotopes in clinical use is recommended to be done at least once. In case of deviations in CC for additional isotopes, it is recommended to adjust the dose calibrator settings accordingly. In cases where this is not possible (e.g., due to legal restrictions concerning the calibration of the dose calibrator) the deviation in quantification needs to be communicated with the respective personal and has to be taken into account if quantitative readings are used for comparison between different PET systems. Further, as a regular QC it is recommended to check the dose calibrator settings for all used isotopes at least yearly (e.g., following a procedure as described in Logan et al. [32]) and, in case of doubt, perform an additional CC test.

With the DQA and the cross-calibration measurements, the proper function of the PET system is essentially ensured. However, in compliance with the EARL initiative, a yearly IQ test is recommended additionally to get an assessment of the overall system performance regarding image quality and, as contrast recovery- and recovery coefficients are dependent on the spatial resolution, also spatial resolution. To do so, a protocol

as described by NEMA NU2 [33] or the EARL accreditation program [34] can be used. Further, the IQ phantom acquisition can be used to assess uniformity evaluating standard deviation and mean values of background regions-of-interest [35]. In case the NEMA IQ phantom is not available on-site, the alternative use of the ACR PET Phantom can be considered to assess overall image quality. Procedures for the measurements and image analysis of the ACR PET Phantom are described in Difilippo et al. [36], American College of Radiology [37], American College of Radiology [38]. However, corresponding valid attenuation correction maps are required when using PET phantoms for QC of PET/MRI systems [10, 39, 40]. Therefore, when adopting the ACR Phantom for IQ assessments, dedicated protocols (e.g., using CT-based templates for AC) must be available.

On top of the tests mentioned above, the synchronization of the clocks of all relevant devices (e.g., PET/MRI, dose calibrator, well-counter) needs to be ensured for accurate quantitative PET readings [41].

For the MRI component of the PET/MRI systems, we recommend doing at least an evaluation of the image quality by means of SNR, geometric accuracy, and artifacts (e.g., ghosting, lines). With an overall IQ test, which includes the parameters mentioned, distortions in resonance frequency, static B0 field, and gradient field can also be detected. For example, magnetic field homogeneity has a direct impact on the SNR. Therefore, GE has an implemented DQA for MRI including IQ assessment, Philips recommends an IQ assessment to be done weekly and Siemens systems allow general performance of the MRI component to be tested by using the head and body spherical phantoms, and thus, IQ assessment through

TABLE 7 | HYBRID consensus recommendations on quality control tests for PET/MRI systems.

Imaging component	Test	Purpose	Frequency	Siemens	GE	Philips
PET	Daily QC	To check the proper operation of the PET detectors, check system response to a given activity source and determine the correct initialization and readiness of the system for scanning.	Daily	$^{68}\text{Ge}/^{68}\text{Ga}$ cylindrical phantom Partial PET detector setup Normalization Sinograms evaluation Block noise Block efficiency Measured randoms Scanner efficiency (E) Scatter ratio E correction factor Image plane efficiency	$^{68}\text{Ge}/^{68}\text{Ga}$ PET annulus phantom Coincidence (sensitivity) Singles Deadtime Timing Energy peak Gain changes	^{22}Na-point source System initialization Hardware sensor test PMT gain calibration Energy Timing Emission sinogram Baseline collection
	Cross-calibration	To ensure proper calibration of the system against a reference device for accurate determination of activity.	Quarterly for ^{18}F After DQA phantom's replacement, software updates or changes in the dose calibrator	Water filled cylinder Calibration Uniformity (axial and transaxial)	Water filled cylinder Calibration Uniformity (axial and transaxial) Normalization	Water filled cylinder Calibration Uniformity (axial and transaxial) Normalization
	PET image quality	For overall evaluation of the reconstructed image for quantitative applications.	Annually	NEMA IQ phantom Contrast recovery Background variability SUV recovery coefficients (alternative: ACR PET phantom and respective evaluations)	NEMA IQ phantom Contrast recovery Background variability SUV recovery coefficients (alternative: ACR PET phantom and respective evaluations)	NEMA IQ phantom Contrast recovery Background variability SUV recovery coefficients (alternative: ACR PET phantom and respective evaluations)
MRI	Coil check	Check proper functioning of the local RF coils. To be performed with different phantom-coils combinations.	Monthly Also, whenever required for new/replaced coils	Different coil-phantom arrangements SNR Artifacts	Different coil-phantom arrangements SNR Artifacts	Different coil-phantom arrangements SNR Artifacts
	MR image quality	For an overall check of the minimum parameters for appropriate MRI performance.	Quarterly or by manufacturer's specifications	Head and body spherical phantoms SNR Artifacts (ghosting, lines) Geometry accuracy	TLT spherical phantom (Included in the DQA) SNR Artifacts (ghosting, lines) Geometry accuracy	200 mm-Head phantoms SNR Artifacts (ghosting, lines) Geometry accuracy
PET-MRI	PET and MRI alignment	To ensure proper co-registration of the PET and MR images, avoiding artifacts for misregistration.	After mechanical manipulations on the PET/MRI gantry and after software updates.	Always after separation of the gantries or other major hardware repair and after software updating		Always after major hardware repair and software updating

Summary of the recommended test, the purpose of the test, testing frequencies. Specific information for the Biograph mMR PET/MR, the GE SIGNA PET/MR, and the Ingenuity TF PET/MR is also included.

artifacts and SNR calculation in the phantom images is feasible. In general, we suggest performing the MR image quality test by using the procedure and phantoms specified by the vendor. If no specifications are provided, the MRI IQ can be tested as described by the AAPM and ACR [42, 43]. The ACR suggests performing an MRI IQ test annually. However, the possibility to discover fails (e.g., in image intensity uniformity) with a higher testing frequency has been demonstrated [44]. Therefore, we suggest performing an MRI IQ test quarterly.

It is also recommended to check the function and quality of additional hardware such as coils. Checking the coil performance permits the detection of issues with the coils before these affect clinical scans and clinical image quality. This test is particularly

important when using flexible coils, which are more susceptible to deterioration. The procedure for coil performance testing may be provided by coil or MRI system manufacturer, but can also be done by analyzing the image SNR and artifacts for specific phantom-coil arrangements, as described in American College of Radiology [43]. International guidelines for dedicated MRI systems suggest to perform an annual coil check; however, PET/MRI systems vendors such as Siemens suggest a daily test of the primary coils in use. Therefore, for easy implementation, we suggest performing a monthly coil check of the most used coils on-site, and whenever new/replacement coils need to be accepted.

Finally, no significant interference between the PET and MRI components has been observed for combined clinical

3T PET/MRI systems [2, 45–47], and therefore, QC test performed simultaneously on PET and MRI might not be required. However, the spatial alignment of both components needs to be ensured. Checking the image co-registration for different sequences used clinically may help to reduce the effect of misalignment artifacts, such as incorrect interpretation of fused images due to improperly localized lesions in oncological PET/MRI studies [48]. The test should always be performed after separation of the gantries and software updating since the offset calibration values can be overwritten.

Considerations for Specific Applications

It should be mentioned that the QC for MRI covers only a basic evaluation of the most critical parameters for proper performance of the imaging modality. Therefore, specific MRI techniques and sequences may require higher standards concerning the stability of specific parameters. For example, MRI applications such as ultrafast imaging (echo-planar imaging, EPI) will be more sensitive to field inhomogeneities and thus, may require more stringent testing [49]. Inhomogeneities in B0 magnetic field produce blurring, distortion, and signal loss at tissue interfaces, particularly at the edge of the field of view. These image distortions are relevant as they may cause errors in tissue segmentation on anatomical images and attenuation correction [50]. Likewise, distortions in the image scale (geometry) may cause significant bias in radiotherapy planning [51]. Therefore, it is recommended to include additional QC procedures tailored to the specific purpose and depending on the MRI application.

As an example, one of the centers involved in this consensus has created three specific QC procedures to monitor the MRI scanner's behavior for specific applications frequently performed on-site. MR spectroscopy QC is performed every week. The procedure entails a single voxel acquisition on the manufacturer-provided spectroscopy phantom containing water, acetone, and lactate. The water and acetone peaks are monitored for peak-frequency, peak-SNR, and peak-width. Furthermore, an MRI diffusion QC is performed weekly. In this case, the acquisition of apparent diffusion coefficient maps (ADC) and fractional anisotropy (FA) in the manufacturer-provided doped water bottle phantom is performed. Average ADC and FA within the bottle are monitored. A monthly QC procedure was implemented to monitor potential RF artifacts created by a blood-sampling pump which operates within the scanner room. The pump is switched on while a manufacturer-created RF noise scan performed. The peaks created by the pump are monitored for location and

SNR, to intervene if the peak amplitude or position shifts away from normal.

CONCLUSION

Existing QC guidelines and recommendations for PET and MR imaging modalities vary both, in detail and range. Likewise, variations in local PET/MRI QC measures across European hybrid imaging sites were reported. However, these variations can partly be attributed to differences in the definitions of the tests and a lack of in-depth knowledge of the tests performed during DQA.

Based on these observations, a recommendation for a minimum set of QC procedures was developed in consensus, to ensure the proper functioning of whole-body PET/MRI systems. This recommendation includes the DQA, a cross-calibration measurement and an assessment of IQ for PET, a regular IQ test for MRI as well as a regular coil check, and checks of the PET and MRI alignment.

DATA AVAILABILITY STATEMENT

All datasets generated for this study are included in the manuscript/supplementary files.

AUTHOR CONTRIBUTIONS

AV, TB, and IR contributed to the conception, design of the study, and performed the analysis. AV organized the database and drafted the first draft of the manuscript. TB, IR, and FP contributed sections of the manuscript. All authors contributed to the collection of information, manuscript revision, and read, and approved the submitted version.

FUNDING

This project has received funding from the European Union's Horizon 2020 research and innovation programme under the Marie Skłodowska-Curie grant agreement No. 764458. The work reflects only the author's view, and the Agency is not responsible for any use that may be made of the information it contains.

ACKNOWLEDGMENTS

The authors thank the PhD students of the HYBRID consortium and imaging physicists across the sites who participated in this study for their contributions.

REFERENCES

1. Zaidi H, Ojha N, Morich M, Griesmer J, Hu Z, Maniawski P, et al. Design and performance evaluation of a whole-body ingenuity TF PET-MRI system. *Phys Med Biol.* (2011) **56**:3091–106. doi: 10.1088/0031-9155/56/10/013
2. Delso G, Fürst S, Jakoby B, Ladebeck R, Ganter C, Nekolla SG, et al. Performance measurements of the siemens mMR integrated whole-body PET/MR scanner. *J Nucl Med.* (2011) **52**:1914–22. doi: 10.2967/jnumed.111.092726
3. Muzic RF Jr, DiFilippo FP. Positron emission tomography-magnetic resonance imaging: technical review. *Semin Roentgenol.* (2014) **49**:242–54. doi: 10.1053/j.ro.2014.10.001
4. Erlandsson K, Dickson J, Arridge S, Atkinson D, Ourselin S, Hutton BF. MR imaging-guided partial volume correction of PET data in PET/MR imaging. *PET Clin.* (2016) **11**:161–77. doi: 10.1016/j.cpet.2015.09.002
5. Keller SH, Hansen C, Hansen C, Andersen FL, Ladefoged C, Svarer C, et al. Motion correction in simultaneous PET/MR brain imaging using sparsely

- sampld MR navigators: a clinically feasible tool. *EJNMMI Phys.* (2015) 2:14. doi: 10.1186/s40658-015-0126-z
6. Huang SY, Franc BL, Harnish RJ, Liu G, Mitra D, Copeland TP, et al. Exploration of PET and MRI radiomic features for decoding breast cancer phenotypes and prognosis. *NPJ Breast Cancer.* (2018) 4:24. doi: 10.1038/s41523-018-0078-2
 7. Rausch I, Bergmann H, Geist B, Schaffarich M, Hirtl A, Hacker M, et al. Variation of system performance, quality control standards and adherence to international FDG-PET/CT imaging guidelines. *Nuklearmedizin.* (2014) 53:242–8. doi: 10.3413/Nukmed-0665-14-05
 8. Beyer T, Czernin J, Freudenberg LS. Variations in clinical PET/CT operations: results of an international survey of active PET/CT users. *J Nucl Med.* (2011) 52:303–10. doi: 10.2967/jnumed.110.079624
 9. Kaalep A, Sera T, Oyen W, Krause BJ, Chiti A, Liu Y, et al. EANM/EARL FDG-PET/CT accreditation - summary results from the first 200 accredited imaging systems. *Eur J Nucl Med Mol Imaging.* (2018) 45:412–22. doi: 10.1007/s00259-017-3853-7
 10. Boellaard R, Rausch I, Beyer T, Delso G, Yaqub M, Quick HH, et al. Quality control for quantitative multicenter whole-body PET/MR studies: a NEMA image quality phantom study with three current PET/MR systems. *Med Phys.* (2015) 42:5961–9. doi: 10.1118/1.4930962
 11. Annual Congress of the European Association of Nuclear Medicine October 13 – 17, 2018 Düsseldorf, Germany. *Eur J Nucl Med Mol Imaging* 2018; 45: 1–844. doi: 10.1007/s00259-018-4148-3
 12. American College of Radiology. *Nuclear Medicine Accreditation Program Requirements.* Reston, VA (2018).
 13. American College of Radiology. *Manual of Procedures Part C: MRI Technical Procedures.* Philadelphia, PA (2013).
 14. Intersocietal Accreditation Commission. *The IAC Standards and Guidelines for MRI Accreditation.* Ellicott City, MD (2017).
 15. Boellaard R, Delgado-Bolton R, Oyen WJ, Giammarile F, Tatsch K, Eschner W, et al. FDG PET/CT: EANM procedure guidelines for tumour imaging: version 2.0. *Eur J Nucl Med Mol Imaging.* (2014) 42:328–54. doi: 10.1007/s00259-014-2961-x
 16. International Atomic Energy Agency. *Quality Assurance for PET and PET/CT Systems.* Vienna (2012).
 17. American College of Radiology and the American Association of Physicists in Medicine. *ACR-SPR Practice Parameters for Performing FDG-PET/CT in Oncology.* Reston, VA (2016).
 18. Lasnon C, Desmonts C, Quak E, Gervais R, Do P, Dubos-Arvis C, et al. Harmonizing SUVs in multicentre trials when using different generation PET systems: prospective validation in non-small cell lung cancer patients. *Eur J Nucl Med Mol Imaging.* (2013) 40:985–96. doi: 10.1007/s00259-013-2391-1
 19. Sattler B, Jochimsen T, Barthel H, Sommerfeld K, Stumpp P, Hoffmann KT, et al. Physical and organizational provision for installation, regulatory requirements and implementation of a simultaneous hybrid PET/MR-imaging system in an integrated research and clinical setting. *Magn Reson Mater Physics, Biol Med.* (2013) 26:159–71. doi: 10.1007/s10334-012-0347-2
 20. Tateishi U, Nakamoto Y, Murakami K, Kaneta T, Toriihara A. *Guidelines for the Clinical Use of 18 F-FDG-PET/MRI 2012 (Ver 1.0): Part 2.* Yokohama (2012).
 21. Umutlu L, Beyer T, Grueneisen JS, Rischpler C, Quick HH, Veit-Haibach P, et al. Whole-body [18F]-FDG-PET/MRI for oncology: a consensus recommendation. *Nuklearmedizin.* (2019) 58:68–76. doi: 10.1055/a-0830-4453
 22. EANM-SNMMI. *Quality Control of Nuclear Medicine Instrumentation and Protocol Standardisation.* Vienna (2017).
 23. Intersocietal Accreditation Commission. *The IAC Standards and Guidelines for Nuclear/PET Accreditation.* Ellicott City, MD (2017).
 24. Maissonobe J-A, Soret M, Kas A. 14. Quantitative performance of a Signa PET/MR based on the NEMA NU 2-2007 standard. *Phys Med.* (2016) 32:347–8. doi: 10.1016/j.ejmp.2016.11.065
 25. Intersocietal Accreditation Commission. *The IAC Standards and Guidelines for CT Accreditation.* (2017). Available online at: <https://www.intersocietal.org/ct/> (accessed June 4, 2018).
 26. National Electrical Manufacturers Association. *NEMA NU 2-2012: Performance Measurements of Positron Emission Tomographs.* Rosslyn, VA (2012).
 27. Keller SH, Jakoby B, Svalling S, Kjaer A, Højgaard L, Klausen TL. Cross-calibration of the Siemens mMR: easily acquired accurate PET phantom measurements, long-term stability and reproducibility. *EJNMMI Phys.* (2016) 3:11. doi: 10.1186/s40658-016-0146-3
 28. Conti M, Eriksson L. Physics of pure and non-pure positron emitters for PET: a review and a discussion. *EJNMMI Phys.* (2016) 3:8. doi: 10.1186/s40658-016-0144-5
 29. Wooten AL, Lewis BC, Szatkowski DJ, Sultan DH, Abidin KI, Voller TF, et al. Calibration setting numbers for dose calibrators for the PET isotopes ⁵²Mn, ⁶⁴Cu, ⁷⁶Br, ⁸⁶Y, ⁸⁹Zr, ¹²⁴I. *Appl Radiat Isot.* (2016) 113:89–95. doi: 10.1016/j.apradiso.2016.04.025
 30. Bailey DL, Hofman MS, Forwood NJ, O'Keefe GJ, Scott AM, van Wyngaardt WM, et al. Accuracy of dose calibrators for ⁶⁸Ga PET imaging: unexpected findings in a multicenter clinical pretrial assessment. *J Nucl Med.* (2018) 59:636–8. doi: 10.2967/jnumed.117.202861
 31. Bauwens M, Pooters I, Cobben R, Visser M, Schnerr R, Mottaghy F, et al. A comparison of four radionuclide dose calibrators using various radionuclides and measurement geometries clinically used in nuclear medicine. *Phys Med.* (2019) 60:14–21. doi: 10.1016/j.ejmp.2019.03.012
 32. Logan WK, Blondeau KL, Widmer DJ, Holmes RA. Accuracy testing of dose calibrators. *J Nucl Med Technol.* (1985) 13:215–7.
 33. National Electrical Manufacturers Association. *Performance Measurements of Positron Emission Tomographs (PET).* (2018). Available online at: <https://www.nema.org/Standards/Pages/Performance-Measurements-of-Positron-Emission-Tomographs.aspx> (accessed March 16, 2019).
 34. European Association of Nuclear Medicine. *EANM Research Ltd (EARL). New EANM FDG PET/CT Accreditation Specifications for SUV Recovery Coefficients.* Available online at: http://earl.eanm.org/cms/website.php?id=/en/projects/fdg_pet_ct_accreditation/accreditation_specifications.htm (accessed March 16, 2019).
 35. Deller TW, Khalighi MM, Jansen FP, Glover GH. PET imaging stability measurements during simultaneous pulsing of aggressive MR sequences on the SIGNA PET/MR system. *J Nucl Med.* (2017) 59:167–72. doi: 10.2967/jnumed.117.194928
 36. Difilippo FP, Patel M, Patel S. Automated quantitative analysis of ACR PET phantom images. *J Nucl Med Technol J Nucl Med Technol.* (2019). doi: 10.2967/jnmt.118.221317
 37. American College of Radiology. *American College of Radiology PET Accreditation Program Testing Instructions.* (2019). Available online at: <https://www.acraccreditation.org/-/media/ACRAccreditation/Documents/NucMed-PET/PET-Forms/PET-Testing-Instructions.pdf?la=en> (accessed July 30, 2019).
 38. American College of Radiology. *PET Phantom Instructions for Evaluation of PET Image Quality.* (2010). Available online at: <https://www.aapm.org/meetings/amos2/pdf/49-14437-10688-860.pdf> (accessed July 30, 2019).
 39. Ziegler S, Jakoby BW, Braun H, Paulus DH, Quick HH. NEMA image quality phantom measurements and attenuation correction in integrated PET/MR hybrid imaging. *EJNMMI Phys.* (2015) 2:18. doi: 10.1186/s40658-015-0122-3
 40. Eldib M, Oesingmann N, Faul DD, Kostakoglu L, Knešarek K, Fayad ZA. Optimization of yttrium-90 PET for simultaneous PET/MR imaging: a phantom study. *Med Phys.* (2016) 43:4768–74. doi: 10.1118/1.4958958
 41. Boellaard R. Standards for PET image acquisition and quantitative data analysis. *J Nucl Med.* (2009) 50:11S–20S. doi: 10.2967/jnumed.108.057182
 42. Price RR, Axel L, Morgan T, Newman R, Perman W, Schneiders N. *AAPM Report No. 28: Quality Assurance Methods and Phantoms for Magnetic Resonance Imaging.* New York, NY (1990).
 43. American College of Radiology. *ACR Magnetic Resonance Imaging (MRI) Quality Control Manual.* (2015). Available online at: <https://shop.acr.org/Default.aspx?TabID=55&ProductId=731499117> (accessed May 18, 2019).
 44. Chen C-C, Wan Y-L, Wai Y-Y, Liu H-L. Quality assurance of clinical MRI scanners using ACR MRI phantom: preliminary results. *J Digit Imaging.* (2004) 17:279–84. doi: 10.1007/s10278-004-1023-5

45. Levin CS, Maramraju SH, Khalighi MM, Deller TW, Delso G, Jansen F. Design features and mutual compatibility studies of the time-of-flight PET capable GE SIGNA PET/MR system. *IEEE Trans Med Imaging*. (2016) **35**:1907–14. doi: 10.1109/TMI.2016.2537811
46. Hong SJ, Kang HG, Ko GB, Song IC, Rhee JT, Lee JS. SiPM-PET with a short optical fiber bundle for simultaneous PET-MR imaging. *Phys Med Biol*. (2012) **57**:3869–83. doi: 10.1088/0031-9155/57/12/3869
47. Vargas MI, Becker M, Garibotto V, Heinzer S, Loubeyre P, Gariani J, et al. Approaches for the optimization of MR protocols in clinical hybrid PET/MRI studies. *Magn Reson Mater Phys Biol Med*. (2013) **26**:57–69. doi: 10.1007/s10334-012-0340-9
48. Roy P, Lee JK, Sheikh A, Lin W. Quantitative comparison of misregistration in abdominal and pelvic organs between PET/MRI and PET/CT: effect of mode of acquisition and type of sequence on different organs. *Am J Roentgenol*. (2015) **205**:1295–305. doi: 10.2214/AJR.15.14450
49. AAPM REPORT NO. 100 Acceptance Testing and Quality Assurance Procedures for Magnetic Resonance Imaging Facilities. (2010). Available online at: https://www.aapm.org/pubs/reports/RPT_100.pdf (accessed May 2, 2019).
50. Exhibit E, Mallia A, Bashir U, Stirling J, Joemon J, MacKewn J, et al. Artifacts and diagnostic pitfalls in PET/MRI. *ECR*. (2016) **C.0773**:1–21. doi: 10.1594/ecr2016/C-0773
51. Rai R, Kumar S, Batumalai V, Elwadia D, Ohanessian L, Juresic E, et al. The integration of MRI in radiation therapy: collaboration of radiographers and radiation therapists. *J Med Radiat Sci*. (2017) **64**:61–8. doi: 10.1002/jmrs.225

Conflict of Interest: The authors declare that the research was conducted in the absence of any commercial or financial relationships that could be construed as a potential conflict of interest.

Copyright © 2019 Valladares, Ahangari, Beyer, Boellaard, Chalampalakakis, Comtat, DalToso, Hansen, Koole, Mackewn, Marsden, Nuyts, Padormo, Peeters, Poth, Solari and Rausch. This is an open-access article distributed under the terms of the Creative Commons Attribution License (CC BY). The use, distribution or reproduction in other forums is permitted, provided the original author(s) and the copyright owner(s) are credited and that the original publication in this journal is cited, in accordance with accepted academic practice. No use, distribution or reproduction is permitted which does not comply with these terms.



Attenuation Correction Approaches for Serotonin Transporter Quantification With PET/MRI

Lucas Rischka¹, Gregor Gryglewski¹, Neydher Berroterán-Infante², Ivo Rausch³, Gregory Miles James¹, Manfred Klöbl¹, Helen Sigurdardottir¹, Markus Hartenbach², Andreas Hahn¹, Wolfgang Wadsak^{2,4}, Markus Mitterhauser^{2,5}, Thomas Beyer³, Siegfried Kasper¹, Daniela Prayer⁶, Marcus Hacker² and Rupert Lanzenberger^{1*}

¹ Department of Psychiatry and Psychotherapy, Medical University of Vienna, Vienna, Austria, ² Division of Nuclear Medicine, Department of Biomedical Imaging and Image-Guided Therapy, Medical University of Vienna, Vienna, Austria, ³ QIMP Group, Center for Medical Physics and Biomedical Engineering, Medical University of Vienna, Vienna, Austria, ⁴ CBmed, Graz, Austria, ⁵ Ludwig Boltzmann Institute Applied Diagnostics, Vienna, Austria, ⁶ Division of Neuroradiology and Musculoskeletal Radiology, Department of Biomedical Imaging and Image-Guided Therapy, Medical University of Vienna, Vienna, Austria

OPEN ACCESS

Edited by:

Claudia Kuntner,
Austrian Institute of Technology (AIT),
Austria

Reviewed by:

Paul Cumming,
University of Bern, Switzerland
Cristina Lois,
Massachusetts General Hospital,
Harvard Medical School,
United States

*Correspondence:

Rupert Lanzenberger
rupert.lanzenberger@
meduniwien.ac.at

Specialty section:

This article was submitted to
Medical Physics and Imaging,
a section of the journal
Frontiers in Physiology

Received: 03 May 2019

Accepted: 04 November 2019

Published: 22 November 2019

Citation:

Rischka L, Gryglewski G,
Berroterán-Infante N, Rausch I,
James GM, Klöbl M, Sigurdardottir H,
Hartenbach M, Hahn A, Wadsak W,
Mitterhauser M, Beyer T, Kasper S,
Prayer D, Hacker M and
Lanzenberger R (2019) Attenuation
Correction Approaches for Serotonin
Transporter Quantification With
PET/MRI. *Front. Physiol.* 10:1422.
doi: 10.3389/fphys.2019.01422

Background: Several MR-based attenuation correction (AC) approaches were developed to conquer the challenging AC in hybrid PET/MR imaging. These AC methods are commonly evaluated on standardized uptake values or tissue concentration. However, in neurotransmitter system studies absolute quantification is more favorable due to its accuracy. Therefore, our aim was to investigate the accuracy of segmentation- and atlas-based MR AC approaches on serotonin transporter (SERT) distribution volumes and occupancy after a drug challenge.

Methods: 18 healthy subjects (7 male) underwent two [¹¹C]DASB PET/MRI measurements in a double-blinded, placebo controlled, cross-over design. After 70 min the selective serotonin reuptake inhibitor (SSRI) citalopram or a placebo was infused. The parameters total and specific volume of distribution (V_T , $V_S = BP_P$) and occupancy were quantified. All subjects underwent a low-dose CT scan as reference AC method. Besides the standard AC approaches DIXON and UTE, a T1-weighted structural image was recorded to estimate a pseudo-CT based on an MR/CT database (pseudoCT). Another evaluated AC approach superimposed a bone model on AC DIXON. Lastly, an approach optimizing the segmentation of UTE images was analyzed (RESOLUTE). PET emission data were reconstructed with all 6 AC methods. The accuracy of the AC approaches was evaluated on a region of interest-basis for the parameters V_T , BP_P , and occupancy with respect to the results of AC CT.

Results: Variations for V_T and BP_P were found with all AC methods with bias ranging from -15 to 17%. The smallest relative errors for all regions were found with AC pseudoCT (<|5%|). Although the bias between BP_P SSRI and BP_P placebo varied markedly with AC DIXON (<|12%|) and AC UTE (<|9%|), a high correlation to AC CT was obtained ($r^2 \sim 1$). The relative difference of the occupancy for all tested AC methods was small for SERT high binding regions (<|4%|).

Conclusion: The high correlation might offer a rescaling from the biased parameters V_T and BP_P to the true values. Overall, the pseudoCT approach yielded smallest

errors and the best agreement with AC CT. For SERT occupancy, all AC methods showed little bias in high binding regions, indicating that errors may cancel out in longitudinal assessments.

Keywords: attenuation correction, PET/MRI, serotonin transporter, [^{11}C]DASB, occupancy, absolute quantification

INTRODUCTION

The introduction of combined imaging systems, such as positron emission tomography/computed tomography (PET/CT) proposed a number of benefits, especially for clinical routine, due to aligned structural and molecular information (Townsend et al., 2004). Furthermore, the development of combined positron emission tomography/magnetic resonance imaging (PET/MRI) systems enabled the simultaneous acquisition of functional and molecular information. This option decreases the intrasubject variability between separate measurements (e.g., caused by habituation effects, differences in motivation and attention or fluctuating intrinsic activity) (Hahn et al., 2017). This is especially of importance when functional changes should be compared to molecular changes within the same setting, e.g., after drug challenge (Sander et al., 2013).

However, PET/MRI brought along a major challenge; photons are attenuated to varying extent by different tissue types traversed on the way to the detectors. Ignoring this photon attenuation causes an erroneous reconstruction of the activity distribution (Huang et al., 1979). Hence, it is crucial that PET data is corrected for attenuation. On stand-alone PET systems, attenuation correction (AC) is performed for example with retractable radioactive rod sources of $^{68}\text{Ga}/^{68}\text{Ge}$, rotating around the patient and generating an AC map (Bailey, 1998). In PET/CT systems, a CT is acquired and scaled from Hounsfield units (HU) to linear attenuation coefficients at 511 keV (Carney et al., 2006). The difficulty with AC in PET/MRI systems is that neither rod sources nor a CT are currently installed due to technical challenges, such as the magnetic field of the MRI (Catana et al., 2013). Another issue is that bone is insufficiently depicted with MRI compared to CT. As gold-standard a separate CT scan would be acquired, further processed and applied for AC on PET/MRI data (Andersen et al., 2014). However, this procedure exposes subjects to additional ionizing radiation and is not practicable for clinical routine. Therefore, several MR-based AC methods have been proposed of which the following are currently implemented as commercial solutions in clinical systems: Siemens Healthineers AG provides solutions such as segmentation of fat and water images (DIXON) (Martinez-Möller et al., 2009) or ultra-short echo time images (UTE) (Catana et al., 2010). General Electric provides a model based approach where a bone model is superimposed on the AC map, derived from segmentation of fat and water images (Sekine et al., 2016). In addition to these commercial approaches, several MR-AC methods have been proposed by the scientific community, such as deep learning algorithms and zero-echo-time sequences (Delso et al., 2015; Gong et al., 2018) or emission-based

attenuation correction (Berker and Li, 2016). However, new MR-based AC approaches are commonly based on segmentation or a template/atlas (Ladefoged et al., 2017).

To evaluate the performance of different AC methods, the activity in tissue or the semi-quantitative measure standardized uptake value (SUV) are often used (Schulz et al., 2011; Berker et al., 2012; Burgos et al., 2014; Izquierdo-Garcia et al., 2014; Rausch et al., 2016; Ladefoged et al., 2017). However, in studies with radioligands targeting neurotransmitter proteins, quantification of distribution volumes and binding potentials (BP) are of major interest. This is usually achieved with kinetic modeling and arterial blood and/or a reference region. Ideally, only non-specifically bound radiotracer is found in a reference region (Nørgaard et al., 2019). In this study the radioligand [^{11}C]DASB was administered to quantify the serotonin transporter (SERT) protein density in the brain. Kinetic modeling can be performed for example with the simplified reference tissue model (SRTM), a 1 or constrained 2 tissue compartment model, or a graphical analysis (Logan plot) (Ginovart et al., 2001; Nørgaard et al., 2019). An adapted radioligand administration protocol was used in this study, enabling the estimation of the BP with a ratio method (Gryglewski et al., 2017).

Furthermore, drug occupancy is frequently studied for example to elucidate the mechanisms of action of a drug or to determine the appropriate dose, potentially translating to clinical applications (Takano et al., 2016). Thus, longitudinal assessments at baseline and after application of a drug are necessary.

Our main goal was to evaluate the performance of segmentation and atlas-based AC methods in the neurotransmitter system by absolutely quantifying distribution volumes. We hypothesize that differences between the AC approaches of total volume of distribution will be comparable with the results of the literature where SUV and tissue concentration is used, for mathematical reasons (see section “Materials and Methods”). Additionally, we aimed to demonstrate the impact of a bias in the reference region on the specific volume of distribution. Finally, we evaluated the difference between the AC methods when measurements of a longitudinal study are compared.

MATERIALS AND METHODS

Subjects

A total of 18 healthy subjects from a larger ongoing trial were included in this study (7 male, mean age 28.0 ± 9.6 years). To assure the healthy status, all subjects underwent medical

examination including blood tests, electrocardiography, neurological and physiological tests as well as a urine drug test at the screening visit. Additionally, all subjects were screened for psychiatric disorders by an experienced psychiatrist with the Structural Clinical Interview according to DSM-IV criteria. A urine pregnancy test was acquired for all female subjects prior to the scans.

Positron Emission Tomography

All subjects underwent two measurements (mean interval: 36.0 ± 29.6 days) on a PET/MRI system (Siemens Biograph mMR) in a double-blind, placebo-controlled, cross-over design. The radioligand [^{11}C]DASB, which specifically binds to the SERT (Wilson et al., 2013), was synthesized as described previously (Haeusler et al., 2009). Radioligand application started outside the scanner, using a syringe pump. The radioligand was infused as bolus for 1 min followed by constant infusion via a cubital vein for a total duration of 180 min. The target dose was calculated as 20 MBq/kg (effective dose for a 75 kg person: 5.55 mSv). PET data was recorded for 120–125 min in list-mode starting 30–45 min post injection. At 70 min post injection the placebo (saline) or 8 mg of the selective serotonin reuptake inhibitor (SSRI) citalopram was infused over 8 min.

Magnetic Resonance Imaging

Simultaneously with the PET acquisition the standard MR-AC sequences DIXON volume-interpolated breath-hold examination (VIBE, $\text{TE}_1/\text{TE}_2/\text{TR} = 1.23/2.46/3.60$ ms, flip angle = 10° , voxel size $2.6 \times 2.6 \times 3.1$ mm³) and ultra-short echo time (UTE, $\text{TE}_1/\text{TE}_2/\text{TR} = 0.07/2.46/11.94$ ms, flip angle = 10° , voxel size $1.6 \times 1.6 \times 1.6$ mm³) were recorded. A magnetization prepared rapid gradient echo sequence (MP-RAGE) was acquired for a T1-weighted anatomical image ($\text{TE}/\text{TR} = 4.21/3000$ ms, voxel size $1 \times 1 \times 1.1$ mm³) for an atlas-based AC approach.

Attenuation Correction Approaches

Positron emission tomography data was reconstructed with the following AC methods in order to assess their influence on SERT binding based on their availability.

CT

According to the EANM guidelines version 2 (Varrone et al., 2009) a regular- or low-dose CT can be used for attenuation correction. All subjects underwent a low-dose CT scan using a PET/CT (Siemens Biograph TruePoint PET/CT, tube potential: 120 kVp, voxel size: $0.59 \times 0.59 \times 1.5$ mm³, effective dose: 1 mSv) to keep the radiation exposure as low as possible. For the applicability of the CT scan as AC method, it was preprocessed as described previously (Carney et al., 2006; Ladefoged et al., 2015). In short, the CT scan was co-registered to the structural MRI. Thereafter, it was segmented into bone and non-bone tissues and a bilinear scaling was applied to estimate the linear attenuation coefficients at 511 keV (Kinahan et al., 1998). AC CT was used as reference AC method.

DIXON

This approach is based on segmentation of fat and water images originating from in- and opposed-phase images (Dixon, 1984). The final AC map contains the classes soft tissue, fatty tissue, air and if applicable lung tissue (Martinez-Möller et al., 2009).

UTE

Two MR images with different ultra-short echo times are segmented into 3 distinctive tissue classes, namely bone, soft tissue and air (Catana et al., 2010).

PseudoCT

The pseudoCT was created from an individual structural T1-weighted MRI using an online tool¹. The method itself is based on a database where pairs of T1-weighted MRIs and co-registered CT scans are stored. The software analyzes the best fitting MRIs, assigns weights and averages the corresponding CTs accordingly. The resulting pseudoCT was then processed equally to the CT (Burgos et al., 2014).

RESOLUTE

This AC method is based on AC UTE but additionally segments CSF as well as other tissue classes and uses continuous linear attenuation coefficients for a more accurate AC map (Ladefoged et al., 2015, 2017). For creation of the AC maps an online tool provided by the authors of Ladefoged et al. (2015) was used.

Bone Demonstrator

The bone demonstrator (BD) is a non-commercial prototype provided by Siemens Healthineers AG. An MRI, aligned with a bone model, is non-rigidly registered to the individual DIXON MR images. The registered bone model is then superimposed on the AC DIXON with continuous linear attenuation coefficients (Paulus et al., 2015; Koesters et al., 2016).

Figure 1A depicts the final AC maps of one representative subject.

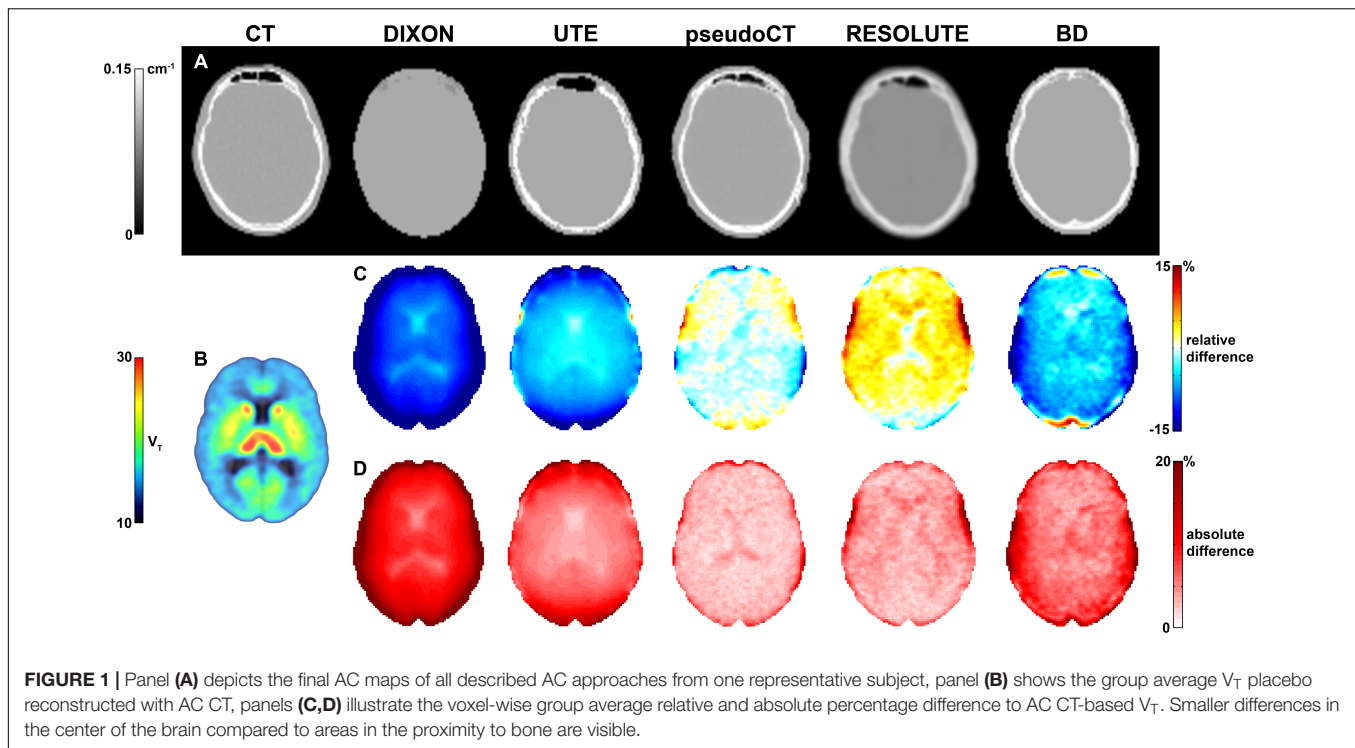
PET Data Reconstruction and Processing

Three consecutive frames (each 10 min) in tracer equilibrium, starting from 95 min post PET acquisition start, were reconstructed with an ordinary Poisson-ordered subset expectation maximization algorithm (OP-OSEM, 3 iterations, 21 subsets, voxel size $2.09 \times 2.09 \times 2.03$ mm³). The data was corrected for dead time, randoms, scatter and attenuation, either with CT, DIXON, UTE, pseudoCT, RESOLUTE or BD. Furthermore, the data was decay-corrected to the start of the radioligand administration to be in accordance with the activity of the blood samples. The offline reconstruction tool was provided by Siemens Healthineers AG.

Subsequently, data was processed with Statistical Parametric Mapping, version 12 (SPM12)² using default algorithms and settings unless indicated otherwise. For motion correction,

¹<http://niftyweb.cs.ucl.ac.uk/program.php?p=PCT>

²www.fil.ion.ucl.ac.uk/spm/software/spm12/



data was realigned to a mean image (quality = 1) which was co-registered to the T1-weighted structural MR image. Thereafter, the MR image was normalized via tissue probability maps to MNI space. The resulting transformation matrix was then applied to the dynamic PET data. Time-activity values for the 3 mentioned frames were derived from 7 regions-of-interest (ROIs) of the Automated Anatomic Labeling atlas (Tzourio-Mazoyer et al., 2002), namely the temporal lobe, anterior cingulate cortex (ACC), amygdala, caudate, putamen, thalamus and cerebellar gray matter excluding the vermis. The left and corresponding right ROI of each hemisphere were averaged for simplification. The regions were chosen to cover areas across the whole brain with varying amount of SERT binding.

SERT Quantification

The bolus plus constant infusion protocol enabled the use of an equilibrium method to quantify the total volume of distribution (V_T), the binding potential in plasma ($BP_P = V_S$) and the occupancy of the SSRI on the SERT with the 3 consecutive frames. This method has been shown to provide valid estimates of SERT binding without the need for kinetic modeling (Ginovart et al., 2001; Gryglewski et al., 2017). V_T is derived from C_T/C_p where C_T is the radioligand concentration in tissue, averaged across the 3 frames and C_p the radioligand concentration in plasma. C_p was calculated as the mean product of whole blood activity, the plasma and the parent fraction in arterial blood samples, drawn 120, 130 and 140 min after start of radioligand infusion. The blood time points were approximately corresponding to the start time points of the PET frames. Radioactivity was

measured in whole blood and, after centrifugation, in plasma in a γ -counter (Wizard², 3'', Perkin Elmer). Additionally, the fraction of unchanged [¹¹C]DASB was determined using cartridges (Ginovart et al., 2001).

BP_P is calculated as $V_T - V_{ND}$ where V_{ND} describes the V_T of a reference region, i.e., the cerebellar gray matter for [¹¹C]DASB (Parsey et al., 2006). Finally, the occupancy was determined as the relative change in BP_P between the placebo and the SSRI scan (Innis et al., 2007). All estimated parameters are based on ROIs.

$$\text{Occupancy (\%)} = \left(1 - \left(\frac{BP_P(\text{SSRI})}{BP_P(\text{Placebo})} \right) \right) \times 100 \quad (1)$$

Statistical Evaluation

To assess the difference between AC methods, the relative difference (RD) of V_T , BP_P , and occupancy was calculated with regard to the reference AC approach CT using ROIs.

$$\text{RD (\%)} = \left(\frac{\text{Parameter}_{\text{ACX}} - \text{Parameter}_{\text{ACCT}}}{\text{Parameter}_{\text{ACCT}}} \right) \times 100 \quad (2)$$

Furthermore, the absolute percentage difference (AD) was calculated as

$$\text{AD (\%)} = \left(\frac{|\text{Parameter}_{\text{ACX}} - \text{Parameter}_{\text{ACCT}}|}{\text{Parameter}_{\text{ACCT}}} \right) \times 100 \quad (3)$$

ACX was defined as one of the investigated AC approaches (DIXON, UTE, pseudoCT, RESOLUTE, or BD). Finally, linear regression of V_T , BP_P , and occupancy was conducted to detect bias (slope, intercept) and to evaluate similarity (r^2) of the different AC approaches with respect to AC CT.

RESULTS

The following paragraphs outline key results for all tested AC methods. A complete list of the group mean relative and absolute percentage differences and standard deviations for V_T (placebo, SSRI), BP_P (placebo, SSRI) and occupancy with all proposed AC methods compared to the reference AC CT can be found in **Tables 1, 2**. RD and AD were mostly in a similar range indicating that the bias of a ROI of a specific AC is almost exclusively in one direction across the group. This effect is especially noticeable for the parameter V_T (see **Table 1**). The results of the ROI-based regression between the proposed AC methods and AC CT can be found in **Table 3**. The values of the SSRI and placebo measurement were merged to have one r^2 , slope and intercept per AC approach and parameter. When analyzed separately the r^2 values were rather comparable with V_T placebo r^2 ranging from 0.996 to 0.998 in comparison to V_T SSRI r^2 ranging from 0.992 to 0.996. Similar results were achieved for BP_P placebo (r^2 ranging from 0.996 to 0.999) and BP_P SSRI (r^2 ranging from 0.983 to 0.992). Furthermore, slope and intercept were similar. **Figure 2** depicts boxplots with relative difference of V_T placebo and occupancy to the reference AC method CT. For illustration

purposes **Figure 1B** shows the voxel-wise AC CT-based V_T placebo averaged across all subjects. **Figures 1C,D** depict the average voxel-wise relative and absolute percentage differences of V_T placebo to AC CT.

DIXON

V_T showed the highest RD in the temporal lobe and the cerebellum with underestimations of around 11% and $r^2 \sim 1$. The errors of the placebo and SSRI scan were similar for V_T . In contrast, for BP_P the difference was markedly non-uniform between the ROIs and varied between placebo and SSRI scans. The most pronounced difference was found in the amygdala (placebo: -2%, SSRI: 9%). The bias for occupancy was less than -5%, except for the ACC with an error of approximately -9%. Regression confirmed the underestimation with a slope below 1 for V_T and BP_P .

UTE

Similar to V_T obtained with AC DIXON, the largest RD was found in the cerebellum (-9%). The error of BP_P varied between the placebo and SSRI scan. For the placebo scan the RD was as low as -1% whereas the SSRI scan showed an overestimation of

TABLE 1 | Group mean relative difference and standard deviation of V_T , BP_P , and occupancy estimated with the proposed AC methods with respect to AC CT for every ROI.

Mean RD (%)	Temporal	ACC	Amygdala	Caudate	Putamen	Thalamus	Cerebellum
AC DIXON							
V_T placebo	-11.0 ± 1.7	-9.7 ± 2.3	-6.4 ± 1.4	-7.8 ± 1.4	-8.2 ± 1.4	-8.4 ± 1.6	-11.7 ± 2.6
V_T SSRI	-11.1 ± 1.6	-9.2 ± 1.6	-6.1 ± 1.7	-7.0 ± 1.6	-7.6 ± 1.5	-7.7 ± 1.5	-11.8 ± 2.7
BP_P placebo	-8.8 ± 4.4	-4.1 ± 7.9	-1.5 ± 3.0	-5.0 ± 1.9	-5.9 ± 1.8	-6.6 ± 1.9	—
BP_P SSRI	-6.9 ± 11.2	7.2 ± 21.2	8.8 ± 9.9	1.7 ± 4.8	-1.2 ± 3.4	-1.5 ± 4.2	—
Occupancy	-2.1 ± 9.3	-8.7 ± 16.0	-4.7 ± 2.7	-3.5 ± 2.5	-2.8 ± 2.3	-2.4 ± 2.0	—
AC UTE							
V_T placebo	-6.5 ± 1.7	-7.1 ± 1.2	-4.1 ± 1.9	-3.9 ± 1.4	-4.2 ± 1.4	-3.5 ± 1.4	-9.0 ± 2.8
V_T SSRI	-6.5 ± 2.0	-7.1 ± 1.0	-4.3 ± 2.2	-4.2 ± 1.5	-4.4 ± 1.4	-3.5 ± 1.6	-9.0 ± 2.9
BP_P placebo	0.8 ± 5.9	-1.1 ± 7.2	0.3 ± 2.1	-0.3 ± 1.4	-1.0 ± 1.4	-0.4 ± 1.3	—
BP_P SSRI	8.7 ± 12.6	7.5 ± 21.7	8.6 ± 9.5	4.7 ± 4.4	3.0 ± 4.0	5.2 ± 4.0	—
Occupancy	-4.4 ± 8.8	-4.3 ± 9.4	-3.0 ± 2.4	-2.3 ± 1.8	-2.0 ± 1.9	-2.4 ± 1.6	—
AC pseudoCT							
V_T placebo	-0.4 ± 2.2	0.0 ± 1.8	-0.1 ± 2.0	0.4 ± 2.3	0.5 ± 2.4	-0.4 ± 1.9	0.0 ± 3.0
V_T SSRI	-0.6 ± 2.2	0.3 ± 1.5	-0.3 ± 2.4	0.4 ± 1.8	0.5 ± 1.8	-0.1 ± 1.7	-0.3 ± 3.0
BP_P placebo	-2.0 ± 7.2	0.5 ± 8.2	-0.3 ± 2.8	0.8 ± 3.5	0.8 ± 3.2	-0.6 ± 2.4	—
BP_P SSRI	-3.7 ± 13.0	4.4 ± 22.3	-0.2 ± 5.8	1.4 ± 4.2	1.7 ± 3.9	0.4 ± 3.9	—
Occupancy	1.0 ± 7.7	-2.2 ± 8.9	0.0 ± 1.6	-0.3 ± 2.2	-0.4 ± 2.0	-0.3 ± 1.7	—
AC RESOLUTE							
V_T placebo	4.5 ± 1.3	1.9 ± 0.9	5.3 ± 1.8	3.8 ± 1.3	3.8 ± 1.1	3.4 ± 1.0	2.5 ± 2.2
V_T SSRI	4.4 ± 1.5	2.2 ± 0.7	5.2 ± 1.5	4.1 ± 1.1	4.5 ± 1.1	4.2 ± 1.1	2.3 ± 2.1
BP_P placebo	10.4 ± 6.0	0.8 ± 7.0	8.0 ± 3.1	4.8 ± 2.3	4.7 ± 1.5	4.0 ± 1.4	—
BP_P SSRI	16.6 ± 10.4	4.0 ± 20.3	13.4 ± 6.6	7.5 ± 3.2	8.0 ± 3.3	7.3 ± 3.3	—
Occupancy	-4.2 ± 6.4	-1.2 ± 8.1	-2.2 ± 2.0	-1.3 ± 2.1	-1.7 ± 1.9	-1.4 ± 1.5	—
AC BD							
V_T placebo	-6.0 ± 1.6	-4.6 ± 2.4	-2.5 ± 1.4	-3.9 ± 1.6	-4.3 ± 1.6	-4.7 ± 1.8	-4.3 ± 2.8
V_T SSRI	-6.5 ± 1.6	-4.1 ± 1.7	-2.9 ± 1.7	-3.6 ± 1.8	-4.0 ± 1.7	-4.4 ± 1.7	-5.2 ± 3.2
BP_P placebo	-11.1 ± 5.0	-5.7 ± 8.8	-0.9 ± 3.2	-3.6 ± 2.2	-4.4 ± 2.0	-4.9 ± 2.1	—
BP_P SSRI	-15.4 ± 10.5	1.2 ± 18.7	2.9 ± 6.5	-1.0 ± 5.9	-2.4 ± 4.4	-3.2 ± 4.9	—
Occupancy	0.9 ± 16.9	-8.3 ± 24.9	-1.9 ± 2.0	-1.5 ± 3.7	-1.3 ± 3.3	-0.8 ± 2.7	—

TABLE 2 | Group mean absolute percentage difference and standard deviation of V_T , BP_P , and occupancy estimated with the proposed AC methods with respect to AC CT for every ROI.

Mean AD (%)	Temporal	ACC	Amygdala	Caudate	Putamen	Thalamus	Cerebellum
AC DIXON							
V_T placebo	11.0 ± 1.7	9.7 ± 2.3	6.4 ± 1.4	7.8 ± 1.4	8.2 ± 1.4	8.4 ± 1.6	11.7 ± 2.6
V_T SSRI	11.1 ± 1.6	9.2 ± 1.6	6.1 ± 1.7	7.0 ± 1.6	7.6 ± 1.5	7.7 ± 1.5	11.8 ± 2.7
BP_P placebo	9.2 ± 3.5	7.0 ± 5.2	2.8 ± 1.6	5.0 ± 1.9	5.9 ± 1.8	6.6 ± 1.9	—
BP_P SSRI	10.8 ± 7.2	14.5 ± 16.8	9.2 ± 9.5	3.7 ± 3.4	2.8 ± 2.2	3.4 ± 2.7	—
Occupancy	6.7 ± 6.5	11.7 ± 13.9	4.7 ± 2.7	3.7 ± 2.1	3.0 ± 2.0	2.7 ± 1.6	—
AC UTE							
V_T placebo	6.5 ± 1.7	7.1 ± 1.2	4.1 ± 1.8	3.9 ± 1.4	4.2 ± 1.4	3.5 ± 1.4	9.0 ± 2.8
V_T SSRI	6.5 ± 2.0	7.1 ± 1.0	4.3 ± 2.2	4.2 ± 1.5	4.4 ± 1.4	3.5 ± 1.6	9.0 ± 2.9
BP_P placebo	5.1 ± 2.8	6.0 ± 3.9	1.6 ± 1.4	1.1 ± 0.8	1.4 ± 1.1	1.1 ± 0.8	—
BP_P SSRI	11.7 ± 9.7	15.1 ± 17.0	9.4 ± 8.8	5.0 ± 4.1	4.0 ± 3.0	5.2 ± 3.9	—
Occupancy	8.3 ± 5.2	8.5 ± 5.6	3.2 ± 2.1	2.4 ± 1.6	2.2 ± 1.6	2.5 ± 1.4	—
AC pseudoCT							
V_T placebo	1.5 ± 1.7	1.3 ± 1.2	1.5 ± 1.4	1.8 ± 1.4	1.9 ± 1.5	1.2 ± 1.5	2.5 ± 1.6
V_T SSRI	1.5 ± 1.7	1.2 ± 0.9	1.7 ± 1.7	1.4 ± 1.1	1.4 ± 1.2	1.2 ± 1.2	2.5 ± 1.6
BP_P placebo	5.1 ± 5.3	6.9 ± 4.1	2.0 ± 1.8	2.9 ± 1.9	2.5 ± 2.0	1.6 ± 1.8	—
BP_P SSRI	9.2 ± 9.7	16.5 ± 15.2	4.3 ± 3.7	3.6 ± 2.4	3.6 ± 2.1	3.1 ± 2.3	—
Occupancy	5.1 ± 5.7	7.5 ± 4.9	1.3 ± 0.9	1.6 ± 1.5	1.6 ± 1.3	1.3 ± 1.2	—
AC RESOLUTE							
V_T placebo	4.5 ± 1.3	1.9 ± 0.9	5.3 ± 1.8	3.8 ± 1.3	3.8 ± 1.1	3.4 ± 1.0	2.8 ± 1.8
V_T SSRI	4.4 ± 1.5	2.2 ± 0.7	5.2 ± 1.5	4.1 ± 1.1	4.5 ± 1.1	4.2 ± 1.1	2.6 ± 1.6
BP_P placebo	10.5 ± 5.9	5.4 ± 4.5	8.0 ± 3.1	5.0 ± 1.9	4.7 ± 1.5	4.0 ± 1.4	—
BP_P SSRI	16.6 ± 10.4	13.7 ± 15.2	13.4 ± 6.6	7.5 ± 3.2	8.0 ± 3.3	7.3 ± 3.3	—
Occupancy	6.0 ± 4.7	6.8 ± 4.3	2.6 ± 1.5	1.7 ± 1.7	2.0 ± 1.6	1.7 ± 1.1	—
AC BD							
V_T placebo	6.0 ± 1.6	4.6 ± 2.4	2.5 ± 1.4	3.9 ± 1.6	4.3 ± 1.6	4.7 ± 1.8	4.3 ± 2.8
V_T SSRI	6.5 ± 1.6	4.1 ± 1.7	2.9 ± 1.7	3.6 ± 1.8	4.0 ± 1.7	4.4 ± 1.7	5.2 ± 3.2
BP_P placebo	11.1 ± 5.0	8.3 ± 6.2	2.6 ± 1.9	3.6 ± 2.2	4.4 ± 2.0	4.9 ± 2.1	—
BP_P SSRI	16.1 ± 9.3	14.3 ± 11.5	5.0 ± 5.0	4.2 ± 4.0	3.8 ± 3.3	4.7 ± 3.4	—
Occupancy	10.9 ± 12.7	16.2 ± 20.5	2.1 ± 1.7	3.1 ± 2.3	2.7 ± 2.3	2.3 ± 1.6	—

9% in the amygdala. The occupancy varied between -4 and -2% in all investigated regions.

PseudoCT

For V_T , the AD across all regions was less than 3%. The RD for BP_P was similar for the placebo and the SSRI scans with the exception of the ACC, where the placebo scan overestimated the BP_P by 1% and the SSRI scan by 4%. The relative variation of the occupancy was between 0 and 1%. However, the AD revealed an increased bias in all estimated parameters, especially for BP_P in low binding regions. Nevertheless, the results of all parameters were similar to the ones obtained with AC CT (r^2 ranging from 0.95 to 1). Outliers found in **Figure 2**, top, were all from the same subject. However, no abnormalities were observed in the pseudoCT AC map, thus, the subject was retained in all analyses.

RESOLUTE

V_T and BP_P were overestimated in all regions. The largest deviation for V_T was 5% in the amygdala whereas the largest RD for BP_P was found in the temporal lobe (17%). The

overestimations were also observed with regression (slope: 1.04, intercept 0.20). In contrast, the occupancy was underestimated in all regions by 1% (caudate) to 4% (temporal lobe). The slope and intercept of the regression was almost in alignment with the line of identity (slope between 0.98 and 1.04, intercept between -0.21 and 0.20) and had an r^2 ranging from 0.95 to 1 for all parameters.

BD

The largest relative errors were found in the low binding region of the temporal lobe (V_T SSRI -7% , BP_P SSRI -15%). In all other areas, the bias varied between -6 and 1%. The RD of the occupancy was between -2 and 1% with an exception of -8% in the ACC. Again, compared to RD, AD was increased in low binding regions for the parameter BP_P as well as occupancy. Regression showed the lowest agreement for occupancy with r^2 of 0.84 (slope = 1.09) and intercept = -6.40 .

Overall, the agreement of V_T and BP_P calculations when using different AC methods was close, with r^2 of approximately 1 for the placebo and the SSRI scans. In almost all regions, the smallest relative error was found for AC pseudoCT without mean relative

TABLE 3 | Region-of-interest-based linear regression parameters (r^2 , slope, and intercept) for V_T , BP_P , and occupancy estimated with the proposed AC methods with respect to AC CT. The values of the placebo and SSRI scan were merged.

Regression to AC CT	r^2	Slope	Intercept
AC DIXON			
V_T	0.997	0.93	-0.34
BP_P	0.997	0.93	0.27
Occupancy	0.898	1.00	-2.10
AC UTE			
V_T	0.998	0.98	-0.55
BP_P	0.998	0.98	0.23
Occupancy	0.929	0.92	2.93
AC pseudoCT			
V_T	0.997	1.01	-0.10
BP_P	0.997	1.00	0.00
Occupancy	0.945	1.00	-0.38
AC RESOLUTE			
V_T	0.999	1.04	-0.04
BP_P	0.998	1.04	0.20
Occupancy	0.948	0.98	-0.21
AC BD			
V_T	0.998	0.96	-0.11
BP_P	0.997	0.96	0.02
Occupancy	0.841	1.09	-6.40

bias in the cerebellum and ACC for V_T placebo. However, AD revealed marked errors in low binding regions which were hidden in the RD alone. The regression of AC RESOLUTE and AC pseudoCT showed a slope and intercept similar to the line of identity. The standard deviation was highest for occupancy with AC BD and lowest with AC RESOLUTE in the temporal lobe and ACC, ranging from ± 6 to $\pm 16\%$ and ± 8 to $\pm 24\%$, respectively.

DISCUSSION

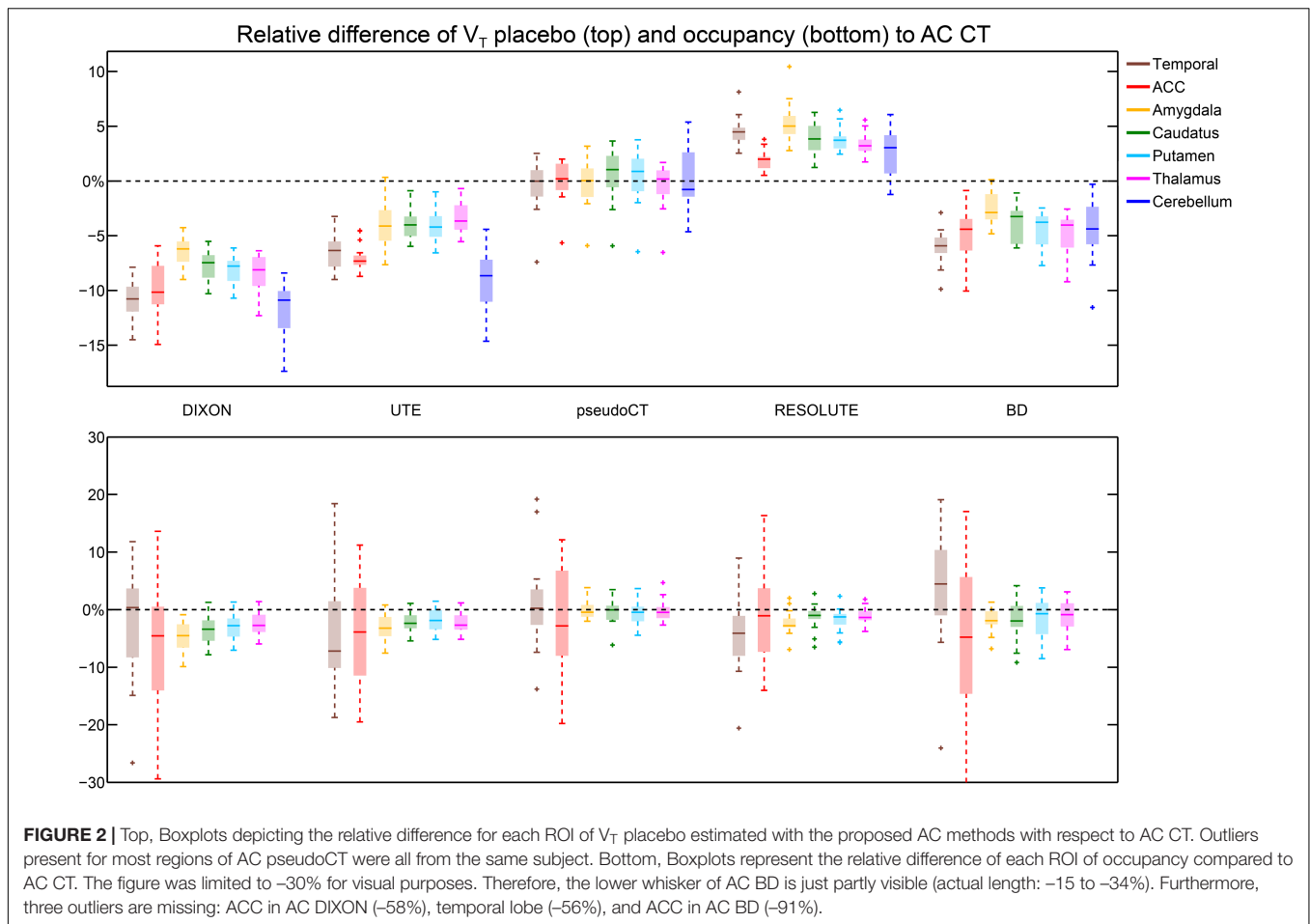
In this study, we analyzed the performance of different PET/MRI AC methods, namely, DIXON, UTE, pseudoCT, RESOLUTE and BD with respect to the CT-reference for the quantification of SERT binding and occupancy. In contrast to most of the previous reports we did not use tissue activity or SUV values but focused on different outcome parameters obtained from absolute quantification.

First, we evaluated the performance of the tested AC methods with regards to the parameter V_T in comparison to the reference AC CT. When using AC DIXON, V_T was underestimated with a regional variability. While subcortical regions close to the center of the brain showed a lower bias, a larger RD was observed in areas close to the skull. This phenomenon and similar RDs were reported by other groups (Izquierdo-Garcia et al., 2014; Rausch et al., 2017) and demonstrated on a voxel-wise basis (Ladefoged et al., 2017). The bias is likely caused by the missing bone information (Andersen et al., 2014).

The lack of bone can be accounted for to some degree by superimposing a bone segment on the AC DIXON map (i.e., the BD method). The improvement approximately halved

the errors in all regions. However, since AC BD is based on AC DIXON, errors in the latter are also transferred to BD (e.g., filled air cavities) (Rausch et al., 2017). Similarly, AC UTE offered an improvement to the RD of V_T , although still with higher underestimations in the vicinity of the skull. The error arises from segmentation misclassifications in the tissue/air border areas (Aasheim et al., 2015). Discontinuities of the segmented skull and neglect of regional variation in bone density are further issues leading to inaccurate PET quantification (Ladefoged et al., 2015). However, overall, the bias was smaller than with AC DIXON and in some regions comparable to AC BD, presumably due to the additional bone segment. In AC RESOLUTE the segmentation of UTE images was optimized with additional tissue classes and masks in areas difficult to segment, such as the nasal septa, ethmoidal-, frontal sinuses and mastoid process. Another difference is that continuous linear attenuation coefficients are used for a more accurate attenuation map (Ladefoged et al., 2015). This improved the V_T values, however, yielded overestimations in all regions. Our results deviate slightly from those of Ladefoged et al. (2015), who reported underestimations in some areas. However, the same group published a larger study with errors similar to the ones found in this work (Ladefoged et al., 2017). The best performance of V_T in terms of bias was found with the atlas-based AC method pseudoCT, yielding high accuracy in all regions. As a limitation for this (Burgos et al., 2016) and similar approaches (Mérida et al., 2017) it is worth to mention the necessity of a representative MRI-CT database. Of note, similar RD and AD are expected between tissue concentration and V_T values since V_T mathematically equals the tissue concentration divided by the radioligand concentration in plasma.

The more commonly used outcome parameter for SERT and other neurotransmitter applications is BP_P . By definition, the difference between BP_P and V_T can only arise from the reference region (here the cerebellar gray matter). It is therefore important to note that the error of the AC methods is markedly non-uniform across the brain, particularly for those methods without or with only limited modeling of bone tissue. Regions in proximity of bone (e.g., cerebellum) show a higher bias than regions in the center of the brain (e.g., striatum). Hence, outcome parameters, which are dependent on interregional differences (e.g., BP_P) or ratios (distribution volume ratio) will incorporate the non-uniform error as additional source of bias. Another issue is that SSRIs decrease the binding also in the reference region. Although the cerebellar gray matter was identified as the optimal reference region for [^{11}C]DASB, a displacement of up to 33% was described after an acute sertraline challenge (Parsey et al., 2006; Turkheimer et al., 2012). However, this will not affect the comparison between the different AC methods as differences in the reference region will be equally present for all AC approaches. Nonetheless, this may indeed have an effect when using outcome parameters such as BP_P or BP_{ND} , which require an unbiased reference region. Here, lower binding or in other words small numerical uncertainties will translate into larger errors of percentage. This is a potential explanation for the differences



between the SSRI and placebo scans observed for BP_p when using DIXON and UTE.

Differently to this study, binding potentials are also commonly estimated with kinetic modeling. Inhomogeneous tracer uptake over time might induce uncertainties in ROIs which can influence the shape of time activity curves and therefore the outcome of the kinetic modeling (Mérída et al., 2017). However, Mansur et al. compared the AC approach pseudoCT to AC CT with the reference kinetic model SRTM as well as an arterial blood-based two tissue compartment model (2TCM) (Mansur et al., 2018). They reported a strong correlation of non-displaceable BP and V_T and mostly similar differences ($<5\%$) as (Mérída et al., 2017), who used comparable AC approaches. As similar bias to the ratio method with AC pseudoCT was found here, it might be concluded that the other AC methods of this study yield comparable differences as BP_p when kinetic modeling is applied.

Given its clinical importance, SERT occupancy induced by i.v. SSRI challenge was also assessed for all AC methods. Of note, the error decreased in almost all areas compared to V_T and BP_p thus, indicating that the inaccuracy cancels out, except for errors in the ACC with AC DIXON and BD. For high binding regions of $[^{11}C]DASB$, such as putamen, thalamus and caudate, RD did not exceed errors of -4% with reasonable SD. This is probably based on the small

test-retest variability between the placebo and SSRI scan in terms of AC reproducibility since RD and AD are almost identical in both measurements. Therefore, our results might be translatable to longitudinal or occupancy studies, were two measurements are brought into context, independent of the tracer of choice.

We could demonstrate that the bias is not only dependent on the AC method but also on the investigated parameter, which is a complementary discovery to (Ladefoged et al., 2017). Interestingly, a high r^2 was obtained for V_T which may enable the rescaling of biased parameters to the true values achieved with AC CT on an ROI-basis. This would enable the usage of all presented AC methods, depending on the scientific question, e.g., investigation of V_T in subcortical regions with $[^{11}C]DASB$. However, issues might occur with other parameters such as BP_p or occupancy with AC DIXON or BD. The lower r^2 of the occupancy caused by fluctuating errors between the SSRI and placebo scans of BP_p limit the applicability of both AC methods to ROIs in the brain center and parameters independent from other regions (e.g., V_T). Furthermore, we would like to mention that the scalability does not apply to voxel level with the same accuracy (Ladefoged et al., 2017). It also has to be mentioned that a cohort of young adults was investigated (mean age

28.0 ± 9.6 years). Different results might be achieved in elderly or diseased subjects due to varying characteristics that cannot be reflected by the presented AC approaches (e.g., differences in skull density or cortical thickness). Another limitation observed in AC DIXON is the inversion of fat and water images, which leads to incorrect segmentation classes (Ladefoged et al., 2014). The tissue inversion occurs either partially or measurement specific and not subject specific, which is especially an issue in longitudinal studies. It is further an issue for AC BD as it is based on AC DIXON. Hence, the error propagates to AC BD. The impact of tissue inversion on BP_P and occupancy was not evaluated due to a lack of data. Another limitation was the necessity for large ROIs in low binding regions which are mostly cortical structures for [¹¹C]DASB. This was essential to calculate reliable BP_P as these regions have almost as little binding as the reference region (i.e., cerebellum). Additionally, since the AC induced bias is non-uniform, large ROIs, spreading from near the center of the brain to the proximity of bone tissue, might average out some regional effects. Hence, dissimilar results might be achieved in cross-sectional studies for the parameters V_T and BP_P with tracers with a different distribution.

CONCLUSION

In this study, we presented the accuracy of different AC approaches for different binding parameters quantified with [¹¹C]DASB. We could show the impact of AC on parameters relying on the accurate quantification of non-displaceable binding (such as BP_P) and a decreased error if two measurements are brought into context (occupancy), for almost all investigated regions. The AC method pseudoCT performed best compared to AC CT since all examined regions and parameters showed acceptable variations within a range of 4%. Based on these results, AC pseudoCT should be considered as a reliable alternative to AC CT.

DATA AVAILABILITY STATEMENT

The datasets generated for this study are available from the corresponding author upon request.

REFERENCES

- Aasheim, L. B., Karlberg, A., Goa, P. E., Häberg, A., Sørhaug, S., Fagerli, U. M., et al. (2015). PET/MR brain imaging: evaluation of clinical UTE-based attenuation correction. *Eur. J. Nucl. Med. Mol. Imaging* 42, 1439–1446. doi: 10.1007/s00259-015-3060-3
- Andersen, F. L., Ladefoged, C. N., Beyer, T., Keller, S. H., Hansen, A. E., Højgaard, L., et al. (2014). Combined PET/MR imaging in neurology: MR-based attenuation correction implies a strong spatial bias when ignoring bone. *Neuroimage* 84, 206–216. doi: 10.1016/j.neuroimage.2013.08.042
- Bailey, D. L. (1998). Transmission scanning in emission tomography. *Eur. J. Nucl. Med.* 25, 774–787. doi: 10.1007/s002590050282
- Berker, Y., Franke, J., Salomon, A., Palmowski, M., Donker, H. C. W., Temur, Y., et al. (2012). MRI-Based attenuation correction for hybrid PET/MRI systems:

ETHICS STATEMENT

The study was approved by the Ethics Committee of the Medical University of Vienna and procedures were carried out in accordance with the Declaration of Helsinki. After a detailed explanation of the study all subjects gave written informed consent.

AUTHOR CONTRIBUTIONS

LR, GG, MK, AH, WW, MM, and RL designed the study. GG recruited subjects and medically assisted the measurements. NB-I and WW synthesized the radioligand. LR, GJ, and MK acquired the data. HS and MM analyzed the blood samples. LR, IR, and AH performed data analysis. MHB and SK were medical supervisors. RL was the principal investigator and scientific supervisor of the study. All authors contributed in writing and reviewing the manuscript.

FUNDING

This scientific project was performed with the support of the Medical Imaging Cluster of the Medical University of Vienna, a grant from the Else Kröner-Fresenius-Stiftung (2014_A192), and support from Siemens (CA-ID: C00214938/06). This work was supported by the Austrian Science Fund (FWF) grant number KLI 516 to RL. LR, GG, and MK are/were recipients of DOC Fellowships of the Austrian Academy of Sciences at the Department of Psychiatry and Psychotherapy, Medical University of Vienna.

ACKNOWLEDGMENTS

We thank Verena Pichler and Chrysoula Vraha for radioligand synthesis, Karolin Eienkel and Benjamin Spurny for organizational support, Alexander Kautzky, Godber Mathis Godbersen, Arkadiusz Komorowski, and Thomas Vanicek for medical support, and Claes Ladefoged for providing the AC method RESOLUTE. We thank the MR-PET Team of Siemens Healthineers AG, Germany.

- a 4-class tissue segmentation technique using a combined ultrashort-echo-time/dixon MRI sequence. *J. Nucl. Med.* 53, 796–804. doi: 10.2967/jnumed.111.092577
- Berker, Y., and Li, Y. (2016). Attenuation correction in emission tomography using the emission data - A review. *Med. Phys.* 43, 807–832. doi: 10.1118/1.4938264
- Burgos, N., Cardoso, M. J., Thielemans, K., Modat, M., Pedemonte, S., Dickson, J., et al. (2014). Attenuation correction synthesis for hybrid PET-MR scanners: application to brain studies. *IEEE Trans. Med. Imaging* 33, 2332–2341. doi: 10.1109/TMI.2014.2340135
- Burgos, N., Thielemans, K., Cardoso, M. J., Markiewicz, P., Jiao, J., Dickson, J., et al. (2016). "Effect of scatter correction when comparing attenuation maps: application to brain PET/MR," in *Proceedings of the 2014 IEEE Nuclear Science Symposium and Medical Imaging Conference, NSS/MIC 2014*, (Seattle, WA: IEEE), doi: 10.1109/NSSMIC.2014.7430775

- Carney, J. P. J., Townsend, D. W., Rappoport, V., and Bendriem, B. (2006). Method for transforming CT images for attenuation correction in PET/CT imaging. *Med. Phys.* 33, 976–983. doi: 10.1118/1.2174132
- Catana, C., Guimaraes, A. R., and Rosen, B. R. (2013). PET and MR imaging: the odd couple or a match made in heaven? *J. Nucl. Med.* 54, 815–824. doi: 10.2967/jnumed.112.112771
- Catana, C., van der Kouwe, A., Benner, T., Michel, C. J., Hamm, M., Fenchel, M., et al. (2010). Toward implementing an MRI-based PET attenuation-correction method for neurologic studies on the MR-PET brain prototype. *J. Nucl. Med.* 51, 1431–1438. doi: 10.2967/jnumed.109.069112
- Delso, G., Wiesinger, F., Sacolick, L. I., Kaushik, S. S., Shanbhag, D. D., Hullner, M., et al. (2015). Clinical evaluation of zero-echo-time MR imaging for the segmentation of the skull. *J. Nucl. Med.* 56, 417–422. doi: 10.2967/jnumed.114.149997
- Dixon, W. T. (1984). Simple proton spectroscopic imaging. *Radiology* 153, 189–194. doi: 10.1148/radiology.153.1.6089263
- Ginovart, N., Wilson, A. A., Meyer, J. H., Hussey, D., and Houle, S. (2001). Positron emission tomography quantification of [(11)C]-DASB binding to the human serotonin transporter: modeling strategies. *J. Cereb. Blood Flow Metab.* 21, 1342–1353. doi: 10.1097/00004647-200111000-00010
- Gong, K., Yang, J., Kim, K., El Fakhri, G., Seo, Y., and Li, Q. (2018). Attenuation correction for brain PET imaging using deep neural network based on Dixon and ZTE MR images. *Phys. Med. Biol.* 63:125011. doi: 10.1088/1361-6560/aac763
- Gryglewski, G., Rischka, L., Philippe, C., Hahn, A., James, G. M., Kleberrmass, E., et al. (2017). Simple and rapid quantification of serotonin transporter binding using [(11)C]DASB bolus plus constant infusion. *Neuroimage* 149, 23–32. doi: 10.1016/j.neuroimage.2017.01.050
- Haeusler, D., Mien, L. K., Nics, L., Ungersboeck, J., Philippe, C., Lanzemberger, R. R., et al. (2009). Simple and rapid preparation of [(11)C]DASB with high quality and reliability for routine applications. *Appl. Radiat. Isot.* 67, 1654–1660. doi: 10.1016/j.apradiso.2009.03.005
- Hahn, A., Gryglewski, G., Nics, L., Rischka, L., Ganger, S., Sigurdardottir, H., et al. (2017). Task-relevant brain networks identified with simultaneous PET/MR imaging of metabolism and connectivity. *Brain Struct. Funct.* 223, 1–10. doi: 10.1007/s00429-017-1558-0
- Huang, S. C., Hoffman, E. J., Phelps, M. E., and Kuhl, D. E. (1979). Quantitation in positron emission computed tomography: 2. Effects of inaccurate attenuation correction. *J. Comput. Assist. Tomogr.* 3, 804–814.
- Innis, R. B., Cunningham, V. J., Delforge, J., Fujita, M., Gjedde, A., Gunn, R. N., et al. (2007). Consensus nomenclature for in vivo imaging of reversibly binding radioligands. *J. Cereb. Blood Flow Metab.* 27, 1533–1539. doi: 10.1038/sj.jcbfm.9600493
- Izquierdo-Garcia, D., Hansen, A. E., Forster, S., Benoit, D., Schachoff, S., Furst, S., et al. (2014). An SPM8-based approach for attenuation correction combining segmentation and nonrigid template formation: application to simultaneous PET/MR brain imaging. *J. Nucl. Med.* 55, 1825–1830. doi: 10.2967/jnumed.113.136341
- Kinahan, P. E., Townsend, D. W., Beyer, T., and Sashin, D. (1998). Attenuation correction for a combined 3D PET/CT scanner. *Med. Phys.* 25, 2046–2053. doi: 10.1118/1.598392
- Koesters, T., Friedman, K. P., Fenchel, M., Zhan, Y., Hermosillo, G., Babb, J., et al. (2016). Dixon sequence with superimposed model-based bone compartment provides highly accurate PET/MR attenuation correction of the brain. *J. Nucl. Med.* 57, 918–924. doi: 10.2967/jnumed.115.166967
- Ladefoged, C. N., Benoit, D., Law, I., Holm, S., Kjaer, A., Hojgaard, L., et al. (2015). Region specific optimization of continuous linear attenuation coefficients based on UTE (RESOLUTE): application to PET/MR brain imaging. *Phys. Med. Biol.* 60, 8047–8065. doi: 10.1088/0031-9155/60/20/8047
- Ladefoged, C. N., Hansen, A. E., Keller, S. H., Holm, S., Law, I., Beyer, T., et al. (2014). Impact of incorrect tissue classification in Dixon-based MR-AC: fat-water tissue inversion. *EJNMMI Phys.* 1:101. doi: 10.1186/s40658-014-0101-0
- Ladefoged, C. N., Law, I., Anazodo, U., St. Lawrence, K., Izquierdo-Garcia, D., Catana, C., et al. (2017). A multi-centre evaluation of eleven clinically feasible brain PET/MRI attenuation correction techniques using a large cohort of patients. *Neuroimage* 147, 346–359. doi: 10.1016/j.neuroimage.2016.12.010
- Mansur, A., Newbould, R., Searle, G. E., Redstone, C., Gunn, R. N., and Hallett, W. A. (2018). PET-MR attenuation correction in dynamic brain PET using [(11)C]cimbi-36: a direct comparison with PET-CT. *IEEE Trans. Radiat. Plasma Med. Sci.* 2, 483–489. doi: 10.1109/TRPMS.2018.2852558
- Martinez-Möller, A., Souvatzoglou, M., Delso, G., Bundschuh, R. A., Ched'hotel, C., Ziegler, S. I., et al. (2009). Tissue classification as a potential approach for attenuation correction in whole-body PET/MRI: evaluation with PET/CT data. *J. Nucl. Med.* 50, 520–526. doi: 10.2967/jnumed.108.054726
- Mérida, I., Reilhac, A., Redouté, J., Heckemann, R. A., Costes, N., and Hammers, A. (2017). Multi-atlas attenuation correction supports full quantification of static and dynamic brain PET data in PET-MR. *Phys. Med. Biol.* 62, 2834–2858. doi: 10.1088/1361-6560/aa5f6c
- Norgaard, M., Ganz, M., Svarer, C., Feng, L., Ichise, M., Lanzemberger, R., et al. (2019). Cerebral serotonin transporter measurements with [(11)C]DASB: a review on acquisition and preprocessing across 21 PET centres. *J. Cereb. Blood Flow Metab.* 39, 210–222. doi: 10.1177/0271678X18770107
- Parsey, R. V., Kent, J. M., Oquendo, M. A., Richards, M. C., Pratap, M., Cooper, T. B., et al. (2006). Acute occupancy of brain serotonin transporter by sertraline as measured by [(11)C]DASB and positron emission tomography. *Biol. Psychiatry* 59, 821–828. doi: 10.1016/j.biopsych.2005.08.010
- Paulus, D. H., Quick, H. H., Geppert, C., Fenchel, M., Zhan, Y., Hermosillo, G., et al. (2015). Whole-Body PET/MR imaging: quantitative evaluation of a novel model-based MR attenuation correction method including bone. *J. Nucl. Med.* 56, 1061–1066. doi: 10.2967/jnumed.115.156000
- Rausch, I., Rischka, L., Ladefoged, C. N., Furtner, J., Fenchel, M., Hahn, A., et al. (2017). PET/MRI for oncological brain imaging: a comparison of standard MR-based attenuation corrections with a novel, model-based approach for the Siemens mMR PET/MR system. *J. Nucl. Med.* 58, 1519–1525. doi: 10.2967/jnumed.116.186148
- Rausch, I., Rust, P., Difranco, M. D., Lassen, M., Stadlbauer, A., Mayerhoefer, M. E., et al. (2016). Reproducibility of MRI Dixon-based attenuation correction in combined PET/MR with applications for lean body mass estimation. *J. Nucl. Med.* 57, 1096–1102. doi: 10.2967/jnumed.115.168294
- Sander, C. Y., Hooker, J. M., Catana, C., Normandin, M. D., Alpert, N. M., Knudsen, G. M., et al. (2013). Neurovascular coupling to D2/D3 dopamine receptor occupancy using simultaneous PET/functional MRI. *Proc. Natl. Acad. Sci. U.S.A.* 110, 11169–11174. doi: 10.1073/pnas.1220512110
- Schulz, V., Torres-Espallardo, I., Renisch, S., Hu, Z., Ojha, N., Börner, P., et al. (2011). Automatic, three-segment, MR-based attenuation correction for whole-body PET/MR data. *Eur. J. Nucl. Med. Mol. Imaging* 38, 138–152. doi: 10.1007/s00259-010-1603-1
- Sekine, T., Burgos, N., Warnock, G., Huellner, M., Buck, A., ter Voert, E. E. G. W., et al. (2016). Multi-atlas-based attenuation correction for brain 18F-FDG PET imaging using a time-of-flight PET/MR scanner: comparison with clinical single-atlas- and CT-based attenuation correction. *J. Nucl. Med.* 57, 1258–1264. doi: 10.2967/jnumed.115.169045
- Takano, A., Varrone, A., Gulyás, B., Salvadori, P., Gee, A., Windhorst, A., et al. (2016). Guidelines to PET measurements of the target occupancy in the brain for drug development. *Eur. J. Nucl. Med. Mol. Imaging* 43, 2255–2262. doi: 10.1007/s00259-016-3476-4
- Townsend, D. W., Carney, J. P. J., Yap, J. T., and Hall, N. C. (2004). PET/CT today and tomorrow. *J. Nucl. Med.* 45(Suppl. 1), 4S–14S. doi: 10.1111/j.1476-5829.2010.00218.x
- Turkheimer, F. E., Selvaraj, S., Hinz, R., Murthy, V., Bhagwagar, Z., Grasby, P., et al. (2012). Quantification of ligand PET studies using a reference region with a displaceable fraction: application to occupancy studies with [(11)C]-DASB

- as an example. *J. Cereb. Blood Flow Metab.* 32, 70–80. doi: 10.1038/jcbfm.2011.108
- Tzourio-Mazoyer, N., Landeau, B., Papathanassiou, D., Crivello, F., Etard, O., Delcroix, N., et al. (2002). Automated anatomical labeling of activations in SPM using a macroscopic anatomical parcellation of the MNI MRI single-subject brain. *Neuroimage* 15, 273–289. doi: 10.1006/nimg.2001.0978
- Varrone, A., Asenbaum, S., Vander Borgh, T., Booij, J., Nobili, F., Någren, K., et al. (2009). EANM procedure guidelines for PET brain imaging using [18F]FDG, version 2. *Eur. J. Nucl. Med. Mol. Imaging* 36, 2103–2110. doi: 10.1007/s00259-009-1264-0
- Wilson, A. A., Hicks, J. W., Sadovski, O., Parkes, J., Tong, J., Houle, S., et al. (2013). Radiosynthesis and evaluation of [11C-carbonyl]-labeled carbamates as fatty acid amide hydrolase radiotracers for positron emission tomography. *J. Med. Chem.* 56, 201–219. doi: 10.1021/jm301492y

Conflict of Interest: Siemens Healthineers AG provided the Bone Demonstrator software as well as dedicated reconstruction software through a research agreement with the Medical University of Vienna.

The authors declare that the research was conducted in the absence of any commercial or financial relationships that could be construed as a potential conflict of interest.

Copyright © 2019 Rischka, Gryglewski, Berroterán-Infante, Rausch, James, Klöbl, Sigurdardóttir, Hartenbach, Hahn, Wadsak, Mitterhauser, Beyer, Kasper, Prayer, Hacker and Lanzenberger. This is an open-access article distributed under the terms of the Creative Commons Attribution License (CC BY). The use, distribution or reproduction in other forums is permitted, provided the original author(s) and the copyright owner(s) are credited and that the original publication in this journal is cited, in accordance with accepted academic practice. No use, distribution or reproduction is permitted which does not comply with these terms.



Regional Accuracy of ZTE-Based Attenuation Correction in Static [^{18}F]FDG and Dynamic [^{18}F]PE2I Brain PET/MR

Georg Schramm^{1*}, Michel Koole¹, Stefanie M. A. Willekens¹, Ahmadreza Rezaei¹, Donatienne Van Weehaeghe¹, Gaspar Delso², Ronald Peeters³, Nathalie Mertens¹, Johan Nuyts¹ and Koen Van Laere¹

¹ Division of Nuclear Medicine, Department of Imaging and Pathology, KU/UZ Leuven, Leuven, Belgium, ² GE Healthcare, Cambridge, United Kingdom, ³ Division of Radiology, UZ Leuven, Leuven, Belgium

OPEN ACCESS

Edited by:

Ivo Rausch,
Medical University of Vienna, Austria

Reviewed by:

Paul Cumming,
University of Bern, Switzerland
Roberta Frass-Kriegel,
Medical University of Vienna, Austria

*Correspondence:

Georg Schramm
georg.schramm@kuleuven.be

Specialty section:

This article was submitted to
Medical Physics and Imaging,
a section of the journal
Frontiers in Physics

Received: 02 October 2019

Accepted: 21 November 2019

Published: 06 December 2019

Citation:

Schramm G, Koole M, Willekens SMA, Rezaei A, Van Weehaeghe D, Delso G, Peeters R, Mertens N, Nuyts J and Van Laere K (2019) Regional Accuracy of ZTE-Based Attenuation Correction in Static [^{18}F]FDG and Dynamic [^{18}F]PE2I Brain PET/MR. *Front. Phys.* 7:211. doi: 10.3389/fphy.2019.00211

Accurate MR-based attenuation correction (MRAC) is essential for quantitative PET/MR imaging of the brain. In this study, we analyze the regional bias caused by MRAC based on Zero-Echo-Time MR images (ZTEAC) compared to CT-based AC (CTAC) static and dynamic PET imaging. In addition, the results are compared to the performance of the Atlas-based AC (AtlasAC) implemented in the GE SIGNA PET/MR software version MP24.

Methods: Thirty static [^{18}F]FDG and eleven dynamic [^{18}F]PE2I acquisitions from a SIGNA PET/MR were reconstructed using ZTEAC (using a research tool, GE Healthcare), single-subject AtlasAC (the default AC in SIGNA PET/MR software version MP24) and CTAC (from a PET/CT acquisition of the same day). In the 30 static [^{18}F]FDG reconstructions, the bias caused by ZTEAC and AtlasAC in the mean uptake of 85 anatomical volumes of interest (VOIs) of the Hammers' atlas was analyzed in PMOD. For the 11 dynamic [^{18}F]PE2I reconstructions, the bias caused by ZTEAC and AtlasAC in the non displaceable binding potential BP_{nd} in the striatum was calculated with cerebellum as the reference region and a simplified reference tissue model.

Results: The regional bias caused by ZTEAC in the static [^{18}F]FDG reconstructions ranged from -8.0 to $+7.7\%$ (mean 0.1% , SD 2.0%). For AtlasAC this bias ranged from -31.6 to $+16.6\%$ (mean -0.4% , SD 4.3%). The bias caused by AtlasAC showed a clear gradient in the cranio-caudal direction (-4.2% in the cerebellum, $+6.6\%$ in the left superior frontal gyrus). The bias in the striatal BP_{nd} for the [^{18}F]PE2I reconstructions ranged from -0.8 to $+4.8\%$ (mean 1.5% , SD 1.4%) using ZTEAC and from -0.6 to $+9.4\%$ using AtlasAC (mean 4.2% , SD 2.6%).

Conclusion: ZTEAC provides excellent quantitative accuracy for static and dynamic brain PET/MR, comparable to CTAC, and is clearly superior to the default AtlasAC implemented in the SIGNA PET/MR software version MP24.

Keywords: MR-based attenuation correction, PET/MR, PET quantification, PET reconstruction, molecular imaging

1. INTRODUCTION

Since the introduction of combined PET/MR, accurate attenuation correction (AC) for brain imaging has always been a field of active research. Neglecting higher bone attenuation of the skull in the first generation segmentation-based AC methods used in product implementations led to a substantial spatially-varying bias in the reconstructed tracer uptake [1]. To include patient-specific information about higher bone attenuation, two concepts for MR-based attenuation correction (MRAC) were investigated by different research groups. On the one hand, ultra short echo time (UTE) MR sequences that allow to generate signal in cortical bone were used to segment bone structures in the skull [2–8]. On the other hand, the use of single [9–11] or multi MR-CT atlas [12, 13] information to generate attenuation images including higher bone attenuation were proposed. On top of methods relying on MR images, Benoit et al. [14] and Rezaei et al. [15] evaluated the use of joint estimation of activity and attenuation for non-TOF and TOF brain PET/MR, respectively. Renner et al. [16] proposed to integrate a transmission source rotating in a MR-compatible hydraulic system directly into a dedicated head coil. Recently, Ladefoged et al. [17] showed in a multi-center evaluation that the bias introduced by MRAC in brain PET/MR imaging can be reduced to $\pm 35\%$ when using different second generation atlas- or UTE-based AC techniques developed by different research groups.

Weiger et al. [18] and Wiesinger et al. [19] showed that zero echo time (ZTE) MR sequences have great potential in imaging materials with short T_2^* such as cortical bone. Since ZTE sequences only use a single echo, their acquisition time is substantially shorter compared to UTE sequences that usually acquire two echos. In addition, faster switching from transmit to receive in the ZTE sequence minimizes loss of signal in tissues with short T_2^* relaxation times such as cortical bone. Due to the use of minimal gradient switching, ZTE is less prone to eddy current artifacts than UTE [19, 20]. Moreover, a correlation between the ZTE MR signal intensity and CT Hounsfield units (HU) in cortical bone was demonstrated in Wiesinger et al. [19].

Consequently, ZTE MR imaging is very promising for accurate AC in brain PET/MR. Delso et al. [21] showed that ZTE-based skull segmentation, which is needed to generate attenuation images including higher bone attenuation, is feasible. Boydev et al. [22] showed that the use of ZTE MR images in their atlas-based prediction of pseudo CTs improved the correctness of the pseudo CTs for radiation therapy planning in case of bone resection surgery prior to the radiation therapy compared to using T1-weighted MR images as input.

Sekine et al. [20], Khalife et al. [23], Yang et al. [24], Leynes et al. [25], Wiesinger et al. [26], and Delso et al. [27] demonstrated that the quantitative accuracy of PET images reconstructed with ZTE-based attenuation images is high. Gong

et al. [28] recently showed that attenuation images generated by a neural network using Dixon and ZTE MR images as input outperform attenuation images from a network that only uses a Dixon MR as input in terms of bias in the reconstructed PET images. Moreover, the approach using the neural network was also superior to the vendor-supplied ZTE segmentation approach.

So far, no evaluation of ZTE-AC for absolute quantification of dynamic receptor studies (e.g., in terms of non-displaceable binding potential or distribution volume) has been published. The influence of attenuation correction on parameters derived from kinetic modeling is more complex especially in case when reference tissue models are used. In those cases, it is important to have accurate attenuation correction for the target region (e.g., the striatum) as well as for the reference region (e.g., the cerebellum).

To study the influence of ZTE-based AC on the accuracy of tracer kinetic modeling using the simplified reference tissue model, we analyzed eleven dynamic PET/MR acquisitions with the highly selective dopamine transporter tracer [^{18}F]PE2I. In addition, we investigated the regional quantitative accuracy of ZTE-based AC in 30 static [^{18}F]FDG PET/MR acquisitions.

2. MATERIALS AND METHODS

2.1. Subjects

We included 48 subjects that participated in two PET/MR research protocols in the context of neurodegenerative diseases. Thirty-four patients suspected for dementia were investigated with a static [^{18}F]FDG PET/MR protocol between October 2016 and June 2017. Three patients were excluded from this comparison study due to dental implants which led to metal artifacts in the MR images. In one case the patient was positioned too low in the head coil which led to very low ZTE MR signal in the caudal end of the head due to low coil sensitivity in that region. This case was excluded as well. The mean age of the remaining 30 patients was 63 y (range 40–77 y). In addition, we analyzed 14 dynamic [^{18}F]PE2I acquisitions of healthy controls (mean age 40.8 y, range 21–70 y). As in the case of the static acquisitions, three cases had to be excluded due to metal artifacts caused by dental implants.

2.2. Imaging Protocol

All patients were examined on a SIGMA 3T TOF PET/MR (GE Healthcare, Chicago, US) [29]. The static [^{18}F]FDG PET/MR protocol included a 25 min static PET acquisition 66 ± 9 min after tracer injection (mean injected dose 144 ± 31 MBq). For the 11 [^{18}F]PE2I cases, 60 min of dynamic PET data were acquired directly after tracer injection (mean injected dose 153 ± 15 MBq). During the PET acquisitions a LAVA flex MR [acquisition details: repetition time (T_R) 4 ms, echo time (T_E) 2.23 ms, flip angle (α) 5° , matrix $256 \times 256 \times 120$, voxel size $1.95 \text{ mm} \times 1.95 \text{ mm} \times 2.6 \text{ mm}$, number of averages 0.7, acquisition time: 18 s], a ZTE MR (acquisition details: 3D radial acquisition, α 8° , matrix $110 \times 110 \times 116$, voxel size $2.4 \text{ mm} \times 2.4 \text{ mm} \times 2.4 \text{ mm}$, number of averages 4, bandwidth $\pm 62.5 \text{ kHz}$, acquisition time 42 s) and other study-specific MR sequences were acquired. Among

Abbreviations: PET, positron emission tomography; MR, magnetic resonance imaging; AC, attenuation correction; MRAC, MR-based AC; ZTE MR, zero echo time MR; ZTEAC, ZTE MR-based AC; CTAC, CT-based AC; AtlasAC, Atlas-based AC; UTE MR, ultra short echo time MR; HU, Hounsfield unit; TOF, time of flight; OSEM, ordered subset maximum likelihood & expectation maximization; FOV, field of view; VOI, volume of interest; TAC, time activity curve.

the study-specific MR sequences were a 3D volumetric sagittal T1-weighted BRAVO sequence [acquisition details: T_E 3.2 ms, T_R 8.5 ms, inversion time (T_I) 450 ms, α 12°, receiver bandwidth \pm 31.2 kHz, number of excitations (NEX) 1, voxel size 1 mm \times 1 mm \times 1 mm] and a 3D sagittal T2-weighted CUBE FLAIR sequence [acquisition details: T_E 137 ms, number of echoes 1, T_R 8,500 ms, T_I 50 ms, receiver bandwidth \pm 31.25 kHz, NEX 1, voxel size 1.2 mm \times 1.3 mm \times 1.4 mm]. The T1-weighted and FLAIR MR sequences were used to define regions of interest in the brain in our analysis. In all cases, a standard head coil (8-channel HR brain, GE Healthcare) was used for the MR acquisitions. This coil was validated to ensure that the achievable transmit to receive switching time was short enough for zero echo time imaging purposes.

All subjects underwent a PET/CT acquisition before ($[^{18}\text{F}]\text{FDG}$ cases) or after ($[^{18}\text{F}]\text{PE2I}$ cases) the PET/MR acquisition. The PET/CT acquisitions were performed on a Siemens Biograph 16 or with a Siemens Biograph 40 (Siemens Healthcare, Erlangen, Germany) PET/CT. All PET/CT examinations included a low-dose CT acquisition (120 kV, 11 mAs) which was used to generate a CT-based attenuation image taken as the ground truth in the study.

2.3. PET Image Reconstruction

The PET raw data from all PET/MR acquisitions were reconstructed with three different methods for attenuation correction, shown in **Figure 1**. First, a GE atlas-based attenuation image (default method in the SIGNA PET/MR software version MP24) was used to reconstruct $\text{PET}_{\text{AtlasAC}}$. Subsequently, a GE ZTE-based attenuation image and a co-registered CT-based attenuation image were used to reconstruct $\text{PET}_{\text{ZTEAC}}$ and PET_{CTAC} , respectively. The generation of all attenuation images is described in detail in the following subsection. The reconstructions of the static PET data sets were performed offline with the GE reconstruction toolbox v.1.28 (GE Healthcare, Chicago, US) using time of flight ordered subset maximum likelihood expectation maximization (TOF OSEM) with 4 iterations and 28 subsets, a voxel size of 1.17 mm \times 1.17 mm \times 2.78 mm, and a Gaussian post-smoothing with an FWHM of 4 mm.

Reconstruction of the dynamic $[^{18}\text{F}]\text{PE2I}$ PET data sets was performed on the scanner (software version MP24.R03). The acquired listmode data were split into 32 frames (frame length 10–360 s). All frames were reconstructed with TOF OSEM with 4 iterations and 28 subsets, a voxel size of 1.56 mm \times 1.56 mm \times 2.78 mm and a Gaussian post-smoothing with an FWHM of 3 mm.

2.4. Generation of Attenuation Images

First, the atlas-based attenuation images were generated with the GE reconstruction toolbox v.1.28 which uses the same post-processing algorithm as implemented in the software release of the SIGNA PET/MR (MP24.R03). The algorithm uses a non-rigid registration of an input in-phase LAVA flex MR image to an atlas of predefined attenuation images [30, 31]. The resulting atlas-based attenuation images are post-smoothed with a Gaussian kernel with FWHM ca. 10 mm.

Second, the ZTE-based attenuation images were generated by post-processing the ZTE MR images with a research tool provided by GE (v.1.6.2). Software release MP26 of the SIGNA PET/MR contains an option to use this algorithm for ZTE-based AC. The ZTE post-processing algorithm identifies bone voxels based on the ZTE image intensity and assigns continuous bone attenuation values [19–21]. The bone segmentation in the ZTE post-processing is completely model-free. To avoid misclassifications of air, tissue and bone in the nasal region, the ZTE post-processing algorithm v.1.6.2 uses the sinus/edge correction evaluated in Yang et al. [24]. Details of the ZTE post-processing algorithm that was used in our analysis are given in Delso et al. [27].

The vendor-provided ZTE post-processing has several input parameters. For all parameters but one (the partial volume slope) we used the default values suggested by the vendor. We used a value of 2 for the parameter for the partial volume slope which was obtained based on an evaluation of the results of the first 15 static subjects. The main influence of the partial volume slope parameter that we observed was a change in the size of the outer contour of the head (transition between background air and soft tissue of the skin). By changing the partial volume slope we obtained better agreement with the size of the outer contours derived from the CT-based attenuation images. When using the default partial volume slope of 1, the outer contour of the head is dilated by 1 voxel (2.4 mm) compared to using a partial volume slope of 2. This in turn led to a small global positive bias of 3%. All ZTE-based attenuation images were post-smoothed with a Gaussian kernel with FWHM 4 mm.

Third, after automatically removing the patient bed and cushions, the low-dose CT images from the PET/CT acquisition were rigidly co-registered to the in-phase LAVA flex MR. Subsequently, the Hounsfield units of the co-registered CT were scaled to 511-keV attenuation coefficients by using the GE-provided multi-linear scaling. We verified that the Siemens and GE scaling for 120 kV are virtually identical up to 1,200 HU (where GE decreases the slope while Siemens does not). After adding the templates for the PET/MR patient table and the head coil, a CT-based attenuation image that could be used to reconstruct the PET/MR raw data was obtained. All CT-based attenuation images were also post-smoothed with a Gaussian kernel with FWHM 4 mm.

The axial field of view (FOV) of the ZTE MR (limited by the sensitivity of the head coil) and the one of the CT was slightly smaller than the axial FOV of the PET detector rings in the SIGNA PET/MR. To complete areas in the neck and shoulders where ZTE or CT image information was not available, a simple segmentation-based two class attenuation image based on the LAVA flex MR image was used.

2.5. Image Analysis of Static Acquisitions

For all static acquisitions the mean uptake in 85 anatomical volumes of interest (VOIs) was calculated in $\text{PET}_{\text{AtlasAC}}$, $\text{PET}_{\text{ZTEAC}}$, and PET_{CTAC} . The VOIs were defined in the neuro tool of PMOD v.3.8 (PMOD technologies LCC, Zurich, Switzerland) using the Hammers atlas [32]. In

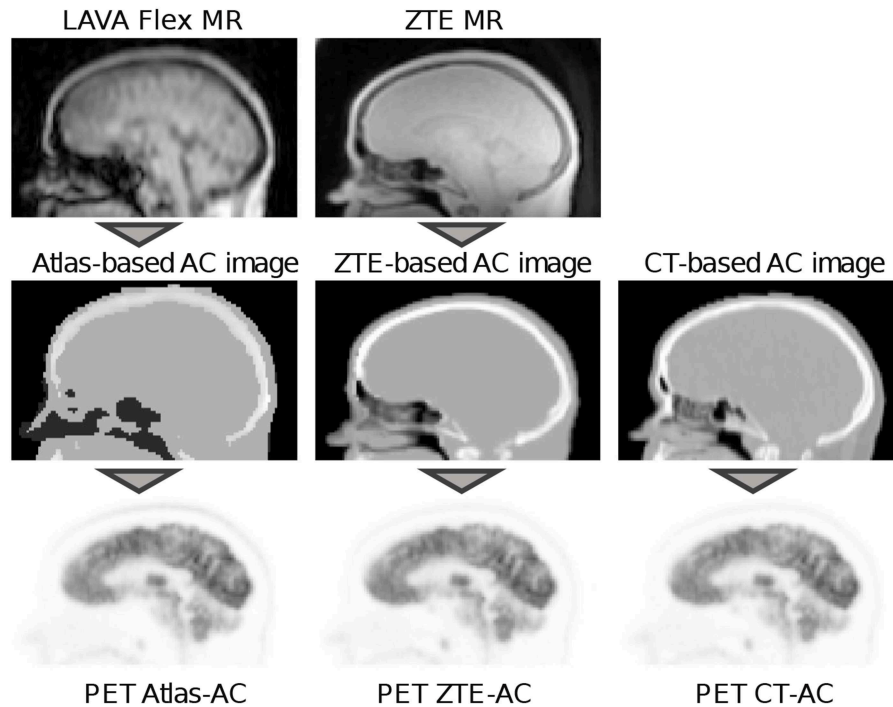


FIGURE 1 | Workflow of the PET reconstructions used in this study. In the reconstruction of $PET_{AtlasAC}$ an atlas-based attenuation image that was derived from a LAVA flex MR image was used for attenuation correction (left column). The atlas-based attenuation image was generated with the vendor-provided software version MP24. In the reconstruction of PET_{ZTEAC} attenuation correction was performed using a ZTE-based attenuation image that was derived from a ZTE MR image (middle column). The ZTE MR post-processing was done with a research tool provided by the vendor. For PET_{CTAC} a co-registered CT-based attenuation image from a PET/CT acquisition of the same day was used. In all attenuation images, templates for the bed and the head coil were added.

every VOI we calculated the fractional bias of the mean uptake as

$$b_{AtlasAC}(VOI) = \frac{a_{AtlasAC}(VOI) - a_{CTAC}(VOI)}{a_{CTAC}(VOI)} \quad (1)$$

$$b_{ZTEAC}(VOI) = \frac{a_{ZTEAC}(VOI) - a_{CTAC}(VOI)}{a_{CTAC}(VOI)}, \quad (2)$$

where $a_{CTAC}(VOI)$ is the mean uptake of the VOI in PET_{CTAC} that was used as the gold standard and $a_{AtlasAC}(VOI)$ and $a_{ZTEAC}(VOI)$ are the mean uptake of the VOI in $PET_{AtlasAC}$ and PET_{ZTEAC} , respectively. In three subjects (6, 7, and 21), the caudal end of the occipital skull was not completely in the FOV in the attenuation CT. In those subjects, the cerebellum VOIs were excluded from the analysis. All VOIs were grouped according to their anatomical location into the following groups: frontal cortex, temporal cortex, parietal cortex, occipital cortex, medial temporal cortex, striatum, thalamus, cerebellum, and cerebral white matter. All VOIs and the assigned groups (regions) are listed in **Tables S1, S2**. A Wilcoxon signed-rank test was used to test whether the subject averaged mean of $a_{AtlasAC}$ and a_{ZTEAC} is different from a_{CTAC} in all VOIs and regions.

To analyze the robustness of the vendor-provided atlas-based and ZTE-based attenuation correction, we applied the metric proposed in the multi-center evaluation of Ladefoged et al. [17]. This metric calculates the fraction of subjects in which the MRAC-introduced voxel bias of at least a given fraction of brain

voxels is within $\pm 5\%$, $\pm 10\%$, $\pm 15\%$. As mentioned in Ladefoged et al. [17], for a perfect AC method, the bias in the whole brain of all subjects would be within $\pm 0\%$. The results of this metric were visualized in a characteristic curve for the three bias thresholds $\pm 5\%$, $\pm 10\%$, $\pm 15\%$. As in Ladefoged et al. [17], we also analyzed three subjects with the biggest fraction of voxels exceeding a bias of $\pm 10\%$.

2.6. Image Analysis of Dynamic Acquisitions

Regional time activity curves (TACs) were extracted for the left and right caudate nucleus, left and right putamen, and the cortex of the cerebellum. All VOIs were defined based on the 3D T1 BRAVO MR image using the Freesurfer image analysis suite which is documented and freely available online (<http://surfer.nmr.mgh.harvard.edu/>) [33]. Subsequently, we used the simplified reference tissue model (SRTM) with the cerebellar grey matter as reference region to estimate binding potential values (BP_{nd}) in the four striatal VOIs.

As proposed in Lammertsma and Hume [34] and validated for [^{18}F]PE2I in Sasaki et al. [35], the tissue response $C_t(t)$ was modeled as

$$C_t(t) = R_1 C_r(t) + \left(k_2 - \frac{R_1 k_2}{1 + BP_{nd}} \right) C_r(t) * \exp \left(\frac{-k_2 t}{1 + BP_{nd}} \right) \quad (3)$$

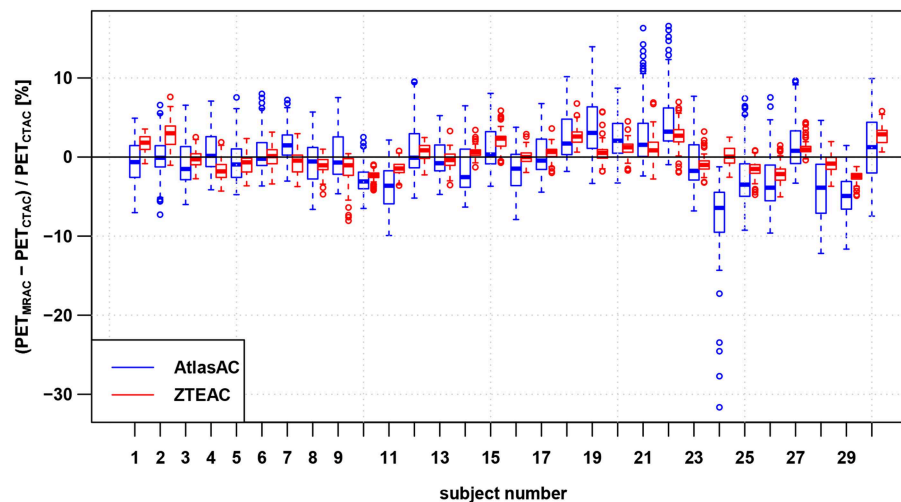


FIGURE 2 | Regional bias in the PET reconstruction caused by AtlasAC (blue) and ZTEAC (red) compared to CTAC for all 30 static PET acquisitions. Each box plot shows the bias distribution over the 85 anatomical VOIs. The rectangular boxes represent the interquartile ranges (IQR) and the horizontal line are the medians. The upper ends of the whiskers are at the minimum of the third quartile plus 1.5IQR and the biggest data point. The lower ends of the whiskers are at the maximum of the first quartile minus 1.5IQR and the smallest data point. Outliers are plotted as open circles. Please note that the VOIs in the cerebellum had to be excluded in three subjects (6, 7, 21).

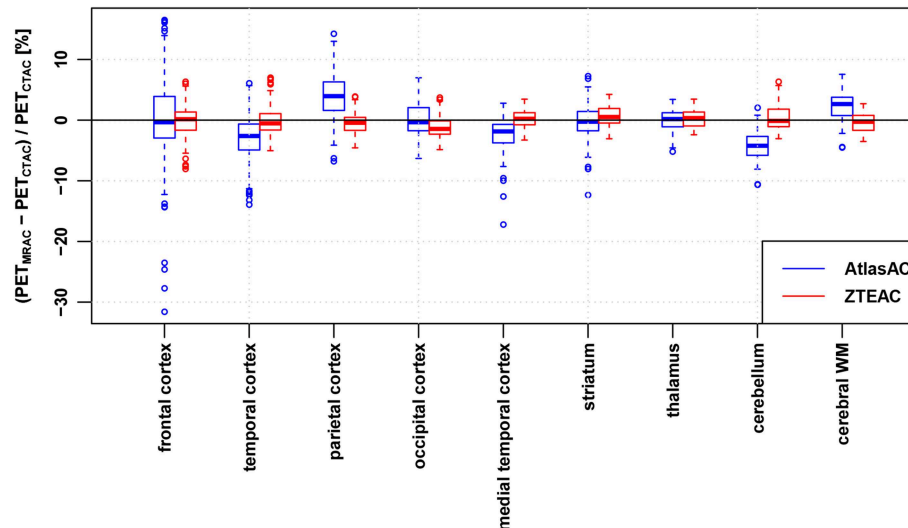


FIGURE 3 | Regional bias in the PET reconstruction caused by AtlasAC (blue) and ZTEAC (red) compared to CTAC as a function of the VOI location in the brain. Please note that the VOIs in the cerebellum had to be excluded in three subjects (6, 7, 21).

where $C_r(t)$ is the TAC of the reference tissue (the cerebellum), R_1 is the ratio between K_1 of the tissue and reference tissue, and $*$ denotes the convolution operator. The parameters R_1 , k_2 , and BP_{nd} were obtained with non-linear curve fitting using the python package lmfit (v.0.9.7).

Similar to Equations (1) and (2), we calculated the bias of BP_{nd} , R_1 , and k_2 in the four striatal VOIs for $PET_{AtlasAC}$ and PET_{ZTEAC} compared to PET_{CTAC} . In all VOIs, a Wilcoxon signed-rank test was used to test whether the subject averaged mean of $BP_{nd,AtlasAC}$ and $BP_{nd,ZTEAC}$ differ from $BP_{nd,CTAC}$.

3. RESULTS

3.1. Regional Bias in Static PET Imaging

Figures 2, 3 and Tables S3, S4 show the results for the regional bias in the static $[^{18}F]FDG$ reconstructions caused by ZTEAC and AtlasAC compared to CTAC on a subject and regional level, respectively. Globally the bias ranges from -31.6 to $+16.6\%$ with a mean of -0.4% and a standard deviation of 4.3% for $PET_{AtlasAC}$. For PET_{ZTEAC} the bias ranges from -8.0 to $+7.7\%$ with a mean of 0.1% and a standard deviation of 2.0% . Excluding

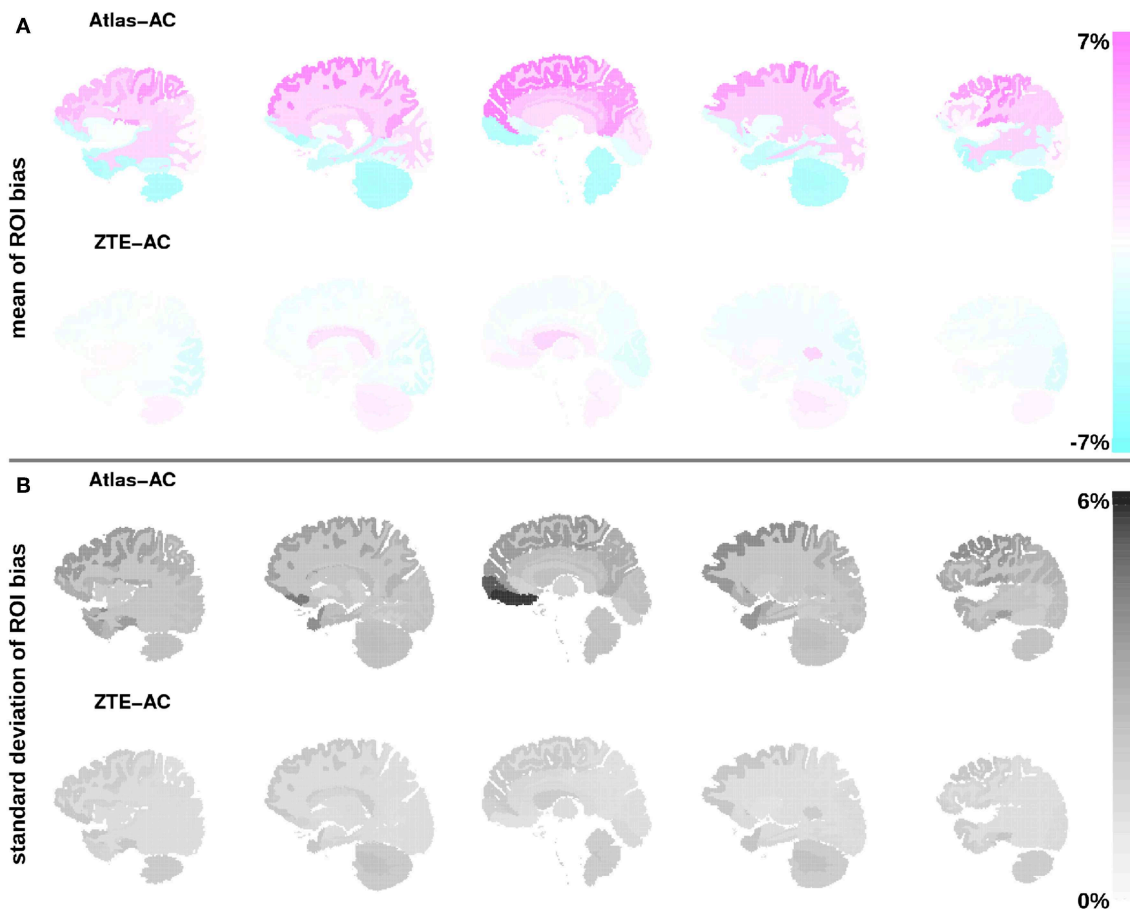


FIGURE 4 | (A) Mean of bias in the PET reconstruction in all 85 anatomical VOIs averaged over all 30 static PET acquisitions for Atlas-AC (top row) and ZTE-AC (bottom row). **(B)** Standard deviation of VOI bias. The VOI location is visualized in five sagittal slices using the brain anatomy of subject 1. Please note that the VOIs in the cerebellum had to be excluded in three subjects (6, 7, 21).

the outliers based on the boxplot shown in **Figure 3** reduces the global bias range to -12 to $+14\%$ for $PET_{AtlasAC}$ and to -5.5 to $+5.5\%$ for PET_{ZTEAC} .

On a subject level, **Figure 2** and **Table S3** demonstrate that ZTEAC strongly reduces the inter- and intra-subject variability in the bias. In subject 24 where the non-rigid alignment to the atlas failed, $PET_{AtlasAC}$ showed severe negative bias of more than -25% in the orbitofrontal cortical VOIs (see **Figure 5**). In these VOIs of subject 24, the bias of PET_{ZTEAC} was $<1.6\%$.

On a regional level, **Figure 3** and **Table S4** show that ZTEAC strongly reduces the inter- and intra-regional variability in the bias, as well as the mean bias in the frontal cortex, temporal cortex, parietal cortex, medial temporal cortex, cerebellum, and cerebral white matter. In all regions shown in **Figure 2**, the mean bias in PET_{ZTEAC} is between -1.2 and $+0.6\%$. $PET_{AtlasAC}$ shows a distinct negative bias in the cerebellum (mean -4.2%) and distinct positive bias in the parietal cortex (mean $+4\%$).

On a VOI level, **Figure 4** and **Tables S1, S2** demonstrate that ZTEAC strongly reduces the inter- and intra-VOI variability in

the bias, as well as the mean bias in almost all VOIs. The mean VOI bias caused by ZTEAC ranges from -1.8% in the lateral remainder of the left occipital lobe to $+2.2\%$ in the left lateral ventricle. In $PET_{AtlasAC}$, a distinct gradient in the mean VOI bias in the cranio-caudal direction is visible. The mean VOI bias caused by AtlasAC ranges from -4.5% in the cerebral white matter to $+6.6\%$ in the left superior frontal gyrus. In PET_{ZTEAC} , only 1.4% of the analyzed VOIs in all subjects had a bias of more than 5% whereas in $PET_{AtlasAC}$ 20.3% of all VOIs showed a bias of more than 5% .

Figure 6 shows the results of the outlier metric [17] for biases within ($\pm 5, \pm 10, \pm 15\%$). Again, the performance of ZTE-based attenuation correction is much better than the one of the atlas-based attenuation correction. At least $95/77\%$ of all brain voxels in all subjects show a bias within $\pm 10\%$ for $PET_{ZTEAC}/PET_{AtlasAC}$. For a bias within $\pm 5\%$ the corresponding values are $82/46\%$ and for a bias within $\pm 15\%$ the corresponding values are $97/89\%$. **Table 1** shows the results of the three worst outliers in terms of subjects with highest voxel bias, highest VOI bias and highest fraction of the brain exceeding a bias of $\pm 10\%$.

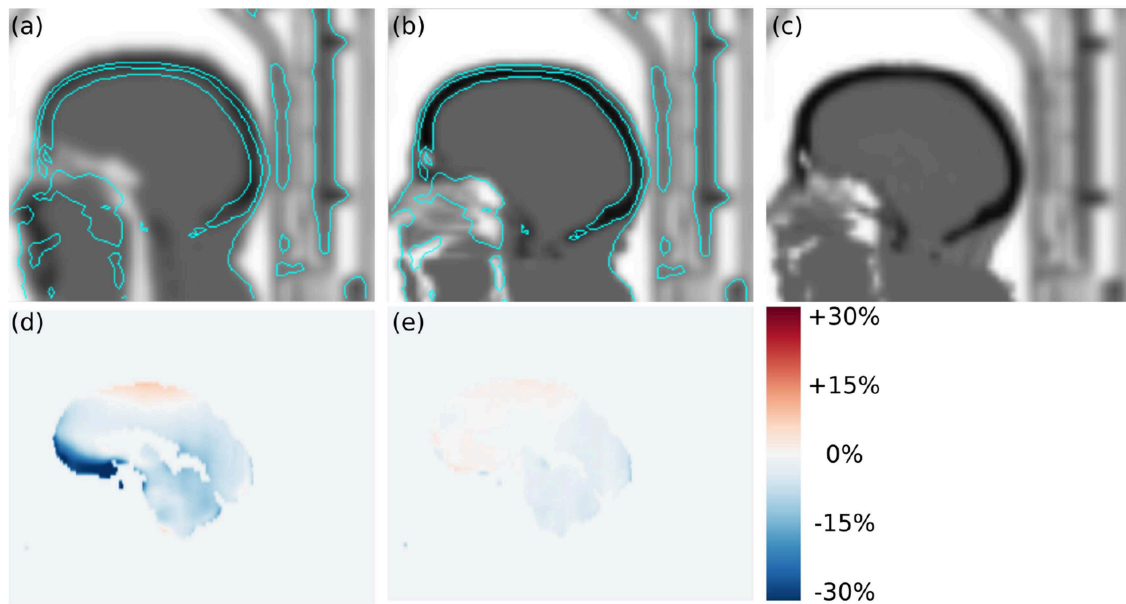


FIGURE 5 | Transversal slices of (a) atlas-based attenuation image, (b) ZTE-based attenuation image, (c) CT-based attenuation image, (d) regional bias in PET_{AtlasAC}, and (e) regional bias in PET_{ZTEAC} of subject 24. In this case, the template registration in the atlas-based attenuation image failed which caused a misclassification of soft tissue voxels as air voxels in the frontal region. The cyan contour lines show the head contour in the CT-based attenuation image for comparison. As a result of the underestimated attenuation PET_{AtlasAC} shows strong negative bias of up to -32% in the left straight gyrus.

3.2. Bias in Kinetic Modeling of [^{18}F]PE2I

Figure 7 and **Table S5** summarize the bias in the modeled BP_{nd} in four different regions of the striatum using the cerebellum as reference region and TACs derived from PET_{AtlasAC} and PET_{ZTEAC} compared to TACs from PET_{CTAC}. The bias in the BP_{nd} ranges from -0.6% (right putamen in subject 11) to $+9.4\%$ (left caudate nucleus subject 9) for PET_{AtlasAC} and from -0.8% (right putamen subject 3) to $+4.8\%$ (right caudate nucleus subject 8) for PET_{ZTEAC}. The right caudate nucleus shows the biggest subject averaged regional bias ($5.1 \pm 2.6\%$, $p = 0.003$ for PET_{AtlasAC} and $2.0 \pm 1.5\%$, $p = 0.006$ for PET_{ZTEAC}). In addition, **Figures S1–S3** show the bias in the time activity curves, and the R_1 and k_2 estimates in PET_{AtlasAC} and PET_{ZTEAC}, respectively.

4. DISCUSSION

Our analysis demonstrates that the bias caused by ZTEAC compared to CTAC as ground truth for brain PET/MR is small. The magnitude of the maximum bias of 8% is in agreement with the analysis of Sekine et al. [20]. In contrast to Sekine et al. [20], we have evaluated more static PET as well as dynamic PET acquisitions. Moreover, the subjects in our analysis underwent a PET/MR protocol with realistic PET acquisition times whereas [20] only used an additional 2 min PET/MR exam after a PET/CT acquisition.

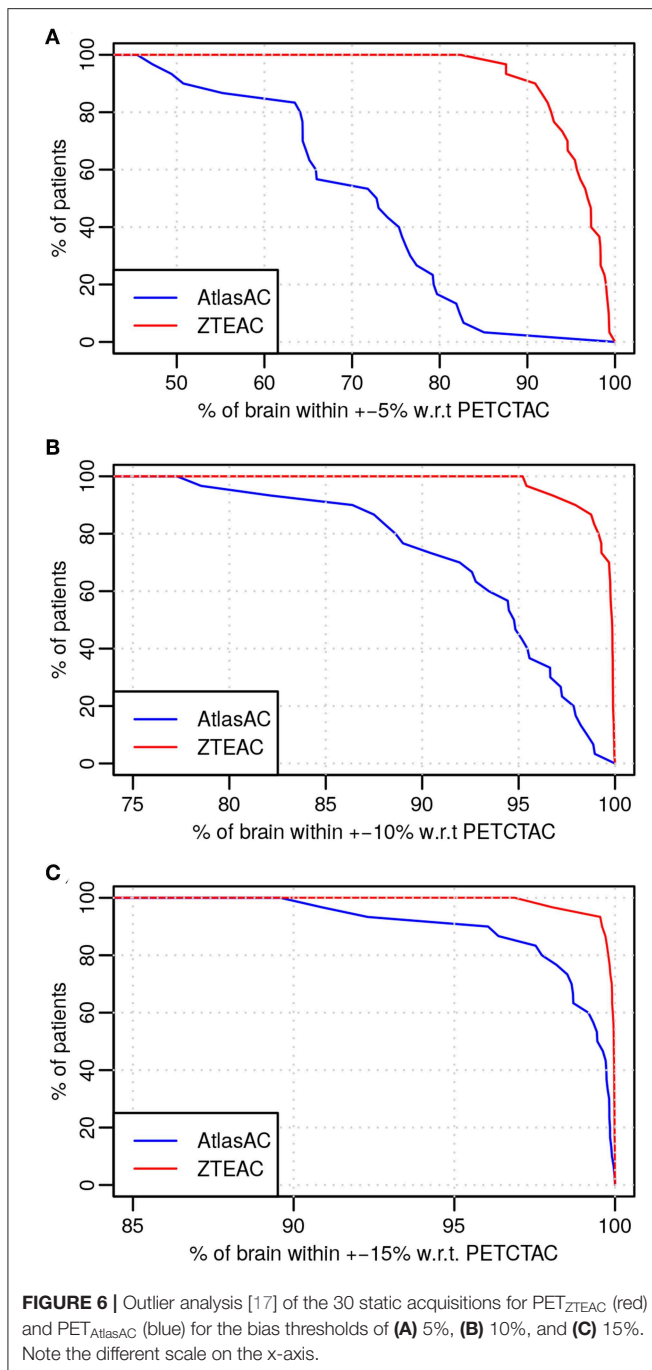
In contrast to the earlier evaluation of the quantitative accuracy of the AtlasAC [30, 31] (range of VOI bias -5 to $+7.3\%$), our analysis showed that the AtlasAC implemented in the SIGNA PET/MR software version MP24, can lead to

individual regional underestimations of up to -32% (as observed in subject 24). A possible reason for the discrepancy is the fact that the number of subjects in Sekine et al. [30, 31] was much smaller compared to our study. In this work, the biggest underestimations were found in a single subject (24) where the alignment of the atlas to the patient anatomy failed (see **Figure 5**) which caused a misclassification of some soft-tissue voxels as air voxels (pharynx) in the frontal region. Since the atlas alignment is highly subject dependent, failures are hard to predict. As demonstrated in subject 24, those failures can occur with the investigated implementation of the AtlasAC leading to severe problems in regional quantification.

As observed in Sekine et al. [20], another drawback of the AtlasAC is the fact that the introduced bias in the PET reconstruction shows a clear gradient in the cranio-caudal direction. Caudal VOIs such as the cerebellum (ca -4.2%) and the anterior lateral temporal lobe (-4.2%) show negative bias. This is because part of the temporal and occipital bone are classified as soft tissue in the AtlasAC. Moreover, there is a gross underestimation of the anterior part of the head including the oropharynx, nasal cavities, and cartilage tissue.

On the other hand, the superior cortical areas (frontal-parietal) show positive bias ($+6.6\%$ in the left superior frontal gyrus). This overestimation is caused by the fact that (a) the thickness of the superior skull seems overestimated in the AtlasAC and (b) the atlas-based attenuation image is heavily post-smoothed such that some soft tissue voxels in the superior gyri in the attenuation image are affected by spill over from skull voxels.

The cranio-caudal gradient in the bias distribution affects especially cerebral kinetic modeling analysis when using the



cerebellum as the reference region. This could be demonstrated in the kinetic modeling of the binding potential in the striatum of the 11 [^{18}F]PE2I subjects. As a consequence of the observed negative bias in the cerebellum compared to the striatum in PET_{AtlasAC} in the static cases, AtlasAC leads to a small but systematic and significant overestimation of the binding potential of [^{18}F]PE2I in the striatum (ca. +5% in the caudate nucleus and +3.3% in the putamen). This positive bias can be understood by looking at Equation (3). Under the assumptions that $\text{BP}_{\text{nd}} \gg 1$

and $1 + \text{BP}_{\text{nd}} \gg R_1$ (which both are fulfilled for [^{18}F]PE2I in the striatum), it can be seen that scaling $C_r(t)$ with α and at the same time scaling R_1 , k_2 , and BP_{nd} with α^{-1} yields the same tissue response $C_t(t)$. Since we can deduce from the analysis of the static examinations that $C_r(t)$ in the cerebellum is underestimated by ca. 4% and that there is almost no bias in the striatum ($C_t(t)$), we would expect a 4% overestimation in R_1 , k_2 , and BP_{nd} which is in accordance with the results of the dynamic analysis as shown in Figure 7 and Figures S2, S3.

Using ZTEAC strongly reduces this bias in BP_{nd} (ca. +2.0% in the caudate nucleus and +1.1% in the putamen). The performance of ZTEAC in the context of dynamic PET imaging is comparable to the MaxProb multi atlas-based attenuation correction method. In [36], Merida et al. showed that the MaxProb method leads to a regional bias of -2 to $+5\%$ in the BP_{nd} of seven subjects examined with [^{18}F]MPPF.

It has been shown [31, 37] and should be noted that the AtlasAC method implemented in the SIGNA PET/MR software version MP24, is clearly outperformed by more advanced atlas-based methods. Since the focus of this study was to analyze the performance of the ZTE-based attenuation correction, a detailed analysis of more advanced atlas-based methods for MR-based attenuation correction is beyond the scope of this study.

Compared to the detailed multi-center study of 11 methods for brain attenuation correction for the Siemens mMR in 359 subjects by Ladefoged et al. [17], it can be seen that the results for the regional quantitative accuracy of ZTEAC are comparable to the best methods in Ladefoged et al. [17] which showed a global mean bias in the range of -0.4% to $+0.8\%$ with a standard deviation of 1.2% to 1.9%. Also in terms of robustness (as seen in the standard deviation in the VOI-averaged bias) and in terms of outlier behavior ZTEAC performs comparably to the best methods of Ladefoged et al. [17]. However, it should be noted that we could only analyze 30 subjects which influences the detection of (rare) outliers.

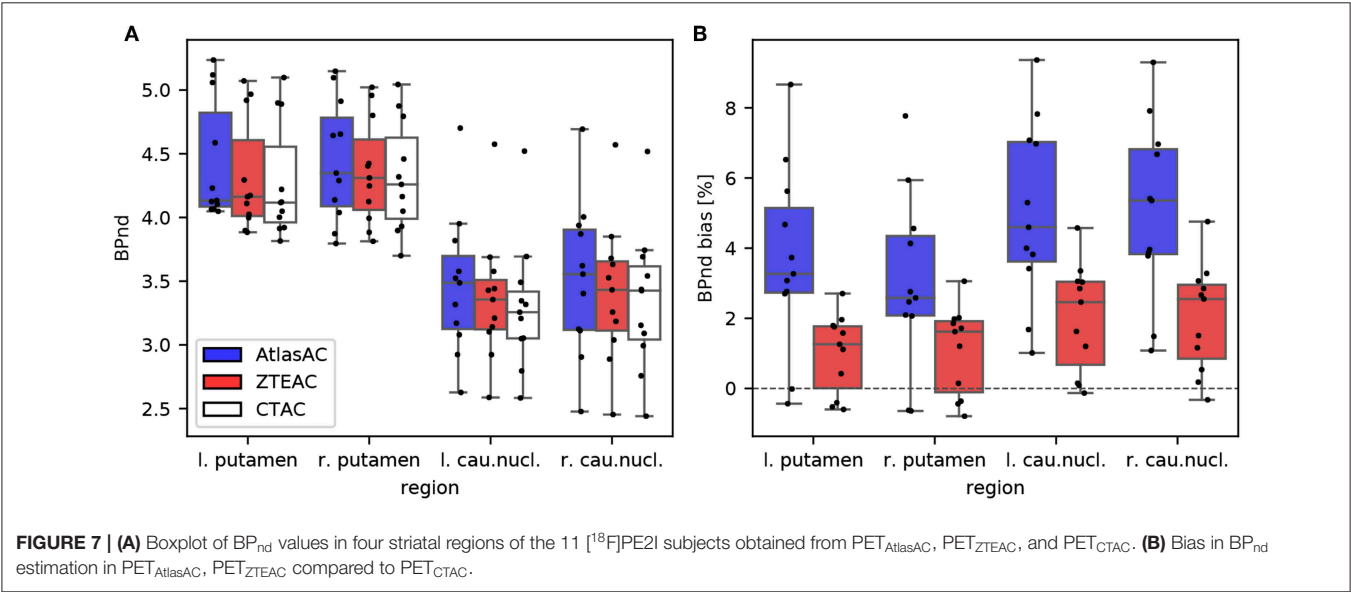
Among the five best methods in Ladefoged et al. [17] are three template-/atlas-based methods [9, 13, 37] and two ultra short echo time MR (UTE) segmentation-based methods [4, 5]. Compared to the template-/atlas-based methods, the current ZTEAC for brain has the advantage that it does not rely on any anatomical prior information. This might be beneficial in subjects with very abnormal brain anatomy (e.g., after surgery or traumatic brain injury) which needs further validation.

Finally, the fact that we had to exclude 6 out of 48 patients (12.5%) due to MR artifacts caused by dental implants demonstrates that there is a need for a reliable method for compensation of metal artifacts that can be applied in clinical routine.

A potential limitation of the study is the fact that the attenuation CTs used for CTAC were acquired on a Siemens PET/CT system, but scaled to linear attenuation coefficients with the multi-linear scaling provided by GE. This might lead to small residual uncertainties in the linear attenuation coefficients of the ground truth CTAC due to the fact that the vendor-specific scaling procedures might be optimized for different effective x-ray spectra. However,

TABLE 1 | Results of outlier analysis of the static acquisitions in terms of subjects with highest voxel bias, highest VOI bias, and highest fraction of brain exceeding a bias of $\pm 10\%$.

Subjects with highest single voxel bias			
AtlasAC	Subject 24 −53% (left straight gyrus)	Subject 29 −43% (left anterior temporal lobe)	Subject 21 +41% (left superior frontal gyrus)
ZTEAC	Subject 5 +45% (left cerebellum)	Subject 18 +43% (left cerebellum)	Subject 21 +41% (right fusiform gyrus)
Subjects with highest VOI bias			
AtlasAC	Subject 24 −31% (left straight gyrus)	Subject 22 +16% (left superior frontal gyrus)	Subject 21 +16% (left precentral gyrus)
ZTEAC	subject 9 −8% (left middle frontal gyrus)	subject 22 +7% (right superior temporal gyrus)	subject 21 +7% (right fusiform gyrus)
Subjects with highest fraction of brain exceeding a bias of $\pm 10\%$			
AtlasAC	Subject 22 23%	Subject 19 22%	Subject 21 18%
ZTEAC	Subject 21 5%	Subject 6 5%	Subject 9 3%



we do not expect this to be a major problem, because the multi-linear scaling curves of GE and Siemens are virtually identical up to 1,200 HU. Note that in software version MP26 of the SIGNA PET/MR, the algorithm that generates the atlas-based attenuation images was updated compared to software version MP24. A detailed analysis of the performance of this updated algorithm is beyond the scope of the manuscript since all our subjects were acquired under software version MP24.

5. CONCLUSION

ZTE-based attenuation correction provides excellent quantitative accuracy for static and dynamic PET/MR imaging in all parts of the brain. It is clearly superior to the Atlas-based head attenuation correction implemented in the SIGNA PET/MR

software version MP24 and hereby obviates the major concern that was present in the quantitative accuracy of brain PET/MR.

DATA AVAILABILITY STATEMENT

The datasets generated for this study are available on request to the corresponding author.

ETHICS STATEMENT

The studies involving human participants were reviewed and approved by Ethical Committee of UZ Leuven. The patients/participants provided their written informed consent to participate in this study.

AUTHOR CONTRIBUTIONS

GS performed the PET reconstructions, the static PET image analysis, and drafted the manuscript. MK performed the analysis of the dynamic PET images. SW coordinated the study and helped to draft the manuscript. AR helped to perform the PET reconstructions. DV coordinated the study and helped to draft the manuscript. GD performed the postprocessing of the ZTE MR images. RP and NM optimized the ZTE MR sequence on the SIGNA PET/MR at UZ Leuven. JN and KV designed the study and helped to draft the manuscript.

REFERENCES

- Andersen FL, Ladefoged CN, Beyer T, Keller SH, Hansen AE, Højgaard L, et al. Combined PET/MR imaging in neurology: MR-based attenuation correction implies a strong spatial bias when ignoring bone. *Neuroimage*. (2014) **84**:206–16. doi: 10.1016/j.neuroimage.2013.08.042
- Keereman V, Fierens Y, Broux T, De Deene Y, Lonnew M, Vandenbergh S. MRI-based attenuation correction for PET/MRI using ultrashort echo time sequences. *J Nucl Med*. (2010) **51**:812–8. doi: 10.2967/jnumed.109.065425
- Delso G, Carl M, Wiesinger F, Sacolick L, Porto M, Hullner M, et al. Anatomic evaluation of 3-dimensional ultrashort-echo-time bone maps for PET/MR attenuation correction. *J Nucl Med*. (2014) **55**:780–5. doi: 10.2967/jnumed.113.130880
- Ladefoged CN, Benoit D, Law I, Holm S, Kjær A, Højgaard L, et al. Region specific optimization of continuous linear attenuation coefficients based on UTE (RESOLUTE): application to PET/MR brain imaging. *Phys Med Biol*. (2015) **60**:8047–65. doi: 10.1088/0031-9155/60/20/8047
- Juttukonda MR, Mersereau BG, Chen Y, Su Y, Rubin BG, Benzinger TLS, et al. MR-based attenuation correction for PET/MRI neurological studies with continuous-valued attenuation coefficients for bone through a conversion from R2* to CT-Hounsfield units. *Neuroimage*. (2015) **112**:160–8. doi: 10.1016/j.neuroimage.2015.03.009
- Anazodo UC, Thiessen JD, Ssali T, Mandel J, Günther M, Butler J, et al. Feasibility of simultaneous whole-brain imaging on an integrated PET-MRI system using an enhanced 2-point Dixon attenuation correction method. *Front Neurosci*. (2015) **9**:434. doi: 10.3389/fnins.2014.00434
- Cabello J, Lukas M, Förster S, Pyka T, Nekolla SG, Ziegler SI. MR-based attenuation correction using ultrashort-echo-time pulse sequences in dementia patients. *J Nucl Med*. (2015) **56**:423–9. doi: 10.2967/jnumed.114.146308
- Cabello J, Lukas M, Rota Kops E, Ribeiro A, Shah NJ, Yakushev I, et al. Comparison between MRI-based attenuation correction methods for brain PET in dementia patients. *Eur J Nucl Med Mol Imaging*. (2016) **43**:2190–200. doi: 10.1007/s00259-016-3394-5
- Izquierdo-Garcia D, Hansen AE, Forster S, Benoit D, Schachoff S, Furst S, et al. An SPM8-based approach for attenuation correction combining segmentation and nonrigid template formation: application to simultaneous PET/MR brain imaging. *J Nucl Med*. (2014) **55**:1825–30. doi: 10.2967/jnumed.113.136341
- Paulus DH, Quick HH, Geppert C, Fenchel M, Hermosillo G, Faul D, et al. Whole-body PET/MR imaging: quantitative evaluation of a novel model-based MR attenuation correction method including bone. *J Nucl Med*. (2015) **56**:1061–6. doi: 10.2967/jnumed.115.156000
- Koesters T, Friedman KP, Fenchel M, Zhan Y, Hermosillo G, Babb J, et al. Dixon sequence With superimposed model-based bone compartment provides highly accurate PET/MR attenuation correction of the brain. *J Nucl Med*. (2016) **57**:918–24. doi: 10.2967/jnumed.115.166967
- Burgos N, Cardoso MJ, Thielemans K, Modat M, Pedemonte S, Dickson J, et al. Attenuation correction synthesis for hybrid PET-MR scanners: application to brain studies. *IEEE Trans Med Imaging*. (2014) **33**:2332–41. doi: 10.1109/TMI.2014.2340135

FUNDING

GS was funded by the NIH project 1P41EB017183-01A1. AR and JN are funded by the Research Foundation Flanders (FWO) projects 12T7118N and G.0275.14N.

SUPPLEMENTARY MATERIAL

The Supplementary Material for this article can be found online at: <https://www.frontiersin.org/articles/10.3389/fphy.2019.00211/full#supplementary-material>

- Merida I, Costes N, Heckemann R, Hammers A. Pseudo-CT generation in brain MR-PET attenuation correction: comparison of several multi-atlas methods. In: *IEEE 12th Int Symp Biomed Imaging*. Vol. 1. Brooklyn, NY (2015). p. 1431–4. Available online at: <http://ejnmmpphys.springeropen.com/articles/10.1186/2197-7364-2-S1-A29>
- Benoit D, Ladefoged CN, Rezaei A, Keller SH, Andersen FL, Højgaard L, et al. Optimized MLAA for quantitative non-TOF PET/MR of the brain. *Phys Med Biol*. (2016) **61**:8854–74. doi: 10.1088/1361-6560/61/24/8854
- Rezaei A, Schramm G, Willekens SM, Delso G, Van Laere K, Nuyts J. A quantitative evaluation of joint activity and attenuation reconstruction in TOF-PET/MR brain imaging. *J Nucl Med*. (2019) **60**:1649–55. doi: 10.2967/jnumed.118.220871
- Renner A, Rausch I, Cal Gonzalez J, Frass-Kriegel R, De Lara LN, Sieg J, et al. A head coil system with an integrated orbiting transmission point source mechanism for attenuation correction in PET/MRI. *Phys Med Biol*. (2018) **63**:225014. doi: 10.1088/1361-6560/aae9a9
- Ladefoged CN, Law I, Anazodo U, St Lawrence K, Izquierdo-Garcia D, Catana C, et al. A multi-centre evaluation of eleven clinically feasible brain PET/MRI attenuation correction techniques using a large cohort of patients. *Neuroimage*. (2017) **147**:346–59. doi: 10.1016/j.neuroimage.2016.12.010
- Weiger M, Stanpanoni M, Pruessmann KP. Direct depiction of bone microstructure using MRI with zero echo time. *Bone*. (2013) **54**:44–7. doi: 10.1016/j.bone.2013.01.027
- Wiesinger F, Sacolick LI, Menini A, Kaushik SS, Ahn S, Veit-Haibach P, et al. Zero TE MR bone imaging in the head. *Magn Reson Med*. (2015) **114**:107–14. doi: 10.1002/mrm.25545
- Sekine T, ter Voert EEGW, Warnock G, Buck A, Huellner M, Veit-Haibach P, et al. Clinical evaluation of zero-echo-time attenuation correction for brain 18F-FDG PET/MRI: comparison with atlas attenuation correction. *J Nucl Med*. (2016) **57**:1927–32. doi: 10.2967/jnumed.116.175398
- Delso G, Wiesinger F, Sacolick LI, Kaushik SS, Shanbhag DD, Hullner M, et al. Clinical evaluation of zero-echo-time MR imaging for the segmentation of the skull. *J Nucl Med*. (2015) **56**:417–22. doi: 10.2967/jnumed.114.149997
- Boydev C, Demol B, Pasquier D, Saint-Jalmes H, Delpon G, Reynaert N. Zero echo time MRI-only treatment planning for radiation therapy of brain tumors after resection. *Phys Med*. (2017) **42**:332–8. doi: 10.1016/j.ejmp.2017.04.028
- Khalifé M, Fernandez B, Jaubert O, Soussan M, Brulon V, Buvat I, et al. Subject-specific bone attenuation correction for brain PET/MR: can ZTE-MRI substitute CT scan accurately? *Phys Med Biol*. (2017) **62**:7814–32. doi: 10.1088/1361-6560/aa8851
- Yang J, Wiesinger F, Kaushik S, Shanbhag D, Hope TA, Larson PEZ, et al. Evaluation of sinus/edge corrected ZTE-based attenuation correction in brain PET/MRI. *J Nucl Med*. (2017) **58**:1873–9. doi: 10.2967/jnumed.116.188268
- Leynes AP, Yang J, Hope TA. Hybrid ZTE/Dixon MR-based attenuation correction for quantitative uptake estimation of pelvic lesions in PET / MRI. *Med Phys*. (2017) **44**:902–13. doi: 10.1002/mp.12122
- Wiesinger F, Bylund M, Yang J, Kaushik S, Shanbhag D, Ahn S, et al. Zero TE-based pseudo-CT image conversion in the head and its application in PET/MR attenuation correction and MR-guided radiation therapy planning. *Magn Reson Med*. (2018) **80**:1440–51. doi: 10.1002/mrm.27134

27. Delso G, Kemp B, Kaushik S, Wiesinger F, Sekine T. Improving PET/MR brain quantitation with template-enhanced ZTE. *NeuroImage*. (2018) **181**:403–13. doi: 10.1016/j.neuroimage.2018.07.029
28. Gong K, Yang J, Kim K, El Fakhri G, Seo Y, Li Q. Attenuation correction for brain PET imaging using deep neural network based on Dixon and ZTE MR images. *Phys Med Biol*. (2018) **63**:125011. doi: 10.1088/1361-6560/aac763
29. Grant AM, Deller TW, Khalighi MM, Maramraju SH, Delso G, Levin CS. NEMA NU 2-2012 performance studies for the SiPM-based ToF-PET component of the GE SIGNA PET/MR system. *Med Phys*. (2016) **43**:2334–43. doi: 10.1118/1.4945416
30. Sekine T, Buck A, Delso G, ter Voert EEGW, Huellner M, Veit-Haibach P, et al. Evaluation of atlas-based attenuation correction for integrated PET/MR in human brain: application of a head atlas and comparison to true CT-based attenuation correction. *J Nucl Med*. (2016) **57**:215–20. doi: 10.2967/jnumed.115.159228
31. Sekine T, Burgos N, Warnock G, Huellner M, Buck A, ter Voert EEGW, et al. Multi-atlas-based attenuation correction for brain 18F-FDG PET imaging using a time-of-flight PET/MR scanner: comparison with clinical single-atlas- and CT-based attenuation correction. *J Nucl Med*. (2016) **57**:1258–64. doi: 10.2967/jnumed.115.169045
32. Hammers A, Allom R, Koeppe MJ, Free SL, Myers R, Lemieux L, et al. Three-dimensional maximum probability atlas of the human brain, with particular reference to the temporal lobe. *Hum Brain Mapp*. (2003) **19**:224–47. doi: 10.1002/hbm.10123
33. Fischl B, Salat DH, Busa E, Albert M, Dieterich M, Haselgrove C, et al. Whole brain segmentation: automated labeling of neuroanatomical structures in the human brain. *Neuron*. (2002) **33**:341–55. doi: 10.1016/S0896-6273(02)00569-X
34. Lammertsma AA, Hume SP. Simplified reference tissue model for PET receptor studies. *Neuroimage*. (1996) **4**:153–8. doi: 10.1006/nimg.1996.0066
35. Sasaki T, Ito H, Kimura Y, Arakawa R, Takano H, Seki C, et al. Quantification of dopamine transporter in human brain using PET with 18F-FE-PE2I. *J Nucl Med*. (2012) **53**:1065–73. doi: 10.2967/jnumed.111.101626
36. Merida I, Reilhac A, Redoute J, Heckemann R, Costes N, Hammers A. Multi-atlas attenuation correction supports full quantification of static and dynamic brain PET data in PET-MR. *Phys Med Biol*. (2017) **62**:2834–58. doi: 10.1088/1361-6560/aa5f6c
37. Burgos N, Cardoso MJ, Thielemans K, Modat M, Dickson J, Schott JM, et al. Multi-contrast attenuation map synthesis for PET/MR scanners: assessment on FDG and Florbetapir PET tracers. *Eur J Nucl Med Mol Imaging*. (2015) **42**:1447–58. doi: 10.1007/s00259-015-3082-x

Conflict of Interest: GD is an employee of GE Healthcare, Cambridge, UK. GS, MK, AR, NM, RP, JN, and KV received travel grants from GE Healthcare for attending workshops. GS and KV received travel grants for presenting PET/MR results at GE user meetings. KU Leuven received a research collaboration grant for partial funding of this study.

The remaining authors declare that the research was conducted in the absence of any commercial or financial relationships that could be construed as a potential conflict of interest.

Copyright © 2019 Schramm, Koole, Willekens, Rezaei, Van Weehaeghe, Delso, Peeters, Mertens, Nuyts and Van Laere. This is an open-access article distributed under the terms of the Creative Commons Attribution License (CC BY). The use, distribution or reproduction in other forums is permitted, provided the original author(s) and the copyright owner(s) are credited and that the original publication in this journal is cited, in accordance with accepted academic practice. No use, distribution or reproduction is permitted which does not comply with these terms.



Optimization of the k'_2 Parameter Estimation for the Pharmacokinetic Modeling of Dynamic PIB PET Scans Using SRTM2

Débora E. Peretti¹, Fransje E. Reesink², Janine Doorduyn¹, Bauke M. de Jong², Peter P. De Deyn^{2,3}, Rudi A. J. O. Dierckx¹, Ronald Boellaard¹ and David Vázquez García^{1*}

¹ Department of Nuclear Medicine and Molecular Imaging, University Medical Center Groningen, University of Groningen, Groningen, Netherlands, ² Department of Neurology, Alzheimer Research Centre, University Medical Center Groningen, University of Groningen, Groningen, Netherlands, ³ Laboratory of Neurochemistry and Behaviour, Institute Born-Bunge, University of Antwerp, Antwerp, Belgium

OPEN ACCESS

Edited by:

Ivo Rausch,
Medical University of Vienna, Austria

Reviewed by:

Barbara Katharina Geist,
Medical University of Vienna, Austria
Anders Bertil Rodell,
Aarhus University Hospital, Denmark

*Correspondence:

David Vázquez García
d.vallez-garcia@umcg.nl

Specialty section:

This article was submitted to
Medical Physics and Imaging,
a section of the journal
Frontiers in Physics

Received: 06 August 2019

Accepted: 21 November 2019

Published: 12 December 2019

Citation:

Peretti DE, Reesink FE, Doorduyn J, de Jong BM, De Deyn PP, Dierckx RAJO, Boellaard R and Vázquez García D (2019) Optimization of the k'_2 Parameter Estimation for the Pharmacokinetic Modeling of Dynamic PIB PET Scans Using SRTM2. *Front. Phys.* 7:212. doi: 10.3389/fphy.2019.00212

Background: This study explores different approaches to estimate the clearance rate of the reference tissue (k'_2) parameter used for pharmacokinetic modeling, using the simplified reference tissue model 2 (SRTM2) and further explores the effect on the binding potential (BP_{ND}) of ¹¹C-labeled Pittsburgh Compound B (PIB) PET scans.

Methods: Thirty subjects underwent a dynamic PIB PET scan and were classified as PIB positive (+) or negative (−). Thirteen regions were defined from where to estimate k'_2 : the whole brain, eight anatomical region based on the Hammer's atlas, one region based on a SPM comparison between groups on a voxel level, and three regions using different BP_{ND}^{SRTM} thresholds.

Results: The different approaches resulted in distinct k'_2 estimations per subject. The median value of the estimated k'_2 across all subjects in the whole brain was 0.057. In general, PIB+ subjects presented smaller k'_2 estimates than this median, and PIB−, larger. Furthermore, only threshold and white matter methods resulted in non-significant differences between groups. Moreover, threshold approaches yielded the best correlation between BP_{ND}^{SRTM} and BP_{ND}^{SRTM2} for both groups ($R^2 = 0.85$ for PIB+, and $R^2 = 0.88$ for PIB−). Lastly, a sensitivity analysis showed that overestimating k'_2 values resulted in less biased BP_{ND}^{SRTM2} estimates.

Conclusion: Setting a threshold on BP_{ND}^{SRTM} might be the best method to estimate k'_2 in voxel-based modeling approaches, while the use of a white matter region might be a better option for a volume of interest based analysis.

Keywords: Alzheimer's disease, pharmacokinetic modeling, Pittsburgh compound B, SRTM, SRTM2

INTRODUCTION

Current research suggests that Alzheimer's disease (AD) is associated with an abnormal deposition of the amyloid- β (A β) peptide in the brain [1, 2]. These A β deposits may lead to progressive dysfunction and nerve cells death, resulting in a neurodegenerative process [3]. It is possible to assess this deposition *in-vivo* through the use of the ¹¹C-labeled Pittsburgh Compound B (PIB)

radiotracer in positron emission tomography (PET) studies [4–6]. A simple visual assessment of standardized uptake value (SUV) images, derived from these PET scans, might suffice to assess whether or not there is A β deposition. However, through pharmacokinetic modeling of dynamic PIB PET scans, it might be possible to further classify the amount of deposition in the brain [7].

Previous studies have already confirmed that the simplified reference tissue model (SRTM) [8] is the preferred method for pharmacokinetic modeling of PIB when arterial input is not available [9, 10]. However, improvements on the accuracy of the model can be done by coupling parameters [11] thereby reducing the number of variables to be fitted by the model. The simplified reference tissue model 2 (SRTM2) [12] has been validated as a model “with better accuracy and precision” [10] than the original SRTM, and has been frequently used in AD PET studies [13–16].

SRTM is a model that fits three parameters: binding potential (BP_{ND}), relative tracer flow (R_1), and clearance rate constant of the reference region (k'_2). Meanwhile, SRTM2 is a model fitted in two runs. During the first run, SRTM is used to obtain an estimate for k'_2 for each voxel in the image. This value is then fixed to the median k'_2 using voxels outside the reference region. Next, a second run is done, fitting the two remaining parameters (BP_{ND} and R_1), thus reducing the noise in the specific binding estimates and functional images. SRTM and SRTM2 were originally developed for the analysis of neuroreceptor binding. Furthermore, SRTM2 was implemented with the intention of reducing noise levels of the model parameters using a well-defined receptor-rich region for the k'_2 estimation. Nonetheless, this assumption might be violated in the case of PIB, especially in healthy subjects, who are not expected to have A β deposition.

Previous studies using SRTM2 for pharmacokinetic modeling employed different approaches for k'_2 estimation. For example, this parameter was evaluated by coupling all target time activity curves for radiotracers designed for D2/D3 receptors [17, 18] and radioligands with a high affinity for the serotonin transporter [19]. Tracers such as [^{11}C]P943 [20], used for quantifying serotonin 5-HT1B receptors, use the median value of the k'_2 estimation for all voxels that have a BP_{ND}^{SRTM} value between 0.5 and 4, and [^{18}F]DPA-714 [21], used for neuroinflammation, the median of all k'_2 values from all voxels in the image.

However, A β deposits are not evenly distributed across the brain [22], and change over time with AD progression [3]. Therefore, there are no well-defined receptor-rich regions. Other radiotracers, such as [^{18}F]Florbetaben [23], [^{18}F]Flutemetamol [24], and [^{18}F]Florbetapir [25], which also bind to the A β plaques, present the same issue. Studies with these tracers have either used SRTM or SRTM2, estimating k'_2 from all voxels of the image outside the reference region. This approach can be challenging in studies that include subjects without amyloid deposition, because the signal is not as high as in subjects that present these deposits. This lack of signal might result in noisy images, which may reduce the reliability of the estimations of the parameters from the models. In the case of PIB, previous investigations performed a pharmacokinetic analysis using SRTM [26, 27], reference Logan [28], and SRTM2 [10, 13–16]. Yet, there is no consensus on how the k'_2 estimation should be

done. Some studies take the mean SRTM-derived k'_2 value from all target regions [13, 14], while others set a minimum threshold on the BP_{ND}^{SRTM} parametric map to select the voxels being used for the k'_2 estimation [10, 15, 16]. To the best of the authors' knowledge, the effects that these approaches to estimate k'_2 have in the final BP_{ND} value, have not yet been explored.

Therefore, the aim of this study was to examine the consequences of estimating k'_2 using different approaches, and to define an optimal method for estimating k'_2 for the analysis of dynamic PIB PET studies using SRTM2.

MATERIALS AND METHODS

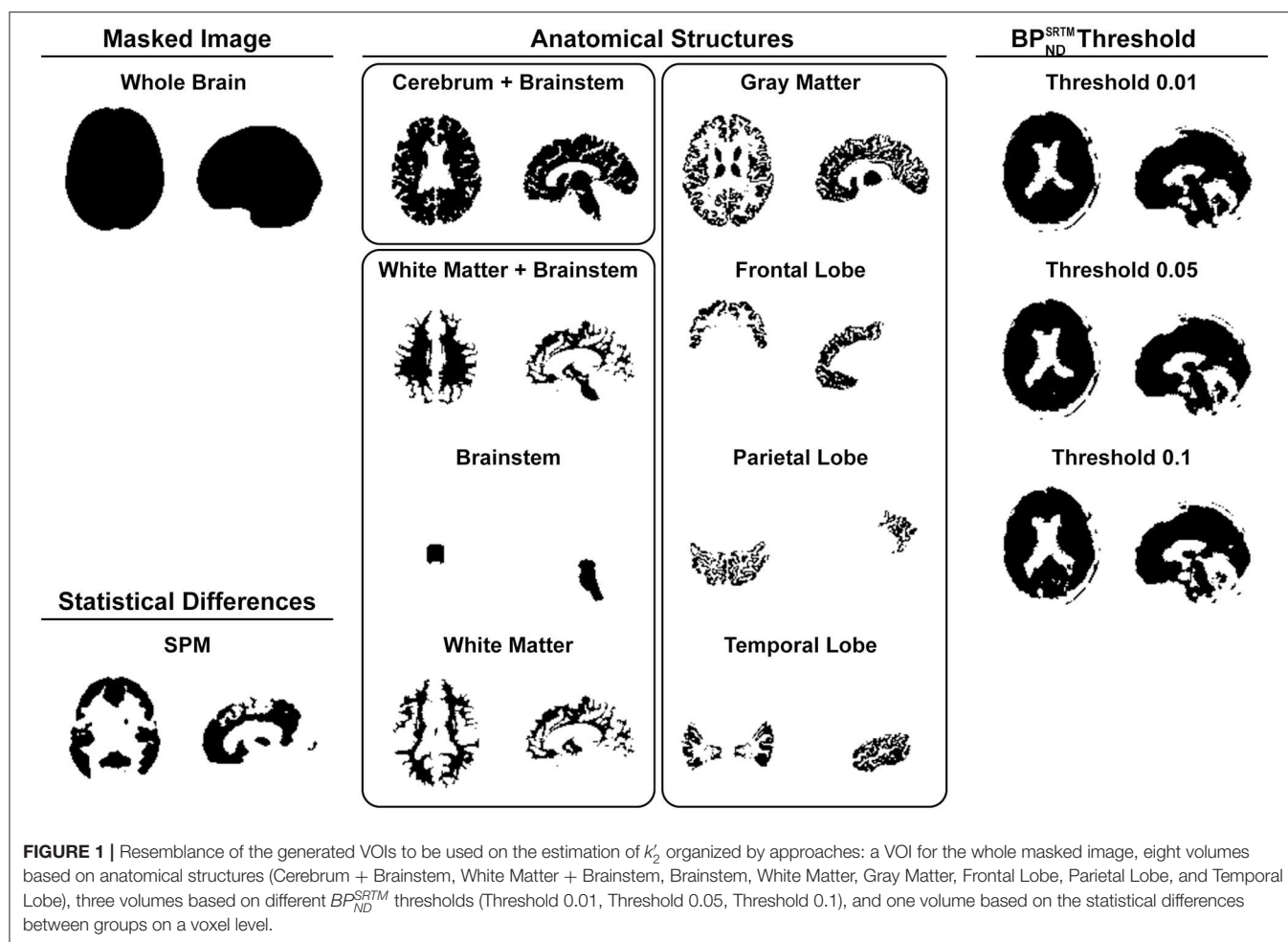
Subjects

A cohort of 30 subjects, which were available at the moment of performing this study, was selected from a larger ongoing study at the memory clinic of the University Medical Center of Groningen (UMCG), Groningen, The Netherlands. Written informed consent to participate in the study was provided. The study was conducted in agreement with the Declaration of Helsinki and subsequent revisions and approved by the Medical Ethical Committee of the UMCG (2014/320).

Patients were clinically diagnosed, by consensus in a multidisciplinary team, either with Alzheimer's Disease (AD), according to the National Institute on Aging and Alzheimer's Association criteria (NIA-AA) [29], or with mild cognitive impairment (MCI), in agreement with the Petersen criteria [30]. Healthy controls (HC) had no cognitive complaints and a minimal state examination score above 28. All subjects underwent standard dementia screening, and multimodal neuroimaging, including PIB PET scans and T1-3D magnetic resonance imaging (MRI). After the PIB PET scan, clinical diagnoses were reconsidered, according to the National Institute on Aging and the Alzheimer's Association Research supposed Framework [1]. Subjects were then divided into two categories, based on visual inspections of cortical levels of PIB binding, as “PIB+,” if binding levels were high, and “PIB–,” if they were low. The demographic characteristics of subjects are presented in **Supplementary Table 1**.

PET Acquisition

Subjects underwent a dynamic PIB PET scan under standard resting conditions with closed eyes. Scans were performed with either a Siemens Biograph 40 or 64 mCT PET scan (Siemens Medical Solutions, USA). Both systems were from the same vendor and from the same generation; the acquisition and reconstruction protocols were harmonized, and the systems were (cross-) calibrated. Therefore, no significant differences were expected from the images provided by these two different scanners. Nonetheless, a comparison between the data used in this study, provided from the different scanners, was made using a *t*-test and, as expected, no significant results were found. PIB tracer was synthesized at the radiopharmacy facility at the Nuclear Medicine and Molecular Imaging department at the UMCG, according to Good Manufacturing Practice. The tracer was administered *via* a venous cannula, and the acquisition started simultaneously with the PIB injection (379 ± 46 MBq).



Dynamic PIB PET acquisition lasted for at least 60 min (frames: 7×10 s, 3×30 s, 2×60 s, 2×120 s, 2×180 s, 5×300 s, and 2×600 s). List-mode data from PET scans were reconstructed using 3D OSEM (three iterations and 24 subsets), point spread function correction and time-of-flight, resulting in images with $400 \times 400 \times 111$ matrix, isotropic 2 mm voxels, smoothed with a 2 mm-Gaussian filter at Full Width and Half Maximum (FWHM).

Image Processing

Registration and data collection from the images were done using the PMOD software package (version 3.8; PMOD Technologies LLC). Using tissue probability maps [31], the T1 3D MRI scans were spatially normalized to the Montreal Neurologic Institute space. To define the anatomical brain regions, the Hammers atlas [32] was selected. A total of 77 regions were drawn, with right and left side separated and white matter distinguished from cortical tissue. Some regions from the original atlas were excluded: cerebellar white matter, the corpus callosum, the third ventricle, the lateral ventricles, and the temporal horns. The PET images were corrected for motion using the average of the first 12 frames and were then aligned to the MRI in individual space. The PET images were also smoothed with a Gaussian filter of 6 mm at FWHM, and voxels that were outside of the brain were masked.

Pharmacokinetic Modeling

Parametric images were generated using pharmacokinetic modeling of the dynamic PIB PET at a voxel level in individual space, and it was done in three steps: (1) a first estimate of the BP_{ND}^{SRTM} , R_1 , and efflux constant of the reference region (k_2) was obtained using a basis function implementation of SRTM [8]; (2) the k_2 parameter was then fixed to the median k_2 value of all voxels in a predefined volume of interest (VOI); and (3) the final parametric BP_{ND}^{SRTM2} map was estimated using SRTM2 [12]. Thirteen approaches were used to generate VOIs to estimate the median k_2 (**Supplementary Table 2, Figure 1**): one approach containing all voxels of the masked brain image, eight approaches based on predefined anatomical structures or VOIs, three approaches based on selecting voxels using fixed BP_{ND}^{SRTM} thresholds, and one VOI approach defined by voxels having a statistically significant difference between the images of each group (SPM). These statistical comparisons at voxel level were performed in SPM12 (Wellcome Trust Center for Neuroimaging, UK) with a two-sample t -test, and T-maps interrogated at $p = 0.005$ (uncorrected) and only clusters with $p < 0.05$, corrected for family-wise error, were considered significant. Then these VOIs were projected onto the k_2 parametric maps and the median value [12] of the voxels within the volumes were taken and used for

the generation of the final parametric BP_{ND} maps with SRTM2 (BP_{ND}^{SRTM2}). The gray matter of the cerebellum was used as a reference region due to its lack, or very late presentation, of specific PIB binding [4, 33–35]. The imposed restriction on the range of possible apparent uptake rate constant (k_{2a}) values, with a minimum of 0.01 and a maximum of 0.3, and 80 basis functions was used. These settings were applied to both the basis function implementations of SRTM and SRTM2. The R_1 parameter was not considered in this study as it is insensitive to small changes in the fixed k_2' [8, 14].

Histograms of k_2' distribution were constructed using voxel values within the VOIs of the average parametric maps per group.

Statistical Analyses

A two sample t -test was performed to evaluate differences in k_2' estimations between the groups. Moreover, since the standard approach from SRTM2 to estimate k_2' is to consider all voxels of the masked brain image outside of the cerebellum, a paired t -test was done to assess the discrepancy between the values yielded by the Whole Brain and the other methods. This approach has been used before in studies with other radiotracers that do not have a region with specific binding [36]. Boxplots of the k_2' distributions for each method were also generated. Comparisons between PIB+ and PIB- groups for each method were done using a t -test.

To explore the effect of the applied k_2' value on BP_{ND}^{SRTM2} , a sensitivity analysis was done, where the k_2' parameter was fixed to a range of values from 0.005 to 0.09 (with steps of 0.005), and the BP_{ND}^{SRTM2} parametric maps were generated for each k_2' . BP_{ND}^{SRTM2} values were retrieved from these images for all brain regions. This effect was plotted with the fixed k_2' values minus the median k_2' of all subjects for the Whole Brain method, against the difference between BP_{ND}^{SRTM2} of the fixed k_2' value and the average BP_{ND}^{SRTM2} of all subjects in the Whole Brain method. In this study, it was chosen to report the BP_{ND} values, nevertheless the results also apply to the distribution volume ratio (DVR) as the values distinguish only by an offset of 1 [11]. Three brain regions were chosen to be shown: a region with high binding (Superior Parietal Gyrus left), a region with medium binding (Inferior Frontal Gyrus right), and a region with low PIB binding (Lateral Remainder of Occipital Lobe right).

A scatter plot was made to visually assess the correlation between the BP_{ND}^{SRTM2} and BP_{ND}^{SRTM} estimations. Then a general linear model was used to compare the values, with the BP_{ND}^{SRTM2} estimations as the independent variable and the BP_{ND}^{SRTM} as the dependent variable.

A Bland-Altman plot was made to evaluate the agreement between the two BP_{ND} measurements. A p -value of 0.05 was used as a significance threshold for all statistical analyses, and no correction for multiple comparisons was made. All statistical

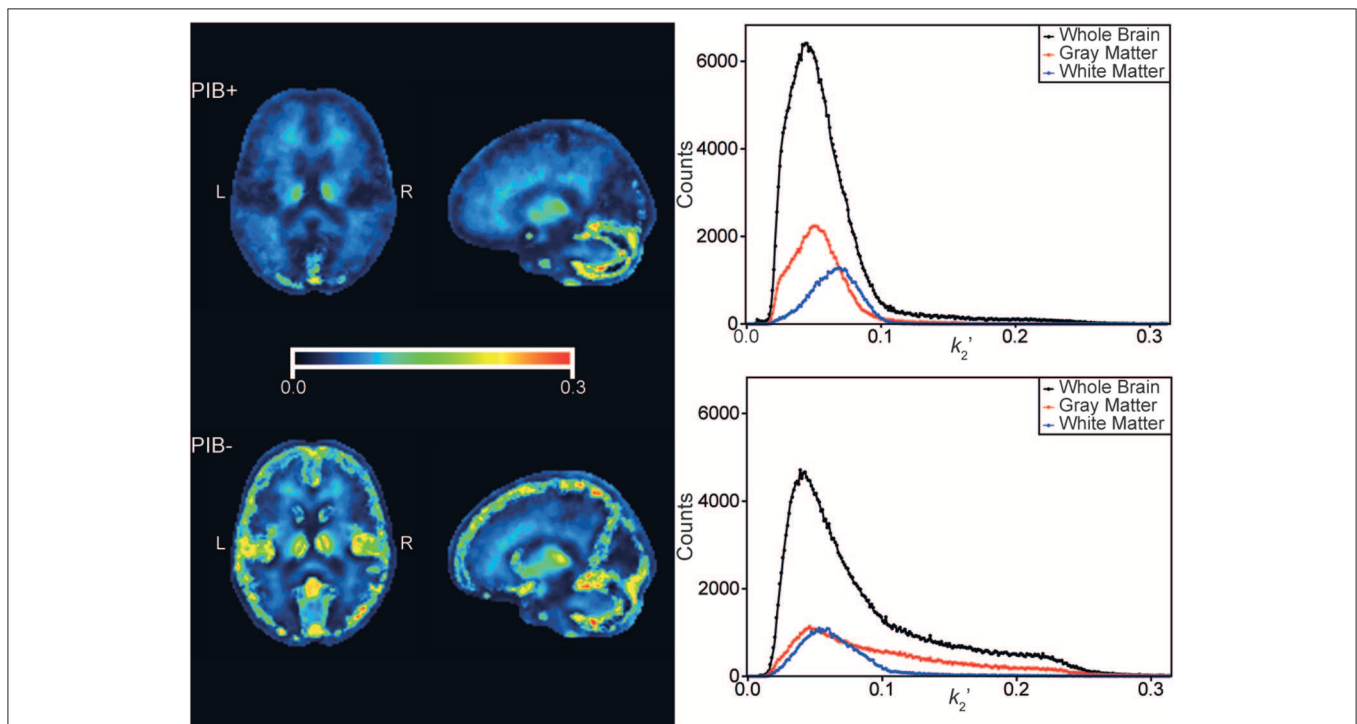


FIGURE 2 | Median k_2' parametric maps of all subjects from the PIB+ (top left), and PIB- (left bottom) groups. Shown are corresponding transaxial, and sagittal slices of the brain. Color scales were adjusted to the same range. On the right, the histograms containing the counts of k_2' values from the voxels of the parametric maps on the left. Black dots and lines correspond to voxels contained inside the Whole Brain VOI, in red, of voxels from the Gray Matter VOI, and in blue, from the White Matter. The range of the histograms was adjusted to the same range of the color scale of the parametric maps.

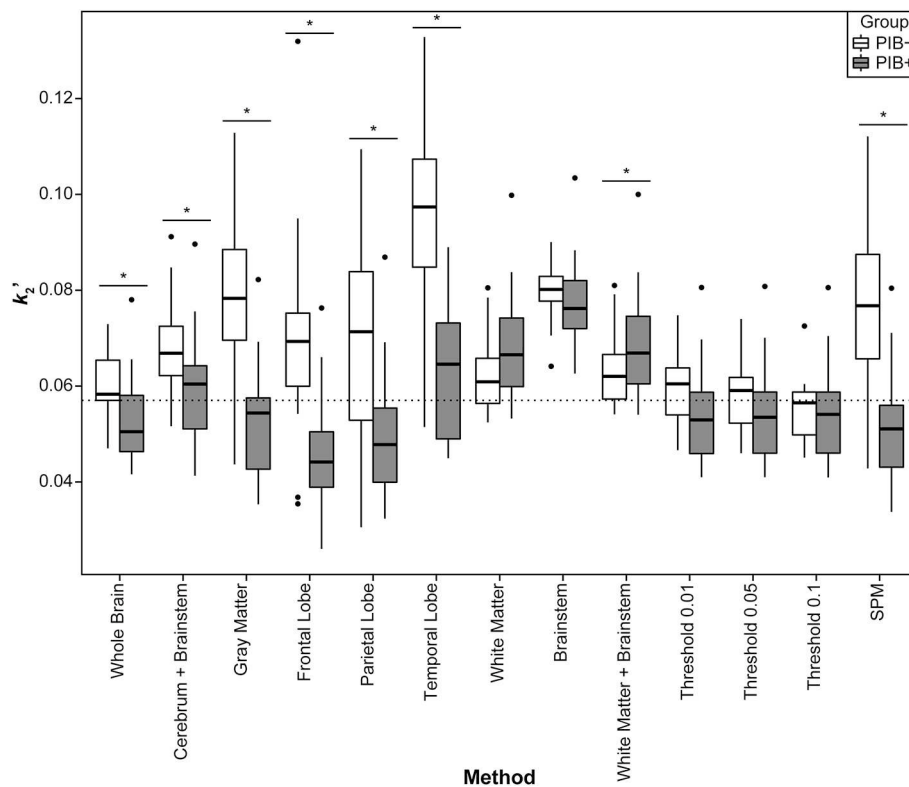


FIGURE 3 | Distribution of individual subject's k'_2 values per group for all methods. The boxes show the interquartile range of distribution, the solid line shows the median k'_2 value for the group, the whiskers expand up to 1.5 times the interquartile range, and the further points are the outlier subjects. In white, the values from the PIB- subjects, and in gray, from the PIB+ patients. The dashed line corresponds to the median value from all subjects combined for the Whole Brain method. The stars show which methods presented a significant difference between groups resulting from the t -tests.

analyses were made using RStudio [RStudio version 1.1.423, R version 3.4.3 [37]].

Criteria for Best Method Selection

To select the best method for estimating k'_2 , the 13 approaches were ranked based on the following criteria, in order of importance: (1) absence of significant differences in k'_2 values between the groups; (2) k'_2 estimation closer to the median value of the population; (3) high correlations between BP_{ND}^{SRTM} and BP_{ND}^{SRTM2} ; (4) linear regression's result with a slope closest to 1, and (5) an intercept closest to 0.

RESULTS

Parametric Maps

The k'_2 parametric maps were noticeably different for PIB+ and PIB- subjects (Figure 2), with the main difference between groups being an increase of gray matter voxel values in the PIB- group. When observing the distribution of the k'_2 values of all voxels across the images, a discrepancy can be seen on the height and position of the peaks and the variance of values in the histograms (Figure 2). The PIB+ group had a peak at 0.04, and a median value of 0.05, while the PIB- group presented values of 0.04 and 0.06, respectively. The histogram counts of gray

and white matter voxels of each image only, also revealed that the main difference between groups was a wider distribution of values in the gray matter voxels of PIB- subjects when compared to PIB+ patients, although there was a shift in both peaks.

Efflux Parameter Estimation (k'_2)

The VOI approaches for retrieving the median k'_2 values yielded different estimations (Figure 3). In general, gray matter VOIs (i.e., Gray Matter, Frontal, Parietal, and Temporal Lobes) resulted in a larger and statistically significant difference in k'_2 estimations between PIB+ and PIB- subjects, while white matter and threshold VOIs did not (Supplementary Table 3). For the PIB+ group, the Parietal Lobe VOI presented the largest range of k'_2 distribution (range 0.03–0.09), and the Whole Brain, the smallest one (0.04–0.08). For the PIB-, the largest range of k'_2 distribution was observed for the Frontal Lobe (0.04–0.13), and the smallest for the Brainstem (0.06–0.09). Most methods presented a statistically significant difference k'_2 when compared with the Whole Brain (Supplementary Table 4). Meanwhile, the threshold approaches presented the smallest discrepancy in k'_2 for both groups, and, in general, this difference was not statistically significant.

The median k'_2 value using the Whole Brain method was 0.057, and the methods that presented the smallest range of

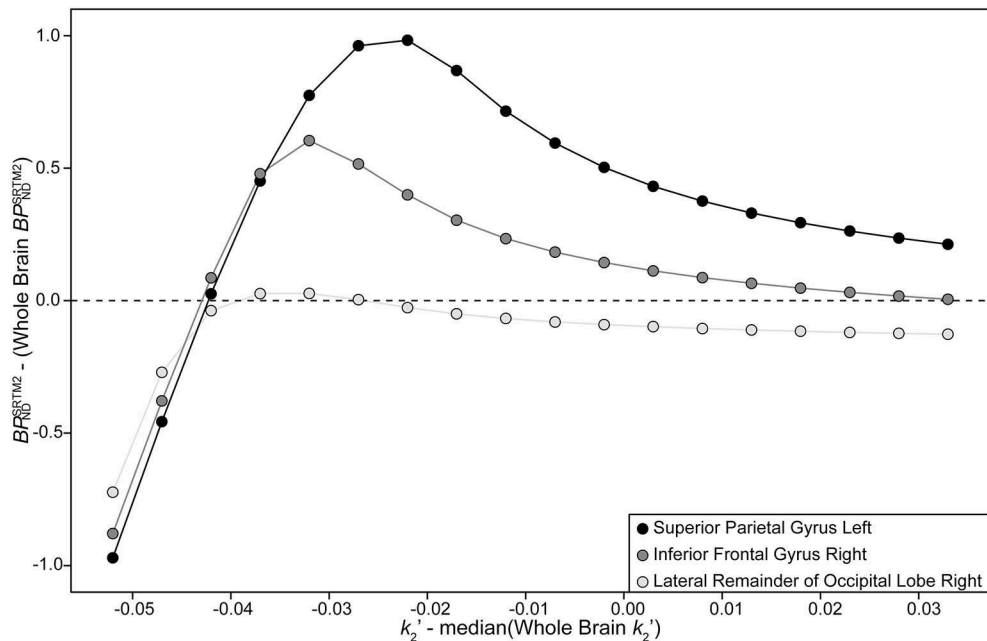


FIGURE 4 | Plot of the relative changes in BP_{ND}^{SRTM2} with relative increment of k'_2 . In the x-axis is the fixed value of k'_2 (which varied from 0.005 to 0.09 with a step of 0.005) minus the median k'_2 from the data of all subjects for the Whole Brain method. In the y-axis is the BP_{ND}^{SRTM2} of the fixed k'_2 value of a specific brain region minus the value of the same region for the Whole Brain method. The dashed line represents a difference in BP_{ND}^{SRTM2} of zero. Black dots represent data from the Superior Parietal Gyrus left region (a region with high PIB binding), in dark gray, the Inferior Frontal Gyrus right (a region with medium binding), and in light gray, the Lateral Remainder of Occipital Lobe right (a region with low binding of PIB).

k'_2 distribution, as well as having a mean k'_2 closest to the Whole Brain value, were Threshold 0.1 and, from the anatomical approaches, the White Matter. The first method presented k'_2 values of (mean \pm SD) 0.05 ± 0.01 (range 0.04–0.08) for the PIB+ group, and 0.06 ± 0.01 (0.05–0.07) for the PIB–. Additionally, the latter resulted in values of 0.07 ± 0.01 (0.05–0.1) for the PIB+, and 0.06 ± 0.01 (0.05–0.08) for the PIB–. This White Matter method yielded, however, an overestimation of the k'_2 parameter of 31.8% for the PIB+ group, and 4.4% for the PIB–, when compared to the Whole Brain. **Supplementary Table 3** shows the means, standard deviations, and ranges of k'_2 per group for all methods, along with the p -value of the t -test that compared the k'_2 differences between groups.

Sensitivity Analysis

When exploring the effect of k'_2 estimations on the BP_{ND}^{SRTM2} , a non-linear relationship between the parameters was observed. This can be seen both in **Figure 4**, which shows the relative change in BP_{ND}^{SRTM2} as a function of the fixed k'_2 value relative to the Whole Brain BP_{ND}^{SRTM2} , vs. the difference between the fixed k'_2 and the estimated value for the Whole Brain; and in **Supplementary Figure 1**, which shows the BP_{ND}^{SRTM2} values for each fixed k'_2 . Overall, all brain regions presented a similar relationship: a steep increase of BP_{ND}^{SRTM2} with the increment of k'_2 values until it reaches a peak, followed by an exponential decrease. It was also observed that the larger the fixed k'_2 , the smaller the change in BP_{ND}^{SRTM2} was. It could further be seen that

for regions with more binding, the BP_{ND}^{SRTM2} was more sensitive to deviations in k'_2 .

Correlation of Binding Potential Values From SRTM and SRTM2

The general linear model suggested a strong correlation between BP_{ND}^{SRTM} and BP_{ND}^{SRTM2} for all methods (**Table 1**, **Figure 5**), with higher R^2 values for PIB– subjects and with all results being significant. For the PIB+ group, the smallest R^2 was 0.79, for Frontal and Parietal Lobe methods, while the highest was 0.83 for Cerebrum + Brainstem, Temporal Lobe, Brainstem, and threshold methods. For the PIB–, the smallest R^2 was 0.85 for the Parietal Lobe, and the highest correlation was 0.88 for the Whole Brain, Cerebrum + Brainstem, and the threshold methods. The slope furthest from 1 was 0.67 for the PIB+ patients, when using the White Matter + Brainstem method, while the closest to 1 slope was 0.95 when using the Parietal Lobe VOI. Additionally, for the PIB– subjects, these values were, 0.99 when using the SPM method, and 0.86 when using the Temporal Lobe VOI, respectively. Threshold methods were not the closest to 1 for each group individually, however this approach had the overall best performance (slope of 0.86 for PIB+; and for PIB– 1.02, 1.03, and 1.05 for Threshold 0.01, 0.05, and 0.1 respectively).

Bias Assessment

The bias between BP_{ND}^{SRTM} and BP_{ND}^{SRTM2} for different methods revealed a negative trend that was proportional to BP_{ND}^{SRTM} for the PIB+ patients, and showed a more disperse distribution for

TABLE 1 | Results from the general linear model comparing BP_{ND}^{SRTM} and BP_{ND}^{SRTM2} from different methods.

Method		PIB+	PIB–
Whole brain	R^2	0.82	0.88
	Intercept	0.05	–0.03
	Slope	0.88	1.02
Cerebrum + brainstem	R^2	0.83	0.88
	Intercept	0.05	–0.03
	Slope	0.81	0.97
Gray matter	R^2	0.82	0.87
	Intercept	0.06	–0.04
	Slope	0.89	0.97
Frontal lobe	R^2	0.79	0.86
	Intercept	0.10	–0.04
	Slope	0.95	1.07
Parietal lobe	R^2	0.79	0.85
	Intercept	0.10	–0.03
	Slope	0.88	1.08
Temporal lobe	R^2	0.83	0.86
	Intercept	0.03	–0.04
	Slope	0.80	0.86
White matter	R^2	0.83	0.87
	Intercept	0.04	–0.03
	Slope	0.73	0.98
Brainstem	R^2	0.83	0.87
	Intercept	0.04	–0.03
	Slope	0.73	0.98
White matter + brainstem	R^2	0.81	0.87
	Intercept	0.03	–0.04
	Slope	0.67	0.88
Threshold 0.01	R^2	0.83	0.88
	Intercept	0.06	–0.03
	Slope	0.86	1.02
Threshold 0.05	R^2	0.83	0.88
	Intercept	0.06	–0.02
	Slope	0.86	1.03
Threshold 0.1	R^2	0.83	0.88
	Intercept	0.06	–0.02
	Slope	0.86	1.05
SPM	R^2	0.81	0.87
	Intercept	0.09	–0.04
	Slope	0.86	0.99

All values were statistically significant.

the PIB– subjects (**Figure 5, Table 2**). Nearly all methods resulted in a statistically significant bias in BP_{ND}^{SRTM2} for the PIB– group. For the PIB+ group, the only methods that did not result in a significant bias were the ones based on three different thresholds, Gray Matter VOI, and SPM (**Table 2**). A wider range was observed for the PIB+ patients (e.g., for the Whole Brain, –0.64–0.86) than for the PIB– subjects (–0.32–0.29, same method). The mean bias between BP_{ND}^{SRTM2} and BP_{ND}^{SRTM} when using the Threshold 0.1 method was -0.04 ± 0.17 for the PIB+ group

(a bias of 2%, slope = 0.02, intercept = –0.05), and -0.01 ± 0.07 (a bias of 16%, slope = 0.16, intercept = –0.03) for the PIB– group, and for the White Matter method, -0.15 ± 0.17 (a bias of 15%, slope = –0.15, intercept = –0.05), and -0.03 ± 0.07 (a bias of 8%, slope = 0.08, intercept = –0.04), respectively.

Ranking of the Methods

In summary, based on the results presented in the previous section, the following ranking of the preferred methods to estimate k'_2 was: Threshold 0.1, Threshold 0.05, Threshold 0.01, White Matter, White Matter + Brainstem, Brainstem, Whole Brain, Cerebrum + Brainstem, Frontal Lobe, Gray Matter, Parietal Lobe, SPM, Temporal Lobe.

DISCUSSION

In this study, different approaches of estimating the optimal k'_2 to be fixed in SRTM2 and their impact on BP_{ND}^{SRTM2} were explored. The k'_2 estimation is an important step in the pharmacokinetic analysis of dynamic PIB PET scans using SRTM2, as a bias in k'_2 affects the obtained binding potential. Although SRTM2 has already been validated as a suitable model for PIB studies [10], the fact that there is no well-defined receptor-rich region might lead to errors in the estimation of BP_{ND}^{SRTM2} , and an examination of the consequences of wrongly determining k'_2 has not yet been done.

For both PIB+ patients and PIB– subjects, the cerebellum is a region without specific binding of A β tracers, so it can be used as a reference region for the pharmacokinetic modeling of the radiotracer using SRTM2 [4, 10, 33–35]. Thus it is not expected that there will be a significant difference between groups when estimating k'_2 , as has already been seen from previous studies [38]. Therefore, it is important to consider this when selecting a method.

The main difference between groups is that the PIB+ subjects present an accumulation of A β plaques on the cortex [3], and thus a higher binding of PIB in these areas, while the PIB– subjects do not, as was seen in the histograms of **Figure 2**. Because of this discrepancy, it was not a surprise that the SPM VOI was composed mainly of gray matter voxels. Furthermore, this distinction between k'_2 group values is the most probable explanation for the poor performance of gray matter (i.e., Gray Matter, Frontal, Parietal, and Temporal Lobes) and SPM methods, especially in the PIB– group. This difference between groups, which can be seen in **Figure 2**, also shows that not all brain regions might be suitable for estimating k'_2 , as the value for this parameter depends on which group the subject belongs to. This further demonstrates that, although the theoretical assumption of SRTM2 is that k'_2 should be constant across the brain, it is not the case in practice.

Moreover, threshold based approaches guarantee that only voxels with some minimal elevated level of PIB binding were included within the VOIs used for the k'_2 estimation. Since PIB does not have a specific target region, these methods might be the best approaches when using SRTM2. Furthermore, this selection of voxels may also explain why there was a smaller difference in k'_2 between groups for these methods (**Figure 3**).

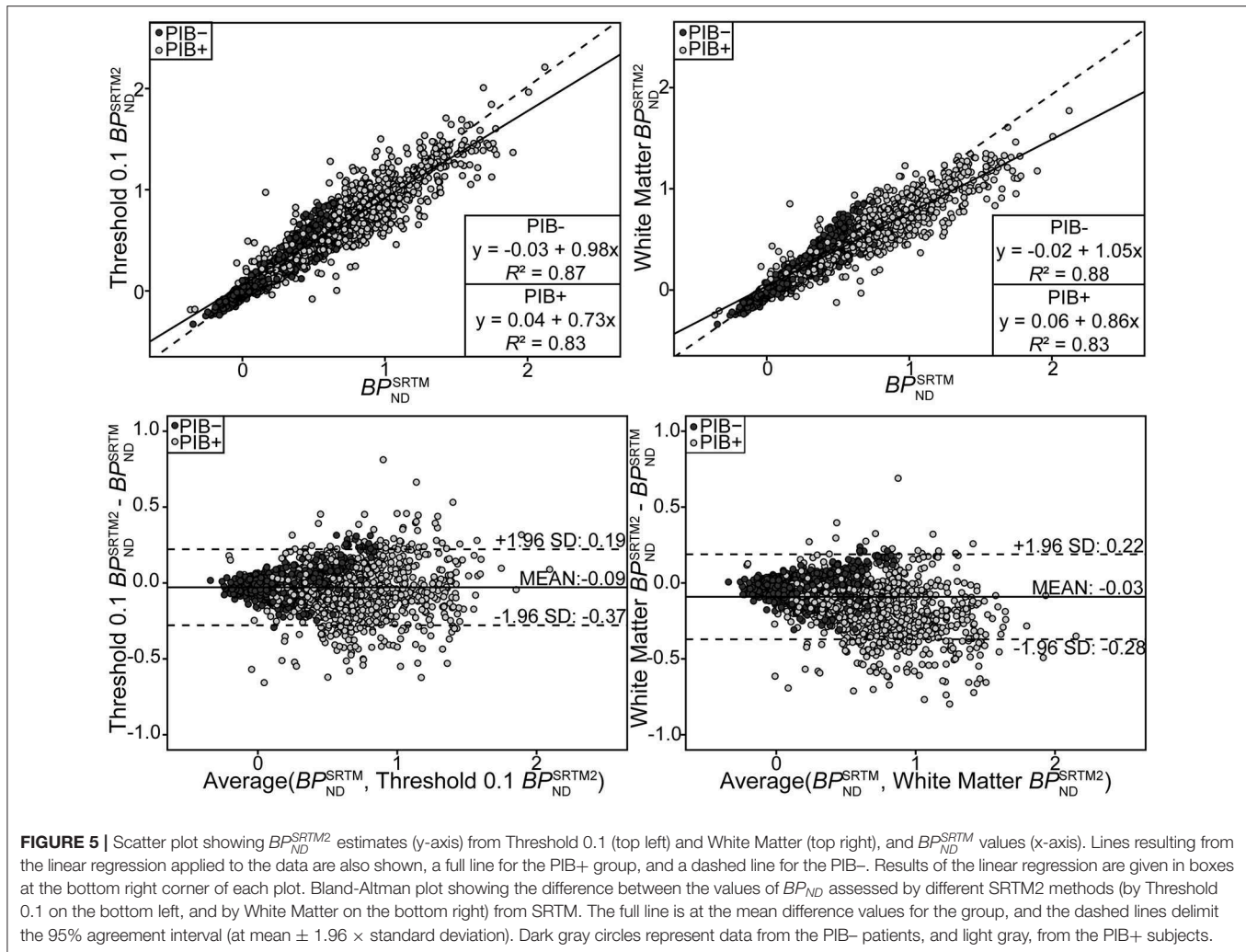


FIGURE 5 | Scatter plot showing BP_{SRTM2}^{SRTM2} estimates (y-axis) from Threshold 0.1 (top left) and White Matter (top right), and BP_{SRTM2}^{SRTM2} values (x-axis). Lines resulting from the linear regression applied to the data are also shown, a full line for the PIB+ group, and a dashed line for the PIB-. Results of the linear regression are given in boxes at the bottom right corner of each plot. Bland-Altman plot showing the difference between the values of BP_{ND} assessed by different SRTM2 methods (by Threshold 0.1 on the bottom left, and by White Matter on the bottom right) from SRTM. The full line is at the mean difference values for the group, and the dashed lines delimit the 95% agreement interval (at mean $\pm 1.96 \times$ standard deviation). Dark gray circles represent data from the PIB- patients, and light gray, from the PIB+ subjects.

The preferred method for estimating k'_2 should be using plasma input. However, blood data is not always available, as in the case of this study, and, therefore, there is a need for finding the best way of estimating this parameter directly from the image since it influences the BP_{SRTM2}^{SRTM2} value. A previous study by Price and colleagues [34] estimated these parameters using plasma input compartmental modeling, and they found a ratio of non-specific trapping ($\frac{k_5}{k_6}$) of 1.4 and an average clearance for target tissues (k_2) was of 0.144. With these measurements, an estimation of k'_2 can be done using $k'_2 = \frac{k_2}{(1 + \frac{k_5}{k_6})}$, resulting in a k'_2 of 0.055. This value is close to the median k'_2 value of 0.057 found in the present study. Interestingly, k'_2 estimates using white matter methods (i.e., White Matter, Brainstem, and White Matter + Brainstem) diverged the most from this expected value for both groups. Meanwhile, gray matter methods only deviated for the PIB- group. From this observation, it might be concluded that regions without specific binding of PIB might result in a k'_2 overestimation. Furthermore, PIB retention has been shown to be similar in white matter for both AD patients and HC subjects

[4], which explains the absence of differences between groups for these methods.

The results presented in the previous section showed that an overestimation of k'_2 might not be an issue as this would lead to a smaller bias in BP_{SRTM2}^{SRTM2} than when underestimating k'_2 . Slight changes in low k'_2 values yield larger shifts in BP_{SRTM2}^{SRTM2} estimation, while for larger k'_2 values, smaller shifts in BP_{SRTM2}^{SRTM2} were observed. Because of this behavior, it is better to impose a lower boundary on k'_2 , to secure a smaller bias in BP_{SRTM2}^{SRTM2} . This limit could be around 0.04, since most of the estimation across methods and subjects were higher, and the sensitivity plot showed larger biases for k'_2 values below 0.04 (Supplementary Figure 1). Because the actual k'_2 estimation can be substantially different between subjects, it is not recommended to fix k'_2 to a single value across all subjects or to use a population based value. Based on all results presented, a ranking of the methods was done. The method Threshold 0.1 was the one that presented the highest correlation between BP_{SRTM2}^{SRTM2} and BP_{SRTM2}^{SRTM2} for both groups. Moreover, it did not show a significant difference in estimated k'_2 between groups and resulted in a median k'_2

TABLE 2 | Results from the bias assessment comparing BP_{ND}^{SRTM} and BP_{ND}^{SRTM2} from different methods.

Method	PIB	Mean	SD	Min	Max	Intercept	Slope	p-value
Whole brain	PIB+	-0.027	0.169	-0.645	0.856	-0.007	-0.030	0.022*
	PIB-	-0.024	0.066	-0.317	0.287	-0.035	0.085	<0.001*
Cerebrum + brainstem	PIB+	-0.088	0.163	-0.677	0.747	-0.027	-0.094	<0.001*
	PIB-	-0.036	0.063	-0.323	0.223	-0.042	0.054	<0.001*
Gray matter	PIB+	-0.016	0.169	-0.655	0.821	-0.032	0.025	0.067
	PIB-	-0.042	0.065	-0.348	0.336	-0.050	0.065	<0.001*
Frontal lobe	PIB+	0.065	0.193	-0.600	1.038	-0.014	0.117	<0.001*
	PIB-	-0.025	0.076	-0.346	0.538	-0.046	0.174	<0.001*
Parietal lobe	PIB+	0.011	0.186	-0.696	0.895	-0.017	0.042	0.004*
	PIB-	-0.022	0.081	-0.324	0.686	-0.044	0.190	<0.001*
Temporal lobe	PIB+	-0.108	0.164	-0.787	0.648	-0.066	-0.063	<0.001*
	PIB-	-0.062	0.066	-0.386	0.226	-0.059	-0.028	0.007*
White matter	PIB+	-0.152	0.170	-0.797	0.690	-0.054	-0.151	<0.001*
	PIB-	-0.029	0.066	-0.308	0.239	-0.039	0.083	<0.001*
Brainstem	PIB+	-0.153	0.170	-0.797	0.690	-0.059	-0.151	<0.001*
	PIB-	-0.029	0.066	-0.308	0.239	-0.039	0.089	<0.001*
White matter + brainstem	PIB+	-0.197	0.184	-0.879	0.628	-0.055	-0.223	<0.001*
	PIB-	-0.052	0.065	-0.371	0.138	-0.051	-0.014	0.179
Threshold 0.01	PIB+	-0.039	0.166	-0.655	0.820	-0.053	0.021	0.121
	PIB-	-0.023	0.066	-0.306	0.288	-0.037	0.132	<0.001*
Threshold 0.05	PIB+	-0.041	0.166	-0.656	0.816	-0.054	0.020	0.144
	PIB-	-0.020	0.067	-0.301	0.298	-0.035	0.140	<0.001*
Threshold 0.1	PIB+	-0.042	0.166	-0.657	0.812	-0.053	0.019	0.170
	PIB-	-0.015	0.070	-0.292	0.315	-0.032	0.156	<0.001*
SPM	PIB+	-0.013	0.173	-0.645	0.856	-0.027	0.022	0.127
	PIB-	-0.038	0.067	-0.340	0.352	-0.050	0.107	<0.001*

* $p < 0.05$.

value closest to the expected value, as estimated before [34]. Therefore, the Threshold 0.1 method is the recommended approach for the SRTM2 voxel-based analysis of dynamic PIB PET images. While this study was done using a voxel-based modeling approach (SRTM2), some of the results can be extended to VOI-based modeling [such as regional time-activity curves (TAC)]. However, the delineation of the threshold VOIs was done using the BP_{ND}^{SRTM} parametric maps, and these maps are not available when performing TAC analysis. Thus, in the case of VOI-based modeling, it might be optimal to select a predefined VOI from where to estimate k'_2 . In this scenario, the White Matter VOI seems to be the recommended region for estimating k'_2 , for the same reasons that Threshold 0.1 was recommended for voxel-based analysis.

In this study, all analyses focused on the use of a reference tissue approach. Previous studies have shown that there is a high correlation between BP_{ND}^{SRTM} and BP_{ND} delivered by a plasma-input two-tissue compartment model [10]. Since plasma input data was not available for this study, no comparison with the ground truth could be done, although there was a good agreement between the median k'_2 estimated from all subjects and that seen in previous studies [10, 34]. Furthermore, another limitation was the lack of a measure for quantifying the accuracy

of the parametric maps generated using both SRTM and SRTM2. Moreover, this study was performed using PIB as a radiotracer, but it can be assumed that the same results are applicable to other tracers, such as [^{18}F]Florbetapir, [^{18}F]Florbetaben, and [^{18}F]Flutemetamol, since their target is also the deposit of A β plaques in the brain [39]. However, further research is required to confirm this.

In conclusion, this study aimed to assess the optimal method for deriving and fixing k'_2 to measure the binding potential with SRTM2. It was found that the different approaches tested yielded distinct k'_2 estimates across methods and subject groups, which, in turn, affected BP_{ND}^{SRTM2} estimates. In this study, it was found that setting a threshold on BP_{ND}^{SRTM} to select brain regions or voxels to estimate k'_2 is the best method for voxel-based pharmacokinetic modeling of PIB PET scans. Moreover, for VOI-based analysis of the images, a white matter volume of interest to derive k'_2 is a good alternative.

DATA AVAILABILITY STATEMENT

The datasets generated for this study are available on request to the corresponding author.

ETHICS STATEMENT

The studies involving human participants were reviewed and approved by Medical Ethical Committee of the UMCG. The patients/participants provided their written informed consent to participate in this study.

AUTHOR CONTRIBUTIONS

DP, DV, FR, JD, and RB were responsible for the study design. FR, PD, and RB coordinated the study. DP and DV were responsible for image processing and data analysis. DP, DV, JD, and RB were responsible for the initial draft of the manuscript. All authors critically revised the final version of the manuscript.

REFERENCES

- Jack CR, Bennett DA, Blennow K, Carrillo MC, Dunn B, Haeberlein SB, et al. NIA-AA Research framework: toward a biological definition of Alzheimer's disease. *Alzheimer's Dement.* (2018) 14:535–62. doi: 10.1016/j.jalz.2018.02.018
- Mattson MP. Pathways towards and away from Alzheimer's disease. *Nature.* (2004) 430:631–9. doi: 10.1038/nature02621
- Thal DR, Rüb U, Orantes M, Braak H. Phases of A β -deposition in the human brain and its relevance for the development of AD. *Neurology.* (2002) 58:1791–800. doi: 10.1212/WNL.58.12.1791
- Klunk WE, Engler H, Nordberg A, Wang Y, Blomqvist G, Holt DP, et al. Imaging brain amyloid in Alzheimer's disease with Pittsburgh Compound-B. *Ann Neurol.* (2004) 55:306–19. doi: 10.1002/ana.20009
- Nordberg A, Rinne JO, Kadir A, Långström B. The use of PET in Alzheimer disease. *Nat Rev Neurol.* (2010) 6:78–87. doi: 10.1038/nrneurol.2009.217
- Rowe CC, Ng S, Ackermann U, Gong SJ, Pike K, Savage G, et al. Imaging beta-amyloid burden in aging and dementia. *Neurology.* (2007) 68:1718–25. doi: 10.1212/01.wnl.0000261919.22630.ea
- Lammertsma AA. Forward to the past: the case for quantitative PET imaging. *J Nucl Med.* (2017) 58:1019–24. doi: 10.2967/jnumed.116.188029
- Lammertsma AA, Hume SP. Simplified reference tissue model for PET receptor studies. *Neuroimage.* (1996) 4:153–8. doi: 10.1006/nimg.1996.0066
- Lopresti BJ, Klunk WE, Mathis CA, Hoge JA, Ziolkowski SK, Lu X, et al. Simplified quantification of Pittsburgh compound B amyloid imaging PET studies: a comparative analysis. *Time.* (2005) 1959–72.
- Yaqub M, Tolboom N, Boellaard R, van Berckel BNM, van Tilburg EW, Luurtsema G, et al. Simplified parametric methods for [11C]PIB studies. *Neuroimage.* (2008) 42:76–86. doi: 10.1016/j.neuroimage.2008.04.251
- Zhou Y, Resnick SM, Ye W, Fan H, Holt DP, Klunk WE, et al. Using a reference tissue model with spatial constraint to quantify [11C]Pittsburgh compound B PET for early diagnosis of Alzheimer's disease. *Neuroimage.* (2007) 36:298–312. doi: 10.1016/j.neuroimage.2007.03.004
- Wu Y, Carson RE. Noise reduction in the simplified reference tissue model for neuroreceptor functional imaging. *J Cereb Blood Flow Metab.* (2002) 22:1440–52. doi: 10.1097/01.WCB.0000033967.83623.34
- Chen YJ, Rosario BL, Mowrey W, Laymon CM, Lu X, Lopez OL, et al. Relative 11C-PiB delivery as a proxy of relative CBF: quantitative evaluation using single-session 15O-water and 11C-PiB PET. *J Nucl Med.* (2015) 56:1199–205. doi: 10.2967/jnumed.114.152405
- Meyer PT, Hellwig S, Amtage F, Rottenburger C, Sahm U, Reuland P, et al. Dual-biomarker imaging of regional cerebral amyloid load and neuronal activity in dementia with PET and 11C-labeled pittsburgh compound B. *J Nucl Med.* (2011) 52:393–400. doi: 10.2967/jnumed.110.083683
- Peretti DE, Vázquez García D, Reesink FE, van der Goot T, De Deyn PP, de Jong BM, et al. Relative cerebral flow from dynamic PIB scans as an

FUNDING

This project (RB and DV) has received partial funding from the European Union's Horizon 2020 research and innovation programme under the Marie Skłodowska-Curie Grant Agreement No 764458.

ACKNOWLEDGMENTS

The authors would like to thank PMOD Technologies staff, especially Cyrill Burger, for technical support.

SUPPLEMENTARY MATERIAL

The Supplementary Material for this article can be found online at: <https://www.frontiersin.org/articles/10.3389/fphy.2019.00212/full#supplementary-material>

- alternative for FDG scans in Alzheimer's disease PET studies. *PLoS ONE.* (2019) 14:e0211000. doi: 10.1371/journal.pone.0211000
- Tolboom N, Yaqub M, Boellaard R, Luurtsema G, Windhorst AD, Scheltens P, et al. Test-retest variability of quantitative [11C]PIB studies in Alzheimer's disease. *Eur J Nucl Med Mol Imaging.* (2009) 36:1629–38. doi: 10.1007/s00259-009-1129-6
- Amtage F, Spehl TS, Hellwig S, Sahm U, Hellwig B, Reuland P, et al. Assessment of striatal dopamine D2/D3 receptor availability with PET and 18F-Desmethoxyfallypride: comparison of imaging protocols suited for clinical routine. *J Nucl Med.* (2012) 53:1558–64. doi: 10.2967/jnumed.112.103812
- Sandiego CM, Gallezot J-D, Lim K, Ropchan J, Lin S-F, Gao H, et al. Reference region modeling approaches for amphetamine challenge studies with [11C]FLB 457 and PET. *J Cereb Blood Flow Metab.* (2015) 35:623–9. doi: 10.1038/jcbfm.2014.237
- Naganawa M, Nabulsi N, Planeta B, Gallezot J-D, Lin S-F, Najafzadeh S, et al. Tracer kinetic modeling of [11C]AFM, a new PET imaging agent for the serotonin transporter. *J Cereb Blood Flow Metab.* (2013) 33:1886–96. doi: 10.1038/jcbfm.2013.134
- Gallezot J-D, Nabulsi N, Neumeister A, Planeta-Wilson B, Williams WA, Singhal T, et al. Kinetic modeling of the serotonin 5-HT 1B receptor radioligand [11C]P943 in humans. *J Cereb Blood Flow Metab.* (2010) 30:196–210. doi: 10.1038/jcbfm.2009.195
- Golla SSV, Boellaard R, Oikonen V, Hoffmann A, van Berckel BNM, Windhorst AD, et al. Parametric binding images of the TSPO ligand 18F-DPA-714. *J Nucl Med.* (2016) 57:1543–7. doi: 10.2967/jnumed.116.173013
- Arnold SE, Hyman BT, Flory J, Damasio AR, Van Hoesen GW. The topographical and neuroanatomic distribution of neurofibrillary tangles and neuritic plaques in the cerebral cortex of patients with Alzheimer's disease. *Cereb Cortex.* (1991) 1:103–16. doi: 10.1093/cercor/1.1.103
- Bullich S, Barthel H, Koglin N, Becker GA, De Santi S, Jovalekic A, et al. Validation of non-invasive tracer kinetic analysis of 18F-Florbetaben PET using a dual time-window acquisition protocol. *J. Nucl. Med.* (2017) 59:1104–10. doi: 10.2967/jnumed.117.200964
- Heurling K, Buckley C, Van Laere K, Vandenberghe R, Lubberink M. Parametric imaging and quantitative analysis of the PET amyloid ligand [18F]flutemetamol. *Neuroimage.* (2015) 121:184–92. doi: 10.1016/j.neuroimage.2015.07.037
- Golla SSV, Verfaillie SCJ, Boellaard R, Adriaanse SM, Zwan MD, Schuit RC, et al. Quantification of [18F] florbetapir : a test–retest tracer kinetic modelling study *J Cereb Blood Flow Metab.* (2018) 39:2172–80.
- Resnick SM, Sojkova J, Zhou Y, An Y, Ye W, Holt DP, et al. Longitudinal cognitive decline is associated with fibrillar amyloid-beta measured by [11C]PiB. *Neurology.* (2010) 74:807–15. doi: 10.1212/WNL.0b013e3181d3e3e9

27. Rodriguez-Vieitez E, Carter SF, Chiotis K, Saint-Aubert L, Leuzy A, Scholl M, et al. Comparison of early-phase 11C-Deuterium-L-Deprenyl and 11C-Pittsburgh compound B PET for assessing brain perfusion in Alzheimer Disease. *J Nucl Med.* (2016) **57**:1071–7. doi: 10.2967/jnumed.115.168732
28. Ikonomic MD, Abrahamson EE, Price JC, Hamilton RL, Mathis CA, Paljug WR, et al. Early AD pathology in a [C-11]PiB-negative case: a PiB-amyloid imaging, biochemical, and immunohistochemical study. *Acta Neuropathol.* (2012) **123**:433–47. doi: 10.1007/s00401-012-0943-2
29. McKhann GM, Knopman DS, Chertkow H, Hyman BT, Jack CR, Kawas CH, et al. The diagnosis of dementia due to Alzheimer's disease: recommendations from the National Institute on Aging-Alzheimer's Association workgroups on diagnostic guidelines for Alzheimer's disease. *Alzheimer's Dement.* (2011) **7**:263–9. doi: 10.1016/j.jalz.2011.03.005
30. Petersen R, Doody R, Kurz A, Al E. Current concepts in mild cognitive impairment. *Arch Neurol.* (2001) **58**:1985–92. doi: 10.1001/archneur.58.12.1985
31. Ashburner J, Friston KJ. Unified segmentation. *Neuroimage.* (2005) **26**:839–51. doi: 10.1016/j.neuroimage.2005.02.018
32. Hammers A, Allom R, Koepp MJ, Free SL, Myers R, Lemieux L, et al. Three-dimensional maximum probability atlas of the human brain, with particular reference to the temporal lobe. *Hum Brain Mapp.* (2003) **19**:224–47. doi: 10.1002/hbm.10123
33. Joachim CL, Morris JH, Selkoe DJ. Diffuse senile plaques occur commonly in the cerebellum in Alzheimer's disease. *Am. J. Pathol.* (1989) **135**:309–19. doi: 10.1097/00005072-198905000-00093
34. Price JC, Klunk WE, Lopresti BJ, Lu X, Hoge JA, Ziolk SK, et al. Kinetic modeling of amyloid binding in humans using PET imaging and Pittsburgh Compound-B. *J Cereb Blood Flow Metab.* (2005) **25**:1528–47. doi: 10.1038/sj.jcbfm.9600146
35. Yamaguchi H, Hirai S, Morimatsu M, Shoji M, Nakazato Y. Diffuse type of senile plaques in the cerebellum of Alzheimer-type dementia demonstrated by β protein immunostain. *Acta Neuropathol.* (1989) **77**:314–9. doi: 10.1007/BF00687584
36. Lopes Alves I, Vázquez García DV, Parente A, Doorduyn J, da Silva AMM, Koole M, et al. Parametric imaging of [11C]Flumazenil binding in the rat brain. *Mol Imaging Biol.* (2018) **20**:114–23. doi: 10.1007/s11307-017-1098-2
37. R Core Team. *R: A Language and Environment for Statistical Computing.* Vienna: R Foundation for Statistical Computing (2017). Available online at: <https://www.R-project.org/>
38. Fodero-Tavoletti MT, Rowe CC, McLean CA, Leone L, Li Q-X, Masters CL, et al. Characterization of PiB binding to white matter in Alzheimer Disease and other dementias. *J Nucl Med.* (2009) **50**:198–204. doi: 10.2967/jnumed.108.057984
39. Morris E, Chalkidou A, Hammers A, Peacock J, Summers J, Keevil S. Diagnostic accuracy of 18F amyloid PET tracers for the diagnosis of Alzheimer's disease: a systematic review and meta-analysis. *Eur J Nucl Med Mol Imaging.* (2016) **43**:374–85. doi: 10.1007/s00259-015-3228-x

Conflict of Interest: The authors declare that the research was conducted in the absence of any commercial or financial relationships that could be construed as a potential conflict of interest.

Copyright © 2019 Peretti, Reesink, Doorduyn, de Jong, De Deyn, Dierckx, Boellaard and Vázquez García. This is an open-access article distributed under the terms of the Creative Commons Attribution License (CC BY). The use, distribution or reproduction in other forums is permitted, provided the original author(s) and the copyright owner(s) are credited and that the original publication in this journal is cited, in accordance with accepted academic practice. No use, distribution or reproduction is permitted which does not comply with these terms.



Magnetic Resonance-Based Attenuation Correction and Scatter Correction in Neurological Positron Emission Tomography/Magnetic Resonance Imaging—Current Status With Emerging Applications

Jarmo Teuho^{1,2,3*}, Angel Torrado-Carvajal^{4,5}, Hans Herzog⁶, Udunna Anazodo⁷, Riku Klén¹, Hidehiro Iida^{1,3,8} and Mika Teräs^{2,9}

¹ Turku PET Centre, University of Turku and Turku University Hospital, Turku, Finland, ² Department of Medical Physics, Turku University Hospital, Turku, Finland, ³ Department of Investigative Radiology, National Cerebral and Cardiovascular Center Research Institute, Osaka, Japan, ⁴ Athinoula A. Martinos Center for Biomedical Imaging, Department of Radiology, Massachusetts General Hospital and Harvard Medical School, Charlestown, MA, United States, ⁵ Medical Image Analysis and Biometry Lab, Universidad Rey Juan Carlos, Madrid, Spain, ⁶ Institute of Neuroscience and Medicine 4, Forschungszentrum, Jülich, Germany, ⁷ Lawson Health Research Institute, London, ON, Canada, ⁸ Graduate School of Information Science and Data Science Center, Nara Institute of Science and Technology, Nara, Japan, ⁹ Institute of Biomedicine, University of Turku, Turku, Finland

OPEN ACCESS

Edited by:

Ivo Rausch,
Medical University of Vienna, Austria

Reviewed by:

Roberta Frass-Kriegl,
Medical University of Vienna, Austria
David B. Stout,
Independent Researcher, Culver City,
United States

*Correspondence:

Jarmo Teuho
jarmo.teuho@tyks.fi

Specialty section:

This article was submitted to
Medical Physics and Imaging,
a section of the journal
Frontiers in Physics

Received: 25 October 2019

Accepted: 19 December 2019

Published: 29 January 2020

Citation:

Teuho J, Torrado-Carvajal A, Herzog H, Anazodo U, Klén R, Iida H and Teräs M (2020) Magnetic Resonance-Based Attenuation Correction and Scatter Correction in Neurological Positron Emission Tomography/Magnetic Resonance Imaging—Current Status With Emerging Applications. *Front. Phys.* 7:243. doi: 10.3389/fphy.2019.00243

In this review, we will summarize the past and current state-of-the-art developments in attenuation and scatter correction approaches for hybrid positron emission tomography (PET) and magnetic resonance (MR) imaging. The current status of the methodological advances for producing accurate attenuation and scatter corrections on PET/MR systems are described, in addition to emerging clinical and research applications. Future prospects and potential applications that benefit from accurate data corrections to improve the quantitative accuracy and clinical applicability of PET/MR are also discussed. Novel clinical and research applications where improved attenuation and scatter correction methods are beneficial are highlighted.

Keywords: positron emission tomography/magnetic resonance imaging, attenuation correction, scatter correction, positron emission tomography image quantification, magnetic resonance-based attenuation correction

INTRODUCTION

Hybrid positron emission tomography/magnetic resonance (PET/MR) systems for clinical imaging have been first introduced nearly a decade ago, with systems capable of either sequential or simultaneous image acquisition. The first concept studies for successful combined PET/MR measurements were initially performed in 1996 [1]. After solving several technical challenges due to the complexity of integration of PET and MR, the first commercial whole-body PET/MR systems were installed in 2010 [2, 3]. PET/MR instrumentation has been an active field and has been discussed in several review articles [4–9]. The introduction of simultaneous PET/MR systems for clinical use has been suggested to mark a paradigm shift for neuroimaging, and the combination of both systems offers a multitude of advantages [10–12]. As can be seen in

several clinical and research scenarios, PET/MR offers many advantages over positron emission tomography/computed tomography (PET/CT) or standalone MR.

Fusion information of MR and PET provides advantages over PET and computed tomography (CT) in neurological applications, as overlaying MR and PET image supplies improved diagnostic information in characterization of many conditions [13]. Beyond image fusion, MR offers a library of multiparametric imaging information from morphology, function to even metabolism that cannot be obtained from CT. MR has also an excellent sensitivity in capturing the small changes in brain structure and function [14]. PET on the other hand, offers a high specificity and a wide quality of radiotracers applicable for investigation of numerous molecular targets [14]. Potential applications include metabolism, receptor function, neurotransmitter distribution, inflammation, antigen targeting, and tissue perfusion. Thus, PET/MR unlocks a multitude of novel research and diagnostic applications. To improve data synergy between PET and MR, the focus from hardware integration has shifted to development of integrated data processing and analyses [14]. It is clear that both the research and the diagnostic capabilities of hybrid PET/MR could be extended from that of PET/CT, once fusion information from PET and MR is realized in a more complementary fashion.

However, as PET imaging is severely affected by both photon attenuation and scatter, effective data corrections for both physical phenomena are needed to produce quantitative images reflecting the true spatial distribution of the radiotracer. The physical basis of both scatter and attenuation is explained in detail in review papers of Zaidi and Hasegawa [15], Zaidi and Montandon [16], and Martinez-Möller and Nekolla [17]. Thus, a prerequisite to these corrections is the availability of an accurate attenuation map containing the attenuation coefficients for 511-keV photons at each voxel [17], which makes attenuation correction fundamental to produce visually and quantitatively accurate PET images. Shortly after the introduction of the first commercial PET/MR systems, this became a fundamental limitation of the modality, until the methodological challenges were addressed and effective methods were introduced.

Rotating transmission sources and a bilinear scaling procedure with CT can be applied for attenuation correction on standalone PET and PET/CT systems, respectively [18]. On PET/MR, there are two basic methodological challenges related to attenuation correction. First, MR-based attenuation correction (MRAC) is a challenge due to the very basic idea of what MR images represent—proton density and relaxation time properties of biological tissues [17]. However, for attenuation correction purposes, tissue electron density information needs to be resolved. Therefore, there is no standardized transformation procedure that can translate the MR tissue intensities to tissue attenuation properties as in CT-based attenuation correction (CTAC). An equally important second challenge is the short T2* relaxation time of bone, which makes it hard to delineate bone, unless MR sequences based on ultrashort echo time (UTE) or zero echo time (ZTE) sequences are used [19].

Thus, the main challenges in MRAC originated from deriving bone density information on an individual basis and differentiating bone in MR images. These two challenges led to

the first clinically implemented MRAC methods ignoring bone entirely in the body and brain region and replacing bone with soft tissue. However, neglecting bone in attenuation map in the head region was shown to cause large, spatially varying bias in regions close to bone, such as in the cortical regions of the gray matter with errors of magnitude across the brain ranging from -10 to -25% [20, 21]. These errors could also be visually regarded as cortical hypometabolism, representing a potential factor for misdiagnosis, thus impairing the diagnostic quality of the PET/MR images [20, 21]. This led to a large and active field of methodological development in MRAC.

To account for these challenges, a multitude of innovative methods for MRAC were developed over the course of years following the introduction of the first simultaneous PET/MR systems. These methods are well-summarized in the excellent review papers of Martinez-Möller and Nekolla [22], Hofmann et al. [23], Berker and Li [24], Bezrukov et al. [18], Chen and An [25], Izquierdo-Garcia and Catana [26], Keereman et al. [17], Wagenknecht et al. [27], and Mehranian et al. [28] and partially in Teuho [29]. These methods have been proven to be fairly accurate, as a recent multicenter study with 11 MRAC methods and three radiotracers including [^{18}F]-fluorodeoxyglucose ([^{18}F]-FDG), [^{11}C]-Pittsburgh compound B ([^{11}C]-PiB), and [^{18}F]-Florbetabir showed. The methods included have an average global performance within $\pm 5\%$ of CT-based reference [30]. To illustrate this, **Figure 1** shows the reported global bias and standard deviation of the methods reported in the MR-Based Attenuation Correction for PET/MR Neuroimaging section, where applicable.

Thus, while the challenge of improving accuracy of MRAC with adult brains with normal anatomy can be considered to be solved [30, 47], future methodological advances are of interest. It seems that the focus of methodological research in MRAC is now shifting on improving the accuracy of the existing methods and applying them to novel clinical and research applications. While the accuracy of MRAC is no longer the major methodological problem, increasing accuracy is always desirable [36] in combination of the assessment and application of MRAC methods for more challenging clinical and research applications. Therefore, any application that involves detection of subtle changes in the brain, such as dementia trajectory or epilepsy lesion detection, will benefit from increased accuracy of MRAC and subsequently from accurate scatter correction.

In addition to attenuation correction, scatter correction is one of the major quantitative corrections performed in PET, as the fraction of scattered photons in three-dimensional (3D) PET acquisitions in the brain region can be increased to over 30% [48]. Both attenuation and scatter correction are related, as the attenuation sinogram is used in the calculation of the scattered photons when performing single scatter simulation (SSS). A few reports have investigated the effects of the accuracy of the attenuation map on scatter correction. These investigations unanimously concluded that the errors in the attenuation map introduced to calculated scatter sinograms are much smaller than errors produced by incorrect attenuation correction [49–52]. While scatter correction has not been a major issue to be addressed for neurological PET/MR imaging, developments in scatter correction are

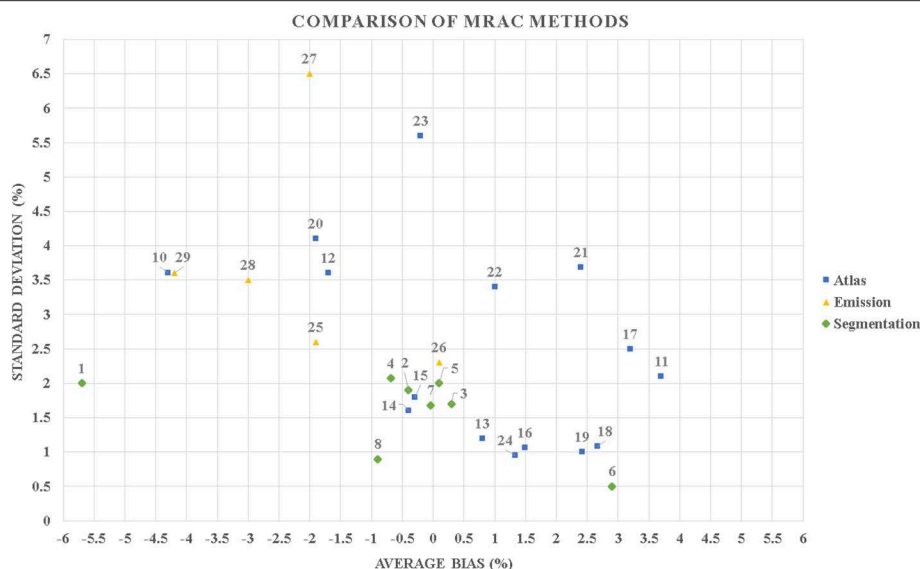


FIGURE 1 | A scatter plot diagram that contains the reported global average bias and standard deviation in percentage of the methods included in this review. It can be seen that majority of the published methods perform with a mean bias up to $\pm 5\%$ in positron emission tomography (PET) evaluation. Most of the methods also have a mean bias in the range of the difference (-6 to $+4\%$) to what was previously reported in a phantom study between different positron emission tomography/computed tomography (PET/CT) and positron emission tomography/magnetic resonance (PET/MR) systems [31]. Segmentation-based methods: 1–4 [30] MR-AC_{DIXON}, MR-AC_{UTE}, MR-AC_{CAR-RIDR}, MR-AC_{RESOLUTE}; 5 [32] 6-class discrete; 6 [33] ZTE; 7 [34] ZTE; 8 [35] ZTE; 9 [36] ZTE. Atlas-based methods: 10–15 [30] MR-AC_{ONTARIO}, MR-AC_{MUNICH}, MR-AC_{SEGBONE}, MR-AC_{UCL}, MR-AC_{MAXPROB}, MR-AC_{BOSTON}; 16 [37] Single-atlas; 17 [38] Pattern recognition; 18–19 [39] Mean atlas, PASSR; 20 [40] GMM regression; 21 [41] UTE; 22 [42] Atlas; 23 [43] U-net AC; 24 [44] Single-template. Emission-based methods: 25 [30] MR-AC_{MLAA}; 26 [45] MR-MLAA; 27–29 [46] MLAA, P-MLAA+, P-MLAA++.

also beneficial for increasing the quantitative accuracy of PET images. Consequently, methodological developments that increase the accuracy of attenuation correction will also result in minimization of errors in scatter correction.

MR-BASED ATTENUATION CORRECTION FOR PET/MR NEUROIMAGING

A multitude of MRAC methods have emerged, and significant methodological advances have been made in the PET/MR field of neuroimaging, since the introduction of the first PET/MR systems. Attenuation correction for PET/MR can be performed based on anatomical MR images, PET data-driven approaches, or a combination of both. The attenuation correction strategies can be roughly divided into (a) methods based on image segmentation, (b) atlas or database approaches including machine learning methods, and (c) emission data-driven approaches, which use PET data alone or in synergy with existing magnetic resonance imaging (MRI) data. A strict division between methods is challenging, as some of the methodology can be used in combination, e.g., segmentation and template. **Table 1** contains a generalized summary of the methodology between different MRAC methods, with concerns, solutions, and future directions.

For a complete list of methods, we refer to the excellent review papers of Hofmann et al. [22], Berker and Li [23], Bezrukov et al. [53], Izquierdo-Garcia and Catana [18], Keereman et al. [25],

Wagenknecht et al. [27], Chen et al. [26], and Mehranian et al. [28]. The physical basis of attenuation correction concerning PET/MR is addressed in Martinez-Möller and Nekolla [17]. In this section, we will focus on methods that allow for bone delineation for brain imaging applications, as methods that ignore bone should be avoided.

MRAC Methods Based on Image Segmentation

The aims of any segmentation-based MRAC method are to divide the tissues from MR images into specific classes and to assign the attenuation coefficients either based on predefined value or determining that value individually. The number of classes used depends on the method, where three tissue classes (bone, soft tissue, air) are considered the minimum, while additional classes might improve the accuracy. The first methodological challenge is to ensure that tissues are segmented and classified in an accurate and reproducible manner, so that the overlap between tissues that have large differences of attenuation coefficients is minimized, such as bone (0.151 cm^{-1}) and air (0.0 cm^{-1}). Challenging regions to segment are those that include, e.g., tissue interfaces such as the sinus region. Challenges for image segmentation for UTE and ZTE can be found, e.g., in Delso et al. [54, 55] and Aasheim et al. [56].

The tissues in the head region might be roughly divided into the following classes: soft tissue ($0.094\text{--}0.100 \text{ cm}^{-1}$), adipose tissue ($0.086\text{--}0.093 \text{ cm}^{-1}$), air cavities, and bone. A further division can be made between the nasal cavities (sinus region),

TABLE 1 | Generalized summary of the methodology between (a) segmentation-, (b) template-, and (c) emission-based MRAC methods. Essential concerns, potential solutions, and future directions are highlighted.

	Segmentation	Atlas	Emission
Requirements	MRI image data—T1, T2, UTE, ZTE.	Database of CT-MRI-PET images.	Emission data.
Need to ensure	Quality of the segmented images (no signal voids, artifacts) and the accuracy of segmentation.	High number of subjects for database creation and method validation, especially for deep learning.	High quality of the emission data by accurate corrections and calibrations.
Specific advantages	Subject-specific anatomy and anatomical variation is accounted for, fast and simple to implement.	Continuous attenuation coefficients for the entire head region.	Can estimate attenuation in the presence of signal voids and implants.
Specific disadvantages	Robustness in challenging anatomical regions (e.g., sinuses) or presence of MRI artifacts.	Accounting anatomical and attenuation coefficient variability.	Non-emitting objects remain invisible.
Issues that have been addressed since previous reviews	Subject-specific continuous attenuation coefficients can be derived with R2* or ZTE intensity to HU calibration. Bone/air delineation in challenging regions can be improved with additional masks and templates.	Methods have been applied to challenging datasets, such as tumor imaging and pediatrics. Computational burden can be reduced by using GPUs. Web-based pipelines have been implemented to ensure that methods are usable outside specific research centers which do not have access to large datasets or are computationally intensive.	Crosstalk reduced with TOF, high-quality data corrections, calibrations, and anatomical priors. Quantitative accuracy is now comparable to atlas- or segmentation-based methods. Clinical validation with a high number of patients has been performed.
Remaining issues that need to be addressed in the future	Image intensity uniformities due to B0/B1 inhomogeneities and image noise. Signal voids due to metal implants or dental fillings.	Wider availability and application of the methodology for both research and clinics. Validation of deep learning algorithms with various datasets and across PET/MR systems. Potential ethical issues when using web-based pipelines.	Specific data requirements and calibrations needed if applied in the clinical routine. Applicability across various radiotracers with specific uptake.
Suggested countermeasures to remaining issues	Implement assisted regional segmentation or improved MR sequences to countermeasure implants or signal voids. Implement emission-based attenuation correction to account the regions where MR signal is not available.	Ensure the availability of the methodology if no intellectual property or ethics issues do not permit to share the methodology. Open access databases of CT-MRI-PET datasets for both training and validation of algorithms, especially for deep learning. Solve the need for large paired datasets by the use of algorithms for deep learning which apply unpaired data (CycleGan).	Provide routine quality control protocols to ensure the consistency of calibrations performed. Apply the methodology for more challenging radiotracers.

MRAC, magnetic resonance-based attenuation correction; MRI, magnetic resonance imaging; UTE, ultrashort echo time; ZTE, zero echo time; CT, computed tomography; PET, positron emission tomography; HU, Hounsfield unit; GPUs, graphics processing units. Essential concerns, potential solutions, and future directions are highlighted.

different classes of bone (spongy and cortical: $0.130\text{--}0.172\text{ cm}^{-1}$), and different brain tissues (gray and white matter: 0.099 cm^{-1} , cerebrospinal fluid: 0.096 cm^{-1}). Each of these tissues has a different attenuation coefficient, which might vary on an inter- or inpatient basis. Thus, the most preferable way would be to account and assign the attenuation coefficients on an individual basis. This would reduce the variation caused by the differences in individual anatomy and different patient groups. Thus, the second methodological challenge is to account for the variation of attenuation coefficients in tissues and in patients.

Segmentation-based methods are popular due to ease of implementation and low computational cost. Multiple methods based on segmentation of T1-weighted images have been proposed. Zaidi and Fei proposed using T1-weighted MRI images, which are co-registered to PET data and segmented by fuzzy C-means clustering to air, scalp, skull, gray matter, white matter, and nasal sinuses [57, 58]. Statistical parametric mapping

version 8 (SPM8) has also been applied to extract the bone component from T1-weighted images, which is added to the Dixon-based attenuation map [59, 60] or by deriving a three- to six-class attenuation map from T1-images alone [32, 61]. The advantage of these methods is that they are straightforward to apply across multitude of datasets, as the only requirement is access to T1 data, which is collected routinely. In addition to T1-weighted MR images, methods based on segmentation of [^{18}F]-sodium fluoride ([^{18}F]-NaF) PET [62] or on a combination of segmentation and a fixed point source have been applied [63].

Methods based on bone delineation from short echo time (STE) sequences such as UTE or ZTE have become one of the most popular fields in segmentation-based MRAC. To visualize and account for bone, UTE-based methods were introduced in Keereman et al. [64], Catana et al. [65], and Berker et al. [66]. While these methods showed improvements in the visual and quantitative accuracy of PET images, inconsistencies in bone

delineation were reported with UTE [21, 56, 67, 68], which later resulted in improved segmentation methods and MRI sequences. After the introduction of UTE, methods based on ZTE emerged [55, 69, 70]. With both UTE and ZTE, the development of more advanced segmentation techniques and new MRI sequences has been an active field of research, to increase the accuracy of bone delineation and segmentation.

To improve the quality of segmentation, several techniques have been applied. One is to use regional masks [71] or anatomical templates [36] to assist in the delineation of different tissues. Specific masks for challenging regions such as the sinus cavities have been also proposed [72, 73]. Delineation of tissues based on tissue clusters from dual echo UTE has also been applied [54]. Recently, improved segmentation with UTE was achieved by using custom templates and tissue probability maps with statistical parametric mapping version 12 (SPM12) segmentation engine to improve the delineation of both air and bone [74]. Machine learning techniques have also been used to refine the quality of the attenuation maps derived with UTE and could potentially be applied in any segmentation-based MRAC method [75].

Improved MRI sequences for UTE include STE/Dixon and fuzzy clustering [76], improved UTE using point-wise encoding time reduction with radial acquisition (PETRA) [77] or likewise a fast dual-echo ramped hybrid encoding (dRHE) [78], and reduction of eddy current artifacts [79]. Sequences based on triple-echo UTE have also been applied [66, 79, 80]. These methods have shown improvements in terms of accuracy of the attenuation map, PET image quality, and quantitative accuracy, compared to UTE-based methods introduced previously. Recent developments include also the use of 3D radial ZTE imaging [81], which is primarily a proton density-weighted sequence. Several studies on successful use of ZTE-based methods on MRAC have been published recently [55, 69, 70, 72] in addition to assessment of repeatability [82].

Nevertheless, all previously described methods assign discrete linear attenuation coefficients to each class. Methods that apply continuous attenuation coefficients for bone have been introduced to address the limitations with discrete attenuation coefficients. A common factor for these methods is to apply a calibration curve (sigmoid, polynomial, or linear function) between the relationship of Hounsfield unit (HU) values vs. $R2^*$ values or ZTE intensities. This allows for mapping of the MR intensities in the bone region to HU values on a voxel basis. HU to $R2^*$ mapping has been successfully applied in Navalpakkam et al.; [41], Ladefoged et al. [71], Baran et al. [74], and Juttukonda et al. [83], while HU to ZTE intensity transformation has been applied in Khalifé et al. [84] and Yang et al. [72]. The performance of methods using continuous attenuation values is generally considered superior over discrete-tissue methods.

In summary, it can be seen that methods based on UTEs, such as UTE and ZTE, have become a very popular option for segmentation-based MRAC as they allow us to visualize and segment bone with fairly good accuracy, addressing the first challenge, which is the delineation of skull bones. Previously, segmentation-based methods were limited by assigning fixed attenuation coefficients to bone, but lately, this problem has

been circumvented by implementing calibration curves between HU and $R2^*$ or HU and ZTE intensities, addressing the second methodological challenge. However, there are several regions, such as air–tissue interfaces in the sinus cavity, which are still challenging for segmentation-based methods. To account for this challenge, a multitude of techniques from improved MR acquisition to masks and templates to assist segmentation have been applied, helping to improve the accuracy of the available methods.

Methods Based on Atlas or Database Approaches Including Machine Learning

Atlas- or template-based methods are typically based on using a co-registered database or atlas of CT and MR images. Methods can be further divided into approaches applying a single probabilistic atlas or a multiple atlas. To create a substitute CT, the subject MR image is matched to an MR image in the database or a predefined template. The best match is determined using a predefined similarity metric. Thereafter, the purpose is to create a CT substitute corresponding to subject anatomy with continuous attenuation coefficients for the whole image volume, usually referred to as pseudo-CT. The substitute pseudo-CT is usually created in a volume-by-volume, slice-by-slice, or voxel-by-voxel basis, using a trained classifier, image intensity mapping, or registration techniques. Recently, methods based on machine learning or deep learning techniques have also become increasingly popular.

The most straightforward implementation is to use a single atlas in combination of a predefined template. Templates can be created by taking an average of multiple co-registered CTAC or transmission-based attenuation correction (TXAC) images to represent mean attenuation coefficients and anatomical variability in a given population [85]. Template-based approaches using registration and nonlinear wrapping of a predefined TXAC or CTAC template to the individual subject anatomy using SPM have been proposed [44, 86]. SPM8 has also been used to perform segmentation and state-of-the-art registration with a probabilistic template to derive a pseudo-CT [87]. Similar approaches have been implemented by either wrapping of a CT atlas to the patient MR image using a two-step registration [88] or registering a subject MR image to an MR template and mask pair, followed by a two-step registration to delineate bony regions with the mask [89]. Limitations of the single-atlas approaches include ignoring the intersubject variation of attenuation coefficients and that the anatomical transformation might be prone to errors in registration between the template and subject images, especially with non-conventional anatomy or in the presence of disease.

Several methods based on a multiatlas approach have been introduced, where an atlas of multiple pairs of CT and anatomical MR images is used to derive patient-specific substitute pseudo-CT either by intensity mapping or by registration. Several approaches to derive the pseudo-CT substitute exist, such as using patches to match CT and MRI intensities [90, 91] or image registration techniques [50, 92–94]. The substitute pseudo-CT can be also derived by linking the intensities between CT and

MR images with a trained model, such as using a Gaussian mixture regression model with probabilistic measures [40, 95, 96] or a Gaussian mixture model based with patches [97]. While methods using multiple atlases are inherently more complex and computationally intensive, they are able to overcome the limitations of single-atlas approaches [98].

Probabilistic measurers in combination of atlases have been also applied for pseudo-CT creation, which can be used to improve the quality of segmentation or to generate continuous-valued attenuation maps [39, 53, 99]. In addition, pattern recognition [38] or machine learning techniques [41] have been successfully applied. Machine learning applying a random forest regression with patch-based anatomical signatures was used to generate pseudo-CT from T1-weighted images in Yang et al. [100]. Recently, several methods based on deep learning have also become increasingly popular in the creation of a suitable attenuation maps for MRAC.

Santos Ribeiro et al. [101] proposed a feed-forward neural network to directly output a continuous-valued head attenuation map by nonlinear regression of several UTE images and a template-based MRAC map. Gong et al. [102] used a convolutional neural network with Dixon images only or in a combination of Dixon and ZTE images to generate a continuous valued attenuation map. Similarly, a deep convolutional neural network that derived attenuation maps based on ZTE images was shown to outperform both ZTE and atlas-based method in Blanc-Durand et al. [43]. Interestingly, while most evaluations have been performed with adults with normal anatomy, Ladefoged et al. [103] evaluated deep learning methods in pediatric brain tumor patients, with robust performance. The preliminary results obtained with these methods are encouraging.

However, it would be advantageous if conventional MR images collected routinely or PET data could be used to obtain an attenuation map. The use of deep convolutional neural networks with T1 images only has been reported in Han [104] and Liu et al. [105], and they have been applied also to synthesize a pseudo-CT from patient-specific transmission data [106]. Recently, Liu et al. [107] proposed to use only uncorrected PET images with a deep convolutional encoder-decoder network to generate a pseudo-CT. Very recently, a multiparametric MRI model was also suggested to generate pseudo-CT maps based only on Dixon MRI images and was evaluated on head and pelvic images [108]. Among other benefits, these methods also show a great potential for whole-body applications. Finally, any deep learning methodology conventionally requires a large dataset of paired CT and MRI images. Recently, methods based on unpaired image-to-image translation using Cycle-Consistent Generative Adversarial Networks (CycleGan) [109] have been applied to pseudo-CT generation [110, 111], which might circumvent this requirement.

In summary, the atlas or database approaches range from simple single-template methods to complex approaches, allowing us to derive continuous attenuation coefficients not just in bone but also in a range of tissues. There is also a multitude of good methods available. Most of these methods, however, have been solely applied in research context. Until recently, a few promising studies in using atlas-based approaches on non-normal populations such as pediatric patients and in brain tumors have emerged. Naturally, pediatric patients require that

an atlas fit for different anatomy will be created. In this regard, the research questions on the applicability of the atlas-based methods for more challenging clinical and research applications is being addressed.

Recently, several machine learning approaches have emerged, which can be applied in a flexible manner. They can be applied in conjunction with segmentation- or emission-based methods, to refine the quality of the segmentation or the resulting attenuation maps. A very promising aspect is that machine learning methods might be able to create accurate attenuation maps solely on conventional T1 and T2 data or from non-attenuation-corrected PET images alone, without requiring specific sequences such as UTE or ZTE. While these methods have initially shown promising results, they need to undergo further validation studies to investigate their applicability in larger patient groups, different datasets, and a variety of radiotracers, in case PET images are used to derive an attenuation map.

Emission-Based Attenuation Correction Approaches for PET/MR

Emission-driven methods allow for estimating attenuation maps (a) based on reconstruction of emission data alone, (b) based on a combination of jointly reconstructed emission and transmission data, and (c) by the use of information from scattered coincidences, background radiation, or radiating sources. An extensive and thorough review of the methods that apply emission data for attenuation correction in PET and single-photon emission computed tomography (SPECT) was conducted by Berker and Li [22]. In this section, we will focus mainly on emerging PET/MR-specific approaches applied for clinical imaging of the head region.

A popular approach for emission-based attenuation correction is the maximum likelihood reconstruction of attenuation and activity (MLAA), which was originally proposed by Nuyts et al. [112], based on a concept introduced by Censor et al. [113]. The MLAA method is based on simultaneous reconstruction of both attenuation and activity using maximum likelihood expectation maximization (MLEM) algorithm and enables deriving an attenuation sinogram up to a constant using measured emission data only. The accuracy of the method is improved if high quality of the emission data can be guaranteed.

To reduce the cross-talk and dependence on count statistics in MLAA, the use of time-of-flight (TOF) information with MLAA has been shown to be beneficial [114]. In addition, incorporating spatial constraints or prior information, e.g., from MR data, can be used to improve the MLAA estimate [115]. MR-guided MLAA imposes MR spatial and CT statistical constraints with a Gaussian mixture model and Markov random field smoothness prior to improving the quality of the attenuation map [116]. Another approach is to jointly estimate the emission distribution and the attenuation correction factors, avoiding the reconstruction of the attenuation map. Rezaei et al. [117] proposed a maximum likelihood algorithm to jointly estimate the activity distribution and attenuation correction factors (MLACF), up to a scaling constant.

Advanced MLAA methods with additional penalty functions might offer better performance in brain imaging as shown

in Ahn et al. [118] and Mehranian et al. [46], which could overcome the limitations of earlier MLAA methods for brain imaging when compared to, e.g., atlas-based methods [42]. Recent developments in the methodology have allowed for reaching <5% of error in brain PET quantification with TOF-based MLAA using an MRI prior [46]. Deep learning has been also applied to improve the quality of the MLAA for attenuation correction in the brain using nonconventional tracers, such as 18F-radiolabeled N-(3-fluoropropyl)-2 β -carboxymethoxy-3 β -(4-iodophenyl) nortropane ([¹⁸F]-FP-CIT) used for brain dopamine transporter imaging [119]. Thus, it would seem that most of the limitations in the emission-based methods are being addressed.

Methods that use either transmission sources or background radiation have been also introduced. Improvement of the accuracy of the attenuation maps with an external transmission source was shown in Mollet et al. [120] and Mollet et al. [121], with supplemental transmission sources [122], and using different source geometries [123]. External radiation, such as 176Lu emitted by lutetium oxyorthosilicate/lutetium-yttrium oxyorthosilicate (LSO/LYSO) scintillation crystals, could also be used to acquire transmission data [124], or the scattered background radiation could be used to derived an attenuation map [125]. However, these methods have been mostly applied solely in research context. Recently, an integrated approach that includes a moving point source on a helical path around a 24-channel MR-receiver coil to perform a transmission scan was introduced in Navarro de Lara et al. [126] and Renner et al. [127], which might offer a clinically feasible approach for transmission imaging on brain PET/MR. Finally, several authors have highlighted the benefits of TOF in reducing the errors in the PET images reconstructed with MRAC [84, 128, 129]. This is due to TOF reconstruction being less sensitive to inconsistencies in emission data and data corrections such as attenuation, normalization, and scatter [130].

It can be seen that emission-based attenuation correction is an active field of research, where large clinical validation studies have begun to emerge. A scale-corrected MLACF has recently been shown to provide images that quantitatively and visually correspond to CTAC-reconstructed PET images in 57 patients [131]. Benoit et al. [132] studied a modified non-TOF MLAA algorithm with a relatively large group of patients, i.e., with 204 [¹⁸F]-FDG patients, 35 [¹¹C]-PiB patients, and 1 O-(2-[¹⁸F]-fluoroethyl)-l-tyrosine ([¹⁸F]-FET) patient. Moreover, in a study consisting of 34 dementia patients imaged with [¹⁸F]-FDG, an MLAA method was compared with state-of-the-art MRAC and CTAC, producing errors within a few percent [45]. The authors suggested that MLAA might be useful in patients where metal implants or other imaging challenges hinder the use of traditional segmentation-based methods.

In summary, emission-based attenuation correction has been an active field of research, and the methods proposed have begun to show both increases in quantitative accuracy (errors below 5%) and advantages compared to segmentation- or atlas-based methods. For example, emission-based methods might be able to estimate the attenuation coefficients in the presence of metal implants, which would pose a problem for segmentation-

or atlas-based methods due to large signal voids. Thus, they would be able to complement both segmentation- or atlas-based methods in challenging cases where they fall short.

There have been traditionally two challenges in emission-based MRAC, which have been addressed in recent methodological studies. Originally, most methods were validated using [¹⁸F]-FDG only and a small group of patients. Very recently, however, the applicability of the emission-based methods to a variety of radiotracers has been shown. Moreover, the sensitivity of MLAA to the quality of emission data has been addressed in the following manners. For example, by carefully improving and ensuring the quality of both TOF calibrations and accuracy of data corrections and by the implementation of anatomical priors from MRI, the accuracy of the attenuation map estimation can be improved. Deep learning methods can be also applied to improve the quality of the emission estimate in non-conventional radiotracers.

Status of PET/MR Attenuation Correction for Neuroimaging for Research and Clinics

As can be seen from above, a multitude of MRAC methods are available for research settings, where most of the presented methods perform with good accuracy [30, 133]. While the problem concerning the availability of accurate attenuation correction in research settings has been solved, investigation of new attenuation correction methods still is of interest to improve the accuracy of the available methods for more challenging research applications. Most of the methods presented in the previous chapters might be also applied on PET/MR systems of different vendors, unless a specialized, vendor-dependent sequence or software is required.

However, it seems that there is still an ongoing discussion whether reasonably accurate methods have become commercially available, especially in challenging clinical applications [134], while the accuracy of MRAC can be considered adequate for the majority of routine clinical situations [47]. Furthermore, future efforts for standardization and quality control are important for accurate and robust results in both research and clinics and are needed for PET/MR as well [135]. In addition to technical efforts, knowledge sharing in terms of new guidelines and procedures for PET interpretation and reading will help to improve clinical confidence [28, 136]. Finally, promising methods available for research use might be eventually translated to commercial platforms and thus result in further benefit for clinical applications.

Perhaps the greatest challenge so far has been to present the knowledge gained in the evaluation of different MRAC methods in terms of clinically interpretable information. Impact of MRAC on clinical reading is generally determined by visual analysis, presence of visible artifacts in MRAC or PET, lesion detectability, and standardized uptake value (SUV) quantification accuracy in PET [28]. Recent studies have proposed that standardized, clinical metrics need to be taken into use for MRAC method evaluation, to make direct comparison of method performance less challenging [30, 137]. Implementing more advanced vendor-based attenuation correction methods

will certainly result in an increase in the clinical evaluations performed with MRAC.

Concerning the availability of accurate MRAC methods outside the research setting, there are currently two state-of-the-art vendor-based attenuation correction methods for imaging of the brain region on the Siemens mMR and General Electric (GE) Signa PET/MR system. The Philips Ingenuity TF is the only PET/MR system that does not account for bone, as it uses the method described in Schulz et al. [138]. In this regard, while it seems that there is an overflow of MRAC methods to be selected in the research setting, there are also vendor-based methods available that have been successfully applied in a multitude of evaluations in clinical setting. Increasing the amount of clinical evaluations will undoubtedly result in increased clinical confidence in applying the vendor-based methods in clinical routine imaging of, e.g., dementia, epilepsy, and other diagnostic applications.

The Siemens mMR system implements a UTE-based method with fixed attenuation coefficients (bone: 0.151 cm^{-1} , soft tissue: 0.100 cm^{-1} , air: 0 cm^{-1}) for delineating bone for the head region, described in the paper of Aasheim et al. [56] from the internal software version of VB20P and above. Another method for delineating bone with continuous attenuation coefficients using a Dixon sequence and superimposed model-based bone compartment is presented in the paper of Koesters et al. [89]. Similarly, the GE Signa system has two methods routinely available. The first method is based on atlas registration to delineate bone with continuous attenuation coefficients for the head region [88]. The second method is based on a ZTE sequence, which derives bone in the head region by segmentation of ZTE images and assigns continuous attenuation coefficients using a ZTE-intensity vs. HU calibration curve [69], available from the internal software version of MP26 and above.

Clinical evaluations of the impact on MRAC with the vendor-based methods have been performed on the Siemens mMR using the Dixon, UTE, and model-based attenuation correction. In the study of Werner et al., 13 patients suspected of having dementia were imaged with [^{18}F]-FDG. Both UTE and Dixon-based attenuation correction were assessed for differentiating hypometabolism [139]. In a similar study consisting of 16 patients, both model-based and Dixon attenuation corrections were assessed for the visual interpretation of regional hypometabolism [140]. Both studies concluded that the typical patterns of hypometabolism were not significantly changed when even the most inaccurate MRAC was used. Furthermore, several research and clinical methods were recently assessed in terms of z-scores, with 27 patients with suspected dementia [141]. The study concluded that while the research methods proved superior, the model-based attenuation correction should be preferred for diagnostic assessment in the clinical routine.

Similar methods have also been applied in the diagnostic evaluations in brain tumors and amyloid imaging. A study from Rausch et al. evaluated Dixon-based attenuation correction and the model-based method described in Koesters et al. [89], where the authors showed no significant change in diagnosis even when an attenuation map without bone was used [137] in brain tumors.

Su et al. [80] showed that an attenuation map without bone is also sufficient for visual interpretation and clinical diagnosis when using [^{18}F]-Florbetapir to determine either amyloid positive or negative status. In a very recent study, Rausch et al. [142] assessed three vendor-based attenuation correction methods, where the authors found no significant changes in time-activity curve (TAC) pattern categorization in [^{18}F]-FET PET and that tumor grading seems to be feasible, regardless of the choice of the MRAC method. Thus, the accuracy of the vendor-based attenuation correction has been shown to be feasible for both amyloid and tumor imaging.

Evaluations of the template-based method described in the paper of Wollenweber et al. [88] have been performed against CTAC [37, 143], a multiatlas method [98], and ZTE-based attenuation correction [70]. The ZTE method has also been evaluated against Ge-68 transmission sources [34], in dynamic PET [33], and in MR-based radiotherapy of the head [35]. In these evaluations, the ZTE-based method proved superior to the template-based method, especially if the intent is to perform kinetic analysis. These studies have shown that the ZTE-based methods can be considered to be feasible in clinical PET/MR imaging applications. Undoubtedly, more evaluations on the vendor-based methods presented above will follow in the near future.

As can be seen, there are a wide range of MRAC options from the first-generation of segmentation-, atlas-, and emission-based methods to second-generation machine learning and deep learning methods. However, the current application of these methods for PET/MRI in multicenter clinical trials is a challenge contrary to PET/CT in population multisite studies such as Alzheimer's Disease Neuroimaging Initiative (ADNI) or Open Access Series of Imaging Studies (OASIS). Since the methods developed for research used perform, to some extent, differently in terms of different magnitude of residual bias and regional accuracy, the community still needs to work on the standardization of MRAC methods in PET/MR neuroimaging. These challenges could be potentially overcome by using either a commonly available and acceptable library of well-established MRAC methods or by using one comparable, integrated method from either of the PET/MR vendors.

SCATTER CORRECTION FOR PET/MR NEUROIMAGING

A 30–35% scatter fraction in brain studies can be expected [16], which makes scatter correction one of the fundamental data corrections in addition to attenuation correction. The majority of the scattered events originate from the patient, whereas the physical hardware components contribute from 5 to 15% of the scatter [144]. The physical basis for scatter correction in PET/MR is addressed in the review paper of Martinez-Möller and Nekolla [17]. In this section, we will summarize the current approaches and highlight some emerging applications for scatter correction in brain PET/MR imaging.

While scatter correction has not been a major issue to be addressed for neurological PET/MR imaging, developments in

accuracy of scatter correction are considered beneficial especially in regard to quantitative PET imaging. Furthermore, advanced scatter correction methods would be beneficial also in whole-body imaging applications. The current approaches for scatter correction can be divided into (a) historical approaches; (b) simulation or model-based methods, which estimate the single Compton scatter events; and (c) emerging Monte-Carlo-based scatter correction methods and methods based on machine learning. In **Table 2**, a flowchart describing the main steps in both SSS and Monte-Carlo scatter correction is described.

Scatter Correction, Historical Approaches

Historically, a multitude of methods were introduced for PET scatter correction, which are summarized in the following books and reviews: [16, 48, 85, 151–154]. These methods were based on either using (1) multiple energy windows to acquire PET data, e.g., Grootenboer et al. [155]; (2) scatter modeling based on convolution and subtraction, e.g., Bergstrom et al. [156] and Bailey and Meikle [157]; and (3) performing Monte Carlo (MC) simulation, e.g., Levin et al. [158]. In addition to software-based methods, hardware approaches such as coarse septa or beam stoppers made from lead were suggested [16]. These methods are no longer in use, with the exception of emerging MC approaches discussed later in this paper.

Much effort was also put into the development of approximate scatter correction techniques for PET, when shifting from two-dimensional (2D) to 3D PET imaging. These techniques are summarized in the following articles: Bailey and Meikle [157], Adam et al. [159], Barney et al. [160], Chen et al. [161], Cherry [162] and Zaidi [163]. The use of full MC methods to derive a “gold standard” approach for scatter modeling was also investigated, although they were considered computationally too intensive to be implemented in clinical routine at the time [158, 164, 165]. Interestingly, MC-based methods have recently

reemerged due to the availability of parallel graphics processing units (GPUs), which offer a boost in computing power at a reasonable cost and availability [166].

In the gradual shift from 2D imaging to 3D imaging in PET, most methods were superseded by mainly two approaches based on direct calculation of scatter distribution, which we will refer to as simulation-based approaches.

Scatter Correction, Simulation- and Model-Based Methods

Simulation-based approaches proved most successful for calculation of scatter in 3D PET. Two methods based on direct estimation of scatter distribution became most widely adopted, generally denoted as the SSS algorithm of Watson et al. [146] and the model-based single scatter approach of Ollinger [147], which are incorporated as part of the iterative reconstruction loop in clinical PET/CT and PET/MR systems. The algorithm implementations vary to some extent across different PET system vendors, e.g., comparing the approaches of Siemens Healthcare [167], Philips Healthcare [145], and GE Healthcare [168].

Both the simulation-based [146] and the model-based approaches [147] are essentially based on the direct calculation of the single scatter distribution, which considers emission and attenuation sinograms as input data and is scaled to match the emission distribution. While there are differences in implementation of how single Compton scattered events are modeled between these two approaches, some common principles can be identified. These are as follows: (1) scatter is due to single Compton scatter events, (2) single scatter distribution can be calculated by application of the Klein–Nishina formula using the known emitter density and attenuation coefficients from emission and attenuation sinogram data, and (3) the derived scatter estimate can be scaled to the emission data tails for subtraction (tail fitting) and to account

TABLE 2 | Flowchart of single scatter simulation following the methodology in Accorsi et al. [145], Watson et al. [146], and Ollinger [147] in comparison to Monte Carlo simulation-based scatter correction shown in Kim et al. [148], Magota et al. [149], and Ma et al. [150].

Single scatter simulation	Monte Carlo simulation
(1) Define activity and attenuation distribution from the scatter uncorrected emission and transmission image.	Provide a scatter uncorrected emission and transmission image and initialize random number generator for Monte Carlo simulation.
(2) Randomly distribute scatter points within the scatter volume.	Generate annihilation photon pairs according to the activity distribution of the input emission image. Generate a table of the information from the materials and physical properties.
(3) Select an line of response (LOR).	Simulate photon propagation including both navigation and detection processes for each photon.
(4) For a given scatter point, calculate the number of events it contributes to this LOR from (a) activity distribution estimate, (b) Klein–Nishina cross section, (c) Compton scattering relationships, (d) solid angles, and (e) scatter medium distribution.	Simulate physical effects such as photoelectric effect and Compton scattering using the Klein–Nishina formula for the emission volume, with potential inclusion of the physical effects occurring in the detector.
(5) Repeat (4) for all simulated scatter points and add all of their contributions to the LOR.	Repeat the steps from (3) to (4) until two photons are either detected or rejected.
(6) Repeat steps 3–5 for all LORs.	Update the corresponding LOR value.
(7) Interpolate in LOR space to obtain the scatter sinogram.	Perform coincidence sorting to simulated trues, scattered and random events.
(8) Scale and subtract the scatter sinogram from the measured sinogram.	Perform scatter sinogram scaling based on the scaling factor derived from the relationship of simulated scatter and trues vs. measured scatter and trues.
(9) Reconstruct the image.	Reconstruct the image.

for multiple scattered photons. For discussion in differences in scatter correction approaches and potential relation of scatter correction to MRAC, we refer the interested reader to Teuho [29].

Both simulation- and model-based methods have been extended and modified since the original publications. The details of the modifications in the model-based method are described in detail in the following references: Ollinger [147], Wollenweber et al. [168], Iatrou et al. [169], and Iatrou et al. [170]. Extensions and modifications to the original work in the simulation-based method are described in the following references: Watson et al. [167, 171–174]. A major extension of the original work was to include the calculation of scatter for TOF PET, described in the works of Werner et al. [175], Watson [173], and Iatrou et al. [170], by inclusion of double scatter in the model, which also excludes the need for tail fitting [174, 176].

While the currently available scatter correction methods for PET neuroimaging in general do not pose problems for the majority of neuroimaging studies on PET/MR, there might be specific applications where more accurate methods for scatter correction would be beneficial. As in the case of MRAC, increasing accuracy of the available methods is always seen beneficial.

Emerging Methods Based on MC Simulation and Machine Learning

Methods based on MC simulation and machine learning have recently gained interest. MC methods offer potential improvements in increasing the accuracy of scatter estimation or tail fitting in cases of challenging acquisition conditions. Machine learning methods allow potentially new approaches to be implemented in scatter correction, where the computationally intensive process of scatter calculation could be ignored entirely. In addition to these, several groups have investigated how current scatter correction methods could be improved in terms of tail scaling [177], out-field of view scatter compensation [178], multiple scatters [179], or speed [180].

Improved scatter correction methodology might prove useful in several applications. Data-driven methodologies such as MLAA benefit from accurate data corrections. Recently, it was shown that improved scatter correction is helpful for increasing the visual and quantitative accuracy of PET and could also result in improved attenuation correction with data-driven methodologies using PET and MRI [45]. Furthermore, accurate scatter correction methods could be useful in improving the quantitative accuracy of dynamic PET data with low count statistics [150], which is often the case in neuroimaging research. While studies in the head region do not suffer from the same effects from, e.g., truncation or large bladder-to-background ratio as PET/MR studies in the body region, accurate methodologies developed for the head region might eventually become useful for whole-body PET/MR as well.

With the introduction of fast GPUs that could be implemented in parallel, promising methods based on MC simulation have been proposed. Doing a full MC simulation combined with a GPU implementation could offer a feasible way to implement a very accurate method for scatter correction [166]. Recently, a method based on the paper of Gaens et al. [166] was further

refined and applied in a phantom and patient study using a brain PET/MR imaging system [150], with promising initial results. MC simulation has been also applied to implement more robust scaling of the scatter sinograms in the presence of high activity in [^{15}O]-inhalation studies [149]. Combining MC simulation in both scatter calculation and scaling would be beneficial for neurological applications as well as whole-body studies, and the availability of GPU-based methods might enable just that.

Finally, several groups have investigated deep learning methods for scatter estimation to calculate both scatter and attenuation estimates without requiring conventional attenuation map generation and time-consuming scatter correction. The works of Qian et al. [181] and Berker et al. [182] have shown promising early results in using deep learning to calculate scatter estimates for PET, which could offer increases in both accuracy and computational speed. Interestingly, both papers discussed that a deep learning network trained with MC-simulated data would offer further improvements in accuracy [181, 182]. Finally, a very recent work proposed performing both scatter and attenuation corrections in image space using non-corrected PET [183]. Undoubtedly, it is expected that more deep learning-based methods for both attenuation and scatter correction will emerge in the upcoming years, given the popularity of the research topic. An intriguing possibility might be to combine the best of both worlds—by the use of fast GPU-based MC for accuracy and deep learning for computational speed.

Finally, concerning PET/MR neuroimaging, the current status for vendor-based, clinically available scatter correction methods could be summarized very shortly. The SSS algorithm and the model-based SSS with current extensions form the basis of vendor-based scatter correction in PET/MR systems, which offer a well-validated and reasonable accurate solution for a multitude of neurologic applications. Although the challenges in traditional approaches, e.g., related to tail fitting, are well-known in whole-body applications, these generally do not pose a problem, with the exception of very specific neuroimaging applications, such as [^{15}O]-inhalation studies.

It could also be argued, as with MRAC, that the increase of accuracy in scatter correction is beneficial in both research and clinical settings, resulting in improved visual quality and quantitative accuracy. With the increasing appeal of using either a GPU-based MC or a deep learning-based approach for scatter correction, it remains to be seen whether these methods will be implemented as an alternative approaches in future clinical PET/MR systems.

EMERGING CLINICAL AND RESEARCH APPLICATIONS

Finally, there are several clinical and research applications where accurate attenuation and scatter correction methods will prove to be beneficial. Eventually, the success of PET/MR depends on the level of confidence revealed by current and future reports on clinical and research applications where combined PET/MR provides useful additional information.

This might lead to more widespread acceptance of PET/MR in clinical setting, particularly in neurology and oncology [28]. However, at the same time, it should be emphasized that PET/MR is much more than mere attenuation and scatter correction.

For emerging applications in neurological PET/MR, we wish to highlight recent reports where accurate data corrections are beneficial. These include, e.g., PET measurements of cerebral blood flow (CBF) using [^{15}O]-labeled water ([^{15}O]-H $_2\text{O}$) PET [184] and receptor binding studies with [18F]-(E)-N-(3-iodoprop-2-enyl)-2 β -carbofluoroethoxy-3 β -(4-methyl-phenyl) nortropane ([^{18}F]-PE2I) [33]. When PET is used to derive the arterial input function for quantification and kinetic modeling, it should be ensured that the method delivers consistent performance in terms of regional bias, accuracy, and precision. The impact of accuracy of attenuation correction on dynamic PET studies in PET/MR has been studied for 3,4-dihydroxy-6-[^{18}F] fluoro-L-phenylalanine ([^{18}F]-FDOPA) [185], [^{11}C]-cimbi-36 [186], 4-(2-methoxyphenyl)-1-[2-(N-2-pyridinyl)-p-[18F]fluorobenzamido]ethylpiperazine ([^{18}F]-MPPF) [50], (R)-[^{11}C]-verapamil [187], and carbonyl-11C]N-(2-(1-(4-(2-methoxyphenyl)-piperazinyl)ethyl)-N-pyridinyl) cyclohexanecarboxamide ([^{11}C]-WAY-100635) with [^{11}C] N, N-dimethyl-2-(2-amino-4-cyanophenylthio)benzylamine ([^{11}C]-DASB) [106]. The methods evaluated in these studies have proven to perform with sufficient accuracy for both dynamic and static PET studies. Furthermore, they have highlighted the importance that bias between the reference region (e.g., cerebellum) and the analyzed region should be kept minimal to ensure accurate quantification in kinetic analysis.

Using an image-derived input function (IDIF) for kinetic modeling on PET/MRI will certainly benefit from accurate data corrections and will be further improved by the complementary nature of both modalities. MRI data could be used to assist and complement PET data in several ways [188]. Using TOF MR angiography can improve the delineation of the arterial volume in PET [184, 189–191]. The IDIF could be implemented in an automated pipeline to provide absolute values of cerebral glucose metabolism in a clinically feasible manner [192]. The IDIF measured from either MRI and PET could also be used interchangeably [193]. The need to measure IDIF could also be circumvented entirely by the measurement of global CBF by phase-contrast MRI [194]. Another approach is to incorporate information from arterial spin labeling (ASL) into PET pharmacokinetic modeling [195]. Thus, methods using complementary information from MR with PET for defining IDIF might be beneficial for kinetic modeling in PET, as MR-driven or MR-assisted approaches might be less dependent on accuracy of data corrections.

In regard to emerging applications and new opportunities that complement the neuroimaging field in PET/MR, we wish to briefly highlight the following review papers. A review of the neurologic applications where the complementary natures of PET and MRI are beneficial in both research and clinics has been provided in Chen et al. [14], Chen et al. [196], Catana et al. [197], Hope et al. [198], Miller-Thomas and Benzinger [199]. The clinical applications where PET/MR might clinically excel are brain tumor imaging, epilepsy, stroke, and

a number of neurodegenerative conditions, to name a few. Another new clinical field where PET/MR might excel is the study of movement disorders [200]. There are also numerous research applications related to neuroreceptor studies, cerebral metabolism, and blood flow, which are not yet explored extensively. From a technical viewpoint, deep learning has several potential applications, although it has been used mainly for attenuation correction. A very recent review of potential applications of artificial intelligence for PET/MR neuroimaging was given in Zaharchuk [201]. Although out of the scope of this review, synergistic PET and MRI reconstruction might be also be applied to improve PET image quality in terms of noise or resolution.

In addition, we would like to specially mention pediatric PET/MRI imaging, which presents a number of specific challenges [202, 203] but also has the utmost benefits [204, 205]. Clinical applications for PET/MR in pediatrics have been highlighted in Gatidis et al. [206], Kwatra et al. [207], Lee et al. [208]. Accurate PET quantification is crucial in this population, and the use of combined PET/MR with accurate attenuation and scatter corrections could lead to reduced injected doses, as well as reduced exposure to CT radiation burden. This aspect has significance for pediatric cancer patients, who may need to undergo repeated diagnostic imaging sessions. In regard to novel applications, a recent study showed the benefit of PET/MR in low activity imaging (14 MBq) of [^{15}O]-H $_2\text{O}$ PET for quantitative relative cerebral blood flow (rCBF) assessment in unsedated healthy newborn infants [209]. In this regard, applying and modifying existing MRAC methods to pediatric cohorts such as in Ladefoged et al. [103] are encouraged.

Finally, MR-based radiotherapy treatment (MR-RT) and PET/MR have a lot in common in terms of methodological applications. PET/MR could be even used to improve radiotherapy treatment planning, after the challenges related to patient positioning for radiotherapy planning have been sufficiently addressed [210, 211]. This requires designing MR compatible and PET transparent radiotherapy (RT) equipment [212] and accounting the attenuation of immobilization devices and flat table tops [213]. The information from MR and generated pseudo-CT images could give a better insight for particle RT where the beam range depends strongly on chemical composition [28]. Numerous accurate MRAC methods exist, which could be used for MR-RT, with careful investigation and application of the methodology for more challenging populations undergoing radiotherapy. Similarly, there are a multitude of methods that are used for MR-RT and could be applied for attenuation correction in PET/MR [214, 215]. The methodological advances in both MR-RT and PET/MR could be applied to derive pseudo-CT images on both platforms to improve the PET quantification or accuracy of RT treatment planning.

DISCUSSION—CONCLUDING REMARKS AND OUTLOOK

In research settings, the accuracy of the attenuation correction is no longer the major methodological factor to be solved, and

promising state-of-the-art methods are in the process of being implemented in vendor-based attenuation correction as well. The remaining issues in research settings are being slowly overcome in all major fields of (a) segmentation-based, (b) template-based, and (c) emission-based attenuation corrections. In this regard, the state of MRAC is very positive, with the major focus on improving the accuracy of the existing methods. This would indicate that in the future, MRAC will no longer be considered as an issue, at least in terms of its impact on the clinical interpretation of the images.

In clinical setting, the next challenge to overcome is for the PET/MR community to work on standardization of the use of different MRAC methods in neuroimaging applications. This concerns especially the application of MRAC in PET/MRI in multicenter clinical trials, as there are a wide range of MRAC options available with varying accuracy and regional bias. These challenges could be potentially overcome by using either a commonly available and acceptable library of well-established MRAC methods with similar accuracy or one comparable, integrated method from either of the PET/MR vendors.

While the currently available scatter correction methods for PET neuroimaging in general do not pose problems for the majority of neuroimaging studies on PET/MR, it could be argued that increasing accuracy for scatter correction would be beneficial in a range of clinical and research studies. Methods based on MC calculation might become clinically feasible for accurate scatter scaling and estimation. GPU-based approaches might eventually be implemented in vendor-based methods for scatter calculation.

Deep learning is an emerging trend in medical imaging in general, where both attenuation and scatter corrections are no exception, and where several methods applying deep learning in both attenuation and scatter estimation have emerged. Undoubtedly, more methods will emerge in the near future. However, for the introduced methods to become eventually popular, the applicability of the methods between different PET/MR systems, different MR sequences, PET tracers, and patient populations should be carefully investigated.

Currently available clinical and research methods for attenuation and scatter corrections will be useful in numerous emerging applications in neurological PET/MR, such as dynamic PET studies with different radiotracers, IDIF used for kinetic modeling, clinical applications for neurology, pediatric imaging, and MR-based radiation therapy. Thus, development, application, and refinement of advanced methods for attenuation

and scatter correction methods in these fields are further encouraged, with the focus on taking into account fully the simultaneous acquisition of both PET and MRI.

AUTHOR CONTRIBUTIONS

JT contributed to the conception and design of the content, conducted the review, and wrote the manuscript. AT-C, HH, and UA contributed to the content design, conducting the review, and writing and revising the manuscript. RK, HI, and MT supervised the work and participated in writing and revising the manuscript. All authors contributed to manuscript revision, read, and approved the submitted version.

FUNDING

This study was financially supported by the Alfred Kordelin Foundation and the Finnish Cultural Foundation, Varsinais-Suomi Regional fund. Financial support was also received from the Hospital District of Southwest Finland (ERVA-project, number 13236) and the funding from the University of Turku Graduate School in the Doctoral Programme in Clinical Research. Finally, the Academy of Finland is acknowledged for the strategic Japanese–Finnish research cooperation program on Application of Medical ICT Devices supported by the Academy of Finland (project number 269977), University of Turku, Turku University Hospital, and the Åbo Akademi University. This project was also partially supported by Real Colegio Complutense at Harvard University Research Fellowships.

ACKNOWLEDGMENTS

JT acknowledges Prof. Ronald Boellaard for the review and feedback received during the pre-examination phase of his thesis, which eventually evolved into this review paper. In addition, M. D. Terhi Tuokkola was acknowledged for providing her clinical expertise, comments, and viewpoint for the manuscript.

This study was conducted within the Finnish Center of Excellence in Molecular Imaging in Cardiovascular and Metabolic Research supported by the Academy of Finland, University of Turku, Turku University Hospital, and Åbo Akademi University.

REFERENCES

- Shao Y, Cherry SR, Farahani K, Meadors K, Siegel S, Silverman RW, et al. Simultaneous PET and MR imaging. *Phys Med Biol.* (1997) 42:1965–70. doi: 10.1088/0031-9155/42/10/010
- Ratib O, Willi JP, Wissmeyer M, Steiner C, Allaoua M, Garibotto V, et al. Clinical application of whole body hybrid PET-MR scanner in oncology. *Eur J Nucl Med Mol Imaging.* (2010) 37:S220.
- Delso G, Fürst S, Jakoby B, Ladebeck R, Ganter C, Nekolla SG, et al. Performance measurements of the Siemens mMR integrated wholebody PET/MR scanner. *J Nucl Med.* (2011) 52:1914–22. doi: 10.2967/jnumed.111.092726
- Vandenberghe S, Marsden PK. PET-MRI: a review of challenges and solutions in the development of integrated multimodality imaging. *Phys Med Biol.* (2015) 60:R115–54. doi: 10.1088/0031-9155/60/4/R115
- Herzog H, Lerche C. Advances in clinical PET/MRI Instrumentation. *PET Clin.* (2016) 11:95–103. doi: 10.1016/j.cpet.2015.09.001
- Cabello J, Ziegler SI. Advances in PET/MR instrumentation and image reconstruction. *Br J Radiol.* (2018) 91:20160363. doi: 10.1259/bjr.20160363
- Disselhorst JA, Bezrukov I, Kolb A, Parl C, Pichler BJ. Principles of PET/MR imaging. *J Nucl Med.* (2014) 55:2S–10S. doi: 10.2967/jnumed.113.129098
- Torigian DA, Zaidi H, Kwee TC, Saboury B, Udupa JK, Cho Z-H, et al. PET/MR imaging: technical aspects and potential clinical applications. *Radiology.* (2013) 267:26–44. doi: 10.1148/radiol.13121038

9. Rausch I, Quick HH, Cal-Gonzalez J, Sattler B, Boellaard R, Beyer T. Technical and instrumental foundations of PET/MRI. *Eur J Radiol.* (2017) **94**:A3–13. doi: 10.1016/j.ejrad.2017.04.004
10. Herzog H, Pietrzyk U, Shah NJ, Ziemons K. The current state, challenges and perspectives of MR-PET. *Neuroimage.* (2010) **49**:2072–82. doi: 10.1016/j.neuroimage.2009.10.036
11. Zaidi H, Ojha N, Morich M, Griesmer J, Hu Z, Maniowski P, et al. Design and performance evaluation of a whole-body ingenuity TF PET–MRI system. *Phys Med Biol.* (2011) **56**:3091–106. doi: 10.1088/0031-9155/56/10/013
12. Barthel H, Schroeter ML, Hoffmann K-T, Sabri O. PET/MR in dementia and other neurodegenerative diseases. *Semin Nucl Med.* (2015) **45**:224–33. doi: 10.1053/j.semnucmed.2014.12.003
13. Ehman EC, Johnson GB, Villanueva-Meyer JE, Cha S, Leynes AP, Larson PEZ, et al. PET/MRI: where might it replace PET/CT? *J Magn Reson Imaging.* (2017) **46**:1247–62. doi: 10.1002/jmri.25711
14. Chen Z, Jamadar SD, Li S, Sforzini F, Baran J, Ferris N, et al. From simultaneous to synergistic MR-PET brain imaging: a review of hybrid MR-PET imaging methodologies. *Hum Brain Mapp.* (2018) **39**:5126–44. doi: 10.1002/hbm.24314
15. Zaidi H, Hasegawa B. Determination of the attenuation map in emission tomography. *J Nucl Med.* (2003) **44**:291–315.
16. Zaidi H, Montandon M-L. Scatter compensation techniques in PET. *PET Clin.* (2007) **2**:219–34. doi: 10.1016/j.cpet.2007.10.003
17. Martinez-Möller A, Nekolla SG. Attenuation correction for PET/MR: problems, novel approaches and practical solutions. *Z Med Phys.* (2012) **22**:299–310. doi: 10.1016/j.zemedi.2012.08.003
18. Hofmann M, Pichler B, Schölkopf B, Beyer T. Towards quantitative PET/MRI: a review of MR-based attenuation correction techniques. *Eur J Nucl Med Mol Imaging.* (2009) **36**:S93–104. doi: 10.1007/s00259-008-1007-7
19. Robson M, Gatehouse P, Bydder M, Bydder G. Magnetic resonance: an introduction to ultrashort TE (UTE) imaging. *J Comput Assist Tomogr.* (2003) **27**:825–46. doi: 10.1097/00004728-200311000-00001
20. Andersen FL, Ladefoged CN, Beyer T, Keller SH, Hansen AE, Højgaard L, et al. Combined PET/MR imaging in neurology: MR-based attenuation correction implies a strong spatial bias when ignoring bone. *Neuroimage.* (2014) **84**:206–16. doi: 10.1016/j.neuroimage.2013.08.042
21. Dickson JC, O'Meara C, Barnes A. A comparison of CT- and MR-based attenuation correction in neurological PET. *Eur J Nucl Med Mol Imaging.* (2014) **41**:1176–89. doi: 10.1007/s00259-013-2652-z
22. Berker Y, Li Y. Attenuation correction in emission tomography using the emission data—a review. *Med Phys.* (2016) **43**:807–32. doi: 10.1118/1.4938264
23. Bezrukov I, Mantlik F, Schmidt H, Schölkopf B, Pichler BJ. MR-Based PET attenuation correction for PET/MR imaging. *Semin Nucl Med.* (2013) **43**:45–59. doi: 10.1053/j.semnucmed.2012.08.002
24. Chen Y, An H. Attenuation correction of PET/MR imaging. *Magn Reson Imaging Clin N Am.* (2017) **25**:245–55. doi: 10.1016/j.mric.2016.12.001
25. Izquierdo-Garcia D, Catana C. MR imaging-guided attenuation correction of PET data in PET/MR imaging. *PET Clin.* (2016) **11**:129–49. doi: 10.1016/j.cpet.2015.10.002
26. Keereman V, Mollet P, Berker Y, Schulz V, Vandenberghe S. Challenges and current methods for attenuation correction in PET/MR. *Magn Reson Mater Phys.* (2013) **26**:81–98. doi: 10.1007/s10334-012-0334-7
27. Wagenknecht G, Kaiser H-J, Mottaghy FM, Herzog H. MRI for attenuation correction in PET: methods and challenges. *Magn Reson Mater Phys.* (2013) **26**:99–113. doi: 10.1007/s10334-012-0353-4
28. Mehranian A, Arabi H, Zaidi H. Vision 20/20: magnetic resonance imaging-guided attenuation correction in PET/MRI: challenges, solutions, and opportunities. *Med Phys.* (2016) **43**:1130–55. doi: 10.1118/1.4941014
29. Teuho J. *MR-based attenuation correction and scatter correction in neurological PET/MR imaging with 18F-FDG* (Ph.D. dissertation), University of Turku, Turku, Finland (2018). Available online at: <http://urn.fi/URN:ISBN:978-951-29-7138-1>
30. Ladefoged CN, Law I, Anazodo U, St. Lawrence K, Izquierdo-Garcia D, Catana C, et al. A multi-centre evaluation of eleven clinically feasible brain PET/MRI attenuation correction techniques using a large cohort of patients. *Neuroimage.* (2017) **147**:346–59. doi: 10.1016/j.neuroimage.2016.12.010
31. Teuho J, Johansson J, Linden J, Hansen AE, Holm S, Keller SH, et al. Effect of attenuation correction on regional quantification between PET/MR and PET/CT: a multicenter study using a 3-dimensional brain phantom. *J Nucl Med.* (2016) **57**:818–24. doi: 10.2967/jnumed.115.166165
32. Teuho J, Tuisku J, Karlsson A, Linden J, Teräs M. Effect of brain tissue and continuous template-based skull in MR-based attenuation correction for brain PET/MR. *IEEE Trans Radiat Plasma Med Sci.* (2017) **1**:246–61. doi: 10.1109/TNS.2017.2692306
33. Schramm G, Koole M, Willekens SMA, Rezaei A, Van Weehaeghe D, Delso G, et al. Regional accuracy of ZTE-based attenuation correction in static and dynamic brain PET/MR. *arXiv.* (2018) 180603481. Available online at: <http://arxiv.org/abs/1806.03481>
34. Sousa JM, Appel L, Engström M, Papadimitriou S, Nyholm D, Larsson E-M, et al. Evaluation of zero-echo-time attenuation correction for integrated PET/MR brain imaging-comparison to head atlas and 68Ge-transmission-based attenuation correction. *EJNMMI Phys.* (2018) **5**:20. doi: 10.1186/s40658-018-0220-0
35. Wiesinger F, Bylund M, Yang J, Kaushik S, Shanbhag D, Ahn S, et al. Zero TE-based pseudo-CT image conversion in the head and its application in PET/MR attenuation correction and MR-guided radiation therapy planning. *Magn Reson Med.* (2018) **80**:1440–51. doi: 10.1002/mrm.27134
36. Delso G, Kemp B, Kaushik S, Wiesinger F, Sekine T. Improving PET/MR brain quantitation with template-enhanced ZTE. *Neuroimage.* (2018) **181**:403–13. doi: 10.1016/j.neuroimage.2018.07.029
37. Sekine T, Buck A, Delso G, Ter Voert EEGW, Huellner M, Veit-Haibach P, et al. Evaluation of atlas-based attenuation correction for integrated PET/MR in human brain: application of a head atlas and comparison to true CT-based attenuation correction. *J Nucl Med.* (2016) **57**:215–20. doi: 10.2967/jnumed.115.159228
38. Hofmann M, Steinke F, Scheel V, Charpiat G, Farquhar J, Aschoff P, et al. MRI-based attenuation correction for PET/MRI: a novel approach combining pattern recognition and atlas registration. *J Nucl Med.* (2008) **49**:1875–83. doi: 10.2967/jnumed.107.049353
39. Chen Y, Juttukonda M, Su Y, Benzinger T, Rubin BG, Lee YZ, et al. Probabilistic air segmentation and sparse regression estimated pseudo CT for PET/MR attenuation correction. *Radiology.* (2015) **275**:562–9. doi: 10.1148/radiol.14140810
40. Larsson A, Johansson A, Axelsson J, Nyholm T, Askund T, Riklund K, et al. Evaluation of an attenuation correction method for PET/MR imaging of the head based on substitute CT images. *MAGMA.* (2013) **26**:127–36. doi: 10.1007/s10334-012-0339-2
41. Navalpakkam BK, Braun H, Kuwert T, Quick HH. Magnetic resonance-based attenuation correction for PET/MR hybrid imaging using continuous valued attenuation maps. *Invest Radiol.* (2013) **48**:323–32. doi: 10.1097/RLI.0b013e318283292f
42. Mehranian A, Arabi H, Zaidi H. Quantitative analysis of MRI-guided attenuation correction techniques in time-of-flight brain PET/MRI. *Neuroimage.* (2016) **130**:123–33. doi: 10.1016/j.neuroimage.2016.01.060
43. Blanc-Durand P, Khalife M, Sgard B, Kaushik S, Soret M, Tiss A, et al. Attenuation correction using 3D deep convolutional neural network for brain 18F-FDG PET/MR: comparison with Atlas ZTE and CT based attenuation correction. *PLoS ONE.* (2019) **14**:e0223141. doi: 10.1371/journal.pone.0223141
44. Rota Kops E, Hautzel H, Herzog H, Antoch G, Shah NJ. Comparison of template-based versus CT-based attenuation correction for hybrid MR/PET scanners. *IEEE Trans Nucl Sci.* (2015) **62**:2115–21. doi: 10.1109/TNS.2015.2452574
45. Rezaei A, Schramm G, Willekens SM, Delso G, Laere KV, Nuyts J. A quantitative evaluation of joint activity and attenuation reconstruction in TOF-PET/MR brain imaging. *J Nucl Med.* (2019) **60**:1649–55. doi: 10.2967/jnumed.118.220871
46. Mehranian A, Zaidi H, Reader AJ. MR-guided joint reconstruction of activity and attenuation in brain PET-MR. *Neuroimage.* (2017) **162**:276–88. doi: 10.1016/j.neuroimage.2017.09.006

47. Bailey DL, Pichler BJ, Gückel B, Antoch G, Barthel H, Bhujwala ZM, et al. Combined PET/MRI: global warming-summary report of the 6th international workshop on PET/MRI, March 27–29, 2017, Tübingen, Germany. *Mol Imaging Biol.* (2018) **20**:4–20. doi: 10.1007/s11307-017-1123-5
48. Zaidi H, Koral KF. Scatter modelling and compensation in emission tomography. *Eur J Nucl Med Mol Imaging.* (2004) **31**:761–82. doi: 10.1007/s00259-004-1495-z
49. Burgos N, Thielemans K, Cardoso MJ, Markiewicz P, Jiao J, Dickson J, et al. Effect of scatter correction when comparing attenuation maps: application to brain PET/MR. In: *2014 IEEE Nuclear Science Symposium and Medical Imaging Conference (NSS/MIC)*. Seattle, WA (2014). p. 1–5. doi: 10.1109/NSSMIC.2014.7430775
50. Mérida I, Reilhac A, Redouté J, Heckemann RA, Costes N, Hammers A. Multi-atlas attenuation correction supports full quantification of static and dynamic brain PET data in PET-MR. *Phys Med Biol.* (2017) **62**:2834–58. doi: 10.1088/1361-6560/aa5f6c
51. Son Y-D, Kim H-K, Kim S-T, Kim N-B, Kim Y-B, Cho Z-H. Analysis of biased PET images caused by inaccurate attenuation coefficients. *J Nucl Med.* (2010) **51**:753–60. doi: 10.2967/jnumed.109.070326
52. Teuho J, Saunavaara V, Tolvanen T, Tuokkola T, Karlsson A, Tuisku J, et al. Quantitative evaluation of 2 scatter-correction techniques for 18F-FDG brain PET/MRI in regard to MR-based attenuation correction. *J Nucl Med.* (2017) **58**:1691–8. doi: 10.2967/jnumed.117.190231
53. Chen KT, Izquierdo-Garcia D, Poynton CB, Chonde DB, Catana C. On the accuracy and reproducibility of a novel probabilistic atlas-based generation for calculation of head attenuation maps on integrated PET/MR scanners. *Eur J Nucl Med Mol Imaging.* (2017) **44**:398–407. doi: 10.1007/s00259-016-3489-z
54. Delso G, Zeimpekis K, Carl M, Wiesinger F, Hüllner M, Veit-Haibach P. Cluster-based segmentation of dual-echo ultra-short echo time images for PET/MR bone localization. *EJNMMI Phys.* (2014) **1**:7. doi: 10.1186/2197-7364-1-7
55. Delso G, Wiesinger F, Sacolick LI, Kaushik SS, Shanbhag DD, Hüllner M, et al. Clinical evaluation of zero-echo-time MR imaging for the segmentation of the skull. *J Nucl Med.* (2015) **56**:417–22. doi: 10.2967/jnumed.114.149997
56. Aasheim LB, Karlberg A, Goa PE, Häberg A, Sørhaug S, Fagerli U-M, et al. PET/MR brain imaging: evaluation of clinical UTE-based attenuation correction. *Eur J Nucl Med Mol Imaging.* (2015) **42**:1439–46. doi: 10.1007/s00259-015-3060-3
57. Zaidi H, Montandon M-L, Slosman DO. Magnetic resonance imaging-guided attenuation and scatter corrections in three-dimensional brain positron emission tomography. *Med Phys.* (2003) **30**:937–48. doi: 10.1118/1.1569270
58. Fei B, Yang X, Nye JA, Aarsvold JN, Raghunath N, Cervo M, et al. MR/PET quantification tools: Registration, segmentation, classification, and MR-based attenuation correction. *Med Phys.* (2012) **39**:6443–54. doi: 10.1118/1.4754796
59. Anazodo UC, Thiessen JD, Ssali T, Mandel J, Günther M, Butler J, et al. Feasibility of simultaneous whole-brain imaging on an integrated PET-MRI system using an enhanced 2-point Dixon attenuation correction method. *Front Neurosci.* (2015) **8**:434. doi: 10.3389/fnins.2014.00434
60. Izquierdo-Garcia D, Eldaief MC, Vangel MG, Catana C. Intrascanner reproducibility of an SPM-based head MR-based attenuation correction method. *IEEE Trans Radiat Plasma Med Sci.* (2019) **3**:327–33. doi: 10.1109/TRPMS.2018.2868946
61. Teuho J, Linden J, Johansson J, Tuisku J, Tuokkola T, Teräs M. Tissue probability-based attenuation correction for brain PET/MR by using SPM8. *IEEE Trans Nucl Sci.* (2016) **63**:2452–63. doi: 10.1109/TNS.2015.2513064
62. Schramm G, Maus J, Hofheinz F, Petr J, Lougovski A, Beuthien-Baumann B, et al. Correction of quantification errors in pelvic and spinal lesions caused by ignoring higher photon attenuation of bone in [18F]NaF PET/MR. *Med Phys.* (2015) **42**:6468–76. doi: 10.1118/1.4932367
63. Kawaguchi H, Hirano Y, Yoshida E, Kershaw J, Shiraiishi T, Suga M, et al. A proposal for PET/MRI attenuation correction with μ -values measured using a fixed-position radiation source and MRI segmentation. *Nucl Instr Methods Phys Res Sect A Acceler Spectrom Detect Assoc Equip.* (2014) **734**:156–61. doi: 10.1016/j.nima.2013.09.015
64. Keereman V, Fierens Y, Broux T, Deene YD, Lonnew M, Vandenberghe S. MRI-based attenuation correction for PET/MRI using ultrashort echo time sequences. *J Nucl Med.* (2010) **51**:812–8. doi: 10.2967/jnumed.109.065425
65. Catana C, van der Kouwe A, Benner T, Michel CJ, Hamm M, Fenchel M, et al. Toward implementing an MRI-based PET attenuation-correction method for neurologic studies on the MR-PET brain prototype. *J Nucl Med.* (2010) **51**:1431–8. doi: 10.2967/jnumed.109.069112
66. Berker Y, Franke J, Salomon A, Palmowski M, Donker HCW, Temur Y, et al. MRI-based attenuation correction for hybrid PET/MRI systems: a 4-class tissue segmentation technique using a combined ultrashort-echo-time/Dixon MRI sequence. *J Nucl Med.* (2012) **53**:796–804. doi: 10.2967/jnumed.111.092577
67. Choi H, Cheon GJ, Kim H-J, Choi SH, Lee JS, Kim Y, et al. Segmentation-based MR attenuation correction including bones also affects quantitation in brain studies: an initial result of 18F-FP-CIT PET/MR for patients with Parkinsonism. *J Nucl Med.* (2014) **55**:1617–22. doi: 10.2967/jnumed.114.138636
68. Delso G, Carl M, Wiesinger F, Sacolick L, Porto M, Hüllner M, et al. Anatomic evaluation of 3-dimensional ultrashort-echo-time bone maps for PET/MR attenuation correction. *J Nucl Med.* (2014) **55**:780–5. doi: 10.2967/jnumed.113.130880
69. Wiesinger F, Sacolick LI, Menini A, Kaushik SS, Ahn S, Veit-Haibach P, et al. Zero TEMR bone imaging in the head. *Magn Reson Med.* (2016) **75**:107–14. doi: 10.1002/mrm.26094
70. Sekine T, Ter Voert EEGW, Warnock G, Buck A, Huellner M, Veit-Haibach P, et al. Clinical evaluation of zero-echo-time attenuation correction for brain 18F-FDG PET/MRI: comparison with atlas attenuation correction. *J Nucl Med.* (2016) **57**:1927–32. doi: 10.2967/jnumed.116.175398
71. Ladefoged CN, Benoit D, Law I, Holm S, Kjær A, Højgaard L, et al. Region specific optimization of continuous linear attenuation coefficients based on UTE (RESOLUTE): application to PET/MR brain imaging. *Phys Med Biol.* (2015) **60**:8047–65. doi: 10.1088/0031-9155/60/20/8047
72. Yang J, Wiesinger F, Kaushik S, Shanbhag D, Hope TA, Larson PEZ, et al. Evaluation of sinus/edge-corrected zero-echo-time-based attenuation correction in brain PET/MRI. *J Nucl Med.* (2017) **58**:1873–9. doi: 10.2967/jnumed.116.188268
73. Teuho J, Tuisku J, Linden J, Teräs M. Effect of sinus attenuation in MR-based attenuation correction in 18F-FDG brain PET/MR. In: *EMBECE & NBC 2017. IFMBE Proceedings*. Singapore: Springer (2017). p. 266–9. doi: 10.1007/978-981-10-5122-7_67
74. Baran J, Chen Z, Sforazzini F, Ferris N, Jamadar S, Schmitt B, et al. Accurate hybrid template-based and MR-based attenuation correction using UTE images for simultaneous PET/MR brain imaging applications. *BMC Med Imaging.* (2018) **18**:41. doi: 10.1186/s12880-018-0283-3
75. Shi K, Fürst S, Sun L, Lukas M, Navab N, Förster S, et al. Individual refinement of attenuation correction maps for hybrid PET/MR based on multi-resolution regional learning. *Comput Med Imaging Graph.* (2017) **60**:50–7. doi: 10.1016/j.compmedimag.2016.11.005
76. Khateri P, Saligheh Rad H, Jafari AH, Fathi Kazerooni A, Akbarzadeh A, Shojae Moghadam M, et al. Generation of a four-class attenuation map for MRI-based attenuation correction of PET data in the head area using a novel combination of STE/Dixon-MRI and FCM clustering. *Mol Imaging Biol.* (2015) **17**:884–92. doi: 10.1007/s11307-015-0849-1
77. Grodzki DM, Jakob PM, Heismann B. Ultrashort echo time imaging using pointwise encoding time reduction with radial acquisition (PETRA). *Magn Reson Med.* (2012) **67**:510–8. doi: 10.1002/mrm.23017
78. Jang H, Liu F, Bradshaw T, McMillan AB. Rapid dual-echo ramped hybrid encoding MR-based attenuation correction (dRHE-MRAC) for PET/MR. *Magn Reson Med.* (2018) **79**:2912–22. doi: 10.1002/mrm.26953
79. Aitken AP, Giese D, Tsoumpas C, Schleyer P, Kozerke S, Prieto C, et al. Improved UTE-based attenuation correction for cranial PET-MR using dynamic magnetic field monitoring. *Med Phys.* (2014) **41**:012302. doi: 10.1118/1.4837315
80. Su K-H, Hu L, Stehning C, Helle M, Qian P, Thompson CL, et al. Generation of brain pseudo-CTs using an undersampled, single-acquisition UTE-mDixon pulse sequence and unsupervised clustering. *Med Phys.* (2015) **42**:4974–86. doi: 10.1118/1.4926756

81. Madio DP, Lowe IJ. Ultra-fast imaging using low flip angles and FIDs. *Magn Reson Med.* (1995) **34**:525–9. doi: 10.1002/mrm.1910340407
82. Delso G, Fernandez B, Wiesinger F, Jian Y, Bobb C, Jansen F. Repeatability of ZTE bone maps of the head. *IEEE Trans Radiat Plasma Med Sci.* (2018) **2**:244–9. doi: 10.1109/TRPMS.2017.2772329
83. Juttukonda MR, Mersereau BG, Chen Y, Su Y, Rubin BG, Benzinger TLS, et al. MR-based attenuation correction for PET/MRI neurological studies with continuous-valued attenuation coefficients for bone through a conversion from R2* to CT-Hounsfield units. *Neuroimage.* (2015) **112**:160–8. doi: 10.1016/j.neuroimage.2015.03.009
84. Khalifé M, Fernandez B, Jaubert O, Soussan M, Brulon V, Buvat I, et al. Subject-specific bone attenuation correction for brain PET/MR: can ZTE-MRI substitute CT scan accurately? *Phys Med Biol.* (2017) **62**:7814–32. doi: 10.1088/1361-6560/aa8851
85. Zaidi H, Montandon M-L, Meikle S. Strategies for attenuation compensation in neurological PET studies. *Neuroimage.* (2007) **34**:518–41. doi: 10.1016/j.neuroimage.2006.10.002
86. Rota Kops E, Herzog H. Template based attenuation correction for PET in MR-PET scanners. In: *IEEE Nuclear Science Symposium Conference Record, 2008 NSS '08*. Honolulu, HI (2008) p. 3786–9. doi: 10.1109/NSSMIC.2007.4437073
87. Izquierdo-Garcia D, Hansen AE, Förster S, Benoit D, Schachoff S, Fürst S, et al. An SPM8-based approach for attenuation correction combining segmentation and nonrigid template formation: application to simultaneous PET/MR brain imaging. *J Nucl Med.* (2014) **55**:1825–30. doi: 10.2967/jnumed.113.136341
88. Wollenweber SD, Ambwani S, Delso G, Lonn AHR, Mullick R, Wiesinger F, et al. Evaluation of an atlas-based PET head attenuation correction using PET/CT & MR patient data. *IEEE Trans Nucl Sci.* (2013) **60**:3383–90. doi: 10.1109/TNS.2013.2273417
89. Koesters T, Friedman KP, Fenchel M, Zhan Y, Hermosillo G, Babb J, et al. Dixon sequence with superimposed model-based bone compartment provides highly accurate PET/MR attenuation correction of the brain. *J Nucl Med.* (2016) **57**:918–24. doi: 10.2967/jnumed.115.166967
90. Andreasen D, Van Leemput K, Hansen RH, Andersen JAL, Edmund JM. Patch-based generation of a pseudo CT from conventional MRI sequences for MRI-only radiotherapy of the brain. *Med Phys.* (2015) **42**:1596–605. doi: 10.1118/1.4914158
91. Torrado-Carvajal A, Herraiz JL, Alcain E, Montemayor AS, Garcia-Cañamaque L, Hernandez-Tamames JA, et al. Fast patch-based pseudo-CT synthesis from T1-weighted MR images for PET/MR attenuation correction in brain studies. *J Nucl Med.* (2016) **57**:136–43. doi: 10.2967/jnumed.115.156299
92. Burgos N, Cardoso MJ, Thielemans K, Modat M, Pedemonte S, Dickson J, et al. Attenuation correction synthesis for hybrid PET-MR scanners: application to brain studies. *IEEE Trans Med Imaging.* (2014) **33**:2332–41. doi: 10.1109/TMI.2014.2340135
93. Burgos N, Cardoso MJ, Thielemans K, Modat M, Dickson J, Schott JM, et al. Multi-contrast attenuation map synthesis for PET/MR scanners: assessment on FDG and florbetapir PET tracers. *Eur J Nucl Med Mol Imaging.* (2015) **42**:1447–58. doi: 10.1007/s00259-015-3082-x
94. Schreibmann E, Nye JA, Schuster DM, Martin DR, Votaw J, Fox T. MR-based attenuation correction for hybrid PET-MR brain imaging systems using deformable image registration. *Med Phys.* (2010) **37**:2101–9. doi: 10.1118/1.3377774
95. Johansson A, Karlsson M, Nyholm T. CT substitute derived from MRI sequences with ultrashort echo time. *Med Phys.* (2011) **38**:2708–14. doi: 10.1118/1.3578928
96. Johansson A, Garpebring A, Asklund T, Nyholm T. CT substitutes derived from MR images reconstructed with parallel imaging. *Med Phys.* (2014) **41**:082302. doi: 10.1118/1.4886766
97. Roy S, Wang W-T, Carass A, Prince JL, Butman JA, Pham DL. PET attenuation correction using synthetic CT from ultrashort echo-time MRI. *J Nucl Med.* (2014) **55**:2071–7. doi: 10.2967/jnumed.114.143958
98. Sekine T, Burgos N, Warnock G, Huellner M, Buck A, Ter Voert EEGW, et al. Multi-atlas-based attenuation correction for brain 18F-FDG PET imaging using a time-of-flight PET/MR scanner: comparison with clinical single-atlas- and CT-based attenuation correction. *J Nucl Med.* (2016) **57**:1258–64. doi: 10.2967/jnumed.115.169045
99. Poynton CB, Chen KT, Chonde DB, Izquierdo-Garcia D, Gollub RL, Gerstner ER, et al. Probabilistic atlas-based segmentation of combined T1-weighted and DUTE MRI for calculation of head attenuation maps in integrated PET/MRI scanners. *Am J Nucl Med Mol Imaging.* (2014) **4**:160–71.
100. Yang X, Wang T, Lei Y, Higgins K, Liu T, Shim H, et al. MRI-based attenuation correction for brain PET/MRI based on anatomic signature and machine learning. *Phys Med Biol.* (2019) **64**:025001. doi: 10.1088/1361-6560/aaf5e0
101. Santos Ribeiro A, Rota Kops E, Herzog H, Almeida P. Hybrid approach for attenuation correction in PET/MR scanners. *Nucl Instr Methods Phys Res Sect A Accel Spectrom Detect Assoc Equip.* (2014) **734**:166–70. doi: 10.1016/j.nima.2013.09.034
102. Gong K, Yang J, Kim K, Fakhri GE, Seo Y, Li Q. Attenuation correction for brain PET imaging using deep neural network based on Dixon and ZTE MR images. *Phys Med Biol.* (2018) **63**:125011. doi: 10.1088/1361-6560/aac763
103. Ladefoged CN, Marner L, Hindsholm A, Law I, Højgaard L, Andersen FL. Deep learning based attenuation correction of PET/MRI in pediatric brain tumor patients: evaluation in a clinical setting. *Front Neurosci.* (2019) **12**:1005. doi: 10.3389/fnins.2018.01005
104. Han X. MR-based synthetic CT generation using a deep convolutional neural network method. *Med Phys.* (2017) **44**:1408–19. doi: 10.1002/mp.12155
105. Liu F, Jang H, Kijowski R, Bradshaw T, McMillan AB. Deep learning MR imaging-based attenuation correction for PET/MR imaging. *Radiology.* (2018) **286**:676–84. doi: 10.1148/radiol.2017170700
106. Spuhler KD, Gardus J, Gao Y, DeLorenzo C, Parsey R, Huang C. Synthesis of patient-specific transmission data for PET attenuation correction for PET/MRI neuroimaging using a convolutional neural network. *J Nucl Med.* (2019) **60**:555–60. doi: 10.2967/jnumed.118.214320
107. Liu F, Jang H, Kijowski R, Zhao G, Bradshaw T, McMillan AB. A deep learning approach for 18F-FDG PET attenuation correction. *EJNMMI Phys.* (2018) **5**:24. doi: 10.1186/s40658-018-0225-8
108. Torrado-Carvajal A, Vera-Olmos J, Izquierdo-Garcia D, Catalano OA, Morales MA, Margolin J, et al. Dixon-VIBE deep learning (DIVIDE) pseudo-CT synthesis for pelvis PET/MR attenuation correction. *J Nucl Med.* (2019) **60**:429–35. doi: 10.2967/jnumed.118.209288
109. Zhu J-Y, Park T, Isola P, Efros AA. Unpaired image-to-image translation using cycle-consistent adversarial networks. In: *2017 IEEE International Conference on Computer Vision (ICCV)*. Venice (2017). p. 2242–51. doi: 10.1109/ICCV.2017.244
110. Yang H, Sun J, Carass A, Zhao C, Lee J, Xu Z, et al. Unpaired brain MR-to-CT synthesis using a structure-constrained CycleGAN. In: Stoyanov D, Taylor Z, Carneiro G, Syeda-Mahmood T, Martel A, Maier-Hein L, et al., editors. *Deep Learning in Medical Image Analysis and Multimodal Learning for Clinical Decision Support. Lecture Notes in Computer Science*. Cham: Springer International Publishing (2018). p. 174–82. doi: 10.1007/978-3-030-00889-5_20
111. Wolterink JM, Dinkla AM, Savenije MHF, Seevinck PR, van den Berg CAT, Išgum I. Deep MR to CT synthesis using unpaired data. In: Tsaftaris SA, Gooya A, Frangi AF, Prince JL, editors. *Simulation and Synthesis in Medical Imaging. Lecture Notes in Computer Science*. Cham: Springer International Publishing (2017). p. 14–23. doi: 10.1007/978-3-319-68127-6_2
112. Nuyts J, Dupont P, Stroobants S, Banninck R, Mortelmans L, Suetens P. Simultaneous maximum a posteriori reconstruction of attenuation and activity distributions from emission sinograms. *IEEE Trans Med Imaging.* (1999) **18**:393–403. doi: 10.1109/42.774167
113. Censor Y, Gustafson DE, Lent A, Tuy H. A new approach to the emission computerized tomography problem: simultaneous calculation of attenuation and activity coefficients. *IEEE Trans Nucl Sci.* (1979) **26**:2775–9. doi: 10.1109/TNS.1979.4330535
114. Rezaei A, Defrise M, Bal G, Michel C, Conti M, Watson C, et al. Simultaneous reconstruction of activity and attenuation in time-of-flight PET. *IEEE Trans Med Imaging.* (2012) **31**:2224–33. doi: 10.1109/TMI.2012.2212719

115. Salomon A, Goedicke A, Schweizer B, Aach T, Schulz V. Simultaneous reconstruction of activity and attenuation for PET/MR. *IEEE Trans Med Imaging*. (2011) **30**:804–13. doi: 10.1109/TMI.2010.2095464
116. Mehranian A, Zaidi H. Joint estimation of activity and attenuation in whole-body TOF PET/MRI using constrained gaussian mixture models. *IEEE Trans Med Imaging*. (2015) **34**:1808–21. doi: 10.1109/TMI.2015.2409157
117. Rezaei A, Defrise M, Nuyts J. ML-reconstruction for TOF-PET with simultaneous estimation of the attenuation factors. *IEEE Trans Med Imaging*. (2014) **33**:1563–72. doi: 10.1109/TMI.2014.2318175
118. Ahn S, Cheng L, Shanbhag DD, Qian H, Kaushik SS, Jansen FP, et al. Joint estimation of activity and attenuation for PET using pragmatic MR-based prior: application to clinical TOF PET/MR whole-body data for FDG and non-FDG tracers. *Phys Med Biol*. (2018) **63**:045006. doi: 10.1088/1361-6560/aaa8a6
119. Hwang D, Kim KY, Kang SK, Seo S, Paeng JC, Lee DS, et al. Improving the accuracy of simultaneously reconstructed activity and attenuation maps using deep learning. *J Nucl Med*. (2018) **59**:1624–9. doi: 10.2967/jnumed.117.202317
120. Mollet P, Keereman V, Clement E, Vandenberghe S. Simultaneous MR-compatible emission and transmission imaging for PET using time-of-flight information. *IEEE Trans Med Imaging*. (2012) **31**:1734–42. doi: 10.1109/TMI.2012.2198831
121. Mollet P, Keereman V, Bini J, Izquierdo-Garcia D, Fayad ZA, Vandenberghe S. Improvement of attenuation correction in time-of-flight PET/MR imaging with a positron-emitting source. *J Nucl Med*. (2014) **55**:329–36. doi: 10.2967/jnumed.113.125989
122. Watson CC. Supplemental transmission method for improved PET attenuation correction on an integrated MR/PET. *Nucl Instr Methods Phys Res Sect A Accel Spectrom Detect Assoc Equip*. (2014) **734**:191–5. doi: 10.1016/j.nima.2013.08.068
123. Bowen SL, Fuin N, Levine MA, Catana C. Transmission imaging for integrated PET-MR systems. *Phys Med Biol*. (2016) **61**:5547–68. doi: 10.1088/0031-9155/61/15/5547
124. Rothfuss H, Panin V, Moor A, Young J, Hong I, Michel C, et al. LSO background radiation as a transmission source using time of flight. *Phys Med Biol*. (2014) **59**:5483–500. doi: 10.1088/0031-9155/59/18/5483
125. Berker Y, Kiessling F, Schulz V. Scattered PET data for attenuation-map reconstruction in PET/MRI. *Med Phys*. (2014) **41**:102502. doi: 10.1118/1.4894818
126. Navarro de Lara LI, Frass-Kriegl R, Renner A, Sieg J, Pichler M, Bogner T, et al. Design, implementation, and evaluation of a head and neck MRI RF array integrated with a 511 keV transmission source for attenuation correction in PET/MR. *Sensors (Basel)*. (2019) **19**:E3297. doi: 10.3390/s19153297
127. Renner A, Rausch I, Cal Gonzalez J, Frass-Kriegl R, de Lara LN, Sieg J, et al. A head coil system with an integrated orbiting transmission point source mechanism for attenuation correction in PET/MRI. *Phys Med Biol*. (2018) **63**:225014. doi: 10.1088/1361-6560/aae9a9
128. Boellaard R, Hofman MBM, Hoekstra OS, Lammertsma AA. Accurate PET/MR quantification using time of flight MLAA image reconstruction. *Mol Imaging Biol*. (2014) **16**:469–77. doi: 10.1007/s11307-013-0716-x
129. Mehranian A, Zaidi H. Impact of time-of-flight PET on quantification errors in MR imaging-based attenuation correction. *J Nucl Med*. (2015) **56**:635–41. doi: 10.2967/jnumed.114.148817
130. Conti M. Why is TOF PET reconstruction a more robust method in the presence of inconsistent data? *Phys Med Biol*. (2011) **56**:155–68. doi: 10.1088/0031-9155/56/1/010
131. Bal H, Panin VY, Platsch G, Defrise M, Hayden C, Hutton C, et al. Evaluation of MLACF based calculated attenuation brain PET imaging for FDG patient studies. *Phys Med Biol*. (2017) **62**:2542–58. doi: 10.1088/1361-6560/aa5e99
132. Benoit D, Ladefoged CN, Rezaei A, Keller SH, Andersen FL, Højgaard L, et al. Optimized MLAA for quantitative non-TOF PET/MR of the brain. *Phys Med Biol*. (2016) **61**:8854–74. doi: 10.1088/1361-6560/61/24/8854
133. Cabello J, Lukas M, Rota Kops E, Ribeiro A, Shah NJ, Yakushev I, et al. Comparison between MRI-based attenuation correction methods for brain PET in dementia patients. *Eur J Nucl Med Mol Imaging*. (2016) **43**:2190–200. doi: 10.1007/s00259-016-3394-5
134. Catana C, Quick HH, Zaidi H. Current commercial techniques for MRI-guided attenuation correction are insufficient and will limit the wider acceptance of PET/MRI technology in the clinic. *Med Phys*. (2018) **45**:4007–10. doi: 10.1002/mp.12963
135. Boellaard R, Rausch I, Beyer T, Delso G, Yaqub M, Quick HH, et al. Quality control for quantitative multicenter whole-body PET/MR studies: a NEMA image quality phantom study with three current PET/MR systems. *Med Phys*. (2015) **42**:5961–9. doi: 10.1118/1.4930962
136. Brendle C, Schmidt H, Oergel A, Bezrukov I, Mueller M, Schraml C, et al. Segmentation-based attenuation correction in positron emission tomography/magnetic resonance: erroneous tissue identification and its impact on positron emission tomography interpretation. *Invest Radiol*. (2015) **50**:339–46. doi: 10.1097/RLI.0000000000000131
137. Rausch I, Rischka L, Ladefoged CN, Furtner J, Fenchel M, Hahn A, et al. PET/MRI for oncologic brain imaging: a comparison of standard MR-based attenuation corrections with a model-based approach for the Siemens mMR PET/MR system. *J Nucl Med*. (2017) **58**:1519–25. doi: 10.2967/jnumed.116.186148
138. Schulz V, Torres-Espallardo I, Renisch S, Hu Z, Ojha N, Börner P, et al. Automatic, three-segment, MR-based attenuation correction for whole-body PET/MR data. *Eur J Nucl Med Mol Imaging*. (2011) **38**:138–52. doi: 10.1007/s00259-010-1603-1
139. Werner P, Rullmann M, Bresch A, Tiepolt S, Jochimsen T, Lobsien D, et al. Impact of attenuation correction on clinical [(18)F]FDG brain PET in combined PET/MRI. *EJNMMI Res*. (2016) **6**:47. doi: 10.1186/s13550-016-0200-0
140. Franceschi AM, Abballe V, Raad RA, Nelson A, Jackson K, Babb J, et al. Visual detection of regional brain hypometabolism in cognitively impaired patients is independent of positron emission tomography-magnetic resonance attenuation correction method. *World J Nucl Med*. (2018) **17**:188. doi: 10.4103/wjnm.WJNM_61_17
141. Øen SK, Keil TM, Berntsen EM, Aanerud JF, Schwarzmüller T, Ladefoged CN, et al. Quantitative and clinical impact of MRI-based attenuation correction methods in [(18)F]FDG evaluation of dementia. *EJNMMI Res*. (2019) **9**:83. doi: 10.1186/s13550-019-0553-2
142. Rausch I, Zitterl A, Berroterán-Infante N, Rischka L, Prayer D, Fenchel M, et al. Dynamic [(18)F]FET-PET/MRI using standard MRI-based attenuation correction methods. *Eur Radiol*. (2019) **29**:4276–85. doi: 10.1007/s00330-018-5942-9
143. Yang J, Jian Y, Jenkins N, Behr SC, Hope TA, Larson PEZ, et al. Quantitative evaluation of atlas-based attenuation correction for brain PET in an integrated time-of-flight PET/MR imaging system. *Radiology*. (2017) **284**:169–79. doi: 10.1148/radiol.2017161603
144. Hirano Y, Koshino K, Iida H. Influences of 3D PET scanner components on increased scatter evaluated by a Monte Carlo simulation. *Phys Med Biol*. (2017) **62**:4017–30. doi: 10.1088/1361-6560/aa6644
145. Accorsi R, Adam L-E, Werner ME, Karp JS. Optimization of a fully 3D single scatter simulation algorithm for 3-D PET. *Phys Med Biol*. (2004) **49**:2577–98. doi: 10.1088/0031-9155/49/12/008
146. Watson CC, Newport D, Casey ME. A single scatter simulation technique for scatter correction in 3D PET. In: *Three-Dimensional Image Reconstruction in Radiology and Nuclear Medicine*. (1996). p. 255–68. doi: 10.1007/978-94-015-8749-5_18
147. Ollinger JM. Model-based scatter correction for fully 3D PET. *Phys Med Biol*. (1996) **41**:153–76. doi: 10.1088/0031-9155/41/1/012
148. Kim KS, Son YD, Cho ZH, Ra JB, Ye JC. Ultra-fast hybrid CPU-GPU multiple scatter simulation for 3-D PET. *IEEE J Biomed Health Inform*. (2014) **18**:148–56. doi: 10.1109/JBHI.2013.2267016
149. Magota K, Shiga T, Asano Y, Shinyama D, Ye J, Perkins AE, et al. Scatter correction with combined single-scatter simulation and Monte Carlo simulation scaling improved the visual artifacts and quantification in 3-dimensional brain PET/CT imaging with 15O-gas inhalation. *J Nucl Med*. (2017) **58**:2020–5. doi: 10.2967/jnumed.117.193060
150. Ma B, Gaens M, Caldeira L, Bert J, Lohmann P, Tellmann L, et al. Scatter correction based on GPU-accelerated Full Monte Carlo simulation for Brain PET/MRI. *IEEE Trans Med Imaging*. (2019) **39**:140–51. doi: 10.1109/TMI.2019.2921872

151. Zaidi H. *Quantitative Analysis of Nuclear Medicine Images*. New York, NY: Springer (2007). p. 205–35. doi: 10.1007/b107410
152. Bendriem B, Townsend DW. *The Theory and Practice of 3D PET*. Kluwer Academic Publishers (1998). doi: 10.1007/978-94-017-3475-2
153. Valk PE, Bailey DL, Townsend DW, Maisey MN, editors. *Positron Emission Tomography: Basic Science and Clinical Practice*. London: Springer (2003). p. 115–46.
154. Zaidi H. Scatter modelling and correction strategies in fully 3-D PET. *Nucl Med Commun.* (2001) **22**:1181–4. doi: 10.1097/00006231-200111000-00003
155. Grootenck S, Spinks TJ, Sashin D, Spyrou NM, Jones T. Correction for scatter in 3D brain PET using a dual energy window method. *Phys Med Biol.* (1996) **41**:2757–74. doi: 10.1088/0031-9155/41/12/013
156. Bergstrom M, Eriksson L, Bohm C, Blomqvist G, Litton J. Correction for scattered radiation in a ring detector positron camera by integral transformation of the projections. *J Comput Assist Tomogr.* (1983) **7**:42–50. doi: 10.1097/00004728-198302000-00008
157. Bailey DL, Meikle SR. A convolution-subtraction scatter correction method for 3D PET. *Phys Med Biol.* (1994) **39**:411–24. doi: 10.1088/0031-9155/39/3/009
158. Levin CS, Dahlbom M, Hoffman EJ. A Monte Carlo correction for the effect of Compton scattering in 3-D PET brain imaging. *IEEE Trans Nucl Sci.* (1995) **42**:1181–8. doi: 10.1109/23.467880
159. Adam LE, Karp JS, Freifelder R. Scatter correction using a dual energy window technique for 3D PET with NaI(Tl) detectors. In: 1998 *IEEE Nuclear Science Symposium Conference Record 1998 IEEE Nuclear Science Symposium and Medical Imaging Conference*. Toronto, ON (1998). p. 2011–8.
160. Barney JS, Rogers JG, Harrop R, Hoverath H. Object shape dependent scatter simulations for PET. *IEEE Trans Nucl Sci.* (1991) **38**:719–25. doi: 10.1109/23.289380
161. Chen CH, Muzic RF Jr., Nelson AD, Adler LP. A non-linear spatially variant object-dependent system model for prediction of partial volume effects and scatter in PET. *IEEE Trans Med Imaging.* (1998) **17**:214–27. doi: 10.1109/42.700733
162. Cherry SR, Huang S-C. Effects of scatter on model parameter estimates in 3D PET studies of the human brain. *IEEE Trans Nucl Sci.* (1995) **42**:1174–9. doi: 10.1109/23.467730
163. Zaidi H. Comparative evaluation of scatter correction techniques in 3D positron emission tomography. *Eur J Nucl Med.* (2000) **27**:1813–26. doi: 10.1007/s002590000385
164. Adam LE, Karp JS, Brix G. Investigation of scattered radiation in 3D whole-body positron emission tomography using Monte Carlo simulations. *Phys Med Biol.* (1999) **44**:2879–95. doi: 10.1088/0031-9155/44/12/302
165. Holdsworth CH, Levin CS, Janacek M, Dahlbom M, Hoffman EJ. Performance analysis of an improved 3-D PET Monte Carlo simulation and scatter correction. *IEEE Trans Nucl Sci.* (2002) **49**:83–9. doi: 10.1109/TNS.2002.998686
166. Gaens M, Bert J, Pietrzyk U, Autret A, Shah NJ, Visvikis D. GPU-accelerated Monte Carlo based scatter correction in brain PET/MR. *EJNMMI Phys.* (2014) **1**:A32. doi: 10.1186/2197-7364-1-S1-A32
167. Watson CC, Casey ME, Michel C, Bendriem B. Advances in scatter correction for 3D PET/CT. In: *IEEE Symposium Conference Record Nuclear Science*. Rome (2004). p. 3008–12.
168. Wollenweber SD. Parameterization of a model-based 3-D PET scatter correction. *IEEE Trans Nucl Sci.* (2002) **49**:722–7. doi: 10.1109/TNS.2002.1039554
169. Iatrou M, Manjeshwar RM, Ross SG, Thielemans K, Stearns CW. 3D implementation of scatter estimation in 3D PET. In: 2006 *IEEE Nuclear Science Symposium Conference Record*. San Diego, CA (2006). p. 2142–5. doi: 10.1109/NSSMIC.2006.354338
170. Iatrou M, Manjeshwar RM, Stearns CW. Comparison of two 3D implementations of TOF scatter estimation in 3D PET. In: 2007 *IEEE Nuclear Science Symposium Conference Record*. Honolulu, HI (2007). p. 3474–7. doi: 10.1109/NSSMIC.2007.4436878
171. Watson CC, Newport D, Casey ME, deKemp RA, Beanlands RS, Schmand M. Evaluation of simulation-based scatter correction for 3-D PET cardiac imaging. *IEEE Trans Nucl Sci.* (1997) **44**:90–7. doi: 10.1109/23.554831
172. Watson CC. New, faster, image-based scatter correction for 3D PET. In: 1999 *IEEE Nuclear Science Symposium Conference Record 1999 Nuclear Science Symposium and Medical Imaging Conference (Cat No99CH37019)*. Seattle, WA (1999). p. 1637–41.
173. Watson CC. Extension of single scatter simulation to scatter correction of time-of-flight PET. *IEEE Trans Nucl Sci.* (2007) **54**:1679–86. doi: 10.1109/TNS.2007.901227
174. Watson CC, Hu J, Zhou C. Extension of the SSS PET scatter correction algorithm to include double scatter. In: 2018 *IEEE Nuclear Science Symposium and Medical Imaging Conference Proceedings (NSS/MIC)*. Sydney, NSW (2018). p. 1–4. doi: 10.1109/NSSMIC.2018.8824475
175. Werner ME, Surti S, Karp JS. Implementation and evaluation of a 3D PET single scatter simulation with TOF modeling. In: *IEEE Nuclear Science Symposium Conference Record*. San Diego, CA (2006). p. 1768–73. doi: 10.1109/NSSMIC.2006.354238
176. Tsoumpas C, Aguiar P, Ros D, Dikaio N, Thielemans K. Scatter simulation including double scatter. In: *IEEE Nuclear Science Symposium Conference Record*. Fajardo (2005). p. 5–1619.
177. Rezaei A, Salvo K, Vahle T, Panin V, Casey M, Boada F, et al. Plane-dependent ML scatter scaling: 3D extension of the 2D simulated single scatter (SSS) estimate. *Phys Med Biol.* (2017) **62**:6515–31. doi: 10.1088/1361-6560/aa7a8c
178. Hori Y, Hirano Y, Koshino K, Moriguchi T, Iguchi S, Yamamoto A, et al. Validity of using a 3-dimensional PET scanner during inhalation of (15)O-labeled oxygen for quantitative assessment of regional metabolic rate of oxygen in man. *Phys Med Biol.* (2014) **59**:5593–609. doi: 10.1088/0031-9155/59/18/5593
179. Polycarpou I, Thielemans K, Manjeshwar R, Aguiar P, Marsden PK, Tsoumpas C. Comparative evaluation of scatter correction in 3D PET using different scatter-level approximations. *Ann Nucl Med.* (2011) **25**:643–9. doi: 10.1007/s12149-011-0514-y
180. Nikulin P, Maus J, Hofheinz F, Loughovski A, van den Hoff J. Time efficient scatter correction for time-of-flight PET: the immediate scatter approximation. *Phys Med Biol.* (2019) **64**:075005. doi: 10.1088/1361-6560/ab0e9b
181. Qian H, Rui X, Ahn S. Deep learning models for PET scatter estimations. In: 2017 *IEEE Nuclear Science Symposium and Medical Imaging Conference (NSS/MIC)*. Atlanta, GA (2017). p. 1–5. doi: 10.1109/NSSMIC.2017.8533103
182. Berker Y, Maier J, Kachelrieß M. Deep scatter estimation in PET: fast scatter correction using a convolutional neural network. In: 2018 *IEEE Nuclear Science Symposium and Medical Imaging Conference Proceedings (NSS/MIC)*. (2018). p. 1–5. doi: 10.1109/NSSMIC.2018.8824594
183. Yang J, Park D, Gullberg GT, Seo Y. Joint correction of attenuation and scatter in image space using deep convolutional neural networks for dedicated brain 18F-FDG PET. *Phys Med Biol.* (2019) **64**:075019. doi: 10.1088/1361-6560/ab0606
184. Okazawa H, Tsujikawa T, Higashino Y, Kikuta K-I, Mori T, Makino A, et al. No significant difference found in PET/MRI CBF values reconstructed with CT-atlas-based and ZTE MR attenuation correction. *EJNMMI Res.* (2019) **9**:26. doi: 10.1186/s13550-019-0494-9
185. Cabello J, Avram M, Brandl F, Mustafa M, Scherr M, Leucht C, et al. Impact of non-uniform attenuation correction in a dynamic [18F]-FDOPA brain PET/MRI study. *EJNMMI Res.* (2019) **9**:77. doi: 10.1186/s13550-019-0547-0
186. Mansur A, Newbould R, Searle GE, Redstone C, Gunn RN, Hallett WA. PET- MR attenuation correction in dynamic brain pet using [11C]cimbi-36: a direct comparison with PET-CT. *IEEE Trans Rad Plasma Med Sci.* (2018) **2**:483–9. doi: 10.1109/TRPMS.2018.2852558
187. Lassen ML, Muzik O, Beyer T, Hacker M, Ladefoged CN, Cal-González J, et al. Reproducibility of quantitative brain imaging using a PET-only and a combined PET/MR system. *Front Neurosci.* (2017) **11**:396. doi: 10.3389/fnins.2017.00396
188. Zhu Y, Zhu X. MRI-driven PET image optimization for neurological applications. *Front Neurosci.* (2019) **13**:782. doi: 10.3389/fnins.2019.00782
189. Khalighi MM, Deller TW, Fan AP, Gulaka PK, Shen B, Singh P, et al. Image-derived input function estimation on a TOF-enabled PET/MR for cerebral blood flow mapping. *J Cereb Blood Flow Metab.* (2018) **38**:126–35. doi: 10.1177/0271678X17691784
190. Jochimsen TH, Zeisig V, Schulz J, Werner P, Patt M, Patt J, et al. Fully automated calculation of image-derived input function in

- simultaneous PET/MRI in a sheep model. *EJNMMI Phys.* (2016) 3:2. doi: 10.1186/s40658-016-0139-2
191. Sundar LK, Muzik O, Rischka L, Hahn A, Rausch I, Lanzenberger R, et al. Towards quantitative [18F]FDG-PET/MRI of the brain: automated MR-driven calculation of an image-derived input function for the non-invasive determination of cerebral glucose metabolic rates. *J Cereb Blood Flow Metab.* (2019) 39:1516–30. doi: 10.1177/0271678X18776820
 192. Shiyam Sundar LK, Muzik O, Rischka L, Hahn A, Lanzenberger R, Hienert M, et al. The promise of fully-integrated PET/MR imaging: non-invasive clinical quantification of cerebral glucose metabolism. *J Nucl Med.* (2019). doi: 10.2967/jnumed.119.229567. [Epub ahead of print].
 193. Poulin E, Lebel R, Croteau E, Blanchette M, Tremblay L, Lecomte R, et al. Conversion of arterial input functions for dual pharmacokinetic modeling using Gd-DTPA/MRI and 18F-FDG/PET. *Magn Reson Med.* (2013) 69:781–92. doi: 10.1002/mrm.24318
 194. Ssali T, Anazodo UC, Thiessen JD, Prato FS, Lawrence KS. A noninvasive method for quantifying cerebral blood flow by hybrid PET/MRI. *J Nucl Med.* (2018) 59:1329–34. doi: 10.2967/jnumed.117.203414
 195. Scott CJ, Jiao J, Melbourne A, Burgos N, Cash DM, De Vita E, et al. Reduced acquisition time PET pharmacokinetic modelling using simultaneous ASL-MRI: proof of concept. *J Cereb Blood Flow Metab.* (2019) 39:2419–32. doi: 10.1177/0271678X18797343
 196. Catana C, Drzezga A, Heiss W-D, Rosen BR. PET/MRI for neurologic applications. *J Nucl Med.* (2012) 53:1916–25. doi: 10.2967/jnumed.112.105346
 197. Cecchin D, Palombit A, Castellaro M, Silvestri E, Bui F, Barthel H, et al. Brain PET and functional MRI: why simultaneously using hybrid PET/MR systems? *Q J Nucl Med Mol Imaging.* (2017) 61:345–59. doi: 10.23736/S1824-4785.17.03008-4
 198. Hope TA, Fayad ZA, Fowler KJ, Holley D, Iagaru A, McMillan AB, et al. Summary of the first ISMRM-SNMMI workshop on PET/MRI: applications and limitations. *J Nucl Med.* (2019) 60:1340–6. doi: 10.2967/jnumed.119.227231
 199. Miller-Thomas MM, Benzinger TLS. Neurologic applications of PET/MR imaging. *Magn Reson Imaging Clin N Am.* (2017) 25:297–313. doi: 10.1016/j.mric.2016.12.003
 200. Tondo G, Esposito M, Dervenoulas G, Wilson H, Politis M, Pagano G. Hybrid PET-MRI applications in movement disorders. *Int Rev Neurobiol.* (2019) 144:211–57. doi: 10.1016/bs.irn.2018.10.003
 201. Zaharchuk G. Next generation research applications for hybrid PET/MR and PET/CT imaging using deep learning. *Eur J Nucl Med Mol Imaging.* (2019) 46:2700–7. doi: 10.1007/s00259-019-04374-9
 202. Purz S, Sabri O, Viehweger A, Barthel H, Kluge R, Sorge I, et al. Potential pediatric applications of PET/MR. *J Nucl Med.* (2014) 55:32S–9S. doi: 10.2967/jnumed.113.129304
 203. Bezrukov I, Schmidt H, Gatidis S, Mantlik F, Schäfer JF, Schwenzer N, et al. Quantitative evaluation of segmentation- and atlas-based attenuation correction for pet/MR on pediatric patients. *J Nucl Med.* (2015) 56:1067–74. doi: 10.2967/jnumed.114.149476
 204. Marner L, Henriksen OM, Lundemann M, Larsen VA, Law I. Clinical PET/MRI in neuro-oncology: opportunities and challenges from a single-institution perspective. *Clin Transl Imaging.* (2017) 5:135–49. doi: 10.1007/s40336-016-0213-8
 205. Marner L, Nysom K, Sehested A, Borgwardt L, Mathiasen R, Henriksen OM, et al. Early postoperative 18F-FET PET/MRI for pediatric brain and spinal cord tumors. *J Nucl Med.* (2019) 60:1053–8. doi: 10.2967/jnumed.118.220293
 206. Gatidis S, Bender B, Reimold M, Schäfer JF. PET/MRI in children. *Eur J Radiol.* (2017) 94:A64–70. doi: 10.1016/j.ejrad.2017.01.018
 207. Kwatra NS, Lim R, Gee MS, States LJ, Vossough A, Lee EY. PET/MR imaging: current updates on pediatric applications. *Magn Reson Imaging Clin N Am.* (2019) 27:387–407. doi: 10.1016/j.mric.2019.01.012
 208. Lee YZ, Oldan JD, Fordham LA. Pediatric applications of hybrid PET/MR imaging. *Magn Reson Imaging Clin N Am.* (2017) 25:367–75. doi: 10.1016/j.mric.2016.12.005
 209. Andersen JB, Lindberg U, Olesen OV, Benoit D, Ladefoged CN, Larsson HB, et al. Hybrid PET/MRI imaging in healthy unsedated newborn infants with quantitative rCBF measurements using 15O-water PET. *J Cereb Blood Flow Metab.* (2019) 39:782–93. doi: 10.1177/0271678X17751835
 210. Thorwarth D, Leibfarth S, Mönnich D. Potential role of PET/MRI in radiotherapy treatment planning. *Clin Transl Imaging.* (2013) 1:45–51. doi: 10.1007/s40336-013-0006-2
 211. Winter RM, Leibfarth S, Schmidt H, Zwirner K, Mönnich D, Welz S, et al. Assessment of image quality of a radiotherapy-specific hardware solution for PET/MRI in head and neck cancer patients. *Radiother Oncol.* (2018) 128:485–91. doi: 10.1016/j.radonc.2018.04.018
 212. Paulus DH, Quick HH. Hybrid positron emission tomography/magnetic resonance imaging: challenges, methods, and state of the art of hardware component attenuation correction. *Invest Radiol.* (2016) 51:624–34. doi: 10.1097/RLI.0000000000000289
 213. Witoszynskij S, Andrzejewski P, Georg D, Hacker M, Nyholm T, Rausch I, et al. Attenuation correction of a flat table top for radiation therapy in hybrid PET/MR using CT- and 68Ge/68Ga transmission scan-based μ -maps. *Phys Med.* (2019) 65:76–83. doi: 10.1016/j.ejmp.2019.08.005
 214. Edmund JM, Nyholm T. A review of substitute CT generation for MRI-only radiation therapy. *Radiat Oncol.* (2017) 12:28. doi: 10.1186/s13014-016-0747-y
 215. Johnstone E, Wyatt JJ, Henry AM, Short SC, Sebag-Montefiore D, Murray L, et al. Systematic review of synthetic computed tomography generation methodologies for use in magnetic resonance imaging-only radiation therapy. *Int J Radiat Oncol Biol Phys.* (2018) 100:199–217. doi: 10.1016/j.ijrobp.2017.08.043

Conflict of Interest: The authors declare that the research was conducted in the absence of any commercial or financial relationships that could be construed as a potential conflict of interest.

Copyright © 2020 Teuho, Torrado-Carvajal, Herzog, Anazodo, Klén, Iida and Teräs. This is an open-access article distributed under the terms of the Creative Commons Attribution License (CC BY). The use, distribution or reproduction in other forums is permitted, provided the original author(s) and the copyright owner(s) are credited and that the original publication in this journal is cited, in accordance with accepted academic practice. No use, distribution or reproduction is permitted which does not comply with these terms.



Study of the Effect of Reconstruction Parameters for Myocardial Perfusion Imaging in PET With a Novel Flow Phantom

Reetta Siekkinen^{1,2,3*}, Jarmo Teuho¹, Nadia A. S. Smith⁴, Andrew Fenwick⁴, Anna K. Kirjavainen⁵, Kalle Koskensalo^{1,2}, Antti Saraste^{1,6} and Mika Teräs^{2,7}

¹ Turku PET Centre, University of Turku and Turku University Hospital, Turku, Finland, ² Department of Medical Physics, Turku University Hospital, Turku, Finland, ³ Department of Future Technologies, University of Turku, Turku, Finland, ⁴ National Physical Laboratory, Teddington, United Kingdom, ⁵ Radiopharmaceutical Chemistry Laboratory, Turku PET Centre, University of Turku, Turku, Finland, ⁶ Heart Center, Turku University Hospital, Turku, Finland, ⁷ Department of Biomedicine, University of Turku, Turku, Finland

OPEN ACCESS

Edited by:

Ivo Rausch,
Medical University of Vienna, Austria

Reviewed by:

David B. Stout,
Independent Researcher, Culver City,
United States
Cristina Lois,
Harvard Medical School,
United States

*Correspondence:

Reetta Siekkinen
reetta.siekkinen@tyks.fi

Specialty section:

This article was submitted to
Medical Physics and Imaging,
a section of the journal
Frontiers in Physics

Received: 24 October 2019

Accepted: 14 April 2020

Published: 06 May 2020

Citation:

Siekkinen R, Teuho J, Smith NAS,
Fenwick A, Kirjavainen AK,
Koskensalo K, Saraste A and Teräs M
(2020) Study of the Effect of
Reconstruction Parameters for
Myocardial Perfusion Imaging in PET
With a Novel Flow Phantom.
Front. Phys. 8:148.
doi: 10.3389/fphy.2020.00148

Myocardial perfusion imaging (MPI) with positron emission tomography (PET) allows quantitative temporal measurements of the radioactive tracer distribution in tissue. The quantification for myocardial blood flow (MBF) is conducted with kinetic modeling of the image-derived time-activity curves (TACs) allowing derivation for MBF in units of mL/min per gram of tissue. The ordered-subset expectation maximization (OSEM) reconstruction algorithm with time-of-flight (TOF) and point spread function (PSF) modeling is now routinely employed in cardiac imaging. However, the varying counting statistics of the MPI measurements conducted with short-lived tracers present a challenge for the PET image reconstruction methods. Thus, the effect of the reconstruction methods on the flow quantification needs to be evaluated in a standardized manner. Recently, a novel PET flow phantom modeling the MBF has been developed for investigation of the standardization of the MBF measurements. In this study, the effect of the reconstruction parameters on the image-derived flow values against a known reference flow of the flow phantom was studied with [¹⁵O]H₂O. The effects were studied by comparison of TACs and relative errors of the image-derived flow values with respect to the phantom-derived reference flow value using 5 repeated PET scans with fixed acquisition parameters using a digital Discovery MI PET/CT system. The reconstruction methods applied were OSEM using both TOF and PSF (OSEM-TOF-PSF) with several matrix sizes (128 x 128, 192 x 192, 256 x 256, 384 x 384), Gaussian filter sizes (4, 8 mm) and OSEM without TOF and PSF (OSEM), with TOF (OSEM-TOF) and with PSF (OSEM-PSF) in addition to recently introduced regularized reconstruction method based on Bayesian-penalized maximum likelihood (Q.Clear). Between repeated measurements, the image-derived flow values showed high repeatability with a SD less than 2 mL/min as well as high accuracy with the maximum error of 7% with respect to the reference flow for all reconstructions. Overall, reconstruction settings had only a small impact on the resulting flow values. In conclusion, due to the small differences detected, any of the implemented reconstruction algorithms on the system can be applied in MPI studies for accurate flow quantification.

Keywords: PET, myocardial perfusion imaging, quantification, flow phantom, reconstruction, myocardial blood flow

INTRODUCTION

Positron emission tomography (PET) is a noninvasive imaging modality allowing quantitative temporal measurements of the radioactive tracer distribution in tissue. By means of myocardial perfusion imaging (MPI) with dynamic PET, the myocardial blood flow (MBF) can be derived by kinetic modeling of the tracer distribution in the myocardium [1–4]. The kinetic modeling employs time-activity-curves (TACs) measured from the blood pool and myocardial tissue, resulting in derivation for MBF in quantitative units of mL/min per gram of tissue. Flow quantification provides important physiologic information, which may be useful to individualize patient therapy. The MPI studies are usually conducted with short-lived radiotracers such as [^{15}O]H $_2$ O, [^{82}Rb]Cl or [^{13}N]NH $_3$ [5].

Iterative reconstruction methods in PET, such as ordered-subset expectation maximization (OSEM) algorithm method with time-of-flight (TOF) and point spread function (PSF) modeling are now routinely employed in cardiac imaging [6–8]. In addition, regularized reconstruction methods based on Bayesian-penalized maximum likelihood (Q.Clear) have recently been introduced [9]. However, dynamic scans with short-lived tracers are a challenge for image reconstruction, especially due to ~ 10 times higher count rates after injection compared to the end of the scan. Moreover, short time frames are used in the beginning of the scan whereas at the end of the scan, the frame times are increased to account for tracer decay and increased noise [7, 10]. Thus, both image quality and quantification need to be preserved in the presence of varying count statistics and image noise.

Previously, Presotto et al. [7] investigated the accuracy of the iterative OSEM reconstruction method, including TOF and PSF, against analytical reconstruction by using a cardiac phantom with [^{18}F]FDG and [^{13}N]NH $_3$. Their study showed an improvement in activity concentration recovery and a decrease in variability when the iterative reconstruction with both TOF and PSF was used. Similarly, Matheoud et al. [11] proved that OSEM reconstruction with TOF and PSF improved the image quality in cardiac [^{18}F]FDG studies. Kero et al. [10] studied the effect of OSEM reconstruction method with TOF on the MBF with [^{15}O]H $_2$ O MPI. The authors compared a simultaneous PET/MR system to a PET/CT system. They showed no differences in MBF with or without TOF with the PET/MR system. In addition, O'Doherty et al. [12] studied the Q.Clear reconstruction in [^{13}N]NH $_3$ perfusion studies showing no adverse effect on MBF quantification.

However, technical standardization and investigation of the approaches used for reconstruction of MBF measurements are still required. For oncological [^{18}F]FDG studies, the reports of standardization organizations, such as EARL, have reviewed a large set of factors affecting quantification of standardized uptake value (SUV) [13]. Ferretti et al. [14] investigated the harmonization of the SUVs and discussed that reconstruction methods that allow accurate image-based SUV quantification and not only optimized lesion detection are required. Therefore, it would be of high interest to study the effect of image reconstruction parameters also in flow quantification.

To our knowledge, no such systematic approach has been applied to MBF quantification in PET with [^{15}O]H $_2$ O with a reference standard. In previous studies, evaluations of reconstruction method accuracies have been conducted with phantoms in static circumstances using [^{18}F]FDG [7, 11, 15]. The authors investigated both the accuracy of recovery of the activity and parameters that are related to the image quality and detectability of myocardial defects. However, it would be of interest to study also parameters that represent the dynamic state and the kinetics of the MBF. O'Doherty et al. [12] suggested that a phantom representing myocardial perfusion should be used as a standard for kinetic modeling in comparison of reconstruction methods.

Recently, a novel flow phantom has been developed and validated to investigate flow quantification accuracy and precision in dynamic PET studies against a known reference flow value [16]. Consequently, the dynamic phantom offers an ideal standard for investigation of the effect of different image reconstruction methods and reconstruction parameters on the quantified flow values. In this paper, we studied the effect of PET image reconstruction on the image-derived flow values with a wide set of parameters. We used a standard protocol based on the reported factors by EARL to minimize other effects related to image quality and flow quantification. We applied a recently introduced PET flow phantom and [^{15}O]H $_2$ O as radiotracer and assessed the effect of image matrix size, Gaussian filter size (GFS), PSF modeling, TOF and regularized reconstruction (Q.Clear) to flow quantification using a recently introduced digital Discovery MI PET/CT system.

MATERIALS AND METHODS

Flow Phantom

This study was conducted with a novel PET flow phantom (DCE Dynamic Flow Phantom, Shelley Medical Imaging Technologies, London, Ontario, Canada). The details of the construction and validation of the phantom are presented in Gabrani-Juma et al. [16]. The phantom set-up includes a peristaltic pump, an injection port, a torso-shaped water-filled shell, flow control valves, flow meters and water containers.

The phantom set-up is represented in **Figure 1** [16]. The outer dimensions of the phantom shell are similar to the NEMA image quality phantom. An input chamber (volume of 15.7 mL) as well as an exchange cylinder (volume of 161 mL) with a perforated tube (volume of 35 mL) are located inside the shell of the phantom. The input chamber corresponds to the left ventricle blood pool, while the exchange cylinder and perforated tube mimic the myocardial tissue. The input chamber and exchange cylinder allow to derive image-based input and tissue activity curves. The flow running in the phantom system is adjusted with a peristaltic pump, where the flow is marked as Q_{pump} in units of mL/min. Q_{pump} is assumed to be equal to the flow inside the input chamber. From the input chamber water proceeds to the perforated tube inside the exchange cylinder. Water passes from the perforated tube to the exchange cylinder through small holes. The water flow inside the perforated tube is marked as Q_{tube} and the water flow out from the exchange cylinder is marked as

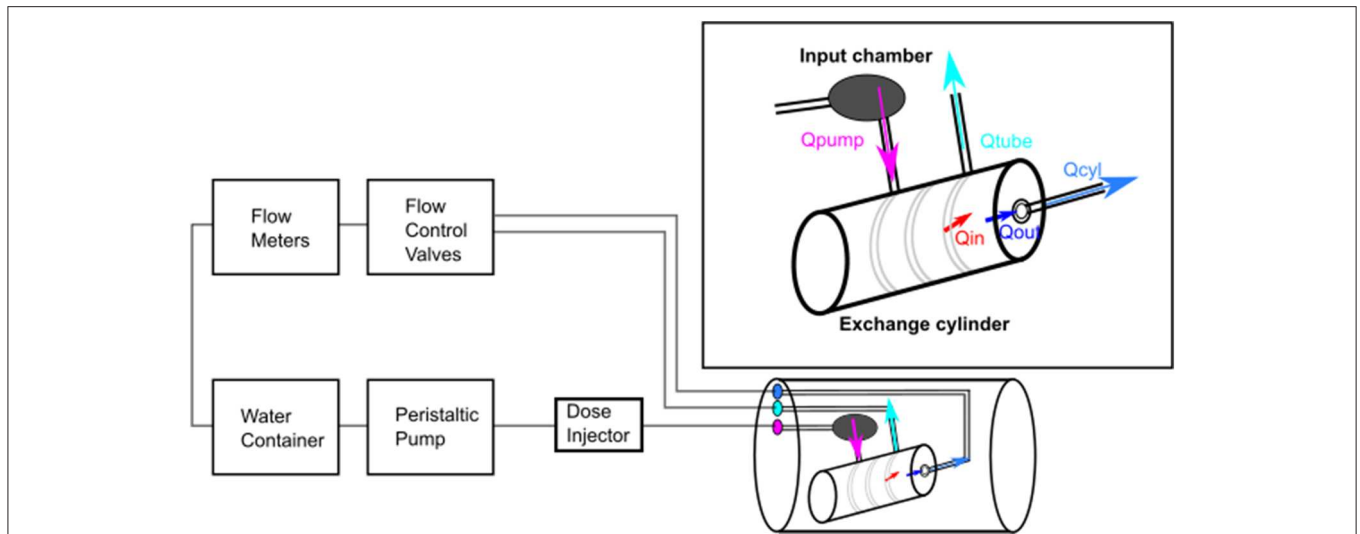


FIGURE 1 | Flow phantom set-up. The peristaltic pump creates the flow inside the phantom with a constant flow rate Q_{pump} . The phantom shell includes an input chamber and an exchange cylinder, where both the image-derived input function and tissue activity curves can be defined by region-of-interest analysis. A perforated tube is located inside the exchange cylinder, where the tracer passes from the tube to the cylinder. The flow inside the perforated tube is Q_{tube} and inside the exchange cylinder Q_{cyl} which are controlled with flow control valves. Q_{in} and Q_{out} are the modeled image-derived flow values. Q_{in} represents flow from the perforated tube to the exchange cylinder and Q_{out} flow out from the exchange cylinder [16].

Q_{cyl} . These values can be controlled with two flow control valves. Overall, it is assumed that the sum of Q_{tube} and Q_{cyl} should be equal to Q_{pump} :

$$Q_{\text{pump}} = Q_{\text{tube}} + Q_{\text{cyl}}. \quad (1)$$

The actual flow meter readings Q_{tube} and Q_{cyl} are recorded during the image acquisition using two microturbine flow meters (Omega Engineering Inc.) [17]. Flow meter calibration is conducted by following the calibration protocol. The system is run with several flow rates and the flow meter readings are recorded. The recorded values are plotted against the theoretical flow rates. Finally, the reference flow (Q_{ref}) to which image derived values are compared is derived based on measured values from Q_{cyl} using a lookup table [16].

Kinetic Modeling of Flow Values

The image-derived flow values with the phantom are derived using kinetic modeling with a two-compartmental model [16]. The two-compartmental model is implemented in the software QuantifyDCE provided by the phantom vendor (QuantifyDCE 1.1, Shelley Medical Imaging Technologies, London, Ontario, Canada).

The modeling of image-derived flow values is based on TACs measured by a volume-of-interest (VOI) analysis. VOI delineation is conducted by selecting the center point of the input chamber and exchange cylinder from the PET images. Spherical region-of-interests (ROIs) at the center points with a specific diameter for input chamber and exchange cylinder are automatically produced and the VOI is delineated by searching all pixel values corresponding a certain threshold range within the ROI. Finally, the activity concentrations in the input chamber

($C_{\text{inletVOI}}(t)$) and in the exchange cylinder ($C_{\text{cylVOI}}(t)$) are derived by summing the VOI pixel values, multiplied by the pixel volume and divided by the input chamber and exchange cylinder volumes, respectively [16].

The software models the tracer activity concentration in the exchange cylinder over time as:

$$C_{\text{cyl}}(t) = q_{\text{in}} * e^{q_{\text{out}} * t} * C_{\text{tube}}(t), \quad (2)$$

where $*$ represents the discrete convolution operation, $C_{\text{cyl}}(t)$ represents the time-dependent tracer concentration in the exchange cylinder, q_{in} represents the tracer wash-in rate to the exchange cylinder (min^{-1}), and q_{out} represents the tracer wash-out rate from the exchange cylinder (min^{-1}). $C_{\text{tube}}(t)$ is equal to the activity concentration in the perforated tube and is estimated based on the $C_{\text{inletVOI}}(t)$ where a time delay factor is taken into account. Finally, as $C_{\text{cyl}}(t)$ contributes signal from both the exchange cylinder and the perforated tube, the pure activity concentration in the exchange cylinder is modeled with an input signal fraction (ISF) corresponding to the signal mixing from the perforated tube to the exchange cylinder as:

$$C_{\text{cylVOI}} = (1 - \text{ISF}) \times C_{\text{tube}}(t) + \text{ISF} \times C_{\text{cyl}}(t) \quad (3)$$

Thus, the model contains four parameters, delay , ISF , q_{in} and q_{out} which are solved using the standard approach of non-linear least-squares fitting. The modeled parameters for rate constants q_{in} and q_{out} in units of min^{-1} can be converted to final image-derived flow values Q_{in} and Q_{out} (units of mL/min) when they are multiplied by the cylinder volume ($V_{\text{cyl}} = 161 \text{ mL}$).

Thus, Q_{in} ($Q_{\text{in}} = V_{\text{cyl}} \times q_{\text{in}}$) represents the flow from the perforated tube to the exchange cylinder and Q_{out}

($Q_{out} = V_{cyl} \times q_{out}$) the flow out from the exchange cylinder. Ultimately, they should be equal to Q_{ref} as no losses should occur in the phantom:

$$Q_{in} = Q_{out} = Q_{ref}. \quad (4)$$

PET/CT System

The phantom was imaged with a digital Discovery MI PET/CT system (DMI, GE Healthcare, Milwaukee, US). The DMI PET detector system consists of 4 rings of detector blocks. One detector ring comprises 136 detector blocks. Each block employs 3 x 6 array of silicon photomultiplier (SiPM) detectors with a 4 x 9 array of lutetium-yttrium oxyorthosilicate (LYSO) crystals with one crystal element size of 3.95 x 5.3 x 25 mm. The axial and transaxial FOV sizes of the DMI are 20 and 70 cm, respectively. The NEMA performance parameters of the DMI are 13.7 cps/kBq for sensitivity, 4.10 cm for radial spatial resolution at 1 cm distance from the FOV center, 193 kcps for peak noise-equivalent count rate (NECR), 21.9 kBq/mL for peak NECR activity, 40.6% for peak NECR scatter fraction, 375 ps for timing resolution and 9.40% for energy resolution [18].

Data Acquisition

The PET data acquisition was conducted using 5 repeated scans in the PET/CT system using the same phantom set-up. To ensure repeatability, the acquisition parameters were fixed for each measurement as recommended in [19]. The measurements were conducted by following the clinical perfusion protocol used in the Turku PET Centre [20] as follows. The injection and measurement of doses were performed using the Hidex automatic dispenser system (Hidex OY, Turku, Finland). [^{15}O]H₂O was injected separately for each measurement with a target dose of 500 MBq. Dynamic PET scan was started after a time delay after the injection and acquired as list-mode. Frame times of 14 x 5 s, 3 x 10 s, 3 x 20 s, and 4 x 30 s were used leading to a total scan time of 4 min and 40 s.

The phantom shell was set on the system table and a CT based attenuation correction (CTAC) scan was acquired using the low-dose protocol with tube voltage of 120 kVp and 63–65 mAs. For each repetition, an individual CTAC was acquired. The PET scan was acquired following the perfusion protocol. The injected doses for repeated measurements were in the range of 463–495 MBq (Table 1). The time delay between the injection and the scan start time are presented in Table 1.

TABLE 1 | Scan parameters for all repeated scans.

	Injected Activity	Scan Start Time	Qcyl	Qtube
	[MBq]	[s]	[mL/min]	[mL/min]
Test 1	495	50.0	121	98.0
Test 2	487	50.0	121	98.0
Test 3	490	50.0	120	97.0
Test 4	463	50.0	123	98.0
Test 5	491	51.0	120	98.0
Mean ± SD	485 ± 12.7	50.2 ± 0.4	121 ± 1.2	97.8 ± 0.4

For each measurement, a fixed Qpump of 200 mL/min was used. Qcyl was adjusted to 60% of Qpump with a flow rate of ~120 mL/min and Qtube of 98 mL/min. The flow meter readings were recorded between CTAC and dynamic PET scans. The recorded flow values are also presented in Table 1. The flow rates follow what has been reported before [16].

PET Image Reconstruction

To investigate the effect of image reconstruction to the image-derived flow values, different reconstruction parameters were used and the reconstructions were performed similarly for all repeated measurements.

The OSEM reconstructions with TOF and PSF (OSEM-TOF-PSF) with different matrix sizes and GFS, as well as OSEM without TOF and PSF (OSEM), with TOF (OSEM-TOF) and with PSF (OSEM-PSF) with a single matrix size (192 x 192) and a single GFS (5 mm) were investigated. In all reconstructions, a 3D-OSEM algorithm with 3 iterations, 16 subsets and a FOV size of 50 cm was used. In addition, we studied the effect of regularized reconstruction Q.Clear with $\beta = 350$ (QCFX) with an image matrix size of 192 x 192. The default value for β on the Discovery MI system was used, which defines the term to penalize image intensity differences between neighboring pixels, such as image noise. The reconstruction methods are summarized in Table 2.

It should be noted that due to technical difficulties in the DICOM data export to QuantifyDCE version 1.1, the OSEM reconstruction (Table 2, VPHD) could not be analyzed for tests 2 and 5 and the OSEM-TOF reconstruction (Table 2, VPFX) could not be analyzed for the test 2, 3, and 5. The phantom vendor has been notified about the issue and will provide an update in the software in the future.

Data Analysis

To study the effect of the reconstruction parameters, the input (input cylinder) and tissue (exchange cylinder) TACs from all the reconstructions were derived from the phantom using QuantifyDCE 1.1 software by a semi-automated VOI analysis performed similarly for all reconstructed images. The parameters used to define the VOIs for all the reconstructions were fixed: sphere radius of 4 and 6 cm for input chamber and exchange cylinder, 15% threshold for both, volume of 15.7 mL and 161 mL for input chamber and exchange cylinder and a pixel volume of 19 mm³. The final VOI was defined based on activity concentration values of 15% of the maximum activity concentration within the sphere semi-automatically by QuantifyDCE software. The extracted TACs were visually inspected to investigate their shape between subsequent repeats and reconstructions. The areas under the input and tissue curves (AUC) were computed to analyze the AUC value over all subsequent measurements and reconstructions.

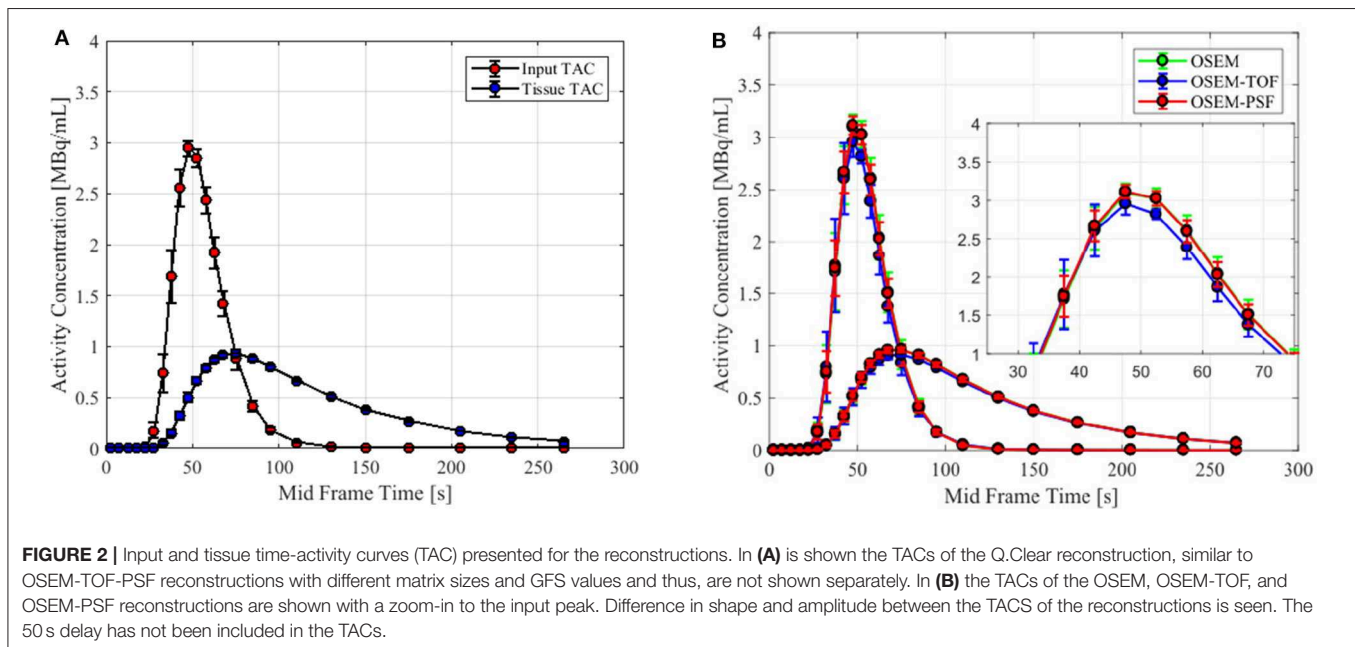
Finally, the phantom-derived flow values Q_{in} and Q_{out} were investigated. The flow values Q_{in} and Q_{out} were derived by the image-based two compartmental kinetic modeling presented in Kinetic Modeling of Flow Values. The mean values and standard deviations (SD) of the AUC and flow values were calculated. The relative errors of the Q_{in} and Q_{out} flow values with respect

TABLE 2 | Reconstruction parameters applied in the flow phantom study, separated according to matrix and filter (GFS) size, TOF and PSF and regularized Q.Clear reconstruction.

	Matrix size	Filter size (GFS) (mm)	TOF	PSF	Algorithm	Iterations	Subsets	Vendor name
Matrix	192 x 192	5	TOF	PSF	OSEM	3	16	VPFX-S
	128 x 128	5	TOF	PSF	OSEM	3	16	VPFX-S
	256 x 256	5	TOF	PSF	OSEM	3	16	VPFX-S
	384 x 384	5	TOF	PSF	OSEM	3	16	VPFX-S
Filter (GFS)	192 x 192	4	TOF	PSF	OSEM	3	16	VPFX-S
	192 x 192	8	TOF	PSF	OSEM	3	16	VPFX-S
TOF-PSF	192 x 192	5	-	-	OSEM	3	16	*VPHD
	192 x 192	5	TOF	-	OSEM	3	16	**VPFX
	192 x 192	5	-	PSF	OSEM	3	16	VP-S
Q.Clear	192 x 192	-	TOF	-	Q.Clear, $\beta = 350$	-	-	QCFX

*Test 1, test 3 and test 4 included in the analysis.

**Test 1 and test 4 included in the analysis.



to the reference flow value Q_{ref} were calculated using the following equation

$$Q_{error} = \frac{flow\ value - Q_{ref}}{Q_{ref}} * 100\% \quad (5)$$

where *flow value* is either Q_{in} or Q_{out} and Q_{ref} is the reference flow value derived from recorded Q_{cyl} values and using a lookup table.

We report the mean and SDs of the input and tissue TACs over all the subsequent measurements and reconstructions. Similarly, we present the AUC values from input and tissue TACs as well as the image-derived Q_{in} and Q_{out} flow values. Q_{in} and Q_{out} errors with respect to Q_{ref} are reported over all subsequent measurements per each reconstruction.

RESULTS

The mean input and tissue TACs with their SDs from all reconstructions are shown in **Figure 2**. No clear difference between the TACs derived from the images reconstructed with OSEM-TOF-PSF with different matrix sizes, GFSs or Q.Clear is noted. Thus, only one input and tissue TAC is presented for those reconstructions in **Figure 2A**. However, TACs derived from images reconstructed with OSEM, OSEM-TOF or OSEM-PSF show differences in the input and tissue curve shape and thus, all those TACs are presented in **Figure 2B**. The input peaks of those reconstructions are shown beside the TACs in order to illustrate the difference. Overall, the deviation in TACs between subsequent measurements is similar for all reconstructions.

The AUC values of the TACs for all the reconstructions are shown in **Figure 3**. The input AUC values were higher in

comparison to the tissue AUC values over all the reconstructions. The AUCs were similar between the TACs that were derived from the images reconstructed with OSEM-TOF-PSF with different matrix sizes and GFS values. Using the OSEM and OSEM-PSF reconstruction, the AUC values were systematically higher for both the input and tissue TAC when compared to other reconstructions. Q.Clear produced similar AUC values for the tissue curves as the OSEM-TOF-PSF with different matrix sizes and GFS values as well as the OSEM-TOF. However, slightly lower values for the input curves were noted with the Q.Clear and OSEM-TOF reconstruction.

The mean values and SDs of both the Q_{in} and Q_{out} flow values and their relative errors with respect to the reference flow over all the subsequent measurements per each individual reconstruction are summarized in **Table 3**. The values for the reference flow Q_{ref} were 140, 140, 139, 142, and 139 mL/min for the five measurements, respectively with a mean value of 140

mL/min. The image-derived wash-in flow Q_{in} is similar over all the reconstructions, whereas the wash-out flow Q_{out} shows the greatest difference to other Q_{out} values when using OSEM and OSEM-PSF reconstruction. This effect is similar to what is seen in the AUC analysis. The error between mean Q_{in} and Q_{out} as well as of the Q_{in} and Q_{out} with respect to Q_{ref} are within 5% for all the reconstructions (**Table 3**).

Figure 4 shows the distribution and median of the flow values Q_{in} and Q_{out} and their relative errors with respect to the reference flow value Q_{ref} . It can be seen that the wash-in flow Q_{in} varies more across different reconstruction parameters. The wash-out flow Q_{out} is relatively stable across different matrix sizes and GFS values. The largest differences in both Q_{in} and Q_{out} are seen when using OSEM or OSEM-PSF reconstruction, with respect to the other reconstruction parameters. The Q.Clear is comparable to the OSEM-TOF-PSF with different matrix sizes and GFS values as well as to OSEM-TOF. For the Q_{out} error with respect to Q_{ref} , the OSEM and OSEM-PSF reconstructions show positive bias towards the reference flow when all the other reconstructions show negative bias. The Q_{in} error with respect to Q_{ref} shows negative bias for all the reconstructions.

DISCUSSION

In this study, the effect of reconstruction parameters to the image-derived flow values (Q_{in} , Q_{out}) using a PET flow phantom was investigated. The reconstruction methods were studied in terms of image matrix size, GFS, TOF, PSF modeling, and Q.Clear. The measurements were conducted with a repeated protocol with fixed acquisition parameters. The effects were analyzed in regard to the AUCs of input and tissue curves as well as to the relative errors of the modeled flow against the reference flow.

The shape and amplitude of both the input and tissue TACs were in mutual agreement in regard to the visual analysis of the TACs between reconstructions. However, images reconstructed with OSEM, OSEM-TOF, or OSEM-PSF, showed a slightly different shape and amplitude of the TACs compared to other

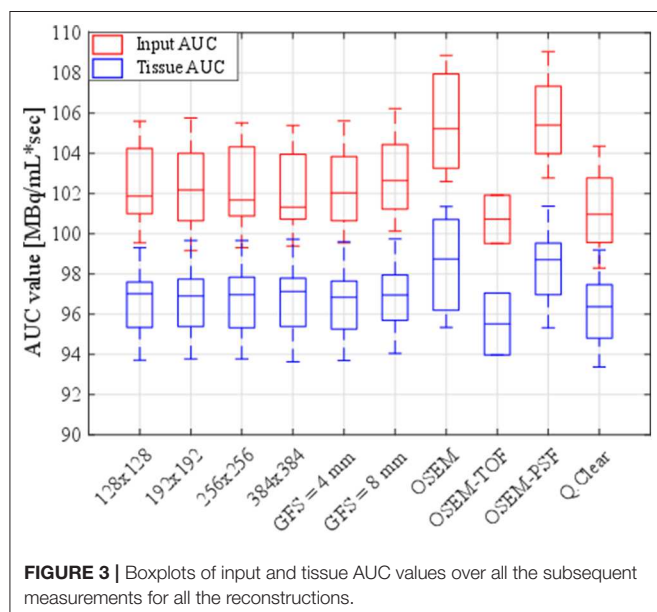


TABLE 3 | The mean and SD values for the Q_{in} and Q_{out} flow values and for their relative differences with respect to the reference flow Q_{ref} (mean Q_{ref} = 140 mL/min) over all the subsequent measurements for all the reconstructions.

		Q_{in}	Q_{out}	Q_{in} to Q_{ref} Error	Q_{out} to Q_{ref} Error
		[mL/min]	[mL/min]	[%]	[%]
Matrix	128 x 128	133.72 ± 0.9	137.53 ± 0.9	-4.38 ± 1.2	-1.65 ± 1
	192 x 192	133.88 ± 0.9	137.65 ± 0.8	-4.26 ± 1.3	-1.56 ± 1.2
	256 x 256	134.35 ± 0.6	137.72 ± 0.9	-3.93 ± 0.7	-1.51 ± 1.3
	384 x 384	134.69 ± 0.8	137.68 ± 0.9	-3.68 ± 1	-1.54 ± 1.2
Filter (GFS)	4 mm	133.39 ± 1	137.58 ± 0.8	-4.61 ± 0.7	-1.62 ± 0.6
	8 mm	133.76 ± 0.8	138.12 ± 0.8	-4.36 ± 0.6	-1.23 ± 0.6
OSEM/TOF/PSF	OSEM	134.5 ± 1	140.35 ± 0.8	-3.82 ± 0.7	0.363 ± 0.6
	OSEM-TOF	134.95 ± 0.1	137.01 ± 0.8	-3.5 ± 0.1	-2.03 ± 0.5
	OSEM-PSF	133.81 ± 1.5	140.42 ± 1	-4.32 ± 1.1	0.407 ± 0.7
Q.Clear	β = 350	134.98 ± 0.8	137.45 ± 0.9	-3.48 ± 0.6	-1.72 ± 0.7

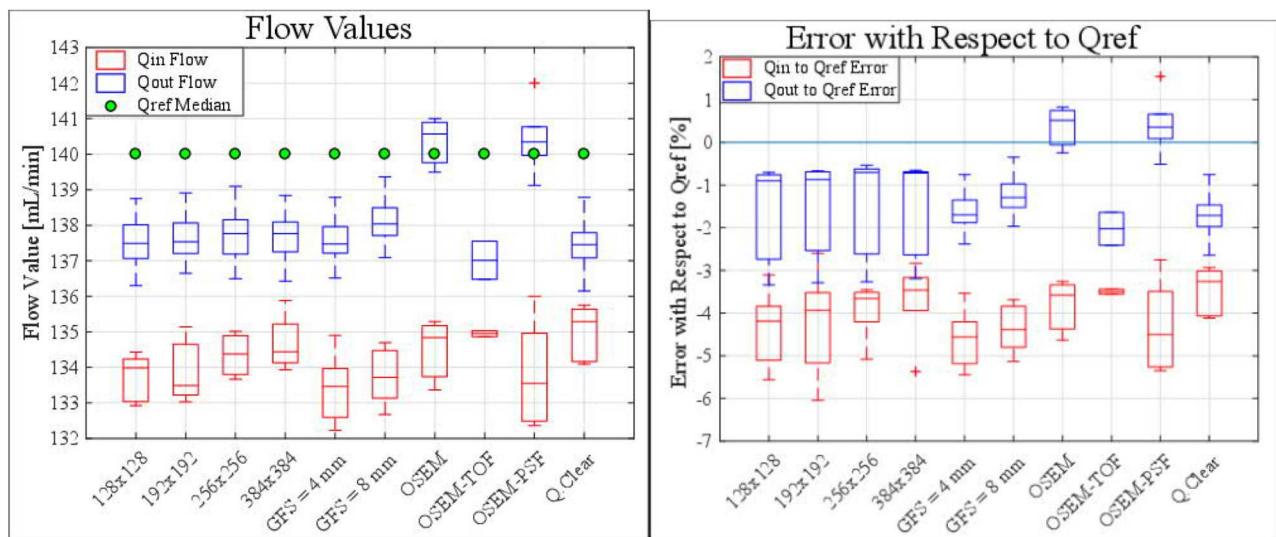


FIGURE 4 | Boxplots show the distribution and median of Q_{in} and Q_{out} (A) flow values and (B) errors with respect to Q_{ref} (reference flow) for all the subsequent reconstructions over all the measurements. The median value for the reference flow Q_{ref} for all reconstructions was measured as 140 mL/min.

reconstructions (Figure 2). As a consequence, their measured AUC values deviated from the other AUCs (Figure 3). When reconstructed with OSEM-TOF-PSF with different matrix sizes and GFS values, as well as with Q.Clear, the AUC values were similar. Moreover, as the SD of both the input and tissue TACs was similar over all reconstructions, the measurements showed good reproducibility. Visually, no differences in image noise between repeated measurements were seen.

Q_{in} and Q_{out} flow values were modeled based on the image-derived TACs. The kinetic modeling was conducted by using a two-compartmental model. Generally, smaller values were measured for Q_{in} compared to Q_{out}, systematically (Figure 4, Table 3). Also, Q_{in} showed more variability across repeated measurements for all reconstructions compared to Q_{out}. Q_{out} is determined from the exponential term (Equation 2), which corresponds to a clearance rate (k_2), making it less susceptible for variations in activity, as explained in the study of Kero et al. [10]. However, it should be noted that regardless of the measurement or the reconstruction parameter applied, the measured absolute relative errors were smaller than 7% for both Q_{in} and Q_{out} flow values with respect to the reference flow value (Figure 4B). This variation can be considered to be small in context of clinical practice, where a test-retest reproducibility of 16% is still considered acceptable [21]. This suggests that overall, the measurements were both accurate and reproducible despite the effect of reconstruction parameters and protocols. Reproducibility is also attributed to similar behavior of image corrections for all repeated measurements, careful and reproducible measurements and consistent orientation of the phantom.

In line with the AUC analysis, the modeled Q_{in} and Q_{out} flow values were higher when using OSEM and OSEM-PSF reconstructions compared to other reconstructions (Figure 4, Table 3). This produced a positive Q_{out} to Q_{ref} error compared

to other reconstructions (Figure 4B, Table 3). OSEM-PSF reconstruction produced the highest variation of Q_{in} with an SD of 1.52 mL/min (Table 3). Overall, the difference between Q_{in} and Q_{out} was similar between other reconstructions, while the OSEM and OSEM-PSF reconstructions showed opposite behavior between Q_{out} and Q_{in} values.

It seems that Q_{in} is affected more by the selected reconstruction parameters than Q_{out} and can be due to the fact that the modeled parameter Q_{in} is more sensitive by the slight variation of the TACs between measurements (Figure 4). Moreover, Q_{in} increases slightly with respect to the reconstruction matrix size (Figure 4, Table 3). In these cases, the Q_{in} errors with respect to Q_{ref} decrease as the reconstruction matrix sizes increase, while the Q_{out} error remain stable (Figure 4, Table 3). Applying a 4 and 8 mm GFS caused an error of similar magnitude but with less variability for both Q_{in} and Q_{out} when compared to the reconstructions with different matrix sizes. Overall, the matrix size or the applied filter does not seem to affect the wash-out flow Q_{out}, whereas the wash-in flow Q_{in} shows a dependency on both the matrix and filter size. However, this dependency can be assumed to be negligible.

With the Q.Clear reconstruction, Q_{in} and Q_{out} as well as their relative errors remain within the same range with OSEM-TOF-PSF reconstructions with different matrix sizes and GFS values as well as with OSEM-TOF. These results also follow to the measured AUC values. Ideally, both Q_{in} and Q_{out} should be equal to each other as well as to Q_{ref}. In this regard, using Q.Clear, the smallest difference between Q_{in} and Q_{out} values as well as Q_{in} and Q_{out} values of similar magnitude with respect to OSEM-TOF-PSF and OSEM-TOF reconstructions were produced. The difference between Q_{in} and Q_{out} flow is attributed by the characteristics of the reconstruction algorithm to handle the accurate activity recovery during both in the

presence of high activity in the early frames and during the increase of noise in later frames. In theory, an accurate image reconstruction algorithm should be able to minimize the bias between Q_{in} and Q_{out} . Naturally, the difference between Q_{in} or Q_{out} with respect to Q_{ref} is affected by the recovery of activity distribution measured with a PET system. In an ideal PET system and perfect measurement, both Q_{in} and Q_{out} would correspond to each other and Q_{ref} fully.

Concerning the effect of different reconstruction parameters to the image quality over the entire scan time in addition to the image-derived flow values, the results indicate that the image quality is stable over the entire dynamic scan, as the SD of the TACs over all the measurements is of similar magnitude for all reconstructions. In addition, the measurements indicate high repeatability, as the SD of the flow values over all the measurements is smaller than 1.6 mL/min for any reconstruction. Moreover, despite of the applied reconstruction parameters, a high accuracy of flow values was achieved, as the absolute relative error was smaller than 7% for any reconstruction and measurement. Overall, the differences were small in terms of AUCs and Q_{in} and Q_{out} flow values. The largest differences for Q_{in} and Q_{out} were in a range of 2% at maximum. This suggests that applied reconstruction parameters had little impact to the resulting flow values. Moreover, the magnitude of these variations can be considered to be small in the clinical context.

Comparison With Previous Studies

Previously, O'Doherty et al. [12] suggested applying a physical reference standard to determine the effects of different PET image reconstruction parameters in dynamic PET studies. We applied a dynamic flow phantom that provides accurate and precise flow measurements by two-compartmental kinetic modeling from image-derived TACs. In relation to the reference flow, the image-derived flow values were used for the analysis of effect of reconstructions over several reconstruction parameters. Moreover, previous evaluations on patients performed by both Kaufmann et al. [22] and Kero et al. [10] have shown that reproducible MBF with [^{15}O]H $_2$ O can be measured in patient studies as well. In that regard, our phantom study using [^{15}O]H $_2$ O complements such findings.

The results from the analysis of the effect of different reconstruction methods and their parameters are in line with the studies of Matheoud et al. [11] and Presotto et al. [7] who reported improved image quality and activity recovery in [^{18}F]FDG cardiac studies when iterative reconstruction OSEM with TOF and PSF was used. Our study showed that the TACs and thus AUCs remain uniform with reconstructions where both TOF and PSF were applied.

The results of this study show a difference in the AUCs between non-TOF and TOF reconstructions, which is explained by the faster convergence rate of TOF reconstruction compared to PET reconstruction in most objects [23–26]. Therefore, less iterations are needed to obtain the same contrast. Preferably, the amount of iterations in the non-TOF reconstruction should be increased to match better the convergence of TOF. However, in practice this is very hard to achieve due to object-dependent convergence in the OSEM reconstruction.

In addition, the difference in image-derived flow values in non-TOF and TOF reconstructions is also attributed by different noise characteristics of the reconstructed PET images and how well the two-compartmental model handles noise. The data in Kero et al. [10] shows that non-TOF reconstruction produces slightly higher MBF compared to TOF reconstruction. We also noted a similar effect between TOF and non-TOF algorithms. As shown in the study of Iida et al. [4], added noise in the input function will result in more positive bias and variance in the modeled flow value. The slightly higher Q_{out} value seen in non-TOF reconstruction is partly attributed by the lower SNR in the non-TOF reconstruction compared to the TOF reconstruction. Kero et al. [10] also discussed that MBF values are not affected by the additional filtering. The results of our study also show that the image-derived flow values are not considerably affected by the different GFS values.

The reproducibility of MBF values has been recently compared between a PET/CT Discovery STE system (GE Healthcare, Milwaukee, US) and a PET/MR Signa system (GE Healthcare, Milwaukee, US) in the study of Kero et al. [10]. The authors reported no difference on MBF when using TOF or altering filter or reconstruction settings in the PET-MR. This is in line with our study, as the difference between Q_{in} and Q_{out} values with respect to Q_{ref} between non-TOF and TOF reconstructions was only 2% at maximum. They also reported an average MBF of 2.74 ± 1.37 on PET/CT stress and average MBF of 2.65 ± 1.15 on PET/MR stress studies. The average difference in the Q_{in} and Q_{out} measurements between different reconstructions are of similar magnitude in our study (Table 3).

Finally, the results from the analysis of Q.Clear reconstructions are in line with the study of O'Doherty et al. [12]. They reported that the Q.Clear noise level is correspondent to the OSEM reconstruction when the value of $\beta = 300$ was used. In our study, the Q.Clear AUC values are in relation with the OSEM-TOF-PSF reconstructions that apply different matrix sizes and GFS values as well as with OSEM-TOF reconstruction when the default value of $\beta = 350$ was used. The minor difference in the β value might be due to different PET/CT systems applied in our study versus the study in [12]. Similarly, O'Doherty et al. [12] showed that the Q.Clear effect to the quantification of MBF is minor, as can also be seen from our study as the image-derived flow values were similar with the Q.Clear reconstruction compared to other reconstructions.

Limitations and Future Considerations

In this study, a novel flow phantom was used. Some fluctuations in the phantom appear between the repetitive measurements due to the [^{15}O]H $_2$ O injections in the system, as can be seen from the reference flow over repeated measurements (140, 140, 139, 142, and 139 mL/min). However, this fluctuation is very small, as it is 3 mL/min at maximum. In an ideal system, the image-derived flow values Q_{in} and Q_{out} should be fully equal to each other, and fully equal to the reference flow Q_{ref} value. In this phantom set-up, we detected a maximum difference of 6 mL/min between Q_{in} and Q_{out} and maximum difference of 9 mL/min between Q_{in} , Q_{out} and Q_{ref} . This fluctuation can be considered small as well.

The relation between clinically used MBF values and the phantom flow values can be regarded to the rate parameters derived from the two-compartmental model as discussed in Gabrani-Juma et al. [16]. As the K_1 and k_2 derived from the clinical two-compartmental model are analogous to the q_{in} and q_{out} derived from the two-compartmental model of the phantom, the behavior of Q_{in} and Q_{out} values can be related to correspond to the behavior of MBF in similar circumstances. However, as the phantom does not fully represent the physiology of blood perfusion in myocardial tissue, the correspondence to MBF should be further investigated in the future. The phantom lacks of background activity, as the only source of activity in the shell is coming from the input chamber and exchange cylinder. Thus, addition of background activity and its effect to the flow quantification accuracy could be studied further in the future. Nevertheless, we have shown that the flow phantom offers a feasible solution for simulation and the modeling of the kinetics in myocardial perfusion imaging with PET and provides a physical reference standard to investigate the effect of different reconstruction methods in a reproducible manner.

This study was also limited by conducting the measurements with only one PET/CT system. Also, it was not possible to assess filtered back projection (FBP) algorithm, as it is not implemented on the Discovery MI. The system also implements only one iterative reconstruction algorithm (OSEM). In addition, the analysis was conducted using a single software specifically designed for flow quantification on the phantom. Thus, the results of this study serve as a baseline for the current status in flow quantification when using different reconstruction parameters on the Discovery MI PET/CT system. The methodologies presented here can be further used to study the reproducibility of flow values among different PET/CT systems, or to implement harmonization and optimization protocols in the future.

Accordingly, the presented methodology with the achieved results could be applied as a basis for harmonizing the reconstruction parameters for MPI studies with $[^{15}\text{O}]\text{H}_2\text{O}$ and other radiotracers as well. However, the optimization of the reconstruction parameters with different combinations, including other radiotracers, should be conducted as an extension of the current study. Optimally, the reconstruction methods should be fixed in terms of parameters to avoid systematic errors and to increase reproducibility. In the future, the reconstruction parameters should be harmonized between several PET/CT systems to improve both the accuracy and precision in the MBF quantification further.

REFERENCES

- Juneau D, Erthal F, Ohira H, Mc Ardle B, Hessian R, deKemp RA, et al. Clinical PET myocardial perfusion imaging and flow quantification. *Cardiol Clin.* (2016) 34:69–85. doi: 10.1016/j.ccl.2015.07.013
- Moody JB, Lee BC, Corbett JR, Ficaro EP, Murthy VL. Precision and accuracy of clinical quantification of myocardial blood flow by dynamic PET: a technical perspective. *J Nucl Cardiol.* (2015) 22:935–51. doi: 10.1007/s12350-015-0100-0
- Iida H, Rhodes CG, Desilva R, Yamamoto Y, Araujo LI, Maseri A, et al. Myocardial tissue fraction - correction for partial volume effects and measure of tissue viability. *J Nucl Med.* (1991) 32:2169–75.
- Iida H, Rhodes CG, de Silva R, Araujo LI, Bloomfield PM, Lammertsma AA, et al. Use of the left ventricular time-activity curve as a noninvasive input function in dynamic oxygen-15-water positron emission tomography. *J Nucl Med.* (1992) 33:1669–77.
- DeGrado TR, Bergmann SR, Ng CK, Raffel DM. Tracer kinetic modeling in nuclear cardiology. *J Nucl Cardiol.* (2000) 7:686–700. doi: 10.1067/mnc.2000.111127

CONCLUSIONS

The effect of different matrix size, Gaussian filter size, TOF and/or PSF as well as Q.Clear reconstruction to image-derived flow values was small. Overall, different reconstruction settings had little impact to the resulting flow values with Discovery MI PET/CT using $[^{15}\text{O}]\text{H}_2\text{O}$. The modeled flow values showed a variation with a SD of less than 2 mL/min as well as absolute relative errors of <7% between subsequent measurements. The differences in measured flow values between reconstruction algorithms were 2% of maximum. In conclusion, the reconstruction algorithms evaluated can be applied in MPI studies for accurate flow quantification.

DATA AVAILABILITY STATEMENT

The datasets generated for this study are available on request to the corresponding author.

AUTHOR CONTRIBUTIONS

RS and JT conceived and designed the study. RS wrote the manuscript with support from JT. RS, JT, and AK carried out the experiments and KK contributed in assisting RS and JT constructing the phantom and collecting the data. NS and AF contributed in the design of the study, evaluation and writing of the manuscript. AS and MT supervised the findings of the work and the project. All authors contributed to the consultation of the results and writing the final manuscript.

FUNDING

This project (15HLT05 PerfusImaging) has received funding from the EMPIR programme co-financed by the Participating States and from the European Union's Horizon 2020 research and innovation programme. This study was funded by the Academy of Finland (grant number 314483, project MINMOTION).

ACKNOWLEDGMENTS

Shelley Medical Imaging Technologies are acknowledged for their assistance with this study. The study was conducted within the Finnish Center of Excellence in Molecular Imaging in Cardiovascular and Metabolic Research supported by the Academy of Finland, University of Turku, Turku University Hospital, and Åbo Akademi University.

6. Søndergaard HM, Madsen MM, Boisen K, Böttcher M, Schmitz O, Nielsen TT, et al. Evaluation of iterative reconstruction (OSEM) versus filtered back-projection for the assessment of myocardial glucose uptake and myocardial perfusion using dynamic PET. *Eur J Nucl Med Mol Imaging*. (2007) 34:320–9. doi: 10.1007/s00259-006-0198-z
7. Presotto L, Gianolli L, Gilardi MC, Bettinardi V. Evaluation of image reconstruction algorithms encompassing time-Of-Flight and point spread function modelling for quantitative cardiac PET: phantom studies. *J Nucl Cardiol*. (2015) 22:351–63. doi: 10.1007/s12350-014-0023-1
8. Le Meunier L, Slomka PJ, Dey D, Ramesh A, Thomson LEJ, Hayes SW, et al. Enhanced definition PET for cardiac imaging. *J Nucl Cardiol*. (2010) 17:414–26. doi: 10.1007/s12350-010-9193-7
9. Teoh EJ, McGowan DR, Macpherson RE, Bradley KM, Gleeson F V. Phantom and clinical evaluation of the bayesian penalized likelihood reconstruction algorithm q.Clear on an IYSO PET/CT system. *J Nucl Med*. (2015) 56:1447–52. doi: 10.2967/jnumed.115.159301
10. Kero T, Nordström J, Harms HJ, Sörensen J, Ahlström H, Lubberink M. Quantitative myocardial blood flow imaging with integrated time-of-flight PET-MR. *EJNMMI Phys*. (2017) 4:1–13. doi: 10.1186/s40658-016-0171-2
11. Matheoud R, Lecchi M, Lizio D, Scabbio C, Marcassa C, Leva L, et al. Erratum to: comparative analysis of iterative reconstruction algorithms with resolution recovery and time of flight modeling for 18F-FDG cardiac PET: a multicenter phantom study (J Nucl Cardiol, 10.1007/s12350-015-0385-Z). *J Nucl Cardiol*. (2017) 24:1101. doi: 10.1007/s12350-016-0415-5
12. O' Doherty J, McGowan DR, Abreu C, Barrington S. Effect of bayesian-penalized likelihood reconstruction on [13N]-NH3 rest perfusion quantification. *J Nucl Cardiol*. (2017) 24:1457. doi: 10.1007/s12350-017-0892-1
13. Aide N, Lasnon C, Veit-Haibach P, Sera T, Sattler B, Boellaard R. EANM/EARL harmonization strategies in PET quantification: from daily practice to multicentre oncological studies. *Eur J Nucl Med Mol Imaging*. (2017) 44:17–31. doi: 10.1007/s00259-017-3740-2
14. Ferretti A, Chondrogiannis S, Rampin L, Bellan E, Marzola MC, Grassetto G, et al. How to harmonize sUVs obtained by hybrid PET/CT scanners with and without point spread function correction. *Phys Med Biol*. (2018) 63:aee27. doi: 10.1088/1361-6560/aee27
15. Mananga ES, El Fakhri G, Schaefferkoetter J, Bonab AA, Ouyang J. Myocardial defect detection using PET-CT: phantom studies. *PLoS ONE*. (2014) 9:e88200. doi: 10.1371/journal.pone.0088200
16. Gabrani-Juma H, Clarkin OJ, Pourmoghaddas A, Driscoll B, Wells RG, Dekemp RA, et al. Validation of a multimodality flow phantom and its application for assessment of dynamic sPECT and PET technologies. *IEEE Trans Med Imaging*. (2017) 36:132–41. doi: 10.1109/TMI.2016.2599779
17. Driscoll B, Keller H, Jaffray D, Coolens C. Development of a dynamic quality assurance testing protocol for multisite clinical trial dCE-CT accreditation. *Med Phys*. (2013) 40:8. doi: 10.1118/1.4812429
18. Hsu DFC, Ilan E, Peterson WT, Uribe J, Lubberink M, Levin CS. Studies of a next-Generation silicon-Photomultiplier-Based time-of-Flight PET/CT system. *J Nucl Med*. (2017) 58:1511–8. doi: 10.2967/jnumed.117.189514
19. Boellaard R. Standards for PET image acquisition and quantitative data analysis. *J Nucl Med*. (2009) 50:11S–20S. doi: 10.2967/jnumed.108.057182
20. Maaniitty T, Stenström I, Bax JJ, Uusitalo V, Ukkonen H, Kajander S, et al. Prognostic value of coronary CT angiography with selective PET perfusion imaging in coronary artery disease. *JACC Cardiovasc Imaging*. (2017) 10:1361–70. doi: 10.1016/j.jcmg.2016.10.025
21. El Fakhri G, Kardan A, Sitek A, Dorbala S, Abi-Hatem N, Lahoud Y, et al. Reproducibility and accuracy of quantitative myocardial blood flow assessment with 82Rb PET: comparison with 13N-ammonia PET. *J Nucl Med*. (2009) 50:1062–71. doi: 10.2967/jnumed.104.007831
22. Kaufmann PA, Gnecci-Ruscione T, Yap JT, Rimoldi O, Camici PG. Assessment of the reproducibility of baseline and hyperemic myocardial blood flow measurements with 15O-labeled water and PET. *J Nucl Med*. (1999) 40:1848–56.
23. Surti S, Karp JS, Popescu LM, Daube-Witherspoon ME, Werner M. Investigation of time-of-flight benefit for fully 3-D PET. *IEEE Trans Med Imaging*. (2006) 25:529–38. doi: 10.1109/TMI.2006.871419
24. Karp JS, Surti S, Daube-Witherspoon ME, Muehllehner G. Benefit of time-of-flight in PET: experimental and clinical results. *J Nucl Med*. (2008) 49:462–70. doi: 10.2967/jnumed.107.044834
25. Surti S. Update on time-of-flight PET imaging. *J Nucl Med*. (2015) 56:98–105. doi: 10.2967/jnumed.114.145029
26. Vandenberghe S, Mikhaylova E, D'Hoe E, Mollet P, Karp JS. Recent developments in time-of-flight PET. *EJNMMI Phys*. (2016) 3:1. doi: 10.1186/s40658-016-0138-3

Conflict of Interest: The authors declare that the research was conducted in the absence of any commercial or financial relationships that could be construed as a potential conflict of interest.

Copyright © 2020 Siekkinen, Teuho, Smith, Fenwick, Kirjavainen, Koskensalo, Saraste and Teräs. This is an open-access article distributed under the terms of the Creative Commons Attribution License (CC BY). The use, distribution or reproduction in other forums is permitted, provided the original author(s) and the copyright owner(s) are credited and that the original publication in this journal is cited, in accordance with accepted academic practice. No use, distribution or reproduction is permitted which does not comply with these terms.



Bayesian Estimation of the ntPET Model in Single-Scan Competition PET Studies

Zacharie Irace^{1,2*}, Inés Mérida¹, Jérôme Redouté¹, Clara Fonteneau^{3,4,5}, Marie-Françoise Suaud-Chagny^{3,4,5}, Jérôme Brunelin^{3,4,5}, Benjamin Vidal⁴, Luc Zimmer^{1,4,6}, Anthonin Reilhac⁷ and Nicolas Costes¹

¹ CERMEP-Life Imaging, Lyon, France, ² SIEMENS Healthcare SAS, Saint Denis, France, ³ INSERM U1028, CNRS UMR5292, Lyon Neuroscience Research Center, Psychiatric Disorders: from Resistance to Response Team, Lyon, France, ⁴ Université Claude Bernard Lyon 1, Lyon, France, ⁵ Centre Hospitalier Le Vinatier, Lyon, France, ⁶ Hospices Civils de Lyon, Lyon, France, ⁷ Clinical Imaging Research Centre, National University of Singapore, Singapore, Singapore

OPEN ACCESS

Edited by:

Michel Koole,
KU Leuven, Belgium

Reviewed by:

Jenny Ceccarini,
KU Leuven, Belgium
David Váñez García,
University Medical Center
Groningen, Netherlands

*Correspondence:

Zacharie Irace
irace@cermep.fr

Specialty section:

This article was submitted to
Medical Physics and Imaging,
a section of the journal
Frontiers in Physiology

Received: 31 October 2019

Accepted: 23 April 2020

Published: 19 May 2020

Citation:

Irace Z, Mérida I, Redouté J, Fonteneau C, Suaud-Chagny M-F, Brunelin J, Vidal B, Zimmer L, Reilhac A and Costes N (2020) Bayesian Estimation of the ntPET Model in Single-Scan Competition PET Studies. *Front. Physiol.* 11:498. doi: 10.3389/fphys.2020.00498

This paper proposes an innovative method, named b-ntPET, for solving a competition model in PET. The model is built upon the state-of-the-art method called lp-ntPET. It consists in identifying the parameters of the PET kinetic model relative to a reference region that rule the steady state exchanges, together with the identification of four additional parameters defining a displacement curve caused by an endogenous neurotransmitter discharge, or by a competing injected drug targeting the same receptors as the PET tracer. The resolution process of lp-ntPET is however suboptimal due to the use of discretized basis functions, and is very sensitive to noise, limiting its sensitivity and accuracy. Contrary to the original method, our proposed resolution approach first estimates the probability distribution of the unknown parameters using Markov-Chain Monte-Carlo sampling, distributions from which the estimates are then inferred. In addition, and for increased robustness, the noise level is jointly estimated with the parameters of the model. Finally, the resolution is formulated in a Bayesian framework, allowing the introduction of prior knowledge on the parameters to guide the estimation process toward realistic solutions. The performance of our method was first assessed and compared head-to-head with the reference method lp-ntPET using well-controlled realistic simulated data. The results showed that the b-ntPET method is substantially more robust to noise and much more sensitive and accurate than lp-ntPET. We then applied the model to experimental animal data acquired in pharmacological challenge studies and human data with endogenous releases induced by transcranial direct current stimulation. In the drug challenge experiment on cats using [¹⁸F]MPPF, a serotonergic 1A antagonist radioligand, b-ntPET measured a dose response associated with the amount of the challenged injected concurrent 5-HT1A agonist, where lp-ntPET failed. In human [¹¹C]raclopride experiment, contrary to lp-ntPET, b-ntPET successfully detected significant endogenous dopamine releases induced by the stimulation. In conclusion, our

results showed that the proposed method b-ntPET has similar performance to lp-ntPET for detecting displacements, but with higher resistance to noise and better robustness to various experimental contexts. These improvements lead to the possibility of detecting and characterizing dynamic drug occupancy from a single PET scan more efficiently.

Keywords: brain imaging, PET, kinetic modeling, competition model, endogenous neurotransmitter release, lp-ntPET, Bayesian inference

1. INTRODUCTION

Positron emission tomography (PET) is a functional 3D *in vivo* imaging technique that allows to visualize and quantify with a very high sensitivity the local concentration of an injected radiotracer molecule. In neuroimaging, PET allows the investigation of key aspects of neurotransmission systems and provides important measurements such as the concentrations in presynaptic transporters and postsynaptic receptors in living human brains. PET data acquired dynamically are commonly analyzed using reference region models (Lammertsma and Hume, 1996; Lammertsma et al., 1996; Gunn et al., 1997) that are built on the assumption that the system under investigation is in steady state regime. In 1995, both Fisher et al. (1995) and Morris et al. (1995) advanced the possibility to use PET to detect dynamic changes in receptor binding or receptor occupancy occurring during activation studies. Their theory relied on the hypothesis that a cognitive task increases the firing rate of the involved neurons, leading to a release of endogenous neurotransmitter in the synaptic level with a measurable effect on the PET kinetics. This idea was then extended to using PET to reveal transient alterations caused by endogenous or exogenous competing binding compounds, as long as the PET tracer fulfills the pharmacokinetic characteristics set forth in Morris et al. (1995). However, the conventional reference region models are invalid in non-steady state conditions as they assume that the parameters to be estimated remain constant over the duration of the study. Consequently, one of the challenges for PET neuroimaging experiments became the design of robust and reliable kinetic analysis approaches with an integrated competition model to account for transient changes in kinetic binding and receptor occupancy in both low and high target density regions.

Several kinetic theories have been developed for non steady-state systems and related resolution methods have been designed to detect and characterize changes in ligand binding during a single PET scan. Alpert et al. (2003) proposed a linear extension of the reference region models, named LSSRM, that includes a time-varying efflux rate terms. The LSSRM model allows the statistical detection of a change in tracer binding, but it does not characterize the modulation. In fact, it assumes that competing endogenous releases or drug effects are instantaneous, maximal at time of stimulation and decay exponentially to baseline thereafter. Any violations of these assumptions might result in decreased sensitivity and specificity. Several kinetic models and associated resolution methods, collectively referred to as “ntPET” for neurotransmitter PET, with less stringent

assumptions have then been proposed (Morris et al., 2005; Constantinescu et al., 2007; Normandin and Morris, 2008; Normandin et al., 2012). Among these methods, Normandin et al. (2012) proposed a linear parametric ntPET (lp-ntPET) as an extension of the LSSRM model that uses gamma variate functions spanning a wide range of feasible shapes, times of onset and duration to characterize the time course of the competing compound. While LSSRM uses three parameters to describe the neurotransmitter release (in addition to three parameters describing the transport of the tracer through the brain to blood barrier, and its binding at equilibrium), the lp-ntPET model uses four for the release characterization (seven in total). Normandin et al. proposed to handle the estimation of the non-linear parameters by discretizing them and employing a predefined library of basis functions. The other parameters are resolved using Weighted Least Squares (WLS) or Non-Negative Least Squares (NNLS) optimization.

Several issues are associated with this resolution approach. First, the use of basis functions leads to a poor accuracy of parameter estimation due to their discretization. In addition, the quality of fit and accuracy of solutions greatly depends on the choice of the basis function (Liu and Morris, 2019). This dependency can result in a moderate sensitivity and an uncertain specificity for the detection of the transient change, and a loss of accuracy for its characterization. Moreover, the lp-ntPET model is over-determined, i.e., different sets of parameters may produce similar response curves. In such context, the least squares-based approaches that are used in the lp-ntPET method to estimate the linear parameters may lead to a lack of reproducibility. Finally, the least squares method is known to be highly sensitive to noise and the classic approach may be unreliable in real applications where high levels of noise are not unusual, especially in small Regions Of Interest (ROIs). An alternative method that does not rely on basis functions is described in Fan et al. (2016), who proposed an estimation method based on Approximate Bayesian Computing (ABC). Their investigations on simplistic simulated data are encouraging but did not lead to conclusive results for real studies.

In this work, we introduce a novel resolution method for ntPET models, called b-ntPET, whereby the parameter estimation relies on a Markov-Chain Monte-Carlo (MCMC) sampling in a Bayesian framework. The presented methodology assesses the probability distribution of the unknown parameters, and consequently allows the quantification of the uncertainty of the parameter estimates. Moreover, we hypothesized that the integration of a priori information on the model parameters, as allowed in this Bayesian framework, will tackle the identifiability

problem by reducing the set of eligible solutions. Finally, we proposed to jointly estimate the noise level with the parameters of the model, for increased robustness. We validated our b-ntPET method and compared its performance against the reference lp-ntPET approach using realistic simulated datasets as well as preclinical and clinical data.

2. METHODS

2.1. Modeling Tracer Competition

In the Simplified Reference Tissue Model (SRTM) (Lammertsma et al., 1996), the kinetic $C_T(t)$ of a target region is defined relative to the kinetic $C_R(t)$ of a reference region.

$$C_T(t) = R_1 C_R(t) + k_2 \int_0^t C_R(u) du - k_{2a} \int_0^t C_T(u) du \quad (1)$$

Where $R_1 = K_{1a}/K_1$ is the local rate of delivery in the target tissue relative to the reference tissue, k_2 is the transfer rate constant from tissue to blood in the reference region, and k_{2a} is the transfer rate constant from tissue to blood in the target region. Alpert et al. (2003) generalized this model by considering a time-varying efflux rate $k_{2a}(t)$ that reflects the competition between the radioligand and the endogenous neurotransmitter at the receptor sites:

$$k_{2a}(t) = k_{2a} + \gamma \cdot h(t) \quad (2)$$

where γ represents the magnitude of transient effects and the function $h(t)$ characterizes the endogenous neurotransmitter discharge or an exogenous concurrent drug concentration level (Figure 1).

This leads to the following operational equation to model the time-activity curve (TAC) $C_T(t)$ of a tissue of interest:

$$C_T(t) = R_1 C_R(t) + k_2 \int_0^t C_R(u) du - k_{2a} \int_0^t C_T(u) du - \gamma \int_0^t C_t(u) h(u) du \quad (3)$$

With regard to the choice of $h(t)$, the exponential function initially proposed in LSSRM (Alpert et al., 2003) has been extended by Normandin et al. (2012) to:

$$h(t) = \begin{cases} \left(\frac{t-t_D}{t_p-t_D} \right)^\alpha \exp \left(\alpha \left[1 - \frac{t-t_D}{t_p-t_D} \right] \right), & \forall t \geq t_D. \\ 0, & \forall t \leq t_D. \end{cases} \quad (4)$$

This model is driven by seven parameters among which four allow to fully characterize the discharge by expressing its magnitude (γ), the time at which it begins (t_D), the time at its peak (t_p) and its global sharpness (α). The combination of these quadruplets results in a set of possible response functions. It is worth noting that the model is over-determined and various combinations of these parameters can result in producing similar shapes of the release. This results in an identifiability issue that may disturb the robustness and the reproducibility of the estimation methods, especially in the presence of high noise.

In the original method from Normandin et al. (2012), the linear coefficients (R_1, k_2, k_{2a}, γ) were estimated with a weighted least-squares method. Since the other parameters (t_D, t_p, α) are non-linear, optimal (R_1, k_2, k_{2a}, γ)_i were estimated for each $h_i(t)$ from a set of basis functions driven by the parameters (t_D, t_p, α)_i. The combination of these three parameters that lead to the best fitting of the measurements determined the best $h_i(t)$ and its associated (R_1, k_2, k_{2a}, γ)_i parameters.

2.2. Overview of the Proposed Estimation Method

The method aims at estimating the parameters driving the tracer displacement model defined by Equations (3) and (4). In the Bayesian paradigm, the parameters to be estimated are no longer considered fixed quantities but random variables on which prior knowledge can be applied. The proposed approach estimates the probability distribution of the parameters given the measurements, also called posterior probability, as an intermediate step. This new paradigm brings more flexibility toward noise and allows to quantify the uncertainty of the estimations. Figure 2 sums up the whole estimation process.

First, the posterior has to be defined by setting a hierarchical Bayesian model. The Bayesian model takes into account the model of the noise (likelihood) and the amount of prior information we may have on the unknown parameters. Due to the complexity of the posterior distribution, its explicit expression is unknown. In this work, we propose to estimate the posterior probability using a sampling technique (Robert and Casella, 1999). This approach draws a relevant amount of samples that are asymptotically distributed according to the posterior distribution. From these estimated probability distributions, Bayesian inference is made to determine the final value of each parameter. The steps of the method are described in the subsections below.

2.3. Hierarchical Bayesian Model

After reparameterization $\Delta_t = t_p - t_D$ for convenience, let us define $\Theta = \{\theta_k\}_{k=1...7} = (R_1, k_2, k_{2a}, \gamma, t_D, \Delta_t, \alpha)$ the set of unknown parameters and $Y = (y_1, \dots, y_N)$ the measured Time Activity Curve (TAC), where y_n is the measured activity at frame n . In that study, the variance of the noise ω^2 is also considered unknown and will be jointly estimated with the model parameters Θ . We want to estimate the joint probability $p(\Theta, \omega^2 | Y)$ of the parameters Θ and the noise level ω^2 given the measurements Y . The Bayes rule states that:

$$p(\Theta, \omega^2 | Y) \propto p(Y | \Theta, \omega^2) \cdot \pi(\Theta) \cdot \pi(\omega^2) \quad (5)$$

Where $p(\Theta, \omega^2 | Y)$ is called the *posterior* distribution, \propto means *proportional to*, $p(Y | \Theta, \omega^2)$ is called the *likelihood* and corresponds to the noise model, $\pi(\Theta)$ is the *prior* that reflects the knowledge we may have on the model parameters and $\pi(\omega^2)$ is the *prior* on the variance of the noise. The likelihood and both priors on the model parameters and on the noise level are defined in the subsections below.

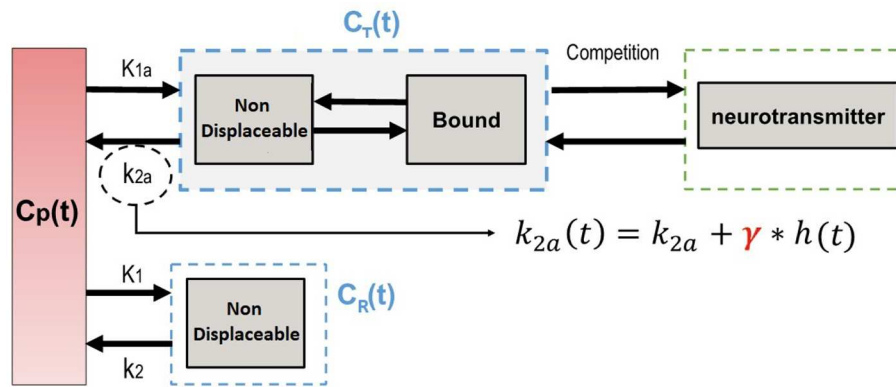


FIGURE 1 | Compartment model illustrating a competition model.

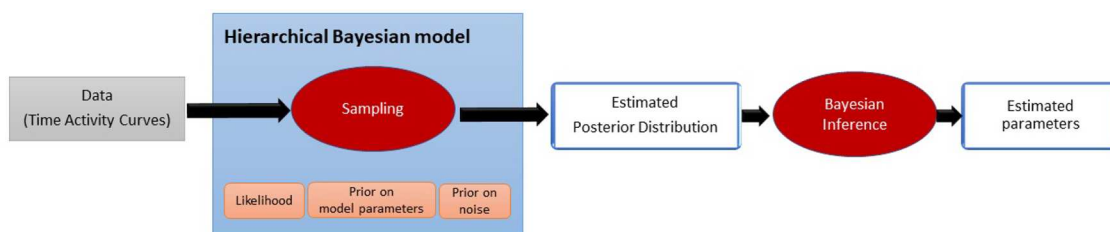


FIGURE 2 | Pipeline illustrating the proposed estimation process. The estimation of the posterior distribution is an intermediate step before estimating the final value of the parameters.

2.3.1. Likelihood

We assume that the noise at each frame is independent from the noise of the other frames. The likelihood can then be factorized as:

$$p(Y|\Theta, \omega^2) = \prod_{n=1}^N p(y_n|\Theta, \omega^2) \quad (6)$$

with y_n the measured value at frame n of the dynamic PET image. The likelihood at each frame $p(y_n|\Theta, \omega^2)$ is considered normally distributed around the value expected by the model at the middle of the frame $\Theta(n)$ and with the variance ω_n^2 :

$$y_n|\Theta, \omega^2 \sim \mathcal{N}(\Theta(n), \omega_n^2) \quad (7)$$

The variance ω_n^2 corresponds to the noise level of each frame. The noise levels vary from one frame to another, but can be linked considering the popular weighting factors used to model the noise, such as the activity $\Theta(n)$ itself, the decay factor t_n and the frame duration d_n according to the following formula:

$$\omega_n^2 = \omega^2 \frac{\Theta(n)}{t_n \cdot d_n}. \quad (8)$$

The value ω^2 corresponds to a noise level that is representative of the whole TAC and is estimated by the algorithm jointly with the parameters of the model.

2.3.2. Prior Definition

2.3.2.1. Prior on the Model Parameters

Assuming that the model parameters are independent, the joint prior distribution of the vector Θ is:

$$\pi(\Theta) = \prod_{k=1}^7 \pi(\theta_k) = \pi(R_1) \cdot \pi(k_2) \cdot \pi(k_{2a}) \cdot \pi(\gamma) \cdot \pi(t_D) \cdot \pi(\Delta_t) \cdot \pi(\alpha) \quad (9)$$

The choice of prior distributions can be based on prior information obtained from preliminary studies or on other known information from the protocol design. The more realistic the prior distributions, the more accurate the solution. While more attention should be paid to the design of the priors for optimal results, in this work, we deliberately chose non-informative priors on the model parameters, so the quality of the results can be credited to the resolution approach only and not to overly helping prior information. To this end, we used a uniform prior distribution $\pi(\theta_k)$ for each parameter, with intervals largely covering its plausible value range:

$$\theta_k \sim \mathcal{U}(\theta_k^{\min}, \theta_k^{\max}) \quad (10)$$

2.3.2.2. Prior on the noise variance

The prior on the noise variance $\pi(\omega^2)$ is chosen as an inverse-gamma distribution with hyper-parameters a_0 and b_0 .

$$\omega^2 \sim \Gamma^{-1}(a_0, b_0) \quad (11)$$

This choice is motivated by the fact that the inverse-gamma distribution is a conjugate prior of the variance for the normal distribution (see next section). The inverse-gamma distribution also ensures that ω^2 is positive.

The values of a_0 and b_0 depict the a priori information we may have on the variance of the noise. In our case, they are chosen so that $\pi(\omega^2)$ is centered on an empirical estimation of the variance of the TAC and the variance (the variance of ω^2 itself) is set to a very large value so that prior assumption on ω^2 are non-informative.

2.4. Sampling

The posterior distribution defined in (5) is too complex to be expressed in closed-form and deriving explicit solutions is intractable. We propose to estimate the posterior distribution using Monte-Carlo sampling in the parameter space. The idea is to draw a sufficient amount of samples that are asymptotically distributed according to the posterior distribution, also called target distribution. More precisely, a hybrid Metropolis-within-Gibbs sampler has been implemented, where the step size of each chain is adjusted to ensure an optimal mixing behavior.

2.4.1. Gibbs

The target distribution $p(\Theta, \omega^2 | Y)$ is defined in an 8-dimensional space. Sampling the whole random vector Θ directly is challenging because of the anisotropic nature of the parameter space (the individual parameters behave in very different ways). The Gibbs sampler considers a random vector as a set of individual random variables. It allows to draw samples of each variable separately according to their univariate posterior conditional distribution $p(\theta_k | Y, \omega^2, \Theta_{-k})$ for each θ_k , where Θ_{-k} is Θ without θ_k , and $p(\omega^2 | Y, \Theta)$ for ω^2 . By sampling iteratively each parameter at a time according to its associated posterior conditional distribution, the Gibbs algorithm defines a Markov Chain whose stationary distribution is the target distribution $p(\Theta, \omega^2 | Y)$. The parameters θ_k are sampled according to their posterior conditional using a Metropolis-Hastings process (see next section), leading to a so-called Metropolis-within-Gibbs algorithm (see Robert and Casella, 1999 for more details).

2.4.2. Metropolis-Hastings for the Model Parameters

The Random Walk Metropolis-Hastings (RWMH) is one of the most common MCMC algorithms. The idea is to draw a sequence of random samples, where the value of each sample is obtained relatively to the value of the previous one. More precisely, given the value of the j th sample θ_k^j , a new sample θ_k^* is proposed according to the following law of motion: $\theta_k^* = \theta_k^j + \epsilon_k \cdot w^j$, where w^j denotes a Brownian motion and ϵ_k is a scaling factor. In order that the sequence of samples are distributed according to the target density, the proposed sample θ_k^* is accepted or rejected with probability $\min\left(1, \frac{p(\theta_k^* | Y, \Theta_{-k}, \omega^2)}{p(\theta_k^j | Y, \Theta_{-k}, \omega^2)}\right)$. If the proposed sample

θ_k^* is accepted, the value of the new sample is set to $\theta_k^{j+1} = \theta_k^*$, if it is rejected, the value of the new sample stays the same $\theta_k^{j+1} = \theta_k^j$. An efficient mixing of the target distribution requires

that the acceptance rate is close to $\frac{1}{2}$. The step size ϵ_k must be chosen accordingly.

The posterior conditional distribution for each model parameter θ_k is $p(\theta_k | Y, \Theta_{-k}, \omega^2) \propto p(Y | \Theta, \omega^2) \pi(\theta_k)$ where one recognizes the likelihood and the prior on θ_k defined in (6) and (10), respectively.

2.4.3. Direct Sampling for the Noise Variance

The posterior conditional associated to the variance is $p(\omega^2 | Y, \Theta) \propto p(Y | \Theta, \omega^2) \pi(\omega^2)$. Here, we take advantage of the fact that the noise is assumed to be normally distributed and that the inverse-gamma distribution is a conjugate prior of the variance for the normal distribution. More precisely, by choosing $\pi(\omega^2)$ as an inverse-gamma distribution with hyper parameters a_0 and b_0 , we know that $p(\omega^2 | Y, \Theta)$ is also an inverse-gamma distribution with parameters $a = a_0 + \frac{N}{2}$ and $b = b_0 + \frac{1}{2} \sum_{n=1}^N (y_n - \Theta(n))^2$. With a closed-form expression for the conditional posterior, it is then possible to draw samples for ω^2 using direct sampling instead of an acceptance-rejection scheme. Note that ω^2 is sampled and not ω .

2.4.4. Step Size Calibration

To avoid difficulties due to anisotropy of the parameter space, each parameter has an adapted step size ϵ_k . The choice of the step size ϵ_k has a direct impact on the efficiency of the sampling process. A large ϵ leads to a high rejection rate, and a low value provides highly correlated samples. In both cases, the algorithm would be characterized by excessively slow mixing. In the proposed method, the optimal values of ϵ_k are estimated empirically during a first phase called burn-in so the acceptance rate of the proposed samples reaches $\frac{1}{2}$. Samples drawn during the burn-in period are then withdrawn.

2.5. Bayesian Inference

The estimated posterior distribution is a result in itself, it can be exploited to perform model selection, to find if one or several modes pop up from the whole distribution, and allows to evaluate the degree of trust we may attribute to a detection. When it comes to extract the final value of the parameters from this distribution, one must perform inference and look for a suitable estimator.

Popular estimators are the Minimum Mean Square Error (MMSE) and the Maximum a Posteriori (MAP). MMSE corresponds to the expectancy of the distribution (or the mean of the samples). It is very robust but may be inappropriate if the posterior distribution is asymmetrical, has several modes, or when the model suffers from identifiability issues. MAP corresponds to the drawn sample whose posterior probability is the highest. However, the MAP estimator lacks accuracy and reproducibility when the MCMC samples are sparse in the parameter space.

In this work, we propose to resort to a mode-seeking algorithm to find the main mode of the target distribution. More precisely, we are looking for the Highest Posterior Density (HPD) region. HPD consists in localizing the smallest region containing a given percentage of the drawn samples. Once the interval has been found, we perform MMSE on the subset of the samples in that region to get the optimal values for each parameter. Since

computing HPD on the multivariate distribution is very time consuming, and may be altered by the sparsity of the samples in a 8D space, we perform univariate HPD on the marginal distributions of each parameter. In this work, we looked for the smallest interval containing the arbitrary amount of 10% of the samples.

3. MATERIAL

The performance of the presented b-ntPET method was evaluated with three brain PET studies and compared to the reference lp-ntPET method. The first study consisted of 21 simulated realistic dynamic [^{11}C]raclopride PET scans. This dataset was used to evaluate the accuracy of the method, as well as its robustness against noise in well-controlled conditions.

The second study consisted of experimental dynamic [^{18}F]MPPF scans in cats involving a drug challenge with an agonist of the 1A sub-type serotonin (5-HT $_{1A}$) receptor. This dataset was used to assess the quantification capacity of the method.

The third study consisted of experimental human dynamic [^{11}C]raclopride acquisitions with a bolus-infusion protocol during which a transcranial direct current stimulation (tDCS) was applied. This third dataset was used to test the sensitivity of the method for detecting and characterizing the dopaminergic discharge induced by tDCS.

The model parameters were estimated with the proposed method b-ntPET, and compared with the lp-ntPET resolution. For b-ntPET, 55,000 samples were drawn including 5,000 samples of burn-in, in the three datasets.

3.1. Simulated [^{11}C]raclopride PET Data and Ground Truth Determination

A total of 21 realistic dynamic brain PET scans corresponding to a 100-min bolus-infusion [^{11}C]raclopride PET protocol were generated using the PET-SORTEO platform (Reilhac et al., 2004, 2005) simulating the performance of the Siemens Biograph mMR scanner (Reilhac et al., 2016). Each PET scan was simulated from a structurally different numerical brain model to account for inter-individual anatomical variability as well as using ideal TACs describing the time course of the tracer, including well controlled variations caused by dopaminergic discharges. Each brain model consisted of (1) a 3D attenuation numerical phantom that described the attenuation coefficients in order to account for photoelectric absorption, elastic (Rayleigh), and inelastic (Compton) scatterings of the photons in the human tissues during the simulation process, and (2) a 3D emission numerical phantom showing the emitting brain structures. Attenuation and emission phantoms were respectively constructed from the 3-tissue class binary image derived from a CT scan and from the parcellation of a T1 MRIs, both acquired on the same subject (Mérida, 2017).

Ideal TACs were defined for the simulation of each emitting brain structure using a full kinetic model involving the definition of a plasmatic input function (IF), from which tissue responses were generated. The ideal IF was defined by fitting experimentally

measured IF data with a three exponential model:

$$C_p(t) = \sum_{i=1}^3 A_i \exp\left(-\left(t - t_{\text{peak}}\right) \cdot \frac{\log(2)}{T_i}\right)$$

with $(T_1, T_2, T_3) = (4.28, 735.5, 183.5)$ sec, $(A_1, A_2, A_3) = (288.6, 1.1, 409.7)$ Bq/ml and $t_{\text{peak}} = 110$ sec. From this ideal plasmatic IF, TAC for the reference region was generated using a one-tissue compartment model $\frac{dC_{\text{ref}}(t)}{dt} = K_1^{\text{ref}} \cdot C_p(t) - k_2^{\text{ref}} \cdot C_{\text{ref}}(t)$ with $K_1^{\text{ref}} = 0.0918$ mL/(min.g), $k_2^{\text{ref}} = 0.242$ min $^{-1}$ (Pappata et al., 2002; Alpert et al., 2003) and a calibration factor of 10.

Ideal TACs that included modulations caused by endogenous dopamine release were then generated for caudate, putamen and accumbens using Equations (3) and (4), with $R_1 = 1.1540$, $k_2 = 0.242$, $k_{2a} = 0.0653$, $t_D = 42$ min, $t_p = 51$ min, $\alpha = 15$ and five different magnitudes of dopamine release: $\gamma = [0; 0.035; 0.078; 0.1284; 0.3]$ corresponding to displacement ratios (Mérida et al., 2018) of 0, 5, 10, 15, and 25 (hereafter referred to by placebo, DR05, DR10, DR15, and DR25 respectively). Endogenous release was lateralized to the left side of the brain and applied to the three structures of the striatum: caudate nucleus, nucleus accumbens, and putamen. Same input kinetics were used for all 21 subjects. TACs for the simulation of activity uptakes in surrounding cerebral regions of lesser interest as well as in extra cerebral regions (air, soft tissue, bone, CSF and ventricles, GM, WM, cerebellar WM, cerebellar vermis) were built from experimental PET/CT data measurements in lieu of from analytical calculation (Mérida, 2017). The whole set of TACs used in this simulated study is shown in **Figure 3**.

Simulated raw emission data of each subject was then rebinned and reconstructed into 33 time-frames of 3 min each with the OP-OSEM3D algorithm incorporating the point spread function (PSF) modeling, normalization as well as attenuation and scatter correction, and using 12 iterations of 21 subsets. A zoom of three was applied to the reconstructions, yielding a voxel size of $0.9 \times 0.9 \times 2.03$ mm 3 in a matrix of $256 \times 256 \times 127$ voxels. TACs were finally extracted from simulated PET data for striatal ROIs and reference region using the emission phantom for brain structure parcellation.

Due to the degradation occurring during reconstruction (partial volume effects mainly), the activity levels measured from the reconstructed image are not systematically retrieved for small brain structures. These alterations have a direct impact on the kinetic parameters to be estimated. To propose a more realistic reference than the unachievable values set as input for simulations, we considered the mean of the measured TACs over all subjects, thereafter called *noiseless* TACs, for each condition. The reference value for R_1 , k_2 , and k_{2a} are set by fitting the noiseless TAC of the placebo condition with the SRTM model (Lammertsma and Hume, 1996). The reference values for the release parameters (γ , t_D , Δ_T , α) have then been defined by fitting the noiseless TACs of each condition with both lp-ntPET and b-ntPET methods.

The prior intervals for the b-ntPET method were set to $R_1 \sim \mathcal{U}(1, 2)$, $k_2 \sim \mathcal{U}(0, 0.5)$, $k_{2a} \sim \mathcal{U}(0, 0.1)$, $\gamma \sim \mathcal{U}(-0.5, 0.5)$, $t_D \sim \mathcal{U}(40, 60)$, $\Delta_T \sim \mathcal{U}(5, 25)$, $\alpha \sim \mathcal{U}(10, 20)$. For the lp-ntPET

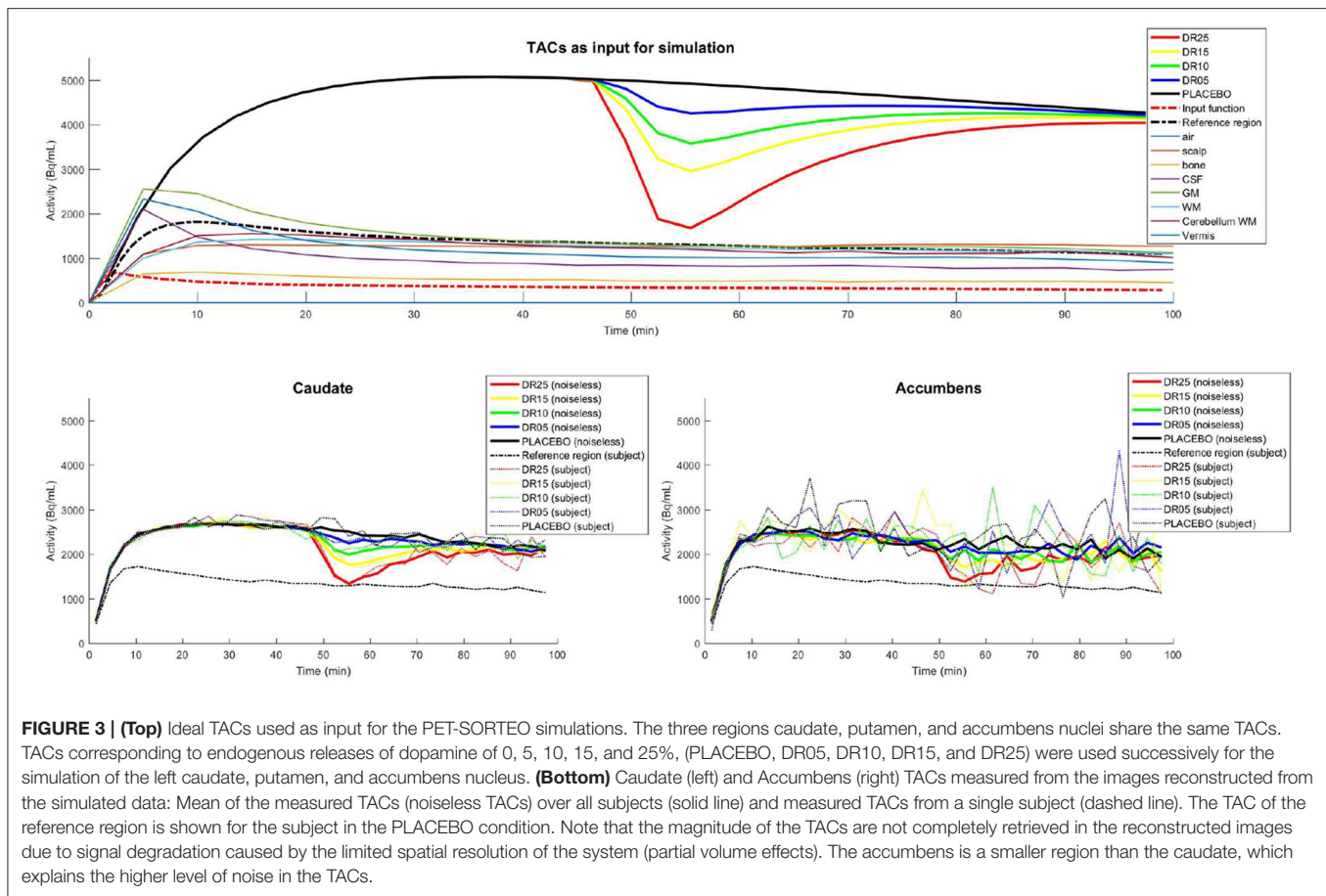


FIGURE 3 | (Top) Ideal TACs used as input for the PET-SORTEO simulations. The three regions caudate, putamen, and accumbens nuclei share the same TACs. TACs corresponding to endogenous releases of dopamine of 0, 5, 10, 15, and 25%, (PLACEBO, DR05, DR10, DR15, and DR25) were used successively for the simulation of the left caudate, putamen, and accumbens nucleus. **(Bottom)** Caudate (left) and Accumbens (right) TACs measured from the images reconstructed from the simulated data: Mean of the measured TACs (noiseless TACs) over all subjects (solid line) and measured TACs from a single subject (dashed line). The TAC of the reference region is shown for the subject in the PLACEBO condition. Note that the magnitude of the TACs are not completely retrieved in the reconstructed images due to signal degradation caused by the limited spatial resolution of the system (partial volume effects). The accumbens is a smaller region than the caudate, which explains the higher level of noise in the TACs.

approach, the basis functions have been chosen by setting the extreme values for t_D and α accordingly, with a step of 30 sec for t_D and t_p , and a step of 0.5 for α .

3.2. Experimental [^{18}F]MPPF Cat Brain PET Data

Four male cats underwent 90 min PET-MRI scans following a bolus injection-infusion of [^{18}F]MPPF, a 5-HT $_{1A}$ antagonist radiotracer, on an integrated Siemens Biograph mMR scanner. Each cat underwent four separate PET-MRI acquisitions: three involving a pharmacological challenge at 50 min with NLX-112, a 5-HT $_{1A}$ agonist, injected at 0.04, 0.08, or 0.16 mg/kg, and one involving saline injection for control. Dynamic PET images were reconstructed from the acquired list-mode with 3D OP-OSEM algorithm, using point spread function modeling, normalization, scatter, and attenuation correction as well as with a zoom 4, yielding to a matrix of $256 \times 256 \times 127$ pixels, with voxels of $0.7 \times 0.7 \times 2.03$ mm 3 . PET images were realigned and registered into the same space using a multi-subject MRI template, coregistered with a labeled atlas defining standard regions of interest (Lancelot et al., 2010). Using this atlas, TACs for the hippocampus and cerebellum were extracted and modeled with the classic lp-ntPET method, and with the b-ntPET method to quantify and characterize the endogenous release. For additional information, the original study can be found in Vidal et al. (2018).

The prior intervals for the b-ntPET method have been set to $R_1 \sim \mathcal{U}(1, 2)$, $k_2 \sim \mathcal{U}(0, 0.5)$, $k_{2a} \sim \mathcal{U}(0, 0.1)$, $\gamma \sim \mathcal{U}(-0.5, 0.5)$, $t_D \sim \mathcal{U}(45, 70)$, $\Delta_t \sim \mathcal{U}(5, 25)$, $\alpha \sim \mathcal{U}(0, 20)$. For the classic lp-ntPET approach, the basis functions were chosen by setting the extreme values for t_D and α accordingly, with a step of 30 s for t_D and t_p , and a step of 0.5 for α .

3.3. Experimental [^{11}C]raclopride Human Brain PET Data

Thirty-two healthy subjects (mean age = 25.25 ± 3.55 years) underwent a 100 min PET acquisition on the Siemens PET/CT Biograph after the intravenous injection of [^{11}C]raclopride (18 MBq + 2.6 MBq/kg) and followed by a constant infusion. During the collection of the PET data, each subject received a single 10 min tDCS session with intensity 2 mA, that started 40 min after the injection of the tracer. Subjects were divided in two parallel groups, active ($n = 14$) vs. sham ($n = 18$) bifrontal tDCS. A total of 20 successive frames of 5 min each was reconstructed with 3D OP-OSEM iterative algorithm incorporating resolution modeling, time of flight, normalization, attenuation, and scatter corrections. Gaussian post-reconstruction filtering (FWHM = 3 mm) was applied to all PET images. Reconstructed volumes consisted of 109 contiguous slices (2.03 mm thickness) of 128×128 voxels each (2.12×2.12 mm 2). Due to excessive head motion that was caused by the stimulation, individual reconstructed

time-frame from the same scan were registered to each other using a 3-D rigid body model. T1 anatomical MRI of each subject was also acquired on a 1.5T Magnetom scanner (Siemens) and parcellated using the Hammersmith maximum probability brain atlas (Hammers et al., 2003; Gousias et al., 2008). Time-activity curves were extracted for the caudate and for the cerebellar gray matter (without vermis) that was used as reference region (devoid of specific dopamine D2-like receptors). For additional information, the original study can be found in Fonteneau et al. (2018).

Regional TACs were submitted to modeling with lp-ntPET and b-ntPET with prior intervals set to $R_1 \sim \mathcal{U}(1, 2)$, $k_2 \sim \mathcal{U}(0, 0.5)$, $k_{2a} \sim \mathcal{U}(0, 0.1)$, $\gamma \sim \mathcal{U}(-0.5, 0.5)$, $t_D \sim \mathcal{U}(35, 90)$, $\Delta_t \sim \mathcal{U}(5, 25)$, $\alpha \sim \mathcal{U}(0, 20)$. For the classic lp-ntPET approach, the basis functions were chosen by setting the extreme values for t_D and α accordingly, with a step of 30 s for t_D and t_p , and a step of 0.5 for α .

4. RESULTS

4.1. Simulated Dataset

In this section we present the results obtained using the 21 simulated [^{11}C]raclopride dynamic PET scans. Results are shown for the caudate and accumbens regions only, which by their difference in size, exhibit two different levels of noise. Caudate as well as putamen are large regions and measured TACs are less noisy than TACs measured from the accumbens.

4.1.1. Illustration of the Sampling Process

Figure 4 illustrates the sampling process and how it is associated with probability distributions. In this example, the Markov Chain associated to the magnitude parameter γ was initialized randomly at a high value. Consequently, the value of γ generally decreases during the first iterations to reach the ergodic distribution between -0.02 and 0.05 , after around 3,000 iterations. During the first iterations, too many proposed samples have been rejected by the Metropolis-Hastings process (the acceptance rate was below $\frac{1}{2}$) so the step size was automatically lowered until it converged to a value close to 0.015 after around 1,500 iterations. After withdrawing the samples that have been drawn before convergence (during burn-in), the remaining samples are ensured to be drawn according to the marginal distribution associated to γ . Histogramming these samples gives us the shape of the distribution. One sees that in this case, ϵ converged in about 1,500 iterations, and the MCMC chain converged in about 3,000 iterations. Our choice of 5,000 iterations for burn-in is by far sufficient. It is important to keep in mind that the sampling is performed in an 8-dimensional space. Each sample of γ is associated with the seven values of the other parameters. **Figure 4** only illustrates the projection of these samples in the dimension associated to γ .

4.1.2. Bayesian Inference

Figure 5 shows an example of marginal distribution estimated for each parameter of one subject for both caudate and accumbens (condition DR25). These marginal distributions correspond to the projection of all samples in each dimension of the

parameter space. Our results showed that the distribution of most parameters were hill-shaped, which demonstrates that a single value is preferred, except for α , that exhibits a rather uniform distribution, and expresses that in this case the parameter α is non-informative. Note that the probability distributions for the accumbens exhibit larger dispersions than for caudate due to the higher noise in the accumbens TACs. That testifies that the estimations are less reliable in the case of accumbens. Such information was not available in the original version of lp-ntPET. **Figure 5** also shows the difference between the different estimators. Since HPD is based on a mode-seeking algorithm, its estimations correspond to the top of the probability distributions, whereas MMSE is deviated when the probability distribution is asymmetrical. MAP, which corresponds to the single sample whose posterior probability is the highest, does not seem to belong to most probable intervals. That can be explained by the fact that the drawn samples are relatively sparse in the 8-dimensional parameter space.

4.1.3. Accuracy

Figure 6 shows an example of a measured TAC for each condition and how it is fitted with both methods lp-ntPET and b-ntPET. One can see that modeled TACs with b-ntPET are generally smoother than the ones modeled with lp-ntPET. On this example, b-ntPET seems to be less conducive to false detections, with lp-ntPET detecting a wider displacement in the placebo condition for accumbens.

Figure 7 shows the relative errors on the estimations of the kinetic parameters for all subjects for each condition. Both methods led to kinetics estimates with similar accuracies for the caudate region. Nevertheless, with b-ntPET, the estimations of the kinetic parameters were closer to the reference for the accumbens where the noise was higher. More importantly, a one-way ANOVA analysis showed that the bias on the estimated kinetic parameters R_1 and k_2 for the caudate region depended on the magnitude of the discharge with lp-ntPET ($p < 0.05$), whereas it remained stable across conditions with the b-ntPET estimations.

Figure 8 shows the estimates of the magnitude parameter γ for all subjects and for all conditions. The reference value of γ was obtained by fitting the *noiseless* TACs with both methods. These reference values are represented as horizontal lines in the figure. One can observe less outliers and a lower variability in the estimations of γ with b-ntPET than with lp-ntPET. More interestingly, the sensitivity of detection was increased with b-ntPET, as it was possible to distinguish the four magnitudes of simulated dopamine release (DR05 to DR25) from the placebo condition, for the caudate as well as for the accumbens, which is not always the case with lp-ntPET. Finally, the estimated magnitude of the release is closer to zero in the placebo condition with b-ntPET than with lp-ntPET.

Figure 9 shows the endogenous release curves ($\gamma \cdot h(t)$) that were estimated by both methods. One can observe that b-ntPET estimated released curves that were closer to the reference and with less variability. Moreover, lp-ntPET presents more aberrant curves in every condition, especially for the accumbens. Finally, lp-ntPET presents more false detections in the placebo condition.

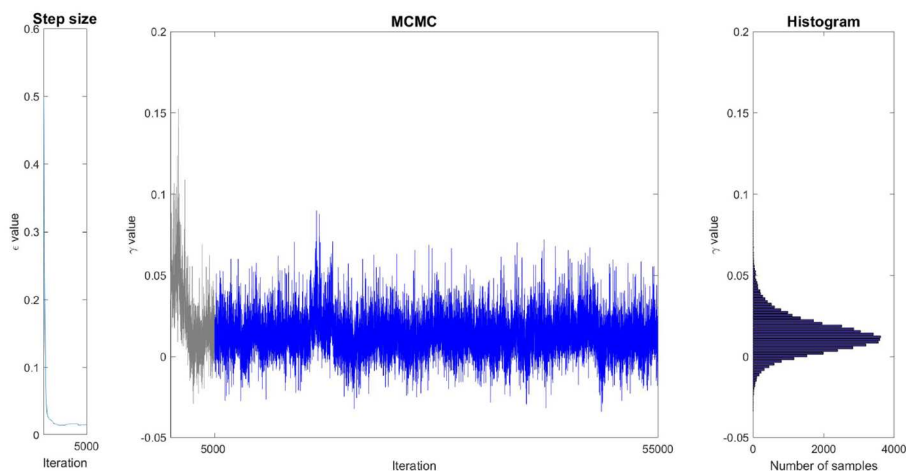


FIGURE 4 | Illustration of the sampling of parameter γ on a single ROI (caudate, condition DR25). **(Left)** Evolution of the step size during the burn-in phase. **(Middle)** Generated samples (Markov Chain). The gray region corresponds to the burn-in phase whose samples are withdrawn. **(Right)** Histogram of the remaining samples corresponding to the estimation of the marginal distribution of γ .

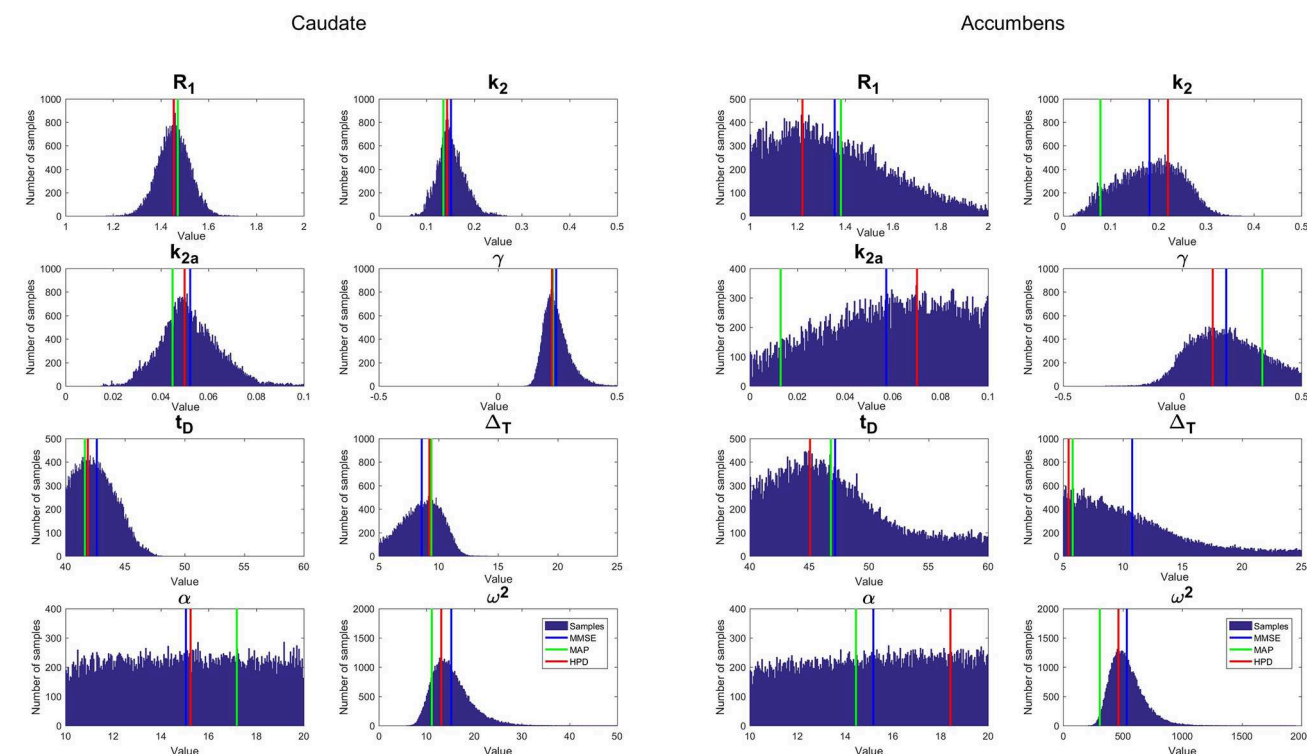


FIGURE 5 | Example of the marginal distribution estimated for each parameter with b-ntPET and for a single simulated subject at condition DR25. Vertical lines show the inferred value of each parameter according to the proposed estimator HPD (red) compared to popular estimators MMSE (blue) and MAP (green). **(Left)**, caudate; **(Right)**, accumbens.

Figure 10 shows the Mean Squared Error (MSE) between each individual estimated curve $\gamma \cdot h(t)$ and the references obtained from the *noiseless* TACs. B-ntPET presents a generally lower MSE than lp-ntPET, especially when high level of noise is present, such as in the accumbens. This suggests a better identification of the shape on the endogenous release. B-ntPET also presents a lower inter-subject variability.

4.2. Experimental Brain Cat Dataset

4.2.1. Dose Effect Gamma Response

The estimations of the γ parameter obtained for the brain cat real dataset, in the hippocampus and for each individual, are reported in Figure 11. Lp-ntPET was not able to evidence any significant differences between the magnitude of the various displacements induced by pharmacological challenge

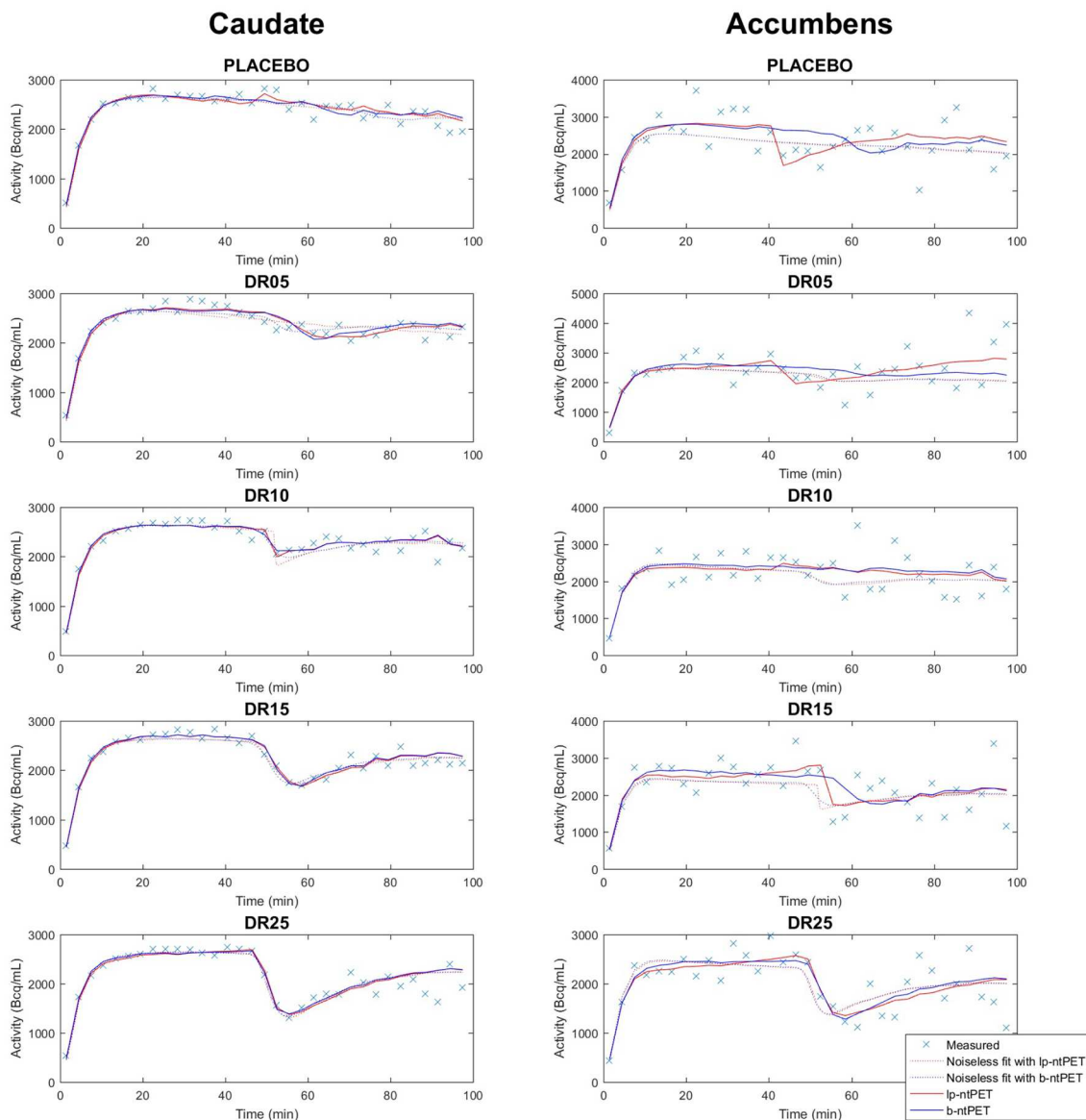


FIGURE 6 | Example of simulated TACs and fitted curves obtained with lp-ntPET (red) and b-ntPET (blue). The fitted curves on the mean TACs over all subjects (here labeled *noiseless* fit) are also shown on this figure for both methods, as reference. **(Left)**, caudate; **(Right)**, accumbens.

compared to the control condition (NaCl injection). In contrast, differences in the magnitude of the displacement measured with b-ntPET between every dose condition and control condition (**Figure 11**) were significant. In addition, characterization of the gamma parameter by b-ntPET showed a lower interindividual dispersion and no outliers.

A linear correlation between the injected dose and the γ response (dose effect) could be computed with an acceptable Pearson coefficient of $r = 0.73$ ($p < 0.0001$, lower and upper bounds for 95% confidence interval = $[0.52; 0.85]$), whereas dispersion of estimated γ parameter failed to show this correlation with lp-ntPET with a Pearson coefficient of $r = 0.21$

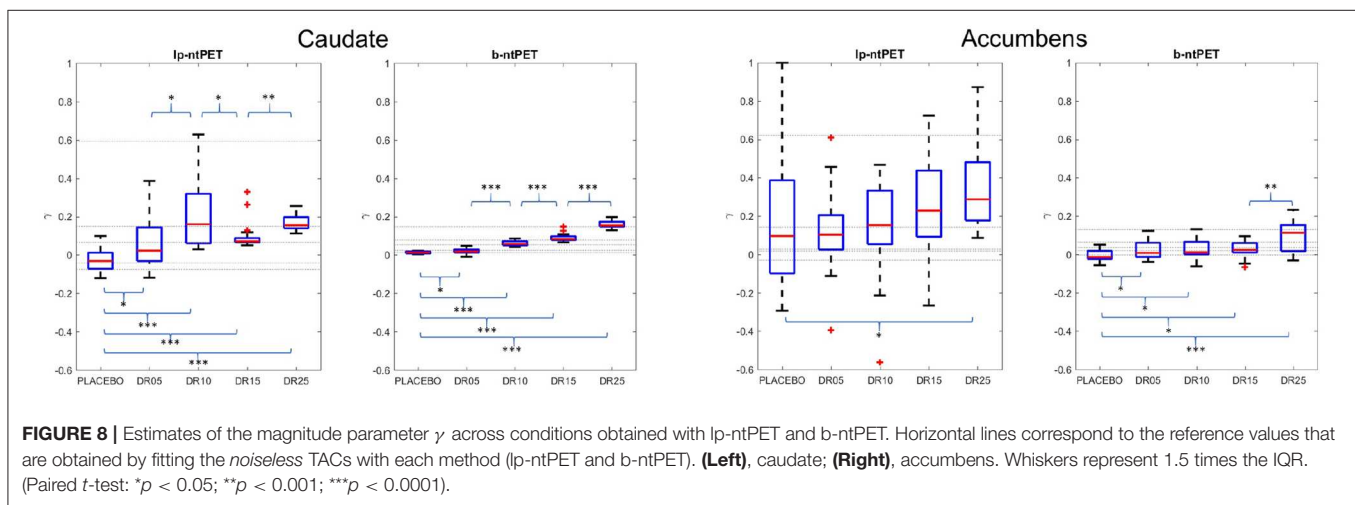
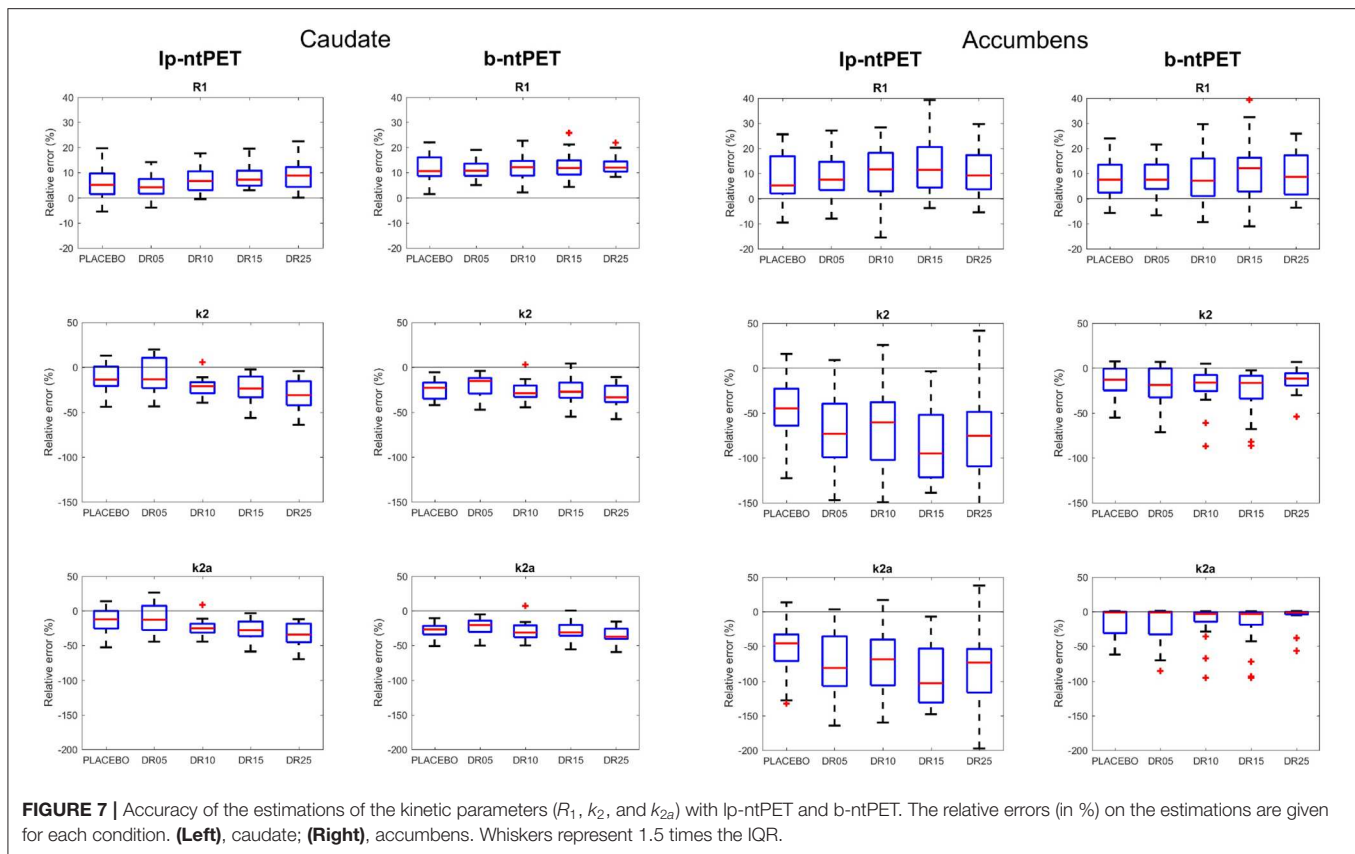
($p = 0.21$, lower and upper bounds for 95% confidence interval = $[-0.12; 0.51]$).

4.2.2. Characterization of the Displacement

The estimated time-course of the radiotracer clearance from the ROI as a percentage of the baseline state $k_{2a}^{\%baseline}(t)$ defined in Equation (12) has been calculated for both methods (Normandin et al., 2012; Angelis et al., 2019).

$$k_{2a}^{\%baseline}(t) = 100 \cdot \frac{k_{2a} + \gamma \cdot h(t)}{k_{2a}} \quad (12)$$

Both lp-ntPET and b-ntPET were able to model the temporal variation of the efflux rate induced by drug competition at the



individual level (Figure 12). The curves obtained with lp-ntPET presented disparate patterns and led to non-interpretable results. In contrast, the responses modeled with b-ntPET were more homogenous across subjects and the amplitude of the curves increased with the injected dose.

4.3. Experimental Brain Human Dataset

Results from the experimental human brain raclopride PET study showed that the b-ntPET resolution method

reduced uncertainties of the model parameter estimates. Figure 13 shows boxplots of the γ parameter estimated by both methods for the right caudate of all subjects. In our study, with lp-ntPET, individual γ estimates ranged from -0.04 to 0.1 with some negative outliers for the placebo group, and from zero to less than 0.1 for the active group. No statistical difference was found between the active and the placebo groups. However, the estimates produced with b-ntPET showed a much lower dispersion and

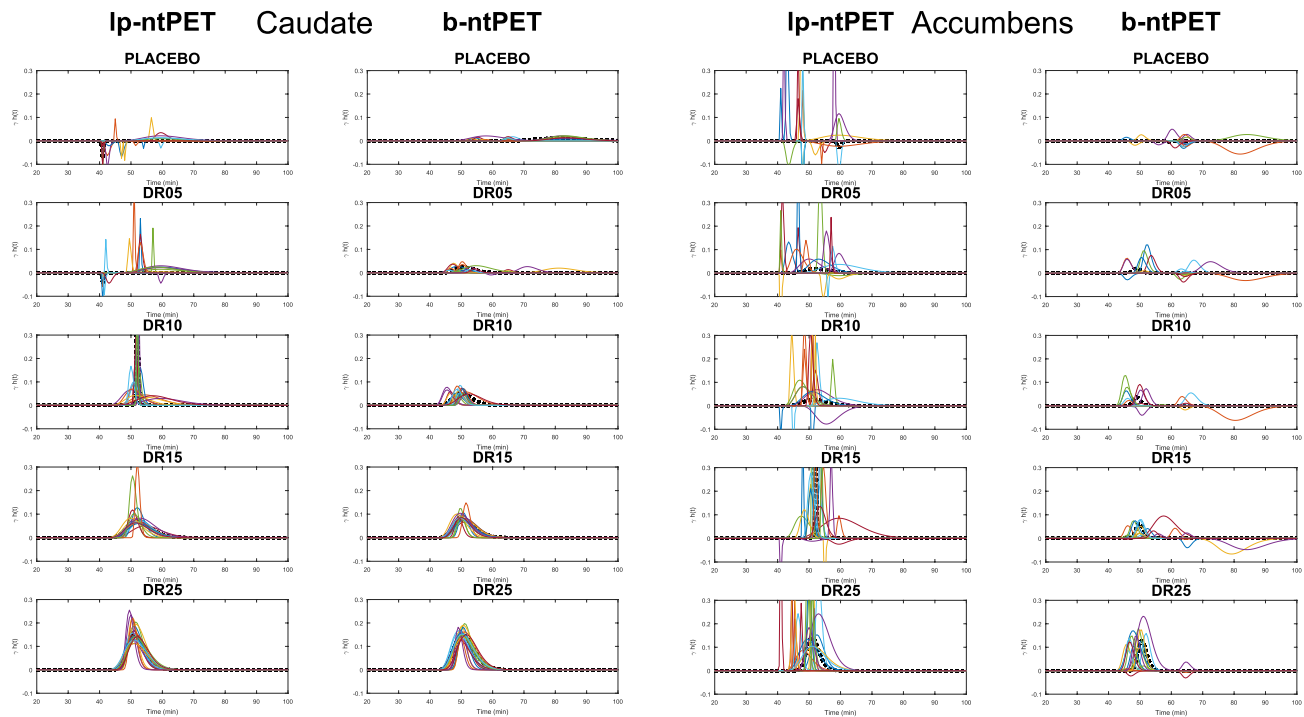


FIGURE 9 | Endogeneous release curves ($\gamma \cdot h(t)$) estimated by both methods for all conditions. Color lines represent the different subjects. The dashed line corresponds to the release curve estimated from the *noiseless* TAC by each method (reference). (Left), caudate; (Right), accumbens.

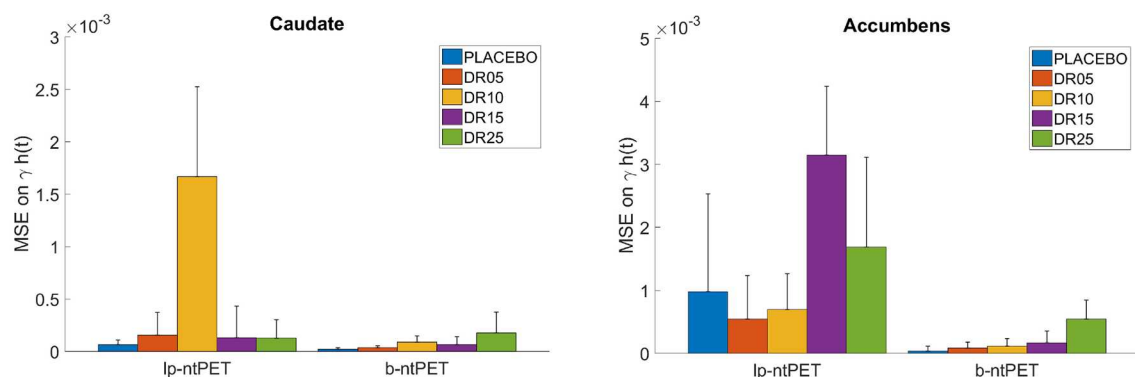


FIGURE 10 | Mean Squared Error (MSE) computed between each individual estimated release curve ($\gamma \cdot h(t)$) and the reference estimated from the *noiseless* TACs, for each estimation method and condition. (Left), caudate; (Right), accumbens. Error bars show the standard deviations.

consequently a significant difference was detected between groups ($p < 0.05$).

The ability of ntPET to model discharge curves is illustrated in **Figure 14**. Mean TACs across subjects, pooled by group (normalized by the activity of the three frames preceding the tDCS stimulation) are shown (left scale). On the right scale, mean displacement curves, per group, are plotted. With the Ip-ntPET model, displacement curves were noisy and increased from the triggering of the stimuli to the end of the experiment for both the placebo and the active groups, reducing their

discrimination. With the b-ntPET model, the mean discharge curve was flat for the placebo group, with the exception of small humps near 70–80 min post injection. For the active group, a hump was visible at the start of the tDCS stimulus, then it was flat before rising up at 60 min. $k_{2a}^{\%baseline}(t)$ curves were much less noisy when estimated with b-ntPET. These results are in accordance with the original publication (Fonteneau et al., 2018), where the binding ratio parameter of the right caudate was significantly different between groups in the time interval 40–55 min post tDCS.

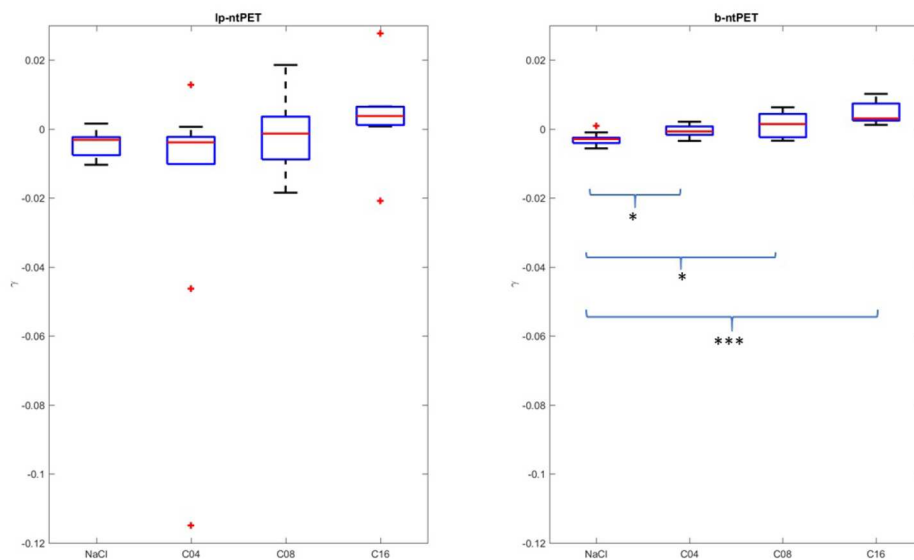


FIGURE 11 | Magnitudes of the displacement (γ) estimated by both methods in the hippocampal region. The conditions NaCl, C04, C08, and C16 correspond to saline injection, and injections of 0.04, 0.08, and 0.16 mg/kg of 5-HT_{1A} agonist, respectively. Whiskers represent 1.5 times the IQR. (Two-sample *t*-test: **p* < 0.05; ****p* < 0.0001).

5. DISCUSSIONS

The possibility to characterize and quantify from a single dynamic PET experiment the system response to a stimulus or to an exogenous administration of a centrally acting cold compound provides a unique tool for the *in vivo* exploration of functional neurochemistry and psychopharmacology. With the advent of simultaneous PET/MR acquisitions, this methodology used in single PET/fMRI protocol paradigms, involving stimulation or pharmacological challenges, will open the door to the simultaneous characterization of the direct response of the neurotransmission system under investigation, as well as the mapping of the induced brain activity, with enormous potential in neurology and psychopharmacology. Several methods have been proposed to analyze neurotransmission systems under non steady state regime, such as the LSSRM and the lp-ntPET, and used for the analysis of experimental animal and human studies. Mapping of increased dopamine release induced by motor planning task was first shown in a [¹¹C]raclopride human study using the LSSRM method (Alpert et al., 2003). Lataster et al. (2011) investigated the *in vivo* dopamine release in the human prefrontal cortex in response to a psychosocial stress challenge, using the radioligand [¹⁸F]fallypride and the same analysis method. Similarly, Ceccarini et al. (2012) detected striatal and extrastriatal reward-induced dopamine release in humans. Kim et al. (2014) revealed for the first time that different temporal patterns were involved in the dopamine response to smoking using the more advanced lp-ntPET method to analyze [¹¹C]raclopride PET data of subjects smoking cigarettes during the acquisition. The same technique was used to associate the *in vivo* displacement of [¹¹C]raclopride with observed behavioral changes of awake, freely moving rats following the

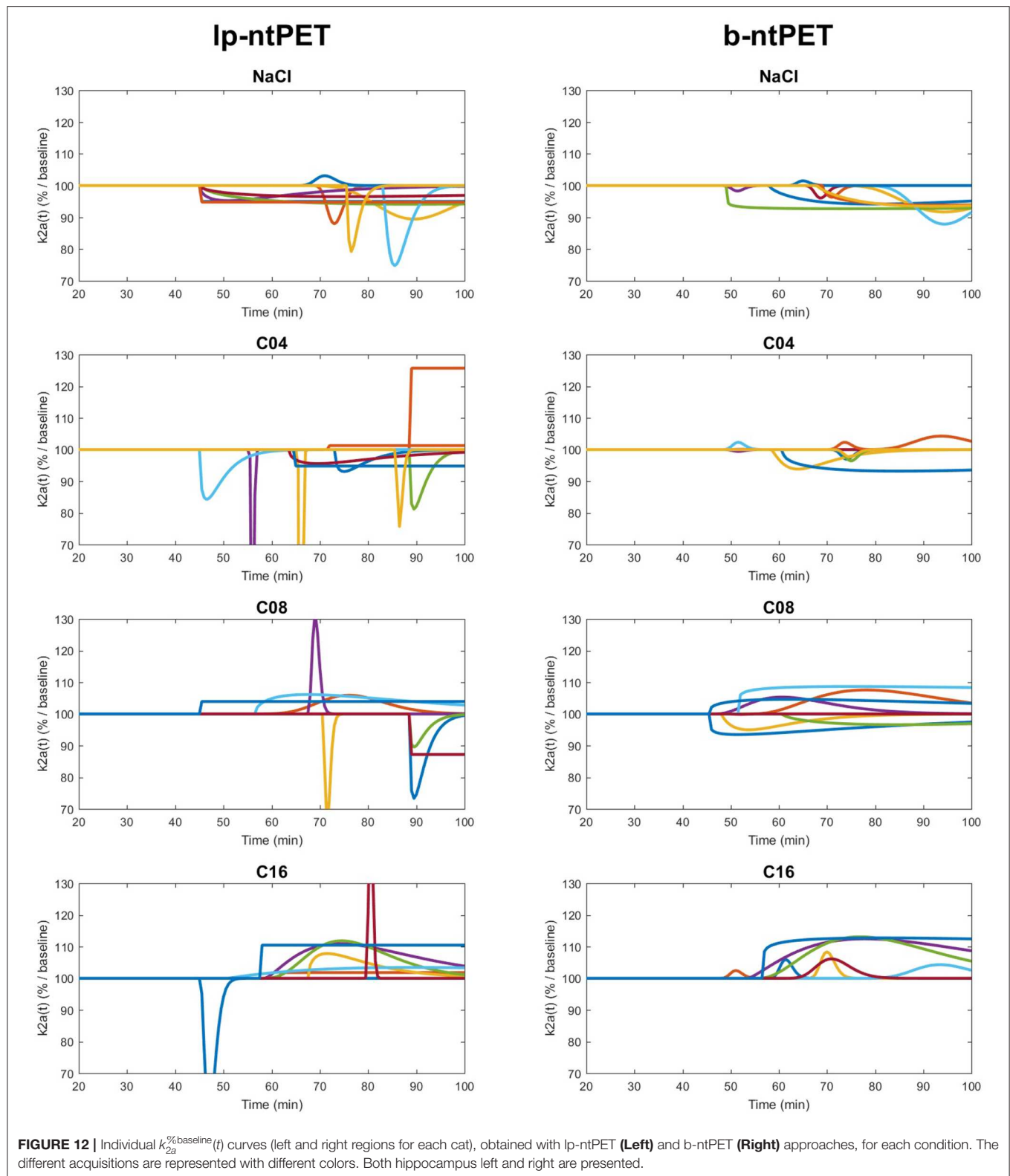
administration of amphetamine (Angelis et al., 2019; Kyme et al., 2019).

In this work, we introduced a novel resolution method for ntPET models, called b-ntPET, that addresses some shortcomings and limitations of the current lp-ntPET model, and whereby the parameter estimation relies on a Markov-Chain Monte-Carlo (MCMC) sampling in a Bayesian framework, allowing the joint estimation of the noise level and the model parameters as well as the use of prior knowledge to guide the estimation process toward realistic solutions.

5.1. Performance of the Parameter Estimations

The use of well-controlled simulated PET data allowed us to show that b-ntPET produced more reliable estimates of R_1 , k_2 , and k_{2a} with higher accuracy and lower variability than lp-ntPET (Figure 7). This was especially the case in high noise context, such as for the accumbens, which is a relatively small region. These kinetic parameters rule the classical exchanges between the plasma and the free, non-specific and bound compartments as in the SRTM methods and their estimates should not be influenced by the presence of any competing ligand. However, and unlike b-ntPET, their estimated values obtained with lp-ntPET depend on the magnitude of the displacements (Figure 7), especially in the presence of noise.

More importantly, experiments on the simulated data showed that the improvement of the estimation quality when using b-ntPET was even more noticeable when estimating the magnitude of the transient effect (Figure 8). Unlike lp-ntPET, b-ntPET was able to detect and estimate the magnitude of the displacement with a high level of accuracy and precision



(reduced variability). Consequently, and contrary to lp-ntPET, differences in magnitude between groups estimated by b-ntPET were found systematically statistically significant even in high

noise situations. The higher performance obtained with our approach was confirmed with the experimental cat dataset where b-ntPET allowed the detection of statistical differences

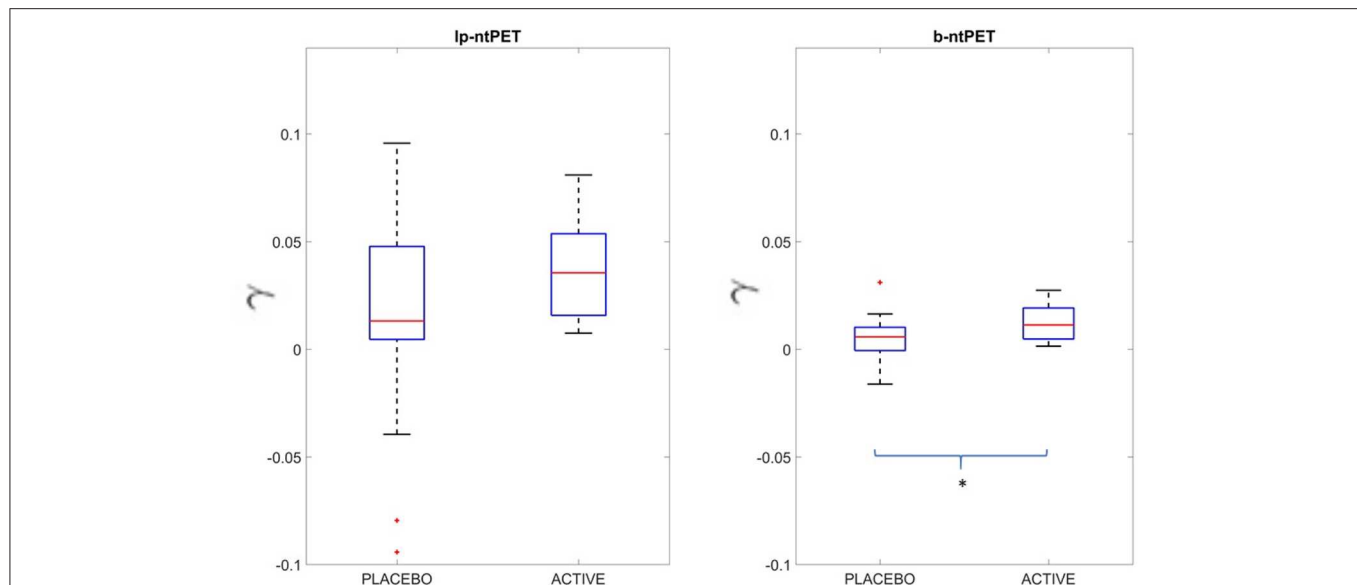


FIGURE 13 | Estimated γ value in the right caudate for both methods lp-ntPET and b-ntPET. Contrary to lp-ntPET, b-ntPET allows the dissociation of the two groups (Two-sample t -test: $p < 0.05$).

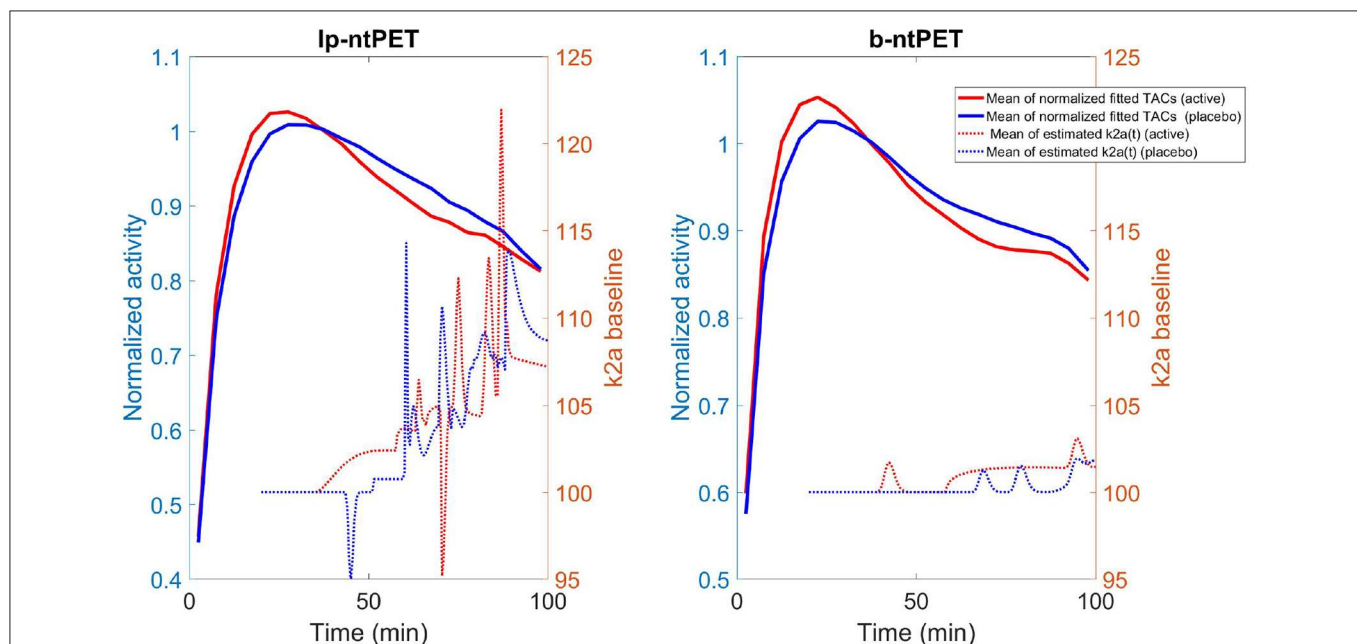


FIGURE 14 | For both methods, solid line: the mean of the endogenous releases estimated for the active (red) and placebo (blue) groups using both methods; dashed line: the mean of the associated $k_{2a}^{\% \text{baseline}}(t)$ curve.

between the placebo group and other conditions, while no statistical differences were found when kinetics were modeled using lp-ntPET.

As a conclusion, γ estimated with b-ntPET reliably distinguished activated vs. control groups with limited sample size of subjects. In addition, γ was able to quantify the level of endogenous release as shown in **Figure 8** as well as drug effect occupancy as shown by the regression results on the cat study (see section 4.2.1).

The analysis of the marginal probability density estimated for each parameter (**Figure 5**) revealed that the α parameter as well as the t_p and t_D parameters in the presence of noise (accumbens region) were poorly determined. Hence, we did not specifically studied the estimation accuracy of each parameter taken independently, but the resulting $\gamma \cdot h(t)$ curves instead. With the simulated study, we were able to quantify the MSE distance between estimated curve and the reference curve (**Figure 10**). Results showed that whereas lp-ntPET frequently

failed to characterize accurately the transient dynamic change, b-ntPET was able to produce individual curves with right magnitude and shape compared to the reference. Lp-ntPET was especially deceiving in placebo condition, in noisy context, and surprisingly in the noiseless curve of the DR10 condition.

In this last case, lp-ntPET over-estimated the value for γ with a value of 0.6 (Figure 8). One can note that the estimated release curve peaked in-between two measured points (Figure 6). It is very likely that lp-ntPET, which seeks the best solution in the least squares sense, favored this extreme solution consisting of a very brief displacement of a high amplitude between two measured points. This problem can happen even in a low noise scenario, as demonstrated with the reference curve of the DR10 condition. Shorter frames could have reduced the risk of such overfitting issue, but would have resulted in a noisier TAC. Given the low robustness to noise of the lp-ntPET method from the other hand, a compromise regarding the duration of the frames can be hard to set. This issue clearly illustrates a limitation in the lp-ntPET implementation with regard to its dependence to the time discretization. By tackling the noise more efficiently and outputting smoother TACs, b-ntPET, on the other hand, is less under the yoke of the temporal resolution.

5.2. B-ntPET as a Generalization of lp-ntPET

B-ntPET can be seen as an extension of the lp-ntPET method and this for several reasons. In an ideal scenario where the parameter space is totally covered by the set of basis functions, the WLS solution returned by the lp-ntPET method corresponds to the best solution in terms of goodness of fit, which is also the solution that maximizes the likelihood $p(Y|\Theta)$. Yet, when using b-ntPET in the special case where non-informative priors are used, as we do in this study, the posterior distribution $p(\Theta|Y)$ equals the likelihood $p(Y|\Theta)$ (up to a normalization factor). Consequently, lp-ntPET and b-ntPET seek to optimize the same objective function. Whereas lp-ntPET uses WLS to obtain directly the single set of parameters that maximizes this objective function, b-ntPET samples the parameter space to assess the objective function in its wholeness. Denser regions of samples correspond to higher probable regions in the parameter space. B-ntPET relies on all these samples to provide the best solution. The global maximum of this objective function corresponds to both the WLS solution returned by lp-ntPET and to the solution returned by b-ntPET when the MAP estimator is used. In the absence of noise, and with moderate noise, this global maximum is well defined, and both lp-ntPET and b-ntPET with the MAP estimator may provide relevant results. However, when data are noisy, the surface of the objective function is highly non-smooth and the global optimum can be translated by local optima. This can lead to overfitting issues, with the best-fit solution becoming no longer representative of the data. In this case, the HPD estimator selects a more robust solution because it relies on the seeking of the most probable cluster of samples in the parameter space rather than the single most probable sample. In other words, a set of parameters is a good candidate for b-ntPET with HPD when it leads to high fit and when small variations

on these parameters also lead to good fit. Another consequence of this regularization effect when using b-ntPET with HPD is the production of smoother characterization curves (Figures 9, 12, 14), while lp-ntPET detected a lot of short releases with high amplitude.

Another conceptual difference between lp-ntPET and b-ntPET is that b-ntPET treats all the model parameters ($R_1, k_2, k_{2a}, \gamma, t_D, \Delta_t, \alpha$) equally and estimates them at once, whereas lp-ntPET distinguishes the linear parameters (R_1, k_2, k_{2a}, γ) and the non-linear parameters (t_D, Δ_t, α). By doing so, we believe b-ntPET reduces the dependence between the two subsets of parameters. Figure 7 illustrates that idea by showing that the estimates of the kinetic parameters (R_1, k_2, k_{2a}) are less sensitive to the displacement with b-ntPET than with lp-ntPET. In addition, in terms of exploration of the parameter space, by relying on a discrete set of basis functions, lp-ntPET restrains the parameter space associated to the non-linear parameters t_D, Δ_T and α to a grid, while b-ntPET explores the parameter space continuously by using MCMC sampling. An immediate consequence is the possibility for b-ntPET to assign any value to these parameters.

One key advantage of b-ntPET is its flexibility to integrate prior knowledge on the parameters. Whereas lp-ntPET allows to restrain the estimations of t_D, Δ_T , and α to plausible solutions by setting the boundaries of the basis functions accordingly, b-ntPET allows the consideration of any kind of prior distribution for t_D, Δ_T, α as well as for the other four parameters of the model.

Finally, another benefit of b-ntPET over lp-ntPET is that the noise is jointly estimated with the parameters of the model. Nevertheless, it is worth noting that the joint estimation of the noise variance can be omitted when the variance of the noise is already known with precision, for example by using some elaborate deterministic models accounting for measured counts, frame duration, deadtime etc.

5.3. Computational Considerations

Whereas no particular effort was made in this work to optimize the implementation of the b-ntPET method, we decided nevertheless to discuss here its computational efficiency and the existing options for improvement. As a very first observation, we can say that b-ntPET is computationally slightly more demanding than lp-ntPET. While a C implementation of lp-ntPET can analyze a TAC in less than 2 s with an i7 core, our current compiled Python implementation of b-ntPET requires about 3 s. This additional cost is not truly notable for ROI-based analysis, but could become significant for a pixel-wise implementation. The computational time required by b-ntPET is directly proportional to the amount of samples drawn. In this work, we employed 55,000 samples, a number that subsequent analyses showed to be far too high, and processing time could be significantly decreased by reducing adequately this number.

The convergence speed of the MCMC is a crucial point. We assessed the convergence properties by running 50 instances of MCMC chains over the same data from random starting values. We then measured the Potential Scale Reduction Factor (PSRF) on each parameter, which is a popular tool to measure convergence rate of MCMC chains (Brooks and Gelman, 1998).

The PSRF value was below 1.02 after <100 drawn samples indicating very early convergence. Fan et al. (2016) reported that they attempted to solve the same model with MCMC but their implementation could not reach convergence within a reasonable amount of time. We believe the higher convergence efficiency of our method is a nice consequence of estimating the noise's variance jointly with the parameters of the model. Indeed, the acceptance ratio during the sampling process highly depends on the accuracy of the noise variance estimate. If overestimated, too many samples are accepted and if underestimated, too many are rejected, both cases leading to poorly-mixed samples (an ineffective exploration of the parameter space) and a risk for the MCMC chain to be stuck in a local optimum. Sampling the noise variance with direct sampling instead of an acceptance-rejection scheme also improves the mixing behavior.

Finally, our current implementation can be reduced significantly by using GPU programming.

5.4. Perspectives on Bayesian-ntPET

We have identified a few axes for future investigations and developments with the primary goal to improve the b-ntPET. First, in this work we did not pay much attention to the choice of the estimator, and we decided to choose HPD over the other approaches. However, inferring independently each parameter from their respective marginal distribution using the HPD estimator (and possibly with the others) is a debatable choice and may lead to suboptimal solutions. The interval with the highest probability on the marginal distributions does not always correspond to a region with high probability in the whole parameter space. One solution is to perform multivariate HPD in the whole 8-dimensional parameter space. Some preliminary tests on the real human dataset led to some very encouraging results (Figure 15). Multivariate HPD is however time consuming and needs appropriate tuning to accommodate the sparseness of the samples in the whole parameter space (the 50,000 samples are dense on marginal distributions, but are sparse in a 8-D space).

The results presented in this article were obtained using rather non-informative priors. More sophisticated priors with realistic constraints would guide the estimation process to more suitable solutions. For example, fortuitous noisy measurements in successive frames can be interpreted as brief tracer displacements leading to false detections, and setting priors that would penalize variations that are too short in time would be appropriate. Priors can also be integrated from other modalities such as fMRI or EEG according to the design of the study.

The stochastic context of the approach is also profitable. For example, one can be interested in doing model selection to classify whether or not the tracer was significantly displaced. For this purpose, Bayesian theory proposes tools to quantify the probability of the TACs to be described by a model rather than one other. Furthermore, the estimation of the posterior probability distributions provided by the methods can be exploited in a number of ways. First, confidence intervals or, more generally, information about the degree of trust on the estimation results can be easily furnished. It would also be

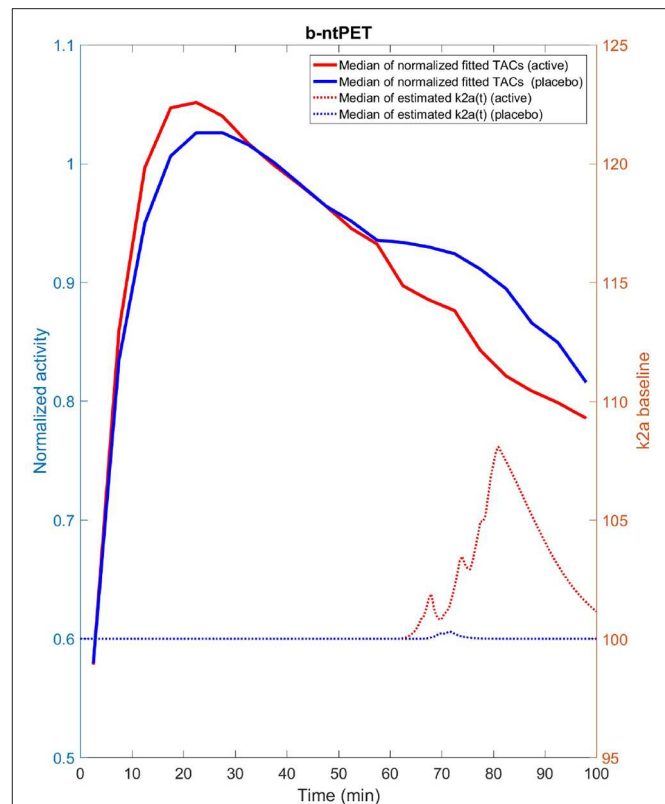


FIGURE 15 | Median estimated TAC fit (solid line) as well as median estimated endogenous releases (dash line) computed for the placebo (blue) and active (red) groups from the experimental [^{11}C]Raclopride study and using the multivariate HPD in lieu of the univariate HPD. We can note that the estimated releases produced with the multivariate HPD exhibit more acceptable and expected features than when the univariate HPD was used (Figure 14 right) with a quasi null release for the placebo group and a more continuous release starting after the beginning of the stimulation for the active group.

conceivable to return more than one solution by seeking the most probable modes in the probability distribution.

In a voxel-wise implementation, spatial regularity can be enforced by a 3-D Markov Random Field, possibly supported by spatial priors such as anatomical information from MRI or CT.

In this work, the validations and the experimental applications of the method were carried out first with the [^{11}C]raclopride tracer, that is known to be displaceable. This nice property is not systematically shared with other tracers, but is not specific to [^{11}C]raclopride either. We showed in the third application, that the method is also applicable to [^{18}F]MPPE, and lead to more exploitable results than with the reference method for this fluorinated tracer. The methodology presented here can be extrapolated to other displaceable tracers without much risk. However, two situations may challenge the efficiency of the resolution process. The first may occur when the dynamics of the transient effect can not be fitted by the current model by lack of flexibility, possibility leading to reduced sensitivity and inaccurate estimates of the magnitude of the phenomena. In this current work, the transient effect is modeled by a gamma

function. We believe that the chance of violating this assumption is however low, as the gamma function can model a large variety of magnitudes and shapes. If this is not the case, the optimization scheme detailed in this study can be adapted to a new model by re-defining the likelihood function accordingly, and adapting the prior distributions to the new parameters. The second situation may occur when a displacement with a low magnitude is to be analyzed in low signal-to-noise ratio condition. We showed in this work that the joint estimation of the noise and the parameters lead to improved performance compared to the reference approach. However, for tracers inducing very low signal-to-noise ratios, the efficiency of the proposed method can be questioned and should be tested, if possible, with well-controlled simulated data before application to actual scans. Finally, the availability of the parameters' probability densities generated with the Markov chain sampling is a clear advantage of b-ntPET over other resolution approaches, as the sharpness of their profile reflects the capacity of a tracer to be displaced and therefore the suitability of the ntPET model. This is still to be tested and is beyond the scope of the current study. This will nevertheless constitute the subject of a future work with other dopamine tracers such as [^{18}F]Fallypride or [^{11}C]FLB45, or with tracers for other neurotransmission systems such as [^{11}C]diprenorphine, which has often been the subject of competition studies.

Another question that may arise is that of the experimental design of a competition study. The stimulation time, the duration of the stimulation and its intensity are often questions asked in relation to the optimization of this design aiming at increasing the chances of detection and characterization of a discharge. In this area too, the b-ntPET approach could be useful for this optimization process, based on the study of the probability distributions and the confidence intervals that b-ntPET can generate.

Lastly, simultaneously acquired PET/MR data can also be exploited to investigate and to characterize the link between the temporal evolution of the drug uptake to the target receptors measured by PET imaging and the cerebral activity/hemodynamic response occurring after administration of drugs measured by BOLD imaging (Sander et al., 2013).

6. CONCLUSION

We have introduced a novel method named b-ntPET, for the resolution of a kinetic model involving a displacement of radiotracer produced by an endogenous neurotransmitter release or a pharmacological challenge. The proposed approach is formulated in a stochastic framework, and provides the probability distribution of the parameters of the model in addition to their estimated values. The method also supplies the level of noise in the data which is estimated jointly with the model parameters for increased robustness.

REFERENCES

Alpert, N. M., Badgaiyan, R. D., Livni, E., and Fischman, A. J. (2003). A novel method for noninvasive detection of neuromodulatory changes

By evaluating the method on simulated and real datasets, we demonstrated that the proposed method has increased performance in terms of sensitivity and resistance to noise compared to the reference method lp-ntPET. These improvements lead to better results in terms of detection and characterization of the displacement.

As a conclusion, b-ntPET offers the possibility to reliably detect and characterize transient variation in receptor occupancy from a single PET scan.

DATA AVAILABILITY STATEMENT

The datasets generated for this study are available on request to the corresponding author.

ETHICS STATEMENT

The studies involving human participants were reviewed and approved by Ethics committee (CPP SUD EST 6, AU1148; ANSM, A01405-42) and registered on ClinicalTrials.gov (NCT02402101). The patients/participants provided their written informed consent to participate in this study. The animal study was reviewed and approved by Comité d'éthique en expérimentation animale neurosciences CELYNE (C2EA-42).

AUTHOR CONTRIBUTIONS

ZI conceived the original idea, developed the theoretical formalism, and carried out the implementation. ZI, IM, JR, AR, and NC conceived the experiments. ZI, IM, JR, AR, and NC designed and carried out the numerical simulations. BV collected the data from the experimental cat dataset. BV and LZ designed the cat study and aided in analyzing the associated data and interpreting the results. CF collected the data from the experimental human dataset. CF, MS-C, and JB designed the human study and aided in analyzing the associated data and interpreting the results. ZI wrote the manuscript and designed the figures with significant input from IM, AR, and NC. NC supervised this project and was in charge of overall direction. All authors provided critical feedback and helped shape the research, analysis, and manuscript.

FUNDING

This work was supported by the Fondation NEURODIS, the IHU CESAME and the French national programme Investissement d'Avenir Programmes (LILI—Lyon Integrated Life Imaging: hybrid MR-PET ANR-11-EQPX-0026) operated by the French National Research Agency (ANR).

in specific neurotransmitter systems. *NeuroImage* 19, 1049–1060. doi: 10.1016/S1053-8119(03)00186-1

Angelis, G. I., Gillam, J. E., Ryder, W. J., Fulton, R. R., and Meikle, S. R. (2019). Direct estimation of voxel-wise neurotransmitter response

- maps from dynamic pet data. *IEEE Trans. Med. Imaging* 38, 1371–1383. doi: 10.1109/TMI.2018.2883756
- Brooks, S. P., and Gelman, A. (1998). General methods for monitoring convergence of iterative simulations. *J. Comput. Graph. Stat.* 7, 434–455. doi: 10.1080/10618600.1998.10474787
- Ceccarini, J., Vrieze, E., Koole, M., Muylle, T., Bormans, G., Claes, S., et al. (2012). Optimized *in vivo* detection of dopamine release using 18f-fallypride pet. *J. Nucl. Med.* 53, 1565–1572. doi: 10.2967/jnumed.111.099416
- Constantinescu, C. C., Bouman, C., and Morris, E. D. (2007). Nonparametric extraction of transient changes in neurotransmitter concentration from dynamic pet data. *IEEE Trans. Med. Imaging* 26, 359–373. doi: 10.1109/TMI.2006.891501
- Fan, Y., Meikle, S. R., Angelis, G., and Sitek, A. (2016). ABC in nuclear imaging. *arXiv [Preprint]* arXiv:1607.08678.
- Fisher, R. E., Morris, E. D., Alpert, N. M., and Fischman, A. J. (1995). *In vivo* imaging of neuromodulatory synaptic transmission using pet: a review of relevant neurophysiology. *Hum. Brain Mapp.* 3, 24–34. doi: 10.1002/hbm.460030104
- Fonteneau, C., Redoute, J., Haesebaert, F., Le Bars, D., Costes, N., Suaud-Chagny, M.-F., et al. (2018). Frontal transcranial direct current stimulation induces dopamine release in the ventral striatum in human. *Cereb. Cortex* 28, 2636–2646. doi: 10.1093/cercor/bhy093
- Gousias, I. S., Rueckert, D., Heckemann, R. A., Dyet, L. E., Boardman, J. P., Edwards, A. D., et al. (2008). Automatic segmentation of brain mris of 2-year-olds into 83 regions of interest. *NeuroImage* 40, 672–684. doi: 10.1016/j.neuroimage.2007.11.034
- Gunn, R. N., Lammertsma, A. A., Hume, S. P., and Cunningham, V. J. (1997). Parametric imaging of ligand-receptor binding in pet using a simplified reference region model. *NeuroImage* 6, 279–287. doi: 10.1006/nimg.1997.0303
- Hammers, A., Allom, R., Koepp, M. J., Free, S. L., Myers, R., Lemieux, L., et al. (2003). Three-dimensional maximum probability atlas of the human brain, with particular reference to the temporal lobe. *Hum. Brain Mapp.* 19, 224–247. doi: 10.1002/hbm.10123
- Kim, S. J., Sullivan, J. M., Wang, S., Cosgrove, K. P., and Morris, E. D. (2014). Voxelwise lp-ntPET for detecting localized, transient dopamine release of unknown timing: sensitivity analysis and application to cigarette smoking in the pet scanner. *Hum. Brain Mapp.* 35, 4876–4891. doi: 10.1002/hbm.22519
- Kyme, A. Z., Angelis, G. I., Eisenhuth, J., Fulton, R. R., Zhou, V., Hart, G., et al. (2019). Open-field pet: simultaneous brain functional imaging and behavioural response measurements in freely moving small animals. *NeuroImage* 188, 92–101. doi: 10.1016/j.neuroimage.2018.11.051
- Lammertsma, A. A., Bench, C. J., Hume, S. P., Osman, S., Gunn, K., Brooks, D. J., et al. (1996). Comparison of methods for analysis of clinical [11c]raclopride studies. *J. Cereb. Blood Flow Metab.* 16, 42–52. doi: 10.1097/00004647-199601000-00005
- Lammertsma, A. A., and Hume, S. P. (1996). Simplified reference tissue model for pet receptor studies. *NeuroImage* 4, 153–158. doi: 10.1006/nimg.1996.0066
- Lancelot, S., Costes, N., Lemoine, L., and Zimmer, L. (2010). “Development and evaluation of a digital atlas for pet neuroimaging in domestic cat (*felis catus*)” in *European Journal of Nuclear Medicine and Molecular Imaging*, Vol. 37 (New York, NY: Springer), S387.
- Lataster, J., Collip, D., Ceccarini, J., Haas, D., Booij, L., van Os, J., et al. (2011). Psychosocial stress is associated with *in vivo* dopamine release in human ventromedial prefrontal cortex: a positron emission tomography study using [18f]fallypride. *NeuroImage* 58, 1081–1089. doi: 10.1016/j.neuroimage.2011.07.030
- Liu, H., and Morris, E. (2019). Controlling the false positive rate for lp-ntpet: A correction to goodness of fit metrics for “effective” number of parameters. *J. Nucl. Med.* 60(Suppl. 1):580. Available online at: http://jnm.snmjournals.org/content/60/supplement_1/580
- Mérida, I. (2017). *Development and application of multi-atlas attenuation correction for brain imaging with simultaneous PET-MR* (Theses), Université de Lyon, Lyon, France.
- Mérida, I., Olivier, F., Hammers, A., Redouté, J., Reilhac, A., Costes, N., and Irace, Z. (2018). “Kinetic modelling for endogenous neurotransmitter discharge characterization using pet imaging: optimization of lp-ntPET,” in *The XII International Symposium of Functional Neuroreceptor Mapping of the Living Brain (NRM18)* (London).
- Morris, E. D., Fisher, R. E., Alpert, N. M., Rauch, S. L., and Fischman, A. J. (1995). *In vivo* imaging of neuromodulation using positron emission tomography: optimal ligand characteristics and task length for detection of activation. *Hum. Brain Mapp.* 3, 35–55. doi: 10.1002/hbm.460030105
- Morris, E. D., Yoder, K. K., Wang, C., Normandin, M. D., Zheng, Q.-H., Mock, B., F. et al. (2005). ntPET: A new application of pet imaging for characterizing the kinetics of endogenous neurotransmitter release. *Mol. Imaging* 4:7290.2005.05130. doi: 10.2310/7290.2005.05130
- Normandin, M. D., and Morris, E. D. (2008). Estimating neurotransmitter kinetics with ntpet: a simulation study of temporal precision and effects of biased data. *NeuroImage* 39, 1162–1179. doi: 10.1016/j.neuroimage.2007.09.046
- Normandin, M. D., Schiffer, W. K., and Morris, E. D. (2012). A linear model for estimation of neurotransmitter response profiles from dynamic pet data. *NeuroImage* 59, 2689–2699. doi: 10.1016/j.neuroimage.2011.07.002
- Pappata, S., Dehaene, S., Poline, J., Gregoire, M., Jobert, A., Delforge, J., et al. (2002). *In vivo* detection of striatal dopamine release during reward: a pet study with [11c] raclopride and a single dynamic scan approach. *NeuroImage* 16, 1015–1027. doi: 10.1006/nimg.2002.1121
- Reilhac, A., Batan, G., Michel, C., Grova, C., Tohka, J., Collins, D. L., et al. (2005). Pet-sorteo: validation and development of database of simulated pet volumes. *IEEE Trans. Nucl. Sci.* 52, 1321–1328. doi: 10.1109/TNS.2005.858242
- Reilhac, A., Lartizien, C., Costes, N., Sans, S., Comtat, C., Gunn, R. N., et al. (2004). Pet-sorteo: a monte carlo-based simulator with high count rate capabilities. *IEEE Trans. Nucl. Sci.* 51, 46–52. doi: 10.1109/TNS.2003.823011
- Reilhac, A., Sjöholm, T., Thomas, B., et al. (2016). “Validation and application of pet-sorteo for the geometry of the siemens MMR scanner,” in *PSMR Conference* (Cologne).
- Robert, C. P., and Casella, G. (1999). *Monte Carlo Statistical Methods*. New York, NY: Springer-Verlag. doi: 10.1007/978-1-4757-3071-5
- Sander, C. Y., Hooker, J. M., Catana, C., Normandin, M. D., Alpert, N. M., Knudsen, G. M., et al. (2013). Neurovascular coupling to D2/D3 dopamine receptor occupancy using simultaneous pet/functional MRI. *Proc. Natl. Acad. Sci. U.S.A.* 110, 11169–11177. doi: 10.1073/pnas.1220512110
- Vidal, B., Fieux, S., Redouté, J., Villien, M., Bonnefoi, F., Le Bars, D., et al. (2018). *In vivo* biased agonism at 5-ht 1a receptors: characterisation by simultaneous pet/MR imaging. *Neuropsychopharmacology* 43, 2310–2319. doi: 10.1038/s41386-018-0145-2

Conflict of Interest: The authors declare that the research was conducted in the absence of any commercial or financial relationships that could be construed as a potential conflict of interest.

Copyright © 2020 Irace, Mérida, Redouté, Fonteneau, Suaud-Chagny, Brunelin, Vidal, Zimmer, Reilhac and Costes. This is an open-access article distributed under the terms of the Creative Commons Attribution License (CC BY). The use, distribution or reproduction in other forums is permitted, provided the original author(s) and the copyright owner(s) are credited and that the original publication in this journal is cited, in accordance with accepted academic practice. No use, distribution or reproduction is permitted which does not comply with these terms.



First Phantom-Based Quantitative Assessment of Scandium-44 Using a Commercial PET Device

Thiago V. M. Lima^{1,2,3*}, Silvano Gnesin², Egbert Nitzsche⁴, Pablo G. Ortega^{5,6}, Cristina Müller⁷ and Nicholas P. van der Meulen^{7,8}

¹ Radiation Protection Group, Aarau Cantonal Hospital (KSA) AG, Aarau, Switzerland, ² Institute of Radiation Physics, Lausanne University Hospital, University of Lausanne, Lausanne, Switzerland, ³ Institute of Radiology and Nuclear Medicine, Cantonal Hospital of Lucerne (LUKS) AG, Lucerne, Switzerland, ⁴ Institute of Nuclear Medicine and PET, Aarau Cantonal Hospital (KSA) AG, Aarau, Switzerland, ⁵ Institute of Fundamental Physics and Mathematics (IUFFyM), Salamanca, Spain, ⁶ Fundamental Physics Department, University of Salamanca, Salamanca, Spain, ⁷ Center for Radiopharmaceutical Sciences ETH-PSI-USZ, Paul Scherrer Institute, Villigen, Switzerland, ⁸ Laboratory of Radiochemistry, Paul Scherrer Institute, Villigen, Switzerland

OPEN ACCESS

Edited by:

Ivo Rausch,
Medical University of Vienna, Austria

Reviewed by:

Terence Riauka,
University of Alberta, Canada
Simon Ferguson,
University of Alberta, Canada, in
collaboration with reviewer TR
Andreas Renner,
Vienna General Hospital, Austria

*Correspondence:

Thiago V. M. Lima
thiago.lima@luks.ch

Specialty section:

This article was submitted to
Medical Physics and Imaging,
a section of the journal
Frontiers in Physics

Received: 15 December 2019

Accepted: 03 June 2020

Published: 10 July 2020

Citation:

Lima TVM, Gnesin S, Nitzsche E,
Ortega PG, Müller C and van der
Meulen NP (2020) First
Phantom-Based Quantitative
Assessment of Scandium-44 Using a
Commercial PET Device.
Front. Phys. 8:241.
doi: 10.3389/fphy.2020.00241

Scandium (Sc) is a promising candidate for theranostic applications due to the existence of radioisotopes suitable for both imaging and therapy. A “proof-of-concept” study regarding first-in-human use of ⁴⁴Sc for imaging metastatic neuroendocrine tumors was reported recently, however, quantitative assessment of ⁴⁴Sc-based PET images was not performed. The aim of this study was to evaluate quantitative capabilities of ⁴⁴Sc-PET using a commercial PET scanner. The NEMA/IEC body phantom with ⁴⁴Sc was acquired according to the local protocol used for whole-body oncological [¹⁸F]FDG PET examinations. Additionally, we characterized the signal recovery (recovery coefficient—RC) according to the iteration number. For all reconstructions, pertinent image corrections (normalization, dead time, activity decay, random coincidence, and attenuation) were applied. Presently, ⁴⁴Sc scatter corrections are not optimized and could, thus, result in quantitative bias. To investigate the best option, the data were reconstructed using different available scatter corrections (relative -RelSC- and absolute -AbsSC-) and an additional prompt-gamma correction (PGC). System cross-calibration with the local dose calibrator (BG_{cal}) and image noise, expressed by the coefficient of variation (COV), were evaluated in the homogeneous background region (5 kBq/mL) of the phantom. Maximum (RC_{max}) and 50% threshold recovery coefficients, corrected for background (RC_{A50}), were measured for all spherical inserts (25 kBq/mL) of the phantom. Acceptable COV (<15%) was achievable with low iteration numbers (<3). BG_{cal} differences were low: mean BG_{cal} were 77.8, 81.3, and 86.7%, for RelSC, AbsSC, and PGC, respectively. RC values exceeded the present RC range recommended for [¹⁸F]FDG procedures. Using the iterations to be evaluated, RC_{A50} ranged from 29.9 to 59.9% for the smallest lesion (spherical insert of 10 mm diameter) and from 45.5 to 80.3% (13 mm), 66.4 to 75.6% (17 mm), 71.7 to 75.7% (22 mm), 75.1 to 78.6% (28 mm), and 76.7 to 80.9% (37 mm) for the, respectively spherical inserts. The results of

this study show that clinical ^{44}Sc -PET imaging has the potential to provide signal recovery in lesions of different sizes comparable to current ^{18}F -PET standards. In order to improve the quantitative accuracy of ^{44}Sc PET, optimized corrections are still necessary and will be investigated further in future.

Keywords: PET imaging, quantification, ^{44}Sc , theranostic, scatter correction, prompt-gamma correction

1. INTRODUCTION

Clinical theranostic application of ^{68}Ga ($T_{1/2} = 68$ min, $E\beta_{av}^+ = 830$ keV, $I = 89\%$) and ^{177}Lu ($T_{1/2} = 6.65$ d, $E\beta^-_{av} = 134$ keV, $I = 100\%$; $E\gamma = 113$ keV $I = 6\%$, 208 keV $I = 10\%$) is now common for PET imaging and targeted radionuclide therapy, respectively. The $^{68}\text{Ga}/^{177}\text{Lu}$ theranostic couple is used for labeling with somatostatin analogs (e.g., DOTATOC or DOTATATE) and, more recently, also for PSMA-targeting ligands (e.g., PSMA-11 and PSMA-617), thereby, enabling radiotheranostics of neuroendocrine and prostate cancer, respectively [1–4].

PET is currently regarded as a more sensitive technology than SPECT and provides images with superior spatial resolution and improved quantification [5]. The switch from ^{111}In -based SPECT imaging, such as ^{111}In -octreotide, to the use of ^{68}Ga for PET imaging, represents a cornerstone in nuclear medicine: [^{68}Ga]Ga-DOTATATE demonstrated significantly superior image quality and, hence, outperformed ^{111}In -octreotide in both diagnostic accuracy and impact on treatment decisions [6].

^{68}Ga is obtained from a $^{68}\text{Ge}/^{68}\text{Ga}$ -generator system, which can be conveniently placed in a radiopharmacy at any hospital. The availability of ^{68}Ga is, however, restricted with regard to activity that can be eluted for radiopharmaceutical preparation, while the generator itself is also costly. A drawback of using ^{68}Ga , however, is its short half-life of only 68 min (compared to 2.81 d for ^{111}In), which does not allow scanning at late time points after injection nor transportation of ^{68}Ga -based radiopharmaceuticals over longer distances (when a $^{68}\text{Ge}/^{68}\text{Ga}$ generator is not present on site). Optimally, the physical half-life is identical to the biological half-life and ^{44}Sc can be used with targeting agents that are retained longer in the body. As an example, ^{44}Sc may be viable in the use of albumin-binding radiopharmaceuticals, which have longer circulation time [7]. Finally, it remains to be mentioned that ^{68}Ga has a different coordination chemistry compared to ^{177}Lu , therefore, ^{68}Ga results in different chelator-radiometal complexes and, hence, chemically unequal radiopharmaceuticals. This may result in different *in vivo* uptake patterns for both diagnostic and therapeutic radioligands [8–10].

Several years ago, ^{44}Sc was proposed as an alternative PET nuclide [11, 12]. The physical decay properties [13] of ^{44}Sc ($T_{1/2} = 4.04$ h, average $E\beta^+ = 632$ keV, $I = 94\%$) are attractive to address the shortcomings of ^{68}Ga mentioned above. It decays with an almost four-fold longer half-life than ^{68}Ga [13] by emitting relatively low energy β^+ -particles that enables the acquisition of PET images with a spatial resolution equal or even superior to that achievable with ^{68}Ga [14]. The coordination chemistry allows the preparation of ^{44}Sc -radioconjugates using a DOTA-chelator in analogy with

^{177}Lu -labeling [9]. Preclinical experiments in mice showed almost identical distribution patterns for ^{44}Sc - and ^{177}Lu -labeled ligands [10, 11]. Consequently, ^{44}Sc may be adopted as a more favorable diagnostic match to ^{177}Lu than ^{68}Ga . In future, ^{47}Sc ($T_{1/2} = 3.35$ d, average $E\beta^- = 162$ keV, $I = 100\%$; $E\gamma = 159$ keV $I = 68\%$) can be employed as a therapeutic match to provide chemically-identical $^{44}\text{Sc}/^{47}\text{Sc}$ -based radiopharmaceuticals for radiotheranostic applications [15–17]. A possible addition to the scandium radioisotope family, due to its theoretically more favorable characteristics for PET imaging, is ^{43}Sc [18]. Although it provides possible advantages in terms of gamma emission, it is currently more challenging to produce in terms of yield, as well as cost [19, 20].

Rösch and co-workers performed preliminary studies using ^{44}Sc obtained from a $^{44}\text{Ti}/^{44}\text{Sc}$ generator system [21]. First PET images of a patient administered with [^{44}Sc]Sc-DOTATOC looked promising, where somatostatin-receptor-positive liver metastases were imaged and visible 18 h after administration of 37 MBq [22]. It was later proposed to produce ^{44}Sc at a cyclotron using natural Ca targets, in an attempt to simplify production and increase yield [23, 24]. At PSI, it was demonstrated for the first time that ^{44}Sc can also be produced in high quantities and good quality when using enriched ^{44}Ca targets [11, 25]. In recent years, the production was constantly improved, currently enabling the preparation of up to 5 GBq ^{44}Sc with small quantities of target material. This production method may be translated to a conventional medical cyclotron commonly installed in PET centers. Subsequently, the application of cyclotron-produced ^{44}Sc in two patients with neuroendocrine neoplasms, receiving a diagnostic administration of [^{44}Sc]Sc-DOTATOC at Zentralklinik Bad Berka (Germany), was reported [26]. First-in-man studies with [^{44}Sc]Sc-PSMA-617, using generator-produced ^{44}Sc , were reported recently in the literature, underlining the excellent features of ^{44}Sc in a clinical setting [27].

Despite the reported clinical advantages of ^{44}Sc , its use could potentially be restricted by the currently limited quantification capability of clinical devices. The first reported human study using ^{44}Sc [26] indicated that absolute quantification was not available, but the authors did not discuss this limitation further. Other studies on the use of non-pure positron emitters started evaluating this limitation. In particular, the importance of adopting adapted and optimized corrections in the acquisition and reconstruction process, in achieving quantitative imaging in clinical setups, was highlighted. As an example, the work by Armstrong et al. [28] addressed the impact of prompt-gamma coincidence inducing quantitative artifacts and underlined the important role of specific corrections in absolute quantification using ^{82}Rb cardiac imaging. The study by Lubberink and Herzog

[29] reviewed different optimization strategies for improving quantification of ¹²⁴I and ⁸⁶Y, including effects from scatter and prompt-gamma corrections.

The aim of this paper was to evaluate the quantification capabilities of ⁴⁴Sc in a clinically-relevant phantom configuration study performed with a commercial PET scanner.

2. MATERIALS AND METHODS

The experimental design presented in this work included (a) image acquisitions of a NEMA/IEC NU2 phantom (see sections 2.1, 2.2) and (b) the subsequent data analysis (see sections 2.3, 2.4). The phantom was scanned under clinically-relevant conditions at the Aarau Cantonal Hospital (KSA) using a mCT Biograph PET-CT (Siemens Healthineers AG) [30]. ⁴⁴Sc was produced via the ⁴⁴Ca(p,n)⁴⁴Sc nuclear reaction at Injector 2 cyclotron facility at Paul Scherrer Institute (PSI), Switzerland, as previously reported [25, 26].

The reference activity received from PSI was used to perform a cross calibration of the local dose calibrator (Veenstra Instruments, Joure, Netherlands VDC-405 with ionization chamber VIK-202). At PSI, the nuclide content in the irradiated targets was identified and quantified by γ -ray spectrometry using an N-type high-purity germanium (HPGe) coaxial detector (EURISYS MESURES, France) and the Ortec InterWinner 5.0 software. A dose calibrator (ISOMED 2010, Nuclear-Medizintechnik Dresden GmbH, Germany) was employed for the quantitative determination of ⁴⁴Sc activity [20]. The reference activity was measured at the end of chemical separation and the time noted, before packing and transportation. This reference activity and time, on its original vial, was used to cross calibrate the local dose calibrator by modifying the isotope settings (factor and scale) to match this reference activity. The factor obtained was then used for all dispensing syringe activities. The activities obtained for various settings, along with the setting chosen for ⁴⁴Sc, are listed in **Table 1**. All measurements were decay-corrected to the reference activity. These values were then used to estimate the injected activity (IA) used to fill the main phantom volume (background volume) and the included spherical inserts, representing lesions. The ⁴⁴Sc cross-calibrated factor (presented in **Table 1**) was then used for all activity dispensing.

TABLE 1 | Reference activity and employed factors for determination of the local dose calibrator factor for ⁴⁴Sc measurements.

Radionuclide	Setting (Factor and scale)	Measurement (GBq)
Ga-68	751 scale 1	2.116
F-18	765 scale 1	1.401
Co-60	889 scale 1	0.392
Sc-44	760 scale 0.56	0.594
Reference activity		0.595

All measurements were decay-corrected to the reference time provided by PSI. The factor is constrained to a given range (0–900) and for some radionuclides, a scale different than 1 is also needed.

2.1. Phantom Preparation

The NEMA/IEC NU2 phantom (PTW, Freiburg, Germany) used in this study enabled the characterization of image quality and quantitative signal recovery in the main background phantom volume and in spherical structures of different size potentially affected by partial-volume-effect (PVE). The NEMA/IEC phantom is composed of a main volume (background) of 9.5 L that mimics the human abdominal shape. The phantom includes a set of hollow-glass-sphere inserts of variable diameters: 10, 13, 17, 22, 18, and 37 mm, respectively. In addition, a lung insert (5-mm-diameter and 16-cm-long cylinder filled with plastic material to reproduce the lung density of 0.3 g/mL) was placed in the center of the phantom to simulate lung tissue attenuation. The phantom was filled with a background activity concentration of 5 kBq/mL and a five-fold higher activity concentration (25 kBq/mL) in the spherical inserts. The activity concentration and background ratio used was chosen to mimic the average hepatic activity concentration measured in patients when using [¹⁸F]FDG oncological PET 1 h after administration of a mass-activity of 3.5 MBq/kg. This corresponded to the recommended dose reference level in Switzerland at the time of this study for this specific examination [31]. The adopted experimental setup allowed comparison with previously published results obtained with [¹⁸F]FDG for the same device [31].

2.2. PET Acquisition and Reconstructions

The Siemens mCT PET, utilized for the phantom acquisitions performed in this work, consists of 4 rings, with 48 detector blocks in each ring and lutetium oxyorthosilicate (LSO) crystals, a PET field-of-view (FOV) of 22.1 cm and transaxial FOV of 70 cm. The detector ring diameter is 84.2 cm, the reported time coincidence window is 4.1 ns, system time-of-flight (TOF) 540 ps, and energy window 435–650 keV. The phantom was placed on the PET bed to have the equatorial plane of the spherical inserts at the center of the device FOV, where the system sensitivity is expected to be at its maximum. A single-bed, step-and-shoot, 300 s, list-mode (LM) acquisition was performed. The LM data were reconstructed according to the local clinic protocol used for whole-body oncological [¹⁸F]FDG PET examinations, with acquisition time of 150 s per bed position. For the acquisition, the vendor specific setup for the radionuclide ⁴⁴Sc was selected, taking a positron fraction of 0.9427 and half-life of 3.97 h into consideration.

Supplementary reconstructions were performed, in addition to the local clinical protocol, by varying the number of iterations from 1 to 10 with 21 fixed subsets. This was done in order to characterize the convergence of the signal recovery in background areas, the spheres, and the lung. Reconstructions were performed using the TOF information and the point-spread function correction implemented in the vendor-based iterative reconstruction algorithm (TrueX + TOF - ultraHD-PET).

2.3. Data Analysis

2.3.1. PET vs. Dose Calibrator Activity Cross-Calibration (BG_{cal})

The PET to local dose calibrator activity cross calibration (BG_{cal}) was tested by calculating the ratio between the measured PET

signal ($\bar{A}_{c,bg}$) and the expected average activity concentration ($A_{c,bg}$) evaluated in the homogeneous background regions of the phantom:

$$BG_{cal} = \frac{\bar{A}_{c,bg}}{A_{c,bg}} \quad (1)$$

$\bar{A}_{c,bg}$ was measured in four cubic regions of interest (40 mm per side) placed in the homogeneous background region of the phantom which surrounded the spheres. When using [¹⁸F]FDG, a deviation <0.1 from the ideal $BG_{cal}=1$ is regarded as acceptable.

2.3.2. Noise

The image noise was evaluated by the coefficient of variation (COV), which is the ratio between the standard deviation and the average activity concentration measured in same cubic volumes of interest (VOIs) of the phantom background described above for the cross-calibration assessment:

$$COV(\%) = \frac{SD_{bg}}{\bar{A}_{bg}} * 100 \quad (2)$$

The background signal-to-noise ratio (SNR) is the reciprocal of the COV. A $COV \leq 15\%$ (background $SNR \geq 6.7$) was considered as an acceptable noise level for clinical image interpretation, as suggested in the EARL procedure [32]. Although this value is somehow arbitrary, it has already been used as a reference value in previously-published works [33–35], which enables a term of comparison for image quality assessments.

2.3.3. Average Residual Lung Error

A cylindrical VOI 30 mm in diameter and 120 mm in length was included in the lung insert. The average residual lung error (in %) was obtaining by:

$$\overline{LE}(\%) = \frac{\bar{L}_c}{\bar{A}_{c,bg}} * 100 \quad (3)$$

where \bar{L}_c is mean counts in the lung region and $\bar{A}_{c,bg}$ is the average activity concentration in the background region.

2.3.4. Recovery Coefficient

A VOI, with a side of 50 mm in length, was centered on each of the six spheres of the phantom. For each spherical insert ($j = 1 \dots 6$) the maximum and the background-adapted recovery coefficients (RC) were obtained as follows:

$$RC_{j,max}(\%) = \frac{a_{c,sph,j,max}}{A_{c,sph}} * 100 \quad (4)$$

$$RC_{j,A50}(\%) = \frac{a_{c,sph,j,A50}}{A_{c,sph}} * 100 \quad (5)$$

where $A_{c,sph}$ is the expected activity concentration in the spheres, $a_{c,sph,j,max}$ is the measured maximum voxel value (in terms of activity concentration) for a given spherical insert. $a_{c,sph,j,A50}$ is, for each considered spherical insert, the average voxel value in a VOI, defined by a 3D-iso-contour adapted for background [as defined in [32]] as recommended by the EANM Guidelines for [¹⁸F]FDG tumor PET imaging [35]. The numerator of Equation (5), for a given sphere j , is the average activity concentration computed from voxels in the $VOI_{sph,j,A50}$. The $VOI_{sph,j,A50}$ includes all voxels with activity concentration $\geq (ac_{j,max} + \bar{A}_{c,bg})/2$, where $ac_{j,max}$ is a maximum activity concentration assumed in the hot sphere j . RC calculations were performed using a Matlab script.

Calculated RC_{max} and RC_{A50} values were compared with reference values provided by the EANM/EARL accreditation protocol [36].

2.3.5. Evaluation of Available Scatter and Prompt Gamma Corrections

Pertinent image corrections (normalization, dead time, activity decay, random coincidence, and attenuation) were applied to all reconstructions performed. A known limitation that applies to radionuclides not routinely used in clinical studies (particularly if they are non-pure positron emitters) exists on the applied system corrections that were optimized for the ¹⁸F PET setting and not, in this case, for the ⁴⁴Sc.

For this reason, along with the clinical corrections, all possible scatter corrections available in the iterative reconstruction algorithm (relative and absolute scatter corrections) were tested, thereby, producing a set of dedicated reconstructions [37]. Additionally, we applied the available prompt-gamma correction (PGC) [38] to evaluate the contributions of high-energy γ -emissions of ⁴⁴Sc to the quantitative accuracy of reconstructed PET images.

Evaluated scatter methods differ mainly on the procedure used to account for scatter events at the sinogram level [39]. The absolute scatter correction relies on the single scatter estimation (SSS) algorithm [37], which estimates the scatter distribution produced by a single scatter event and integrates this contribution over the whole acquired FOV volume. The relative scatter correction, on the other hand, scales the SSS (plane-by-plane) to the net trues based on a scaling mask computed outside the emission object. The volume covered by the emission object is known from the transmission sinogram obtained from the CT acquisition. Based on the CT information, the emitting object and the outside region masks are generated and applied to correct the emission object sinogram. Similar to the methodology, the PGC is estimated by the single event rates. The PG model is combined with a scatter sinogram estimated by the SSS algorithm, and the total background model is scaled to fit the tails of the measured data [38]. Additionally, further contributions from PGC can be addressed as described by Armstrong et al. [28] and Lubberink and Herzog [29].

Statistical analyses were performed with Python Scipy statistical module using the Wilcoxon signed rank test. Additionally, differences between the obtained COV and BG_{cal} were calculated between the reconstructions obtained in

comparison to the original/reference reconstruction (absolute scatter correction with PSF and TOF).

$$\text{Difference}(\%) = \frac{S_{\text{refrecon}} - S_{\text{testedrecon}}}{S_{\text{refrecon}}} * 100 \quad (6)$$

3. RESULTS

The effect of the iteration number on the noise (COV), average residual lung error and the BG calibration obtained in the tested reconstructed images are presented in **Figure 1**.

Noise level within acceptable ranges (15% was used as level of comparison to [¹⁸F]FDG [32]) is achievable with low iteration numbers (iterations ≤ 3 when subsets = 21) and increases as the iteration number increases for all evaluated corrections.

Figure 1 also shows the effect of the used scatter correction (SC) model (absolute vs. relative) on the obtained COV and background calibration values. The main observed result is the reduced background calibration level obtained for reconstructions employing the relative scatter in comparison to other evaluated corrections. The BG calibration values did not vary with the tested number of iterations, averaged at 0.81 (± 0.01), 0.78 (± 0.01), and 0.87 (± 0.01), respectively for the absolute scatter correction, relative scatter correction and PGC. With the results obtained with PGC, it was observed that the BG calibration improved in relation to the original (absolute scatter correction and no PGC), and the previously-evaluated relative scatter. Both differences were statistically significant with p -value < 0.001 . **Figure 1** also shows the average residual lung error obtained.

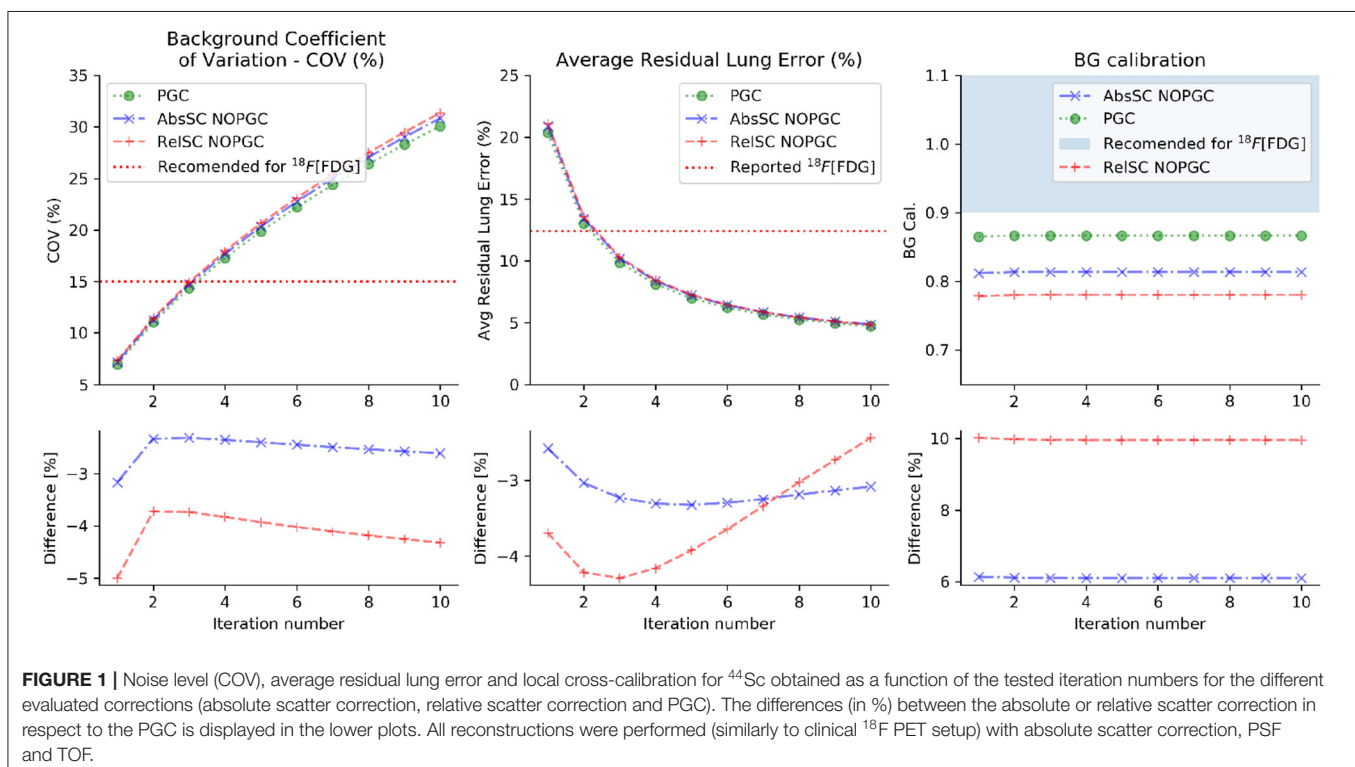
Additionally, **Figure 1** shows that the average residual lung error reduces with the increase of iteration number and a small difference ($\leq 4\%$) was observed between the evaluated corrections.

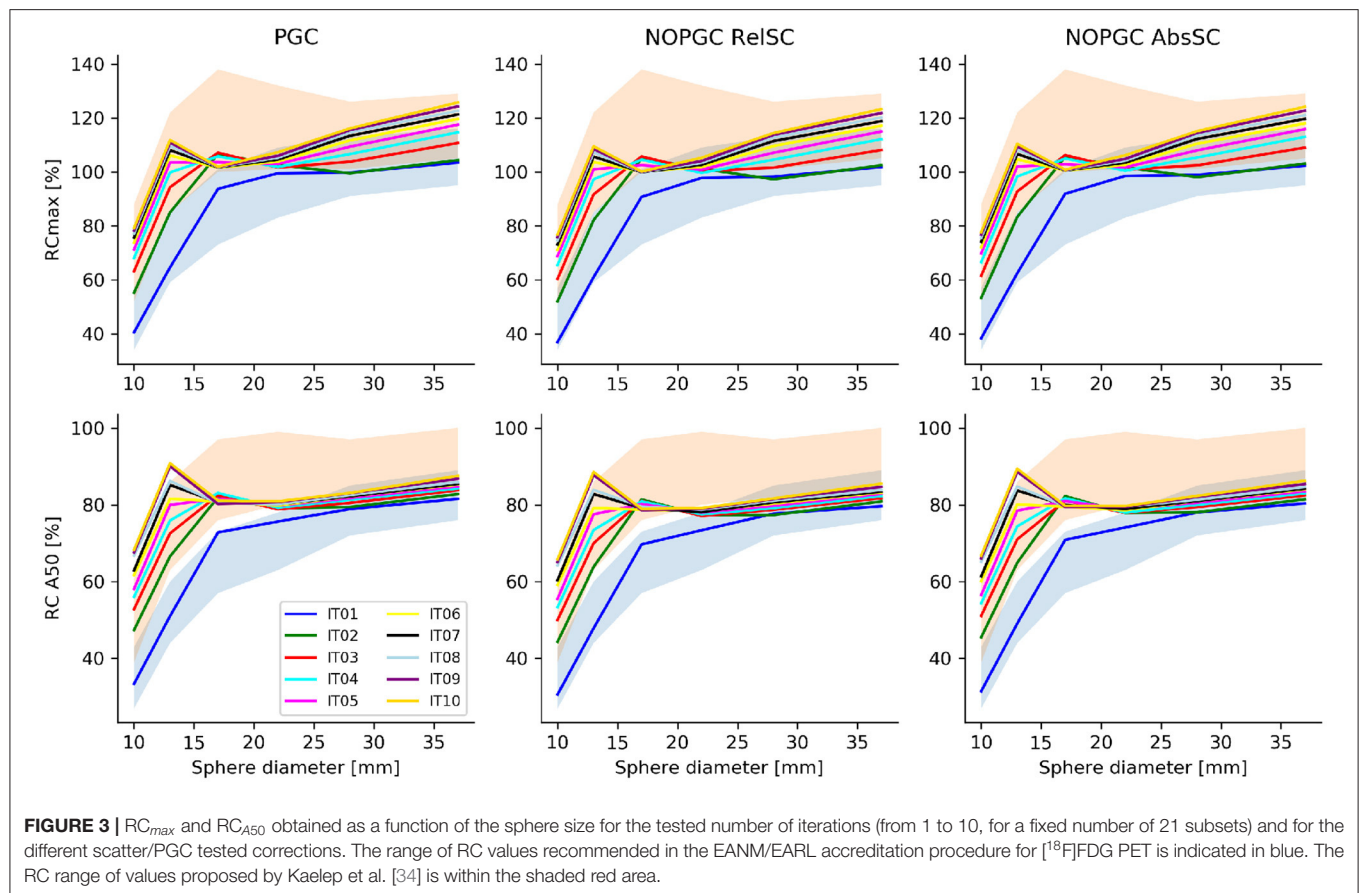
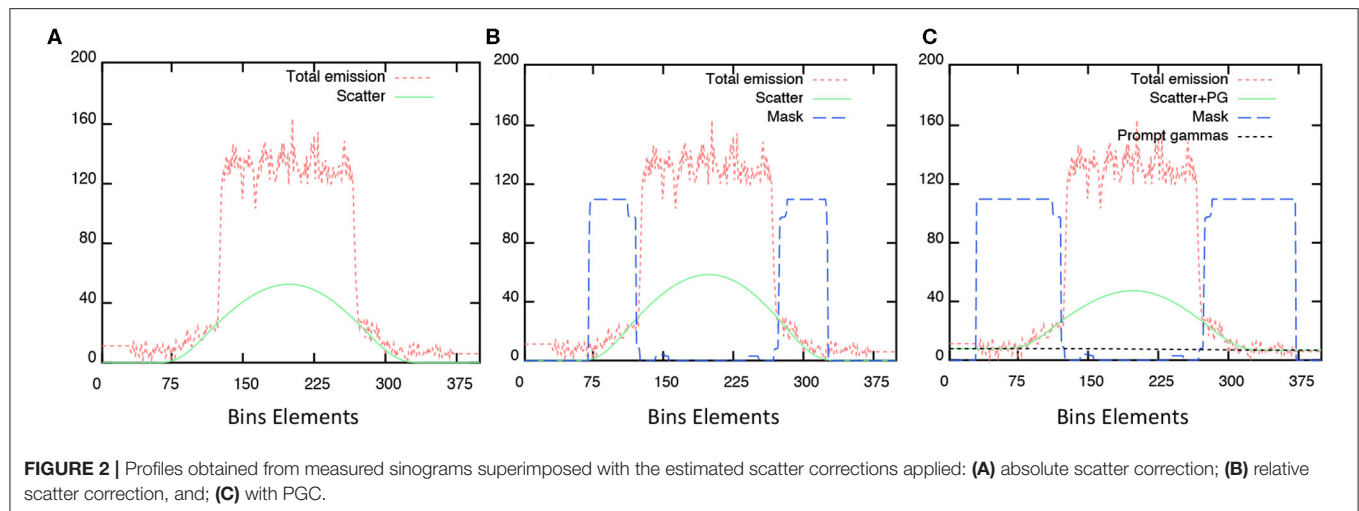
Figure 2 shows scatter corrections and PGC profiles obtained on the acquired sinogram. All plots discriminate the contributions from the emission and scatter estimate sinograms and the subtraction mask used for scatter modeling without (B–relative scatter) and with PGC (C), respectively. Differences depends on the size of the applied scatter mask (blue dashed line) and, subsequently, the extrapolation of events obtained outside the central part of the sinogram and the scaled scatter estimate (green line). Noticeably, the initial scatter sinogram (SSS) is further overestimated with the relative scatter by using the wider mask, the PGC is able to improve the applied correction. The effect of this was seen in the BG calibration in **Figure 1**.

Lastly, recovery coefficients were evaluated for all reconstructed PET images, depending on the applied correction (PGC, no PGC with absolute scatter correction and no PGC with relative scatter correction), as a function of the number of iterations. **Figure 3** shows the obtained RC_{A50} and RC_{max} for all spherical inserts of the phantom across the evaluated reconstructions.

4. DISCUSSION

In this work, the quantitative capabilities of a clinical PET/CT device using ⁴⁴Sc in a well-characterized phantom-based setup was investigated for the first time. Quantitative ⁴⁴Sc PET/CT





performances were compared with reference performance levels known for the well-established ^{18}F PET imaging. We reported quantitative accuracy (BG calibration) and noise level (COV) assessed in a PVE-free background volume (the main volume of the NEMA/IEC NU2 phantom) and recovery coefficients obtained in spherical inserts of different size. In particular, we investigated the impact of different scatter models and PGC available in the vendor-based iterative reconstruction algorithm.

With regard to the noise, the results presented showed that, with clinically relevant activity concentrations, scan duration and reconstruction setups, noise levels below 15% can be achieved for a low number of iterations. These results, in terms of noise levels and, additionally, to the average residual lung error, are comparable to published results obtained with ^{18}F FDG [31, 40] in similar clinical configurations for the same device.

Of note, it was found, according to the local dose calibrator cross-calibration, that the background quantitative signal was significantly below the acceptable performance levels considered for commonly-used PET radionuclides (for instance, BG_{cal} out of the 1 ± 0.1 range defined as acceptable for ^{18}F ; **Figure 1**). In a recent publication [41], the authors reported the results from a survey across Dutch hospitals (8 centers, 13 different PET/CT), describing performance standard achievable in quantitative PET for both ^{68}Ga and ^{18}F . In particular, they found a system cross-calibration within 15% deviation in all tested devices and within 10% in 10 of 13 devices. We previously reported a background cross calibration of <5% deviation using ^{18}F for the mCT PET/CT system used in this work [31].

The low level of the measured background activity concentration could possibly be attributed to the specificity of the ^{44}Sc decay (non-pure positron emission with associated high-energy prompt-gamma emission) which would significantly bias quantitative PET images in absence of optimized scatter and prompt-gamma corrections.

We initially considered the measured low level of BG calibration potentially ascribed to a non-appropriate scatter correction which, in the specific case, acted as an over-correction that resulted in an artificial depletion of the signal from the background volume. Further reconstructions were, therefore, performed using the scatter correction methods (relative

and absolute) available from the vendor-based reconstruction algorithm implemented in the tested commercial PET/CT device.

Based on the results presented in this study, the available PGC improved the absolute quantitative accuracy of ^{44}Sc PET, in agreement with results reported by Armstrong et al. [28] and Lubberink and Herzog [29] for other PET radionuclides. The impact of this correction is visible in **Figure 2**, where the overall scatter contribution was reduced, subsequently, improving the quantitative accuracy of the recovered activity concentration in the phantom background (**Figure 1**). The PGC fraction, although small, was not negligible: the difference between PGC reconstruction and non-PGC reconstructions was significant in terms of background calibration (p-values < 0.01 for non-PGC absolute and relative scatter corrections, respectively). Although the application of the PGC resulted in an improved quantitative accuracy, this was still well below accuracy levels obtained for ^{18}F and ^{68}Ga , which could indicate that further optimization could be performed. The average residual lung error was also found to be close to the reported ^{18}F values for a similar device [40].

According to data presented in **Figure 3**, we observed that, even in the presence of a sub-optimal signal recovery, the uniform background, the signal recovery for spherical inserts with a diameter of <20 mm exceeded the reference range on values provided by the EANM/EARL recommendation [33]. It has been observed that RC values significantly higher than

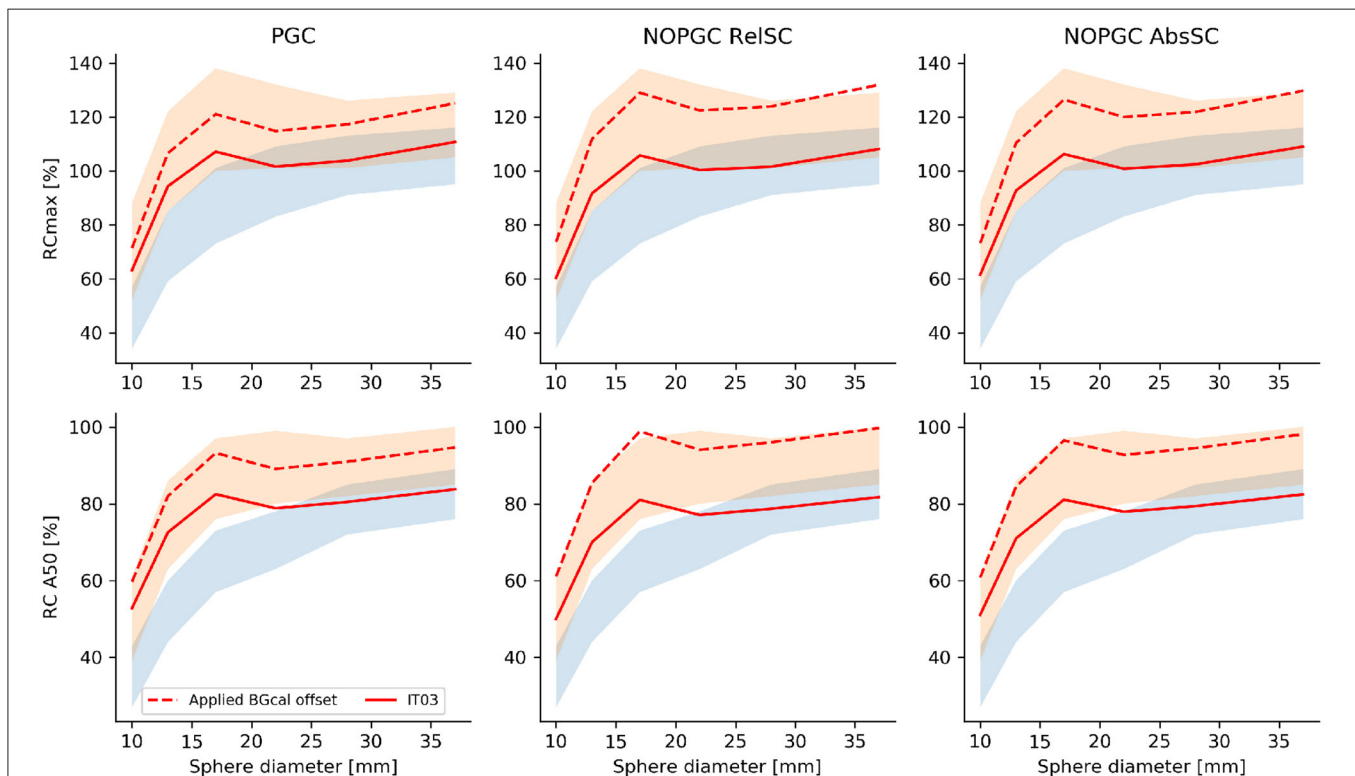


FIGURE 4 | RC_{max} and RC_{A50} obtained as a function of the sphere size for the optimal reconstruction (3 iterations and 21 subsets) and for the different scatter/PGC tested corrections (red full lines). Additionally we presented corrected RCs obtained by compensating for the low BGcal measured in the PET reconstructions to match a BGcal offset of 1 (red dashed lines). The EANM/EARL reference range of values is within the blue shaded area, the RC range of values proposed by Kaelap et al. [34] is within the red shaded area.

EANM/EARL reference values are commonly obtained when iterative reconstruction using both PSF and TOF information are used [34]. For this reason, the recommended range of RC values recommended by Kaalep et al. was also considered (red shaded area in **Figure 3**). Recovery coefficients (RC_{A50}) were [31.5:66.8], [45.5:80.3], [66.4:75.6], [71.7:75.7], [75.1:78.6], and [76.7:80.9] for the 10, 13, 17, 22, 28, and 37 mm spherical inserts, respectively, on the reconstruction with absolute scatter and no PGC; confirming a quantitative signal recovery in the lower range of the values provided by Kaalep et al. [34]. To compensate for the quantitative offset caused by the background calibration ($\text{BGcal} < 1$), we presented, for the optimal reconstruction setup (3 iterations), corrected RCs obtained by scaling up the measured RCs presented in **Figure 3** by the respective BGcal offset compared to $\text{BGcal} = 1$ adopted in the NEMA approach. Corrected RCs are shown in **Figure 4** and falls well within the range of values proposed by Kaalep et al. [34], for PET reconstructions adopting TOF and PSF information. This observation further supports the hypothesis that achievable signal recovery in ^{44}Sc PET is comparable to that achievable with ^{18}F and ^{68}Ga .

4.1. Limitations

This paper focused on the quantitative accuracy performances of a clinical PET scanner to quantify ^{44}Sc . The present study does not investigate possible sources of quantitative bias, such as the effect of the positron range, in addition to the configured branching factor and its impact on quantification of ^{44}Sc .

A possible explanation for the measured low level of background calibration could arise from the methodology adopted to determine the ^{44}Sc activity. In this work the cross calibration relied on a reference activity value provided by PSI. The obtained factor was then used for all dispensing syringe activities. A different approach described in the literature [12, 42] defines the absolute ^{44}Sc activity as the measured activity using the ^{18}F dose calibrator settings multiplied by a factor (0.7). Although this approach has been tested, we found that this doesn't correlate to our findings. By using this approach, we would have received 980.7 MBq at the reference time although the dispatched activity was 595.0 MBq. As a result, this approach was not further considered.

Phantom preparation and data analysis applied in our study differs in some points from the EARL (or NEMA) procedures (for instance, the lesion-to-background activity concentration ratio) and might impair a full comparability of results obtained with the cited procedures. Nevertheless, we consider that comparing our results with EARL proposed reference values (for the COV and RCs) would still be meaningful.

5. CONCLUSION

In this work, we evaluated the capability of a commercial PET/CT device to produce accurate quantitative imaging with ^{44}Sc , for

the first time. We performed dedicated ^{44}Sc PET acquisitions using a controlled and clinical relevant phantom-based setup. Quantitative ^{44}Sc PET performances, in terms of quantitative accuracy and noise levels, were shown to be comparable to that achieved in ^{18}F PET. In particular, this study outlined that available scatter and prompt-gamma corrections plays an important role in ^{44}Sc PET quantification. In view of a broader clinical application of ^{44}Sc -based radiopharmaceuticals, it is essential to further improve and optimize these features.

DATA AVAILABILITY STATEMENT

The datasets generated for this study are available on request to the corresponding author.

AUTHOR CONTRIBUTIONS

All listed authors made substantial contributions in all four of the following categories.

- Substantial contributions to the conception or design of the work, or the acquisition, analysis, or interpretation of data for the work.
- Drafting the work or revising it critically for important intellectual content.
- Provide approval for publication of the content.
- Agree to be accountable for all aspects of the work in ensuring that questions related to the accuracy or integrity of any part of the work are appropriately investigated and resolved.

More specifically, TL, SG, EN, CM, and NM coordinated the project and set up the framework. NM and CM coordinated the ^{44}Sc production. TL and SG performed the phantom preparation, measurements, and analysis. PO contributed to the data analysis.

FUNDING

CM and NM were supported by the Swiss National Science Foundation (IZLIZ3-156800).

ACKNOWLEDGMENTS

The authors thank Alexander Sommerhalder and Walter Hirzel, Radionuclide Production and Maintenance group at the Center for Radiopharmaceutical Sciences, PSI, for technical assistance toward the production of ^{44}Sc , as well as the people responsible for radioactive transports. Additionally, the authors would like to thank Dr. M. Conti and Dr. H. Bal from Siemens Healthineers AG for their support and discussions on the current and research corrections.

REFERENCES

1. Afshar-Oromieh A, Holland-Letz T, Giesel FL, Kratochwil C, Mier W, Haufe S, et al. Diagnostic performance of ⁶⁸Ga-PSMA-11 (HBED-CC) PET/CT in patients with recurrent prostate cancer: evaluation in 1007 patients. *Eur J Nucl Med Mol Imaging*. (2017) **44**:1258–68. doi: 10.1007/s00259-017-3711-7
2. Fendler WP, Rahbar K, Herrmann K, Kratochwil C, Eiber M. ¹⁷⁷Lu-PSMA radioligand therapy for prostate cancer. *J Nucl Med*. (2017) **58**:1196–200. doi: 10.2967/jnumed.117.191023
3. Haug AR, Cindea-Drum R, Auernhammer CJ, Reincke M, Wängler B, Uebles C, et al. The role of ⁶⁸Ga-DOTATATE PET/CT in suspected neuroendocrine tumors. *J Nucl Med*. (2012) **53**:1686–92. doi: 10.2967/jnumed.111.101675
4. Kwekkeboom DJ, Kam BL, Van Essen M, Teunissen JJ, van Eijck CH, Valkema R, et al. Somatostatin receptor-based imaging and therapy of gastroenteropancreatic neuroendocrine tumors. *Endocr Relat Cancer*. (2010) **17**:R53–73. doi: 10.1677/ERC-09-0078
5. Rahmim A, Zaidi H. PET versus SPECT: strengths, limitations and challenges. *Nucl Med Commun*. (2008) **29**:193–207. doi: 10.1097/MNM.0b013e3282f3a515
6. Deppen SA, Blume J, Bobbey AJ, Shah C, Graham MM, Lee P, et al. ⁶⁸Ga-DOTATATE compared with ¹¹¹In-DTPA-octreotide and conventional imaging for pulmonary and gastroenteropancreatic neuroendocrine tumors: a systematic review and meta-analysis. *J Nucl Med*. (2016) **57**:872–8. doi: 10.2967/jnumed.115.165803
7. Lau J, Jacobson O, Niu G, Lin KS, Bénard F, Chen X. Bench to bedside: albumin binders for improved cancer radioligand therapies. *Bioconj Chem*. (2019) **30**:487–502. doi: 10.1021/acs.bioconjchem.8b00919
8. Sainz-Esteban A, Prasad V, Schuchardt C, Zachert C, Carril JM, Baum RP. Comparison of sequential planar ¹⁷⁷Lu-DOTA-TATE dosimetry scans with ⁶⁸Ga-DOTA-TATE PET/CT images in patients with metastasized neuroendocrine tumours undergoing peptide receptor radionuclide therapy. *Eur J Nucl Med Mol Imaging*. (2012) **39**:501–11. doi: 10.1007/s00259-011-2003-x
9. Domnanich KA, Müller C, Farkas R, Schmid RM, Ponsard B, Schibli R, et al. ⁴⁴Sc for labeling of DOTA- and NODAGA-functionalized peptides: preclinical *in vitro* and *in vivo* investigations. *EJNMMI Radiopharm Chem*. (2017) **1**:8. doi: 10.1186/s41181-016-0013-5
10. Umbricht CA, Benešová M, Schmid RM, Türlér A, Schibli R, van der Meulen NP, et al. ⁴⁴Sc-PSMA-617 for radiotheragnostics in tandem with ¹⁷⁷Lu-PSMA-617—preclinical investigations in comparison with ⁶⁸Ga-PSMA-11 and ⁶⁸Ga-PSMA-617. *EJNMMI Res*. (2017) **7**:9. doi: 10.1186/s13550-017-0257-4
11. Müller C, Bunka M, Reber J, Fischer C, Zhernosekov K, Türlér A, et al. Promises of cyclotron-produced ⁴⁴Sc as a diagnostic match for trivalent β -emitters: *in vitro* and *in vivo* study of a ⁴⁴Sc-DOTA-folate conjugate. *J Nucl Med*. (2013) **54**:2168–74. doi: 10.2967/jnumed.113.123810
12. Roesch F. Scandium-44: benefits of a long-lived PET radionuclide available from the ⁴⁴Ti/⁴⁴Sc generator system. *Curr Radiopharm*. (2012) **5**:187–201. doi: 10.2174/1874471011205030187
13. Garcia-Torano E, Peyres V, Roteta M, Sanchez-Cabezudo A, Romero E, Ortega AM. Standardisation and precise determination of the half-life of ⁴⁴Sc. *Appl Radiat Isotopes*. (2016) **109**:314–8. doi: 10.1016/j.apradiso.2015.12.007
14. Bunka M, Müller C, Vermeulen C, Haller S, Türlér A, Schibli R, et al. Imaging quality of ⁴⁴Sc in comparison with five other PET radionuclides using Derenzo phantoms and preclinical PET. *Appl Radiat Isotopes*. (2016) **110**:129–33. doi: 10.1016/j.apradiso.2016.01.006
15. Müller C, Bunka M, Haller S, Köster U, Groehn V, Bernhardt P, et al. Promising prospects for ⁴⁴Sc-/⁴⁷Sc-based theragnostics: application of ⁴⁷Sc for radionuclide tumor therapy in mice. *J Nucl Med*. (2014) **55**:1658–64. doi: 10.2967/jnumed.114.141614
16. Siwowska K, Guzik P, Domnanich KA, Monné Rodríguez JM, Bernhardt P, Ponsard B, et al. Therapeutic potential of ⁴⁷Sc in comparison to ¹⁷⁷Lu and ⁹⁰Y: preclinical investigations. *Pharmaceutics*. (2019) **11**:424. doi: 10.3390/pharmaceutics11080424
17. Domnanich KA, Müller C, Benešová M, Dressler R, Haller S, Köster U, et al. ⁴⁷Sc as useful β -emitter for the radiotheragnostic paradigm: a comparative study of feasible production routes. *EJNMMI Radiopharm Chem*. (2017) **2**:5. doi: 10.1186/s41181-017-0024-x
18. Chaple IF, Lapi SE. Production and use of the first-row transition metal PET radionuclides ⁴³Sc, ⁵²Mn, and ⁴⁵Ti. *J Nucl Med*. (2018) **59**:1655–9. doi: 10.2967/jnumed.118.213264
19. Carzaniga TS, Auger M, Braccini S, Bunka M, Ereditato A, Nesteruk KP, et al. Measurement of ⁴³Sc and ⁴⁴Sc production cross-section with an 18 MeV medical PET cyclotron. *Appl Radiat Isotopes*. (2017) **129**:96–102. doi: 10.1016/j.apradiso.2017.08.013
20. Domnanich KA, Eichler R, Müller C, Jordi S, Yakusheva V, Braccini S, et al. Production and separation of ⁴³Sc for radiopharmaceutical purposes. *EJNMMI Radiopharm Chem*. (2017) **2**:14. doi: 10.1186/s41181-017-0033-9
21. Filosofov D, Loktionova N, Rösch F. A ⁴⁴Ti/⁴⁴Sc radionuclide generator for potential application of ⁴⁴Sc-based PET-radiopharmaceuticals. *Radiochim Acta*. (2010) **98**:149–56. doi: 10.1524/ract.2010.1701
22. Rösch F, Baum RP. Generator-based PET radiopharmaceuticals for molecular imaging of tumours: on the way to THERANOSTICS. *Dalton Trans*. (2011) **40**:6104–11. doi: 10.1039/c0dt01504k
23. Krajewski S, Cydzik I, Abbas K, Bulgheroni A, Simonelli F, Holzwarth U, et al. Cyclotron production of ⁴⁴Sc for clinical application. *Radiochim Acta*. (2013) **101**:333–8. doi: 10.1524/ract.2013.2032
24. Severin G, Engle J, Valdovinos H, Barnhart T, Nickles R. Cyclotron produced ⁴⁴Sc from natural calcium. *Appl Radiat Isotopes*. (2012) **70**:1526–30. doi: 10.1016/j.apradiso.2012.04.030
25. van der Meulen NP, Bunka M, Domnanich KA, Müller C, Haller S, Vermeulen C, et al. Cyclotron production of ⁴⁴Sc: from bench to bedside. *Nucl Med Biol*. (2015) **42**:745–51. doi: 10.1016/j.nucmedbio.2015.05.005
26. Singh A, van der Meulen NP, Müller C, Klette I, Kulkarni HR, Türlér A, et al. First-in-human PET/CT imaging of metastatic neuroendocrine neoplasms with cyclotron-produced ⁴⁴Sc-DOTATOC: a proof-of-concept study. *Cancer Biother Radiopharm*. (2017) **32**:124–32. doi: 10.1089/cbr.2016.2173
27. Eppard E, de la Fuente A, Benešová M, Khawar A, Bundschuh RA, Gärtner FC, et al. Clinical translation and first in-human use of [⁴⁴Sc] Sc-PSMA-617 for PET imaging of metastasized castrate-resistant prostate cancer. *Theranostics*. (2017) **7**:4359. doi: 10.7150/thno.20586
28. Armstrong IS, Memmott MJ, Tonge CM, Arumugam P. The impact of prompt gamma compensation on myocardial blood flow measurements with rubidium-82 dynamic PET. *J Nucl Cardiol*. (2018) **25**:596–605. doi: 10.1007/s12350-016-0583-3
29. Lubberink M, Herzog H. Quantitative imaging of ¹²⁴I and ⁸⁶Y with PET. *Eur J Nucl Med Mol Imaging*. (2011) **38**:10. doi: 10.1007/s00259-011-1768-2
30. Jakoby B, Bercier Y, Conti M, Casey M, Bendriem B, Townsend D. Physical and clinical performance of the mCT time-of-flight PET/CT scanner. *Phys Med Biol*. (2011) **56**:2375. doi: 10.1088/0031-9155/56/8/004
31. Gnesin S, Kieffer C, Zeimpekis K, Papazyan J-P, Guignard R, Prior J, et al. Phantom-based image quality assessment of clinical ¹⁸F-FDG protocols in digital PET/CT and comparison with conventional PMT-based PET/CT devices. *EJNMMI Phys*. (2020) **7**:1. doi: 10.1186/s40658-019-0269-4
32. Boellaard R, Willemsen A, Arends B, Visser E. *EARL Procedure for Assessing PET/CT System Specific Patient FDG Activity Preparations for Quantitative FDG PET/CT Studies*. (2014). Available online at: http://earl.eanm.org/html/img/pool/EARL-procedure-for-optimizing-FDG-activity-for-quantitative-FDG-PET-studies_version_1_1.pdf (accessed October 23, 2019).
33. Graham MM, Wahl RL, Hoffman JM, Yap JT, Sunderland JJ, Boellaard R, et al. Summary of the UPICT protocol for ¹⁸F-FDG PET/CT imaging in oncology clinical trials. *J Nucl Med*. (2015) **56**:955–61. doi: 10.2967/jnumed.115.158402
34. Kaalep A, Sera T, Rijnsdorp S, Yaqub M, Talsma A, Lodge MA, et al. Feasibility of state of the art PET/CT systems performance harmonisation. *Eur J Nucl Med Mol Imaging*. (2018) **45**:1344–61. doi: 10.1007/s00259-018-3977-4
35. Boellaard R, Delgado-Bolton R, Oyen WJ, Giammarile F, Tatsch K, Eschner W, et al. FDG PET/CT: EANM procedure guidelines for tumour imaging: version 2.0. *Eur J Nucl Med Mol Imaging*. (2015) **42**:328–54. doi: 10.1007/s00259-014-2961-x
36. Boellaard R. *EARL: Accreditation Specifications*. (2017). Available online at: http://www.earl.eanm.org/cms/website.php?id=/en/projects/fdg_pet_ct_accreditation/accreditation_specifications.htm (accessed September 9, 2019).

37. Watson CC, Casey ME, Michel C, Bendriem B. Advances in scatter correction for 3D PET/CT. In: *IEEE Symposium Conference Record Nuclear Science*, Vol. 5. Rome (2004). p. 3008–12. doi: 10.1109/NSSMIC.2004.1466317
38. Hayden CH, Casey ME, Watson CC. *Prompt Gamma Correction for Non-Standard Isotopes in a Pet Scanner*. U.S. Patent No. 20080283758A1 (2008). Available online at: <https://patents.google.com/patent/US20080283758>
39. Zaidi H, Koral KF. Scatter modelling and compensation in emission tomography. *Eur J Nucl Med Mol Imaging*. (2004) **31**:761–82. doi: 10.1007/s00259-004-1495-z
40. van Sluis J, de Jong J, Schaar J, Noordzij W, van Snick P, Dierckx R, et al. Performance characteristics of the digital Biograph Vision PET/CT system. *J Nucl Med*. (2019) **60**:1031–6. doi: 10.2967/jnumed.118.215418
41. Huizing DM, Koopman D, van Dalen JA, Gotthardt M, Boellaard R, Sera T, et al. Multicentre quantitative ^{68}Ga PET/CT performance harmonisation. *EJNMMI Phys*. (2019) **6**:19. doi: 10.1186/s40658-019-0253-z
42. Rosar F, Buchholz HG, Michels S, Hoffmann MA, Piel M, Waldmann CM, et al. Image quality analysis of ^{44}Sc on two preclinical PET scanners: a comparison to ^{68}Ga . *EJNMMI Phys*. (2020) **7**:1–17. doi: 10.1186/s40658-020-0286-3

Conflict of Interest: The authors declare that the research was conducted in the absence of any commercial or financial relationships that could be construed as a potential conflict of interest.

Copyright © 2020 Lima, Gnesin, Nitzsche, Ortega, Müller and van der Meulen. This is an open-access article distributed under the terms of the Creative Commons Attribution License (CC BY). The use, distribution or reproduction in other forums is permitted, provided the original author(s) and the copyright owner(s) are credited and that the original publication in this journal is cited, in accordance with accepted academic practice. No use, distribution or reproduction is permitted which does not comply with these terms.



Methods for Quantifying Neurotransmitter Dynamics in the Living Brain With PET Imaging

Jenny Ceccarini^{1,2*}, Heather Liu³, Koen Van Laere^{1,2}, Evan D. Morris^{3,4,5,6} and Christin Y. Sander^{7,8}

¹ Division of Nuclear Medicine, University Hospitals Leuven, Leuven, Belgium, ² Department of Imaging and Pathology, KU Leuven, Leuven, Belgium, ³ Department of Biomedical Engineering, Yale University, New Haven, CT, United States, ⁴ Department of Radiology and Biomedical Imaging, Yale University, New Haven, CT, United States, ⁵ Department of Psychiatry, Yale University, New Haven, CT, United States, ⁶ Invivo LLC, New Haven, CT, United States, ⁷ Athinoula A. Martinos Center for Biomedical Imaging, Department of Radiology, Massachusetts General Hospital, Charlestown, MA, United States, ⁸ Harvard Medical School, Boston, MA, United States

OPEN ACCESS

Edited by:

Ivo Rausch,
Medical University of Vienna, Austria

Reviewed by:

Daniele De Paula Faria,
University of São Paulo, Brazil
Andreas Hahn,
Medical University of Vienna, Austria

*Correspondence:

Jenny Ceccarini
jenny.ceccarini@uzleuven.be

Specialty section:

This article was submitted to
Medical Physics and Imaging,
a section of the journal
Frontiers in Physiology

Received: 14 April 2020

Accepted: 15 June 2020

Published: 21 July 2020

Citation:

Ceccarini J, Liu H, Van Laere K,
Morris ED and Sander CY (2020)
Methods for Quantifying
Neurotransmitter Dynamics
in the Living Brain With PET Imaging.
Front. Physiol. 11:792.
doi: 10.3389/fphys.2020.00792

Positron emission tomography (PET) neuroimaging in neuropsychiatry is a powerful tool for the quantification of molecular brain targets to characterize disease, assess disease subtype differences, evaluate short- and long-term effects of treatments, or even to measure neurotransmitter levels in healthy and psychiatric conditions. In this work, we present different methodological approaches (*time-invariant models* and *models with time-varying terms*) that have been used to measure dynamic changes in neurotransmitter levels induced by pharmacological or behavioral challenges in humans. The developments and potential use of hybrid PET/magnetic resonance imaging (MRI) for neurotransmission brain research will also be highlighted.

Keywords: brain imaging quantification, neurotransmitter release, kinetic modeling, dopamine, PET/fMRI

INTRODUCTION

Many transformative therapies for neurological and psychiatric disease states over the last decades have targeted neurotransmitter systems through serotonin, dopamine, or opioid receptors and transporters. Neurotransmitters play an important role in regulating brain activity at the molecular and neurochemical level and are centrally involved in many brain functions, including, for example, cognition, behavior, sleep, appetite, and mood. Endogenous and exogenous stimuli, including behaviorally relevant stimuli, mood changes, and pharmacological challenges, evoke widespread changes in neurotransmitter systems. These changes are important to understand neural function in health and disease. One of the most and extensively characterized neurotransmitter system is the mesocorticolimbic dopaminergic pathway. Dopamine, both the “*pleasure*” and “*goal-directed movement*” chemical neurotransmitter, has been the main central pathway target for the pharmacological effects of habit-forming drugs. For example, dynamic changes in the dopaminergic system are known to contribute to a wide range of behaviors including affect, reward, decision-making, and inhibitory control.

Using *in vivo* functional molecular positron emission tomography (PET) imaging, we are able to image and quantify with very high sensitivity and specificity the local concentration of a range of neuroreceptor targets in a non-invasive way. PET radiotracers for imaging of neurotransmission

had been primarily focused on studying changes in endogenous levels of dopamine in the striatum (Finnema et al., 2015), mainly using ^{11}C -raclopride, but has not yet been adequately extended to other neurotransmitter systems (Paterson et al., 2010; da Cunha-Bang et al., 2019). More recently, advances have been made in developing new antagonist radioligands with higher dopamine D_2 receptor affinity, such as ^{11}C -FLB457 or ^{18}F -fallypride and agonist radioligands like ^{11}C -PHNO. Together with developments in the methodology for measuring neurotransmitter dynamics extending to extrastriatal brain regions, this has provided an increased understanding of the role of synaptic dopamine in drug action, normal neuropsychology, pathophysiology of addiction, Parkinson's disease, and schizophrenia. Efforts in measuring neurotransmitter dynamics have currently extended to other targets such as the serotonin (Gryglewski et al., 2014; Erritzoe et al., 2019), noradrenaline, γ -aminobutyric acid, glutamate, acetylcholine, and opioid peptides [see review (Sander and Hesse, 2017)].

Data analysis methods have been developed to detect and characterize endogenous neurotransmitter release during dynamic PET imaging with a displaceable radioligand, in response to pharmacological, behavioral, or cognitive interventions, through mechanisms of a “pure competition” radioligand-target displacement model. Changes in binding potential (BP_{ND}) represent receptors as static targets that are not dynamically regulated by processes like internalization within post-synaptic membranes [see Ginovart (2005) for a review of this topic]. Models that incorporate receptor internalization and its effect on PET quantification have been proposed in by integrating PET with functional magnetic resonance imaging (fMRI) studies [see section “Imaging Dynamic Neurotransmission Using Simultaneous PET and Functional MRI” and Sander et al. (2015)]. The most commonly used drug to induce dopamine change is amphetamine, exhibiting several well-documented effects on dopamine neurotransmission, including increased synthesis and release together with inhibited degradation and uptake.

Conventional PET methods to estimate the BP_{ND} are commonly based on kinetic models that assume that the system under investigation is at equilibrium. However, this assumption is intentionally violated in studies using pharmacological or behavioral stimuli to invoke transient dopamine release. When the assumption of a steady-state neurotransmitter level is violated, conventional analysis methods, which rely on time-invariant parameters (*time-invariant model*), may produce biased BP_{ND} estimates (Yoder et al., 2004; Sullivan et al., 2013). Therefore, methods to detect neurotransmitter release during an activation study have been developed allowing for a non-constant dopamine level during the scan (i.e., *time-variant parameter models*). For example, the linearized simplified reference tissue model or the linearized simplified reference region model (LSRTM or LSRRM) models dopamine release as an exponential decay that peaks instantaneously at the start of the stimulus (Alpert et al., 2003). A more flexible and innovative kinetic model to fully characterize endogenous neurotransmission, named the linear parametric neurotransmitter PET (lp-ntPET) model (Morris et al., 2005; Normandin et al., 2012; Wang et al., 2017),

allows the dopamine curve to take on a variety of forms with a peak dopamine concentration to occur sometime *after* the start of the task. However, the performance of lp-ntPET remains suboptimal. It is sensitive to noise and limited in sensitivity and accuracy.

Additionally, dynamic changes in neurotransmission are also known to contribute to blood oxygenation level dependent (BOLD) and cerebral blood volume (CBV) changes (Mandeville et al., 2013). The advent of hybrid PET/MRI scanners paved the way for more comprehensive investigation of the relationship of simultaneous changes in neuroreceptor occupancy and hemodynamic parameters, therefore clarifying the contributions of specific neurotransmitter systems to dynamic changes in BOLD response (Sander et al., 2013).

In this article, we first summarize the basics of various PET methodological approaches to measure dynamic changes in endogenous neurotransmitter levels induced by pharmacological or behavioral challenges. Next, we discuss how the use of simultaneous PET and fMRI can provide complementary and new views on quantitative imaging of neurotransmission.

APPROACHES FOR MEASURING ENDOGENOUS NEUROTRANSMITTER RELEASE: THE CURRENT STATUS

Time-Invariant Models

Traditional analyses of dynamic PET quantification of changes in neurotransmitter levels estimate the BP_{ND} , a static parameter that represents the potential for specific binding of the radioligand to specific enzymes in the brain, by fitting the dynamic data with compartmental or graphical (linearized) models. These models, including reference region models, such as the SRTM (Lammertsma and Hume, 1996), the Logan graphical reference method (Logan et al., 1990), and equilibrium analysis, assume that the system under investigation is in equilibrium condition. Another assumption is that the endogenous neurotransmitter and receptor concentration does not change during the course of the scan. Under these conditions, BP_{ND} is estimated from a reference tissue model considering the time activity curve of the reference region as an indirect input function to the kinetic model of the target region.

In these traditional studies, BP_{ND} is measured at rest and after a specific (cognitive or pharmacological) stimulus, during two separate PET sessions. The standard calculated endpoint to quantify neurotransmitter release is formulated as the fractional reduction in the radiotracer BP_{ND} following the stimulus (post-stimulus, $BP_{\text{ND}}^{\text{post}}$) compared to the BP_{ND} at rest or baseline (pre-stimulus) ($BP_{\text{ND}}^{\text{pre}}$), Eq. (1):

$$\Delta BP_{\text{ND}} = \frac{(BP_{\text{ND}}^{\text{post}} - BP_{\text{ND}}^{\text{pre}})}{BP_{\text{ND}}^{\text{pre}}} \quad (1)$$

A decrease in BP_{ND} is used as an index of neurotransmitter release induced by a stimulus. This approach has been used

conventionally with ^{11}C -raclopride, ^{18}F -fallypride, ^{11}C -(+)-PHNO, ^{11}C -FLB457, ^{11}C -CIMBI-36, and ^{11}C -carfentanil PET, to quantify respective endogenous dopamine (Martinez et al., 2003; Montgomery et al., 2007; Wai et al., 2019; Zakariaeiz et al., 2019; Whitton et al., 2020), serotonin (Erritzoe et al., 2019), and opioid release (Turton et al., 2018) before and after the administration of cannabis, nicotine, methylphenidate, and amphetamine.

However, traditional models that estimate BP_{ND} do not contain explicit functions to describe short-lived neurotransmitter responses. When the stimulus is applied during a single scanning session, inconsistency in the results [of smoking studies, for example, Brody et al. (2004, 2010)] could be attributed to limitations of the conventional models. As BP_{ND} estimates become sensitive to the amount of data used post-stimulus, poor fitting of the data can lead to biased estimates of BP demonstrated by Sullivan et al. (2013), as critically reviewed by Liu et al. (2019). Therefore, a more flexible time-varying kinetic model would be better configured than conventional time-invariant models to reliably and reproducibly capture transient responses.

Temporal Changes in Neurotransmitter Levels: Models With Time-Varying Terms

The first neurotransmitter competition kinetic model that was implemented to detect and characterize changes in ligand binding using only a single PET experiment is the linear extension of the reference region model (LSRTM or LSRRM), proposed by Alpert et al. (2003). LSRRM accounts for time-dependent changes in radiotracer binding, influx, and clearance induced by cognitive or drug effects in a single scan session, with the inclusion of both baseline and activation terms. LSRRM models neurotransmitter release as an exponential decay that peaks instantaneously at the start of the stimulus. It assumes that the physiologic steady state is not maintained throughout the paradigm but accounts for time-variation in the dissociation rate of ligand $k_{2a} = k_2/[1 + BP_{ND}]$, where k_2 is the tissue-to-plasma efflux constant in the tissue region. The dopamine–radioligand competition at the receptor site is reflected by a temporal change in apparent dissociation rate, which is accounted for by adding a time-dependent parameter $\gamma h(t)$ to a fixed k_{2a} . The parameter γ represents the amplitude of the ligand displacement, hence the peak dopamine level. The function $h(t)$ in Eq. (2) describes the rapid change after task onset and dissipation over time, where $u(t)$ is the unit step function, while τ controls the rate at which activation effects die away and T indicates the timing of stimulus initiation:

$$h(t) = e^{[-\tau(t-T)]} u(t - T) \quad (2)$$

An increased k_{2a} reflects a decreased BP_{ND} for D_2/D_3 receptors, which in turn can be ascribed to an increased dopamine release and will result in a positive value of γ .

There have been promising results using a single ^{18}F -fallypride injection protocol and the LSRRM to describe extrastriatal and striatal dopamine release induced by emotional processing (Badgaiyan et al., 2009), attention, reward, and stress task (Christian et al., 2006; Lataster et al., 2011; Ceccarini et al.,

2012; Kasanova et al., 2017), and also during dopamine-releasing pharmacological challenges, such as intravenous alcohol administration (Leurquin-Sterk et al., 2018) and Δ^9 -THC (Kuepper et al., 2013), as can be seen in Figure 1.

However, LSRRM assumes that effects of the stimuli on endogenous neurotransmitter release are instantaneous, maximal at the start time of stimulation [equal to T , see Eq. (2)], and decay exponentially to baseline thereafter (at rate τ). When any of these assumptions are violated, the estimates of the model parameters could be biased and/or inaccurate.

More flexible kinetic approaches and associated resolution models have been proposed to resolve these limitations, such as the lp-ntPET model (Morris et al., 2005; Normandin et al., 2012; Kim et al., 2014). In order to estimate the temporal characteristics of a transient neurotransmitter component in PET data with less stringent assumptions than LSRRM, lp-ntPET employs gamma-variate basis functions spanning a wide range of feasible neurotransmitter shapes, times of onset, and duration.

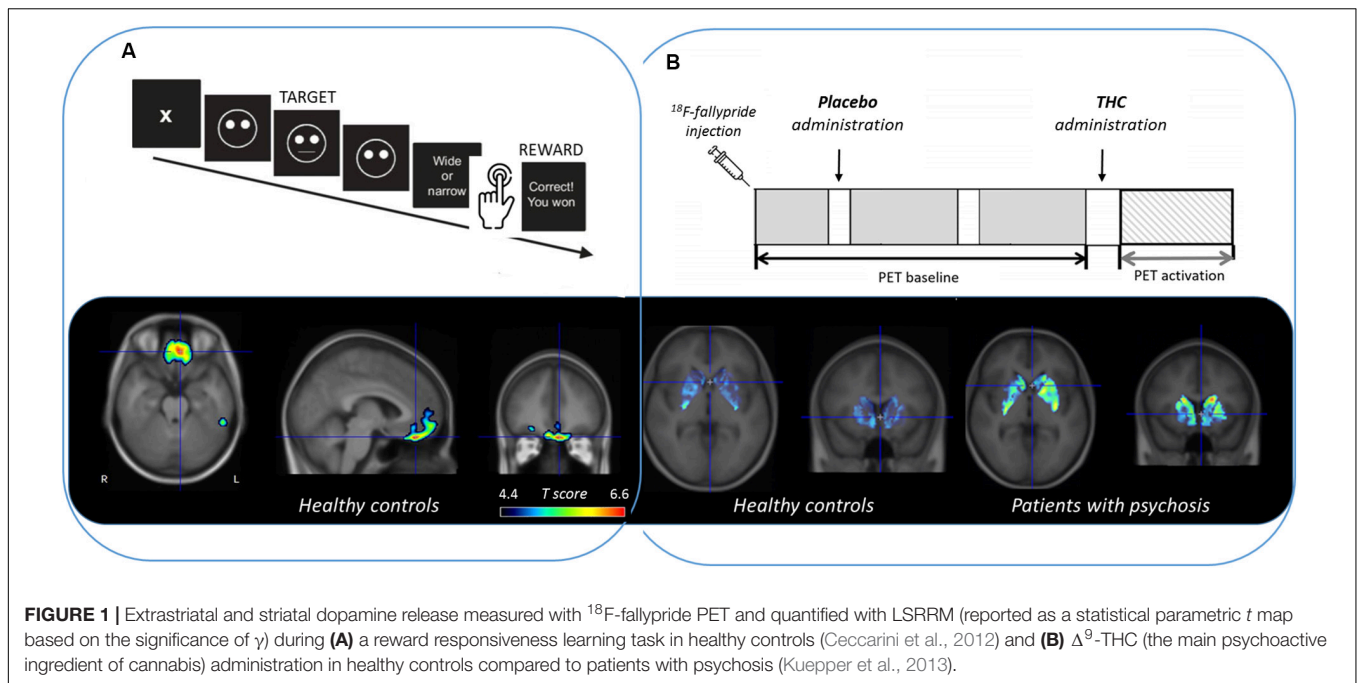
Specifically, lp-ntPET is the union of the conventional multilinear reference tissue model (MRTM) (Ichise et al., 2003) and a time-varying term that describes the transient neurotransmitter term, Eq. (3):

$$C_T = R_1 C_R(t) + k_{2a} \int_0^t C_R(u) du - k_{2a} \int_0^t C_T(u) du - \gamma \int_0^t C_T(u) h_i(u) du \quad (3)$$

$$h_i(t) = \left(\frac{t - t_D}{t_p - t_D} \right)^\alpha \exp \left(\alpha \left(1 - \frac{t - t_D}{t_p - t_D} \right) \right) u(t - t_D) \quad (4)$$

The novelty and the flexibility of the lp-ntPET approach consists of the use of the, γ , gamma-variate functions $h_i(t)$, where γ describes the response magnitude, and the three implicit parameters (t_D , t_p , α) describe the time course of the response (t_D , the start of the response or time delay; t_p , the peak time; and α , the decay rate or sharpness), assuming values incremented over finite intervals. The efficiency of lp-ntPET makes it practical to perform a voxel-by-voxel analysis of the whole brain or for localized activation patterns. The model has been successfully applied to ^{11}C -raclopride data to estimate the temporal dynamics of dopamine release in the mesolimbic circuit during smoking (Cosgrove et al., 2014; Kim et al., 2014). Recently, lp-ntPET has been applied in preclinical ^{11}C -raclopride PET studies following amphetamine administration (Angelis et al., 2019).

To evaluate the validity of extending lp-ntPET to the cortex, Liu et al. (2018) compared the ability of the lp-ntPET model and LSRRM to detect and characterize cortical dopamine release induced by a stress task with simulated ^{18}F -fallypride PET data. In ^{18}F -fallypride PET studies that detect cortical DA release induced by a sustained behavioral stress challenge, simulations suggest that both LSRRM and MRTM methods produce comparable t -scores over a wide range of sharpness, α , and rise time for DA signals. However, LSRRM consistently outperformed MRTM in terms of fitting accuracy. This may be relevant if the study goal is to characterize the PET signal and/or to deduce the dopamine signal shape or duration. Further, LSRRM and other



time-varying models may be the safer choice when the duration of the dopamine response and/or its shape are pertinent or unknown (Liu et al., 2018).

The significance of the responses estimated by lp-ntPET can be assessed using model selection criteria and statistical testing on γ , the estimated response magnitude, obtained by either t or F -test values comparing the goodness of fit of MRTM and lp-ntPET for each data set (Normandin et al., 2012). However, it has been reported that the t -score is not an indicator of goodness of fit but merely a measure of the magnitude of an estimated parameter relative to its variability (Liu et al., 2018). Additionally, the goodness of fit metrics depend critically on the number of parameters in the model and, together with the number of basis functions, have an impact on the false positive rate (FPR) (Liu and Morris, 2019). Given their findings, Liu and Morris (2019) proposed a set of modified goodness-of-fit metrics that adapt to the number of basis functions to maintain a stable FPR (Liu and Morris, 2020). Another recent Monte Carlo method proposed by Bevington et al. (2020) improves the detection sensitivity while preserving the cluster size threshold.

An optimization of the lp-ntPET displacement modeling method, called 2-step lp-ntPET, has been proposed by Mérida et al. (2018) where the model parameters are estimated in two steps, starting with the estimation of R_1 , k_2 , and k_{2a} with MRTM followed by the estimation of the release parameters (t_D , t_p , α , and γ) (unpublished results). In this way, the kinetic parameters are estimated more accurately, independently from the magnitude of the endogenous neurotransmitter release, and the macroparameter, the displacement ratio, seems to allow better detection of neurotransmitter discharge.

Finally, recent developments regarding the investigation of neurotransmitter dynamics have been introduced. For instance, the assessment of temporal changes in dopamine release has been proposed to advance to a resolution of a few minutes using

detailed modeling of dopamine dynamics (Lippert et al., 2019). Furthermore, the assessment of rapid changes in dopamine release and synthesis rates during cognitive performance have also been investigated by extending the technique of functional PET (fPET) imaging using ^{11}C -raclopride (Zhang et al., 2019) and ^{18}F -FDOPA (Hahn et al., 2019).

IMAGING DYNAMIC NEUROTRANSMISSION USING SIMULTANEOUS PET AND FUNCTIONAL MRI

With the current availability of scanners capable of simultaneous dynamic PET/MRI acquisitions, there is an increasing interest in measuring endogenous neurotransmitter release and time-varying measures of receptor occupancies in combination with dynamic neurovascular changes using fMRI techniques. The capability to combine multi-modal fMRI measures and neuroreceptor PET during activation paradigms provides an unprecedented opportunity to study neurotransmission dynamics through multiple lenses in the living brain. Indeed, as technical and methodological advances in simultaneous PET/MRI have matured (Ladefoged et al., 2017; Sari et al., 2017; Chen et al., 2018), we have seen an emergence of biological questions that favor simultaneous acquisitions of PET and MR signals (Cecchin et al., 2017; Streeter Barrett et al., 2019; Sander et al., 2020).

A revolution offered by PET/fMRI is the potential for resolving dynamic transitions in brain physiology, chemistry, and neurotransmission in space and time. Being able to acquire simultaneous functional measurements under the same physiological or pharmacological conditions not only reduces

confounding factors, interscan, and intrasubject variability but also enables cross-validation of biological measurements. A key importance of simultaneously acquired PET/fMRI signals for imaging dynamic neurotransmission is the ability to link actions at receptors, such as ligand binding or adaptations, to changes in hemodynamics. Alterations in local hemodynamics (such as BOLD, local perfusion, or CBV) have been shown to occur in response to changes in neuronal activity and during neurotransmission (Logothetis et al., 2001; Jenkins, 2012), although the topic of neurovascular coupling is still an active research area. The opportunity to now study a new facet of neurotransmission—neurotransmitter or receptor changes and its relationship to fMRI signal—will further elucidate the nature and interpretation of fMRI. Conversely, being able to track vascular changes during PET receptor measurements can address important questions like the dependence of PET signals on radiotracer delivery. On the latter topic, it has been demonstrated that blood flow is not a confound during dynamic PET neuromodulation experiments that evaluate within-scan time-dependent challenges (Sander et al., 2019). The advent of simultaneous PET/MR scanners has paved the way for investigations that evaluate how dopamine receptor densities may organize functional cortical networks during working memory (Roffman et al., 2016) or delineate the role of opioid receptor availability while evaluating pain processing pathways (Karjalainen et al., 2017). Time-varying PET kinetic models will be a crucial component of a comprehensive investigation between functional brain organization, physiological and molecular processes within similar timescales.

Several PET/MRI studies have been performed that have investigated the effects of time-varying neurotransmitter modulations (using pharmacological challenges) on fMRI and receptor-specific PET signals simultaneously. Much of this line of work has focused on establishing contributions of the dopaminergic system on the fMRI response, demonstrating that the hemodynamic response can be directly linked to D₂/D₃ receptor occupancy through neurovascular coupling

mechanisms (Sander et al., 2013). The relationship between hemodynamic changes (e.g., BOLD, CBV, or CBF) as measured with different fMRI techniques, receptor occupancy, and endogenous neurotransmitter has been described with a neurovascular coupling model (Sander et al., 2013, 2015). Considering specifically a ligand L (e.g., an administered drug) with efficacy ε_L that binds to D₂ receptors and displaces dopamine (DA), a linear relationship between hemodynamic changes (ΔH) and receptor occupancy (θ) is expressed as:

$$\Delta H(t) = N_{D2} \varepsilon_L B_{max, D2} \theta_L(t) - N_{D2} B_{max, D2} \Delta \theta_{DA}(t) \quad (5)$$

where N_{D2} is a neurovascular coupling constant (determined experimentally), $B_{max, D2}$ is the total concentration of D₂ receptors, $\theta_L(t)$ is the time-varying occupancy of an exogenous ligand (if present), and $\Delta \theta_{DA}(t)$ is the time-varying occupancy of dopamine. In a more general framework, the functional hemodynamic response ΔH can be expressed as the sum of receptor occupancies by different ligands, L, (endogenous and exogenous) and receptors, R, as:

$$\Delta H(t) = \sum_{R=1}^{\#receptors} \sum_{L=1}^{\#ligands} N_{R \varepsilon_R, L} B_{max, R} \Delta \theta_{R, L}(t) \quad (6)$$

This model incorporates the possibility of any number of receptors and neurotransmitters (or ligands) that may contribute to the hemodynamic response. Experimental evidence for this relationship has been demonstrated using D₂/D₃ antagonism and agonism (Figure 2), yet remains to be evaluated for multiple receptor systems working in parallel. The temporal correlation proposed in this model can be complicated by other biological parameters like receptor desensitization and internalization *in vivo* and requires further expansion of these model frameworks (Sander et al., 2015).

The effects of a partial serotonin receptor agonist have also been evaluated using simultaneous PET/fMRI

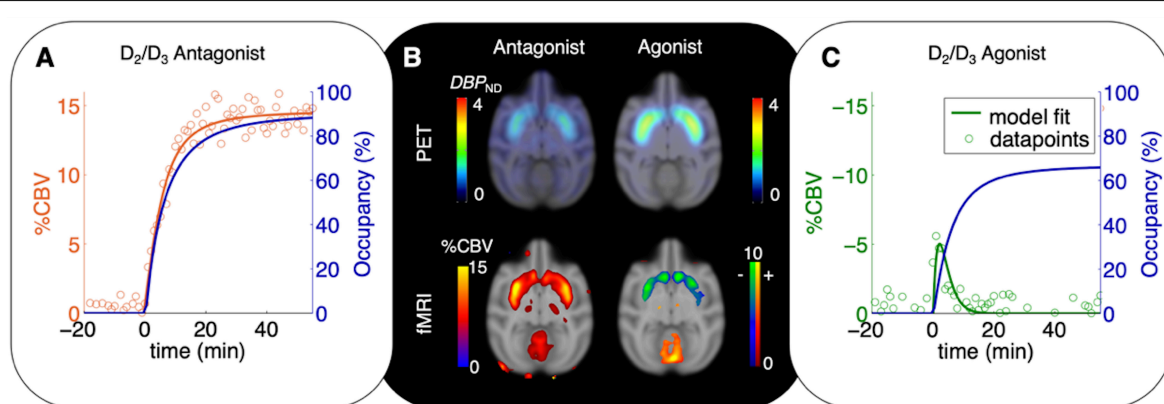


FIGURE 2 | Time-varying occupancy (blue) and cerebral blood volume (CBV) responses [positive (orange) or negative (green) percent change] due to a pharmacological response from the D₂/D₃ antagonist prochlorperazine (A) and the D₂/D₃ agonist quinpirole (C) in non-human primates. Occupancy curves are derived from a time-varying specific binding term during kinetic modeling, and the CBV curves are fitted using the general linear model. (B) ¹¹C-raclopride-PET binding potential maps (upper row) and CBV maps shown at peak value of the dynamic modeling term (Sander et al., 2015).

(Hansen et al., 2017), demonstrating that biphasic functional signals can be linked to serotonin receptor occupancies. As an example of stimulus-based simultaneous PET/fMRI studies, the opioid pain system has been examined using ^{11}C -diprenorphine (Wey et al., 2014). In the thalamus, co-localized and positively correlated fMRI and PET signal changes suggest that opioid neurotransmission contributes to pain-induced fMRI changes.

The use of time-varying models to quantify dynamic receptor occupancy together with fMRI has been key to these types of studies. For the purpose of comparing time-dependent kinetic rate constants, outcome measures such as “dynamic binding potential” (DBP) have been proposed to signify the dynamic nature of the system (Sander et al., 2013). Since dynamic measurements with PET versus fMRI still operate on different time resolutions (minutes vs. seconds), the combination of time-varying outcome measures from PET kinetic models with fast-changing repetitive signals in fMRI can present a challenge for direct and equivalent comparisons in the temporal domain. As more studies are carried out in this area, careful multi-modal experimental design together with integrating multi-modal models will no doubt play a key role.

The exploration of dynamic neurotransmission with simultaneous PET/fMRI is still in its infancy. Within the field of neuropsychiatry, PET/fMRI can help evaluate whole-brain functional effects of antipsychotic drug treatments in relation to neurotransmitter or receptor changes (Selvaggi et al., 2019) and shed a light on distributed networks that these drugs modulate. Connecting findings from multi-modal outcomes in complex mental illness, e.g., in schizophrenia, can also serve to connect hyper- and hypo-neurotransmitter tone to cortical function during relevant cognitive tasks (Slifstein et al., 2015). These approaches extend the field beyond traditional hemodynamic-based functional imaging methods or pure pharmacological target evaluations.

REFERENCES

- Alpert, N. M., Badgaiyan, R. D., Livni, E., and Fischman, A. J. (2003). A novel method for noninvasive detection of neuromodulatory changes in specific neurotransmitter systems. *Neuroimage* 19, 1049–1060. doi: 10.1016/S1053-8119(03)00186-1
- Angelis, G. I., Gillam, J. E., Ryder, W. J., Fulton, R. R., and Meikle, S. R. (2019). Direct estimation of voxel-wise neurotransmitter response maps from dynamic PET data. *IEEE Trans. Med. Imaging* 38, 1371–1383. doi: 10.1109/TMI.2018.2883756
- Badgaiyan, R. D., Fischman, A. J., and Alpert, N. M. (2009). Dopamine release during human emotional processing. *Neuroimage* 47, 2041–2045. doi: 10.1016/j.neuroimage.2009.06.008
- Bevington, C. W., Cheng, J.-C. K., Klyuzhin, I. S., Cherkasova, M. V., Winstanley, C. A., and Sossi, V. (2020). A monte carlo approach for improving transient dopamine release detection sensitivity. *J. Cereb. Blood Flow Metab.* 12:271678X20905613. doi: 10.1177/0271678X20905613
- Brody, A. L., London, E. D., Olmstead, R. E., Allen-Martinez, Z., Shulenberg, S., Costello, M. R., et al. (2010). Smoking-induced change in intrasynaptic dopamine concentration: effect of treatment for tobacco dependence. *Psychiatry Res.* 183, 218–224. doi: 10.1016/j.psychres.2009.06.004
- Brody, A. L., Olmstead, R. E., London, E. D., Farahi, J., Meyer, J. H., Grossman, P., et al. (2004). Smoking-induced ventral striatum dopamine release. *Am. J. Psychiatry* 161, 1211–1218. doi: 10.1176/appi.ajp.161.7.1211

CONCLUSION

Quantifying dynamic neurotransmission in the living brain with PET has provided insight into the molecular dynamics of the living brain. Both time-invariant and time-varying pharmacokinetic models have played an important role in the ability to accurately quantify neurotransmitter dynamics. In the age of multi-modal methods, simultaneous PET/fMRI can have a profound impact on our understanding of neuropsychiatric diseases, drawing connections between neurotransmitter imbalances to wide-spread changes in functional activation in diseases such as addiction, psychosis, and depression. Overall, models and methods for imaging neurotransmission, non-invasively, will play an important role in elucidating mechanisms underlying brain (dys)function in health and disease.

AUTHOR CONTRIBUTIONS

JC and CS revised the literature and wrote the first draft of the manuscript. HL, KV, and EM revised it critically for important intellectual content. All authors contributed to the article and approved the submitted version.

FUNDING

JC is a postdoctoral fellow from Research Foundation Flanders (FWO/12R1619N). KV is a senior clinical research fellow from FWO. HL received support from Robert E. Apafel Fellowship. HL and EM received support from the National Institutes of Health (NIH) (Grant No. R01DA038709). CS received support from the NIH (Grant Nos. R00DA043629 and R01NS112295).

- Ceccarini, J., Vrieze, E., Koole, M., Muylle, T., Bormans, G., Claes, S., et al. (2012). Optimized in vivo detection of dopamine release using ^{18}F -fallypride PET. *J. Nucl. Med.* 53, 1565–1572. doi: 10.2967/jnumed.111.099416
- Cecchin, D., Palombit, A., Castellaro, M., Silvestri, E., Bui, F., Barthel, H., et al. (2017). Brain PET and functional MRI: why simultaneously using hybrid PET/MR systems? *Q. J. Nucl. Med. Mol. Imaging* 61, 345–359. doi: 10.23736/S1824-4785.17.03008-4
- Chen, K. T., Salcedo, S., Chonde, D. B., Izquierdo-Garcia, D., Levine, M. A., Price, J. C., et al. (2018). MR-assisted PET motion correction in simultaneous PET/MRI studies of dementia subjects. *J. Magn. Reson. Imaging* 48, 1288–1296. doi: 10.1002/jmri.26000
- Christian, B. T., Lehrer, D. S., Shi, B., Narayanan, T. K., Strohmeyer, P. S., Buchsbaum, M. S., et al. (2006). Measuring dopamine neuromodulation in the thalamus: using ^{18}F -fallypride PET to study dopamine release during a spatial attention task. *Neuroimage* 31, 139–152. doi: 10.1016/j.neuroimage.2005.11.052
- Cosgrove, K. P., Wang, S., Kim, S. J., McGovern, E., Nabulsi, N., Gao, H., et al. (2014). Sex differences in the brain's dopamine signature of cigarette smoking. *J. Neurosci.* 34, 16851–16855. doi: 10.1523/JNEUROSCI.3661-14.2014
- da Cunha-Bang, S., Ettrup, A., Mc Mahon, B., Skibsted, A. P., Schain, M., Lehel, S., et al. (2019). Measuring endogenous changes in serotonergic neurotransmission with ^{11}C -Cimbi-36 positron emission tomography in humans. *Transl. Psychiatry* 9:134. doi: 10.1038/s41398-019-0468-8
- Erritzoe, D., Ashok, A. H., Searle, G. E., Colasanti, A., Turton, S., Lewis, Y., et al. (2019). Serotonin release measured in the human brain: a PET study with

- [11C]CIMBI-36 and d-amphetamine challenge. *Neuropsychopharmacology* 45, 804–810. doi: 10.1038/s41386-019-0567-5
- Finnema, S. J., Scheinin, M., Shahid, M., Lehto, J., Borroni, E., Bang-Andersen, B., et al. (2015). Application of cross-species PET imaging to assess neurotransmitter release in brain. *Psychopharmacology* 232, 4129–4157. doi: 10.1007/s00213-015-3938-6
- Genovart, N. (2005). Imaging the dopamine system with in vivo [11C]raclopride displacement studies: understanding the true mechanism. *Mol. Imaging Biol.* 7, 45–52. doi: 10.1007/s11307-005-0932-0
- Gryglewski, G., Lanzenberger, R., Kranz, G. S., and Cumming, P. (2014). Meta-analysis of molecular imaging of serotonin transporters in major depression. *J. Cereb. Blood Flow Metab.* 34, 1096–1103. doi: 10.1038/jcbfm.2014.82
- Hahn, A., Reed, M. B., Pichler, V., Michenthaler, P., Rischka, L., Godbersen, G. M., et al. (2019). Sex differences in monetary reward and punishment processing are associated with fast dynamics of dopamine synthesis. *bioRxiv* [Preprint]. doi: 10.1101/2019.12.23.886812
- Hansen, H. D., Mandeville, J. B., Sander, C. Y., Hooker, J. M., Catana, C., Rosen, B. R., et al. (2017). Functional characterization of 5-HT1B receptor drugs in nonhuman primates using simultaneous PET-MR. *J. Neurosci.* 37, 10671–10678. doi: 10.1523/JNEUROSCI.1971-17.2017
- Ichise, M., Liow, J. S., Lu, J. Q., Takano, A., Model, K., Toyama, H., et al. (2003). Linearized reference tissue parametric imaging methods: application to [11C]DASB positron emission tomography studies of the serotonin transporter in human brain. *J. Cereb. Blood Flow Metab.* 23, 1096–1112. doi: 10.1097/01.WCB.0000085441.37552.CA
- Jenkins, B. G. (2012). Pharmacologic magnetic resonance imaging (phMRI): imaging drug action in the brain. *Neuroimage* 62, 1072–1085. doi: 10.1016/j.neuroimage.2012.03.075
- Karjalainen, T., Karlsson, H. K., Lahnakoski, J. M., Glerean, E., Nuutila, P., Jääskeläinen, I. P., et al. (2017). Dissociable roles of cerebral μ -opioid and type 2 dopamine receptors in vicarious pain: a combined PET-fMRI study. *Cereb. Cortex* 27, 4257–4266. doi: 10.1093/cercor/bhx129
- Kasanova, Z., Ceccarini, J., Frank, M. J., Amelsvoort, T. V., Booij, J., Heinz, A., et al. (2017). Striatal dopaminergic modulation of reinforcement learning predicts reward-oriented behavior in daily life. *Biol. Psychol.* 127, 1–9. doi: 10.1016/j.biopsycho.2017.04.014
- Kim, S. J., Sullivan, J. M., Wang, S., Cosgrove, K. P., and Morris, E. D. (2014). Voxelwise lp-ntPET for detecting localized, transient dopamine release of unknown timing: sensitivity analysis and application to cigarette smoking in the pet scanner. *Hum. Brain Mapp.* 35, 4876–4891. doi: 10.1002/hbm.22519
- Kuepper, R., Ceccarini, J., Lataster, J., Van Os, J., and Van Kooenburgh, M. (2013). Delta-9-tetrahydrocannabinol-induced dopamine release as a function of psychosis risk: 18 F-Fallypride positron emission tomography study. *PLoS One* 8:70378. doi: 10.1371/journal.pone.0070378
- Ladefoged, C. N., Law, I., Anazodo, U., St Lawrence, K., Izquierdo-Garcia, D., Catana, C., et al. (2017). A multi-centre evaluation of eleven clinically feasible brain PET/MRI attenuation correction techniques using a large cohort of patients. *Neuroimage* 147, 346–359. doi: 10.1016/j.neuroimage.2016.12.010
- Lammertsma, A. A., and Hume, S. P. (1996). Simplified reference tissue model for PET receptor studies. *Neuroimage* 4, 153–158. doi: 10.1006/nimg.1996.0066
- Lataster, J., Collip, D., Ceccarini, J., Haas, D., Booij, L., van Os, J., et al. (2011). Psychosocial stress is associated with in vivo dopamine release in human ventromedial prefrontal cortex: a positron emission tomography study using [18F]fallypride. *Neuroimage* 58, 1081–1089. doi: 10.1016/j.neuroimage.2011.07.030
- Laurquin-Sterk, G., Ceccarini, J., Crunelle, C. L., Weerasekera, A., de Laat, B., Himmelreich, U., et al. (2018). Cerebral dopaminergic and glutamatergic transmission relate to different subjective responses of acute alcohol intake: an in vivo multimodal imaging study. *Addict. Biol.* 23, 931–944. doi: 10.1111/adb.12542
- Lippert, R. N., Cremer, A. L., Edwin Thanarajah, S., Korn, C., Jahans-Price, T., Burgeno, L. M., et al. (2019). Time-dependent assessment of stimulus-evoked regional dopamine release. *Nat. Commun.* 10:336. doi: 10.1038/s41467-018-08143-4
- Liu, H., Ceccarini, J., de Laat, B., Lataster, J., Myin-Germeys, I., and Morris, E. D. (2018). A comparison of kinetic models for PET imaging of cortical dopamine release induced by a task. *J. Nucl. Med.* 59(Suppl. 1):502.
- Liu, H., and Morris, E. D. (2019). Controlling the false positive rate for lp-ntPET: a correction to goodness of fit metrics for “effective” number of parameters. *J. Nucl. Med.* 60(Suppl. 1):580.
- Liu, H., Zakariaiz, Y., Cosgrove, K. P., and Morris, E. D. (2019). Toward whole-brain dopamine movies: a critical review of PET imaging of dopamine transmission in the striatum and cortex. *Brain Imaging Behav.* 13, 314–322. doi: 10.1007/s11682-017-9779-7
- Liu, H., and Morris, E. D. (2020). Model comparison metrics require adaptive correction if parameters are discretized: proof-of-concept applied to transient signals in dynamic PET. *IEEE Trans. Med. Imaging* doi: 10.1109/TMI.2020.2969425
- Logan, J., Fowler, J. S., Volkow, N. D., Wolf, A. P., Dewey, S. L., Schlyer, D. J., et al. (1990). Graphical analysis of reversible radioligand binding from time-activity measurements applied to [N-11C-methyl]-(-)-cocaine PET studies in human subjects. *J. Cereb. Blood Flow Metab.* 10, 740–747. doi: 10.1038/jcbfm.1990.127
- Logothetis, N. K., Pauls, J., Augath, M., Trinath, T., and Oeltermann, A. (2001). Neurophysiological investigation of the basis of the fMRI signal. *Nature* 412, 150–157. doi: 10.1038/35084005
- Mandeville, J. B., Sander, C. Y. M., Jenkins, B. G., Hooker, J. M., Catana, C., Vanduffel, W., et al. (2013). A receptor-based model for dopamine-induced fMRI signal. *Neuroimage* 75, 46–57. doi: 10.1016/j.neuroimage.2013.02.036
- Martinez, D., Slifstein, M., Broft, A., Mawlawi, O., Hwang, D.-R., Huang, Y., et al. (2003). Imaging human mesolimbic dopamine transmission with positron emission tomography. Part II: amphetamine-induced dopamine release in the functional subdivisions of the striatum. *J. Cereb. Blood Flow Metab.* 23, 285–300. doi: 10.1097/01.WCB.0000048520.34839.1A
- Mérida, I., Olivier, F., Hammers, A., Redouté, J., Reilhac, A., Costes, N., et al. (2018). “Kinetic modelling for endogenous neurotransmitter discharge characterization using pet imaging: optimization of lp-ntPET,” in *The XII International Symposium of Functional Neuroreceptor Mapping of the Living Brain (NRM18)* (London).
- Montgomery, A. J., Asselin, M.-C., Farde, L., and Grasby, P. M. (2007). Measurement of methylphenidate-induced change in extrastriatal dopamine concentration using [11 C]FLB 457 PET. *J. Cereb. Blood Flow Metab.* 27, 369–377. doi: 10.1038/sj.jcbfm.9600339
- Morris, E. D., Yoder, K. K., Wang, C., Normandin, M. D., Zheng, Q.-H., Mock, B., et al. (2005). ntPET: a new application of PET imaging for characterizing the kinetics of endogenous neurotransmitter release. *Mol. Imaging* 4, 473–489.
- Normandin, M. D., Schiffer, W. K., and Morris, E. D. (2012). A linear model for estimation of neurotransmitter response profiles from dynamic PET data. *Neuroimage* 59, 2689–2699. doi: 10.1016/j.neuroimage.2011.07.002
- Paterson, L. M., Tyacke, R. J., Nutt, D. J., and Knudsen, G. M. (2010). Measuring endogenous 5-HT release by emission tomography: promises and pitfalls. *J. Cereb. Blood Flow Metab.* 30, 1682–1706. doi: 10.1038/jcbfm.2010.104
- Roffman, J. L., Tanner, A. S., Eryilmaz, H., Rodriguez-Thompson, A., Silverstein, N. J., Ho, N. F., et al. (2016). Dopamine D1 signaling organizes network dynamics underlying working memory. *Sci. Adv.* 2:e1501672. doi: 10.1126/sciadv.1501672
- Sander, C. Y., Hansen, H. D., and Wey, H.-Y. (2020). Advances in simultaneous PET/MR for imaging neuroreceptor function. *J. Cereb. Blood Flow Metab.* 40, 1148–1166. doi: 10.1177/0271678X20910038
- Sander, C. Y., and Hesse, S. (2017). News and views on in-vivo imaging of neurotransmission using PET and MRI. *Q. J. Nucl. Med. Mol. Imaging* 61, 414–428. doi: 10.23736/S1824-4785.17.03019-9
- Sander, C. Y., Hooker, J. M., Catana, C., Normandin, M. D., Alpert, N. M., Knudsen, G. M., et al. (2013). Neurovascular coupling to D2/D3 dopamine receptor occupancy using simultaneous PET/functional MRI. *Proc. Natl. Acad. Sci. U.S.A.* 110, 11169–11174. doi: 10.1073/pnas.1220512110
- Sander, C. Y., Hooker, J. M., Catana, C., Rosen, B. R., and Mandeville, J. B. (2015). Imaging agonist-induced D2/D3 receptor desensitization and internalization in vivo with PET/fMRI. *Neuropsychopharmacology* 41, 1427–1436. doi: 10.1038/npp.2015.296
- Sander, C. Y., Mandeville, J. B., Wey, H. Y., Catana, C., Hooker, J. M., and Rosen, B. R. (2019). Effects of flow changes on radiotracer binding: simultaneous measurement of neuroreceptor binding and cerebral blood flow modulation. *J. Cereb. Blood Flow Metab.* 39, 131–146. doi: 10.1177/0271678X17725418

- Sari, H., Erlandsson, K., Law, I., Larsson, H. B., Ourselin, S., Arridge, S., et al. (2017). Estimation of an image derived input function with MR-defined carotid arteries in FDG-PET human studies using a novel partial volume correction method. *J. Cereb. Blood Flow Metab.* 37, 1398–1409. doi: 10.1177/0271678X16656197
- Selvaggi, P., Hawkins, P. C. T., Dipasquale, O., Rizzo, G., Bertolino, A., Dukart, J., et al. (2019). Increased cerebral blood flow after single dose of antipsychotics in healthy volunteers depends on dopamine D2 receptor density profiles. *Neuroimage* 188, 774–784. doi: 10.1016/j.neuroimage.2018.12.028
- Slifstein, M., van de Giessen, E., Van Snellenberg, J., Thompson, J. L., Narendran, R., Gil, R., et al. (2015). Deficits in prefrontal cortical and extrastriatal dopamine release in schizophrenia: a positron emission tomographic functional magnetic resonance imaging study. *JAMA Psychiatry* 72, 316–324. doi: 10.1001/jamapsychiatry.2014.2414
- Streeter Barrett, F., Shi, K., Minhas, D. S., Juhasz, C., Zhu, X., and Zhu, Y. (2019). MRI-Driven PET image optimization for neurological applications. *Front. Neurosci.* 13:782. doi: 10.3389/fnins.2019.00782
- Sullivan, J. M., Kim, S. J., Cosgrove, K. P., and Morris, E. D. (2013). Limitations of SRTM, Logan graphical method, and equilibrium analysis for measuring transient dopamine release with [(11)C]raclopride PET. *Am. J. Nucl. Med. Mol. Imaging* 3, 247–260.
- Turton, S., Myers, J. F. M., Mick, I., Colasanti, A., Venkataraman, A., Durant, C., et al. (2018). Blunted endogenous opioid release following an oral dexamphetamine challenge in abstinent alcohol-dependent individuals. *Mol. Psychiatry* 25, 1–10. doi: 10.1038/s41380-018-0107-4
- Wai, J. M., Grassetti, A., Slifstein, M., Matuskey, D., Nabulsi, N., Ropchan, J., et al. (2019). Binge alcohol use is not associated with alterations in striatal dopamine receptor binding or dopamine release. *Drug Alcohol. Depend* 205:107627. doi: 10.1016/j.drugalcdep.2019.107627
- Wang, S., Kim, S., Cosgrove, K. P., and Morris, E. D. (2017). A framework for designing dynamic lp-ntPET studies to maximize the sensitivity to transient neurotransmitter responses to drugs: application to dopamine and smoking. *Neuroimage* 146, 701–714. doi: 10.1016/j.neuroimage.2016.10.019
- Wey, H.-Y., Catana, C., Hooker, J. M., Dougherty, D. D., Knudsen, G. M., Wang, D. J. J., et al. (2014). Simultaneous fMRI-PET of the opioidergic pain system in human brain. *Neuroimage* 102(Pt 2), 275–282. doi: 10.1016/j.neuroimage.2014.07.058
- Whitton, A. E., Reinen, J. M., Slifstein, M., Ang, Y.-S., McGrath, P. J., Iosifescu, D. V., et al. (2020). Baseline reward processing and ventrostriatal dopamine function are associated with pramipexole response in depression. *Brain* 143, 701–710. doi: 10.1093/brain/awaa002
- Yoder, K. K., Wang, C., and Morris, E. D. (2004). Change in binding potential as a quantitative index of neurotransmitter release is highly sensitive to relative timing and kinetics of the tracer and the endogenous ligand. *J. Nucl. Med.* 45, 903–911.
- Zakariaeiz, Y., Hillmer, A. T., Matuskey, D., Nabulsi, N., Ropchan, J., Mazure, C. M., et al. (2019). Sex differences in amphetamine-induced dopamine release in the dorsolateral prefrontal cortex of tobacco smokers. *Neuropsychopharmacology* 44, 2205–2211. doi: 10.1038/s41386-019-0456-y
- Zhang, X., Wang, F., Hamilton, J. P., Sacchet, M. D., Chen, J. E., Khalighi, M., et al. (2019). Decoupling of dopamine release and neural activity in major depressive disorder during reward processing assessed by simultaneous fPET-fMRI. *bioRxiv* [Preprint]. doi: 10.1101/861534

Conflict of Interest: EM is a half-time employee of the company Invicro LLC.

The remaining authors declare that the research was conducted in the absence of any commercial or financial relationships that could be construed as a potential conflict of interest.

Copyright © 2020 Ceccarini, Liu, Van Laere, Morris and Sander. This is an open-access article distributed under the terms of the Creative Commons Attribution License (CC BY). The use, distribution or reproduction in other forums is permitted, provided the original author(s) and the copyright owner(s) are credited and that the original publication in this journal is cited, in accordance with accepted academic practice. No use, distribution or reproduction is permitted which does not comply with these terms.



Monte Carlo Simulations of the GE Signa PET/MR for Different Radioisotopes

Paulo R. R. V. Caribé^{1*}, Stefaan Vandenberghe¹, André Diogo², David Pérez-Benito³, Nikos Efthimiou⁴, Charlotte Thyssen¹, Yves D'Asseler⁵ and Michel Koole⁶

¹ Medical Imaging and Signal Processing – MEDISIP, Ghent University, Ghent, Belgium, ² Faculty of Sciences of the University of Lisbon (FCUL), Lisbon, Portugal, ³ Bioengineering and Aerospace Department, Universidad Carlos III de Madrid, Madrid, Spain, ⁴ Department of Physics, University of York, York, United Kingdom, ⁵ Department of Diagnostic Sciences, Faculty of Medicine, Ghent University, Ghent, Belgium, ⁶ Nuclear Medicine and Molecular Imaging, Department of Imaging & Pathology, KU Leuven, Leuven, Belgium

OPEN ACCESS

Edited by:

Ivo Rausch,
Medical University of Vienna, Austria

Reviewed by:

Wazir Muhammad,
Yale University, United States
Jacobo Cal-Gonzalez,
Ion Beam Applications, Spain

*Correspondence:

Paulo R. R. V. Caribé
paulo.caribe@ugent.be

Specialty section:

This article was submitted to
Medical Physics and Imaging,
a section of the journal
Frontiers in Physiology

Received: 09 January 2020

Accepted: 13 August 2020

Published: 15 September 2020

Citation:

Caribé PRRV, Vandenberghe S, Diogo A, Pérez-Benito D, Efthimiou N, Thyssen C, D'Asseler Y and Koole M (2020) Monte Carlo Simulations of the GE Signa PET/MR for Different Radioisotopes.
Front. Physiol. 11:525575.
doi: 10.3389/fphys.2020.525575

NEMA characterization of PET systems is generally based on ^{18}F because it is the most relevant radioisotope for the clinical use of PET. ^{18}F has a half-life of 109.7 min and decays into stable ^{18}O via β^+ emission with a probability of over 96% and a maximum positron energy of 0.633 MeV. Other commercially available PET radioisotopes, such as ^{82}Rb and ^{68}Ga have more complex decay schemes with a variety of prompt gammas, which can directly fall into the energy window and induce false coincidence detections by the PET scanner.

Methods: Aim of this work was three-fold: (A) Develop a GATE model of the GE Signa PET/MR to perform realistic and relevant Monte Carlo simulations (B) Validate this model with published sensitivity and Noise Equivalent Count Rate (NECR) data for ^{18}F and ^{68}Ga (C) Use the validated GATE-model to predict the system performance for other PET isotopes including ^{11}C , ^{15}O , ^{13}N , ^{82}Rb , and ^{68}Ga and to evaluate the effect of a 3T magnetic field on the positron range.

Results: Simulated sensitivity and NECR tests performed with the GATE-model for different radioisotopes were in line with literature values. Simulated sensitivities for ^{18}F and ^{68}Ga were 21.2 and 19.0 /kBq, respectively, for the center position and 21.1 and 19.0 cps/kBq, respectively, for the 10 cm off-center position compared to the corresponding measured values of 21.8 and 20.0 cps/kBq for the center position and 21.1 and 19.6 cps/kBq for the 10 cm off-center position. In terms of NECR, the simulated peak NECR was 216.8 kcps at 17.40 kBq/ml for ^{18}F and 207.1 kcps at 20.10 kBq/ml for ^{68}Ga compared to the measured peak NECR of 216.8 kcps at 18.60 kBq/ml and 205.6 kcps at 20.40 kBq/ml for ^{18}F and ^{68}Ga , respectively. For ^{11}C , ^{13}N , and ^{15}O , results confirmed a peak NECR similar to ^{18}F with the effective activity concentration scaled by the inverse of the positron fraction. For ^{82}Rb , and ^{68}Ga , the peak NECR was lower than for ^{18}F while the corresponding activity concentrations were higher. For the higher energy positron emitters, the positron range was confirmed to be

tissue-dependent with a reduction of the positron range by a factor of 3 to 4 in the plane perpendicular to the magnetic field and an increased positron range along the direction of the magnetic field.

Conclusion: Monte-Carlo simulations were used to predict sensitivity and NECR performance of GE Signa PET/MR for ^{18}F , ^{15}O , ^{13}N , ^{11}C , ^{82}Rb , and ^{68}Ga radioisotopes and were in line with literature data. Simulations confirmed that sensitivity and NECR were influenced by the particular decay scheme of each isotope. As expected, the positron range decreased in the direction perpendicular to the 3T magnetic field. However, this will be only partially improving the resolution properties of a clinical PET/MR system due to the limiting spatial resolution of the PET detector.

Keywords: nuclear medicine, PET/MR, NEMA NU 2–2012, high energy positron emitters, positron range

INTRODUCTION

The simultaneous acquisition of both PET and MRI was first developed for small animal imaging (Shao et al., 1997) whereas the development of an integrated PET/MR system for human studies only dated from a decade ago (Catana et al., 2010). The development of solid-state detectors such as avalanche photodiodes (APDs) and silicon photomultipliers (SiPMs) made it possible to integrate a PET detector ring into the bore of an MR scanner and to develop fully integrated PET/MR systems. The main advantage of using SiPMs over APDs is the faster detector response, therefore enabling simultaneous Time-of-Flight (TOF) PET and MR scanning, as demonstrated with the GE Signa PET/MR system (Yamamoto et al., 2003; Levin et al., 2016b; Vandenberghe et al., 2016; Efthimiou et al., 2019).

In terms of resolution, the PET spatial resolution is mainly limited by the detector size of discrete detector elements, the positron range, non-collinearity of the gamma rays resulting from an annihilation event and the decoding scheme of the PET scanner (Levin and Hoffman, 1999; Moses, 2011). The positron range, that is the distance the positron travels from the emitting nucleus to the location where the annihilation occurs, is the main non-detector related factor that limits the PET resolution (Moses, 1994; Palmer et al., 2005; Park et al., 2007; Peng and Levin, 2012) and the use of a magnetic field to limit its impact has already been proposed in the nineties (Iida et al., 1986; Rickey et al., 1992; Hammer et al., 1994; Laforest and Liu, 2008; Vallabhajosula et al., 2011). Because of the Lorentz force, a moving charged particle such as a positron describes a helical path along the direction of a magnetic field. As such, the positron range is reduced in the plane perpendicular to the magnetic field, while it remains unaltered or becomes slightly enlarged in the direction of the magnetic field (Eleftheriou et al., 2014; Kolb et al., 2015). Furthermore, the positron range relates directly to the energy of the positron (Kemerink et al., 2011; Emond et al., 2019). Studies with various PET radioisotopes have reported a larger reduction of the positron range for isotopes emitting positrons with a higher energy such as ^{120}I (Herzog et al., 2010), ^{82}Rb (Rahmim et al., 2008); or ^{68}Rb (Wirrwar et al., 1997; Cal-González et al., 2009; Soultanidis et al., 2011; Alva-Sánchez et al., 2016; Li et al., 2017). In order to reduce the blurring effect of the positron

range, it can be modeled as part of Point Spread Function (PSF), used in the reconstruction algorithm to model the PET system response. However, as stated in Jodal et al. (2012), different values for the positron range of different PET isotopes have been reported in literature, probably because of the limited accuracy of the experimental setup used in some of these studies such that the intrinsic detector resolution might be comparable to the positron range. As reference values for this study, we used the positron range values reported in Cal-González et al. (2009), Jodal et al. (2012) for the most relevant PET isotopes and various surrounding tissues.

Generally, the evaluation of the performance of a PET system is done for ^{18}F because it is the most widely used PET isotope in a clinical setting to evaluate the glucose metabolism in mainly oncological but also specific cerebral (Phelps et al., 1979) and cardiac diseases (Marshall et al., 1983). However, with the increasing clinical relevance of other radioisotopes, such as ^{15}O , ^{13}N , ^{11}C , ^{82}Rb , and especially ^{68}Ga (Hoffend et al., 2005), the need to evaluate the PET system performance for these isotopes is increasing because of their different decay scheme and physical properties. ^{18}F almost exclusively decays via positron emission with a branching ratio of 96.8% and has a relatively low maximum positron energy (0.6335 MeV). Properties of ^{15}O , ^{13}N , and ^{11}C , are in line with ^{18}F properties and are considered pure β^+ emitters, with the probability of positron emission being close to 100% and with a maximum positron energy of 1.735, 1.198, and 0.960 MeV, respectively. On the other hand, ^{82}Rb and ^{68}Ga have more complex decay schemes with multiple positron emission branches with different energies and with a significant contribution of prompt gamma emissions (Banerjee and Pomper, 2013; Afshar-Oromieh et al., 2014; Conti and Eriksson, 2016; Papp et al., 2018; Mayerhoefer et al., 2020). In addition, these PET radioisotopes emit positrons with a higher maximum energy of 3.381 and 1.8991 MeV, respectively (energy of the most abundant positron). In the context of simultaneous PET/MR imaging, the impact of a high magnetic field on positron range during PET scanning still needs extensive evaluation, especially for high-energy positron emitters.

Among the NEMA acceptance tests, the sensitivity and Noise Equivalent Count Rate (NECR) tests are essential to evaluate the PET system performance. Sensitivity expresses the fraction

of coincidences resulting from β^+ decay that is registered by the PET system for low activity concentrations. NECR is related to signal-to-noise ratio (SNR) and evaluates the impact of an increased activity concentration on the PET signal. It determines the interplay between true events, scatter and randoms to estimate which increase of activity concentration is still beneficial to improve the SNR.

The aim of this work was three-fold and can be summarized as follows: (A) Develop a realistic GATE model for the GE Signa PET/MR (B) Validate this model with sensitivity and NECR measurements performed on the 3T GE Signa PET/MR for ^{18}F and ^{68}Ga according to the NEMA NU 2–2012 protocol (National Electrical Manufacturers Association [NEMA], 2012; Caribé et al., 2019) (C) Use the validated GATE-model to predict the PET/MR system performance for other isotopes including ^{18}F , ^{11}C , ^{15}O , ^{13}N , ^{82}Rb , and ^{68}Ga and to evaluate the effect of the 3T magnetic field on the positron range.

MATERIALS AND METHODS

GATE Model for the GE Signa PET/MR

GATE is a toolbox for Monte Carlo (MC) simulations based on GEANT4 and adapted for nuclear medicine applications (Jan et al., 2004). GATE Monte Carlo (MC) simulations were performed on a high-performance computer installed at Ghent University (Vlaams Supercomputer Centrum – VSC). The GATE model was implemented to mimic the PET hardware configuration of the integrated GE Signa PET/MR system consisting of five rings of 28 detector blocks each, covering an axial Field Of View (FOV) of 25 cm while the transaxial FOV is 60 cm. Each detector element consisted of a lutetium-yttrium-orthosilicate (LYSO) scintillator with crystal elements of 25 mm \times 4.0 mm \times 5.3 mm and MR-compatible SiPM technology (Levin et al., 2016a). In addition, an energy window of 425–650 keV was used while the coincidence window was set to 4.57 ns (± 2.29 ns). The geometry was modeled using the cylindrical PET system model in GATE, which also takes into account the foam, plastic and copper shielding between the bore and the detectors. This model was used to simulate the annihilation distribution of positrons for different tissue types and included the following physical processes: positron decay, multiple scattering, ionization, bremsstrahlung and electron annihilation. To evaluate the effect of a magnetic field on the positron range, a magnetic field with a field strength of 3.0 Tesla was in the axial direction to model the MR component of the GE Signa PET/MR system which has a static magnetic field of 3.0 Tesla with a maximum radiofrequency amplitude of 44 mT/m and a maximum slew rate of 200 T/m/s.

Validation of the GATE Model for the GE Signa PET/MR

To validate the GATE model for the GE Signa PET/MR, we compared the sensitivity and NECR results of the NEMA NU 2–2012 acceptance measurements of the GE Signa PET/MR system using ^{18}F and ^{68}Ga with simulated sensitivity and NECR for ^{18}F

and ^{68}Ga using GATE and the appropriate model for the GE Signa PET/MR and the hardware phantoms.

Sensitivity Measurements

Sensitivity measurements were performed at two different locations in the FOV according to the NEMA NU 2–2012 protocol (National Electrical Manufacturers Association [NEMA], 2012). At each location, multiple measurements were performed of a 700 mm long source filled with low levels of activity. The line source was surrounded by an aluminum cylinder of initially 2.5 mm thickness with successively adding four 2.5 mm thick aluminum sleeves. Low activity levels were used to minimize random events and dead time effects while the dense aluminum surroundings of the line source ensured sufficient annihilation events to measure the PET signal. To obtain sufficient count statistics, sensitivity data were measured as long as it took to have at least 10,000 true events collected per slice. The sensitivity was calculated by extrapolating the sensitivity values for the line source surrounded by an aluminum sleeve with varying thickness to the sensitivity value corresponding to the attenuation-free measurement of the line source via the following equation:

$$S_i = S_0 \times e^{-2\mu_{Al}X_i} \quad (1)$$

where S_i is the sensitivity corresponding to the i th measurement, X_i the thickness of the aluminum sleeve for the i th measurement, μ_{Al} the linear attenuation coefficient of aluminum and S_0 actual sensitivity corresponding to a measurement with no aluminum surrounding the line source.

Sensitivity Simulations Using GATE

The simulations consisted of modeling a low activity line source filled with 5 MBq, positioned first in the center of the FOV and then at a radial distance of 10 cm from the center. To measure the sensitivity, simulations were performed of the line source surrounded by an aluminum sleeve with five different thicknesses ranging from 2.5 to 12.5 cm in steps of 2.5 cm. For each simulation, the count rate of true events only was obtained ROOT's "Coincidences" tree which stores pairs of single events that meet the conditions specified in the digitizer. Each pair is identified by an *eventID* for each of the two single events (*eventID1* and *eventID2*), which identifies the radioactive decay generating the singles. Furthermore, the entire history of interactions, including Compton or Rayleigh scattering, occurring from their location of origin till they reach the detector, is recorded for each event of a pair. A coincidence detection is considered to be random when the *eventID* between the two single events of one pair is different. When they are identical, a coincidence event can still be either a scattered or true event. True coincidences are obtained by excluding paired events with a history of Compton or Rayleigh scattering. Corresponding sensitivity values were determined as described for the sensitivity measurements and the final sensitivity was reported as the average of both positions in the FOV.

NECR Measurements

Noise Equivalent Count Rate was measured with a 700 mm long and 203 mm wide polyethylene cylinder containing a 700 mm long plastic tube line source (3.2 mm inner diameter) filled with high activity. To evaluate the impact of random counts and dead time effects for different activity levels, the measurements were repeated to take advantage of the physical decay and cover different levels of activity. Through a sinogram-based analysis, as described below, the peak NECR, corresponding activity concentration and scatter fraction were extracted from these measurements (National Electrical Manufacturers Association [NEMA], 2012).

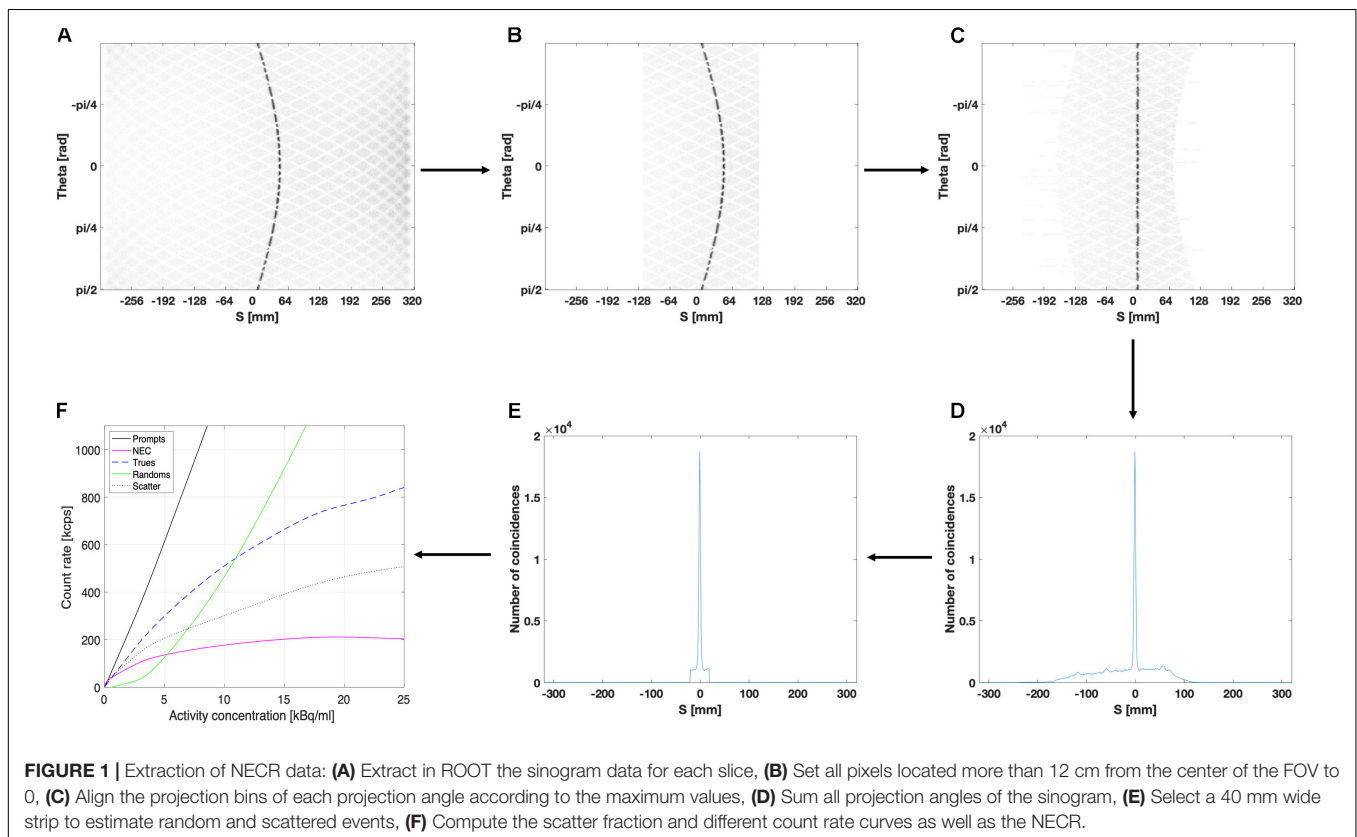
NECR Simulations Using GATE

For NECR simulations, the activity in the line source was varied from 1 to 800 MBq using a total of 11 different levels in order to reduce the computation time. In order to estimate the rate at which the scanner acquires coincidence data, that is *true*, *random*, or *scattered* coincidences, a sinogram based analysis was performed. For each slice, the sinogram stores the LOR as function of the projection angle and the distance from the center of the FOV. The GATE output file containing the sinogram data were imported as a 2D matrix and transformed into a 2D histogram with 320 bins for the vertical axis, representing the projection angle from 0 to π , and 640 projection bins for the horizontal axis, representing the distance from the center of the FOV ranging from -300 to 300 mm for the GE Signa PET/MR. All processing steps are shown in **Figure 4**.

According to the NEMA protocol, an alignment of the sinogram data was performed by finding the maximum value for each projection angle and shifting the projection data such that the maximum value for each projection angle is at the center of the sinogram, as shown in **Figures 1A–C**. After alignment, the corresponding projection bins of all projection angles are summed to obtain a summed projection profile, as shown in **Figure 1D**. Next, a 40 mm wide strip (see **Figure 1E**) was centralized around the peak of the summed projection profile in order to estimate the background counts according to NEMA procedures. The values of the projection bins at left and right edge of this central 40 mm wide strip were averaged and multiplied by the number of projection bins within the strip. This value was considered as a representative estimate for the fraction of random and scattered events detected within the strip and used to estimate the corresponding fraction of true events. Once the fractions of random, scattered and true events are estimated for different activity levels, the corresponding count rate curves as well as NECR can be extracted (**Figure 1F**).

Simulated Sensitivity and NECR of the GE Signa PET/MR for Other Isotopes Using GATE

The GATE-model for the GE Signa PET/MR was used to simulate the sensitivity and NECR of the PET/MR system for isotopes other than ^{18}F and ^{68}Ga including ^{11}C , ^{15}O , ^{13}N , and ^{82}Rb . In terms of sensitivity, the simulated values were compared with the



theoretical sensitivities based the branching ratio of each isotope and the average sensitivity of 21.5 cps/kBq measured for ^{18}F (Caribé et al., 2019).

Positron Range Evaluation Using the GATE Model for the GE Signa PET/MR

The GATE-model for the GE Signa PET/MR was used to simulate the presence of the magnetic field and evaluate its impact on the positron range in different tissue media. To characterize the effect of the 3T magnetic field on the positron range, we simulated point sources of positron-emitting radionuclides including ^{18}F , ^{11}C , ^{15}O , ^{13}N , ^{68}Ga , and ^{82}Rb positioned in the middle of a homogeneous $20\text{ cm} \times 20\text{ cm} \times 20\text{ cm}$ cube with different tissue media: lung (mass density of 0.3 g/cm^3), soft tissue (mass density of 1.0 g/cm^3), bone (mass density of 1.42 g/cm^3). To evaluate the tissue-dependence, we simulated the spatial distribution of positron annihilation for ^{68}Ga in an inhomogeneous region. The region comprises two adjacent cubes of $20\text{ cm} \times 20\text{ cm} \times 20\text{ cm}$ filled with lung and soft tissue. For each isotope, 5 million events were simulated with and without 3T magnetic field applied in the axial direction. As output, the spatial coordinates of the location of the annihilation end point were saved to a file for each recorded positron.

TABLE 1 | Sensitivity for ^{18}F and ^{68}Ga in the center of the FOV and 10 cm off center in the presence of 3T MR field.

	Measured (cps/kBq)		Simulated (cps/kBq)	
	0 cm	10 cm	0 cm	10 cm
^{18}F	21.831	21.173	21.205	21.112
^{68}Ga	20.063	19.689	19.098	19.017

These results are compared to the measured ^{18}F and ^{68}Ga -values (Caribé et al., 2019).

RESULTS

GATE Model for the GE Signa PET/MR

The GATE model for the GE Signa PET/MR including the MR-body (gray) is presented in **Figure 2** together with the phantom configurations for the sensitivity and NECR simulations according to the NEMA NU 2-2012 protocols.

Validation of the GATE Model for the GE Signa PET/MR

The simulated and measured sensitivity values for ^{18}F and ^{68}Ga at the center of the FOV and 10 cm off-center are presented in

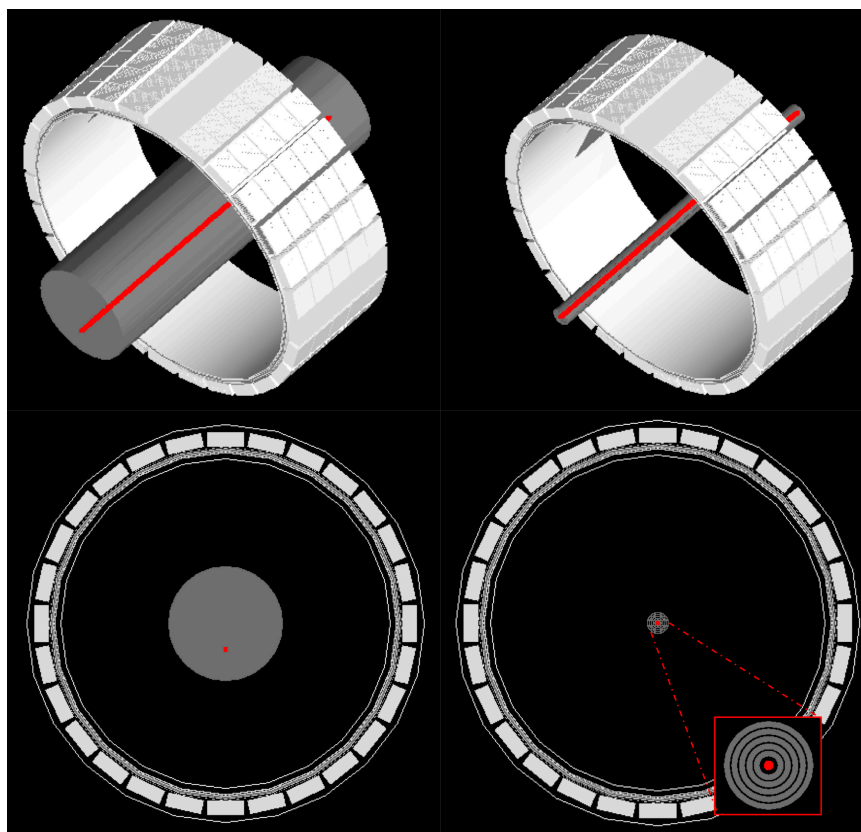


FIGURE 2 | Visualization of the GATE model of the GE Signa PET/MR system including the NEMA NECR (right) and sensitivity (left) phantom with a 70-cm-line activity source (red). The PET system consists of 5 rings of 28 detector blocks ($25\text{ mm} \times 4.0\text{ mm} \times 5.3\text{ mm}$) based on lutetium-yttrium-orthosilicate (LYSO) crystals with MR-compatible SiPM technology (Alva-Sánchez et al., 2016). This results in an axial and transaxial FOV of 25 and 60 cm, respectively.

TABLE 2 | Measured and simulated scatter fraction, peak NECR and the corresponding activity concentration for different isotopes in the presence of 3T magnetic field.

	Scatter fraction at peak (%)	Peak NECR (kcps)	Activity concentration at peak NECR (kBq/ml)
Measured			
^{18}F (Caribé et al., 2019)	43.3	216.8	18.60
^{18}Ga (Caribé et al., 2019)	42.9	205.6	20.40
Simulated			
^{18}F	38.8	216.8	17.4
^{15}O	38.8	216.4	18.2
^{13}N	38.2	212.0	16.5
^{11}C	38.5	217.6	16.7
^{82}Rb	39.1	173.5	19.6
^{68}Ga	38.7	207.1	20.1

Table 1 while the simulated and measured peak NECR with the corresponding activity concentration and scatter fraction at peak NECR are presented for ^{18}F and ^{68}Ga in Table 2.

Simulated Sensitivity and NECR of the GE Signa PET/MR for Other Isotopes Using GATE

Table 3 shows the simulated NEMA sensitivity for ^{18}F , ^{15}O , ^{13}N , ^{82}Rb , and ^{68}Ga as the average value of the sensitivity at

the center of the FOV and 10 cm off-center. Figure 3A shows the underestimation of the simulated sensitivity for ^{82}Rb when only one aluminum sleeve is surrounding the line source while Figure 3B presents the estimated sensitivity without taken into account the sensitivity values using only one aluminum sleeve. As such, the sensitivity value averaged over the center and 10 cm off center position in the FOV is increased to 21.4 cps/kBq (Figure 3B), compared to 19.9 cps/kBq when taken into account all five sleeve thicknesses (Figure 3A).

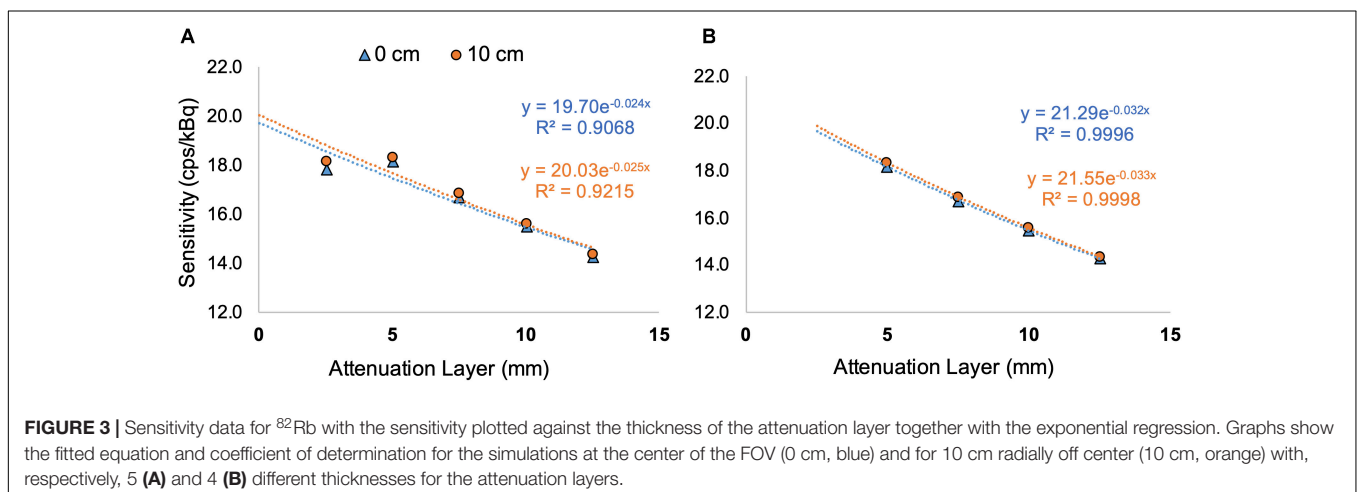
The results for the simulated peak NECR, the corresponding activity concentration and the scatter fraction at peak NECR for ^{18}F , ^{11}C , ^{15}O , ^{13}N , ^{68}Ga , and ^{82}Rb are presented in Table 2 while Figure 4 shows the simulated true, random and scattered coincidence rates as well as NECR curves for these isotopes as a function of the activity concentration.

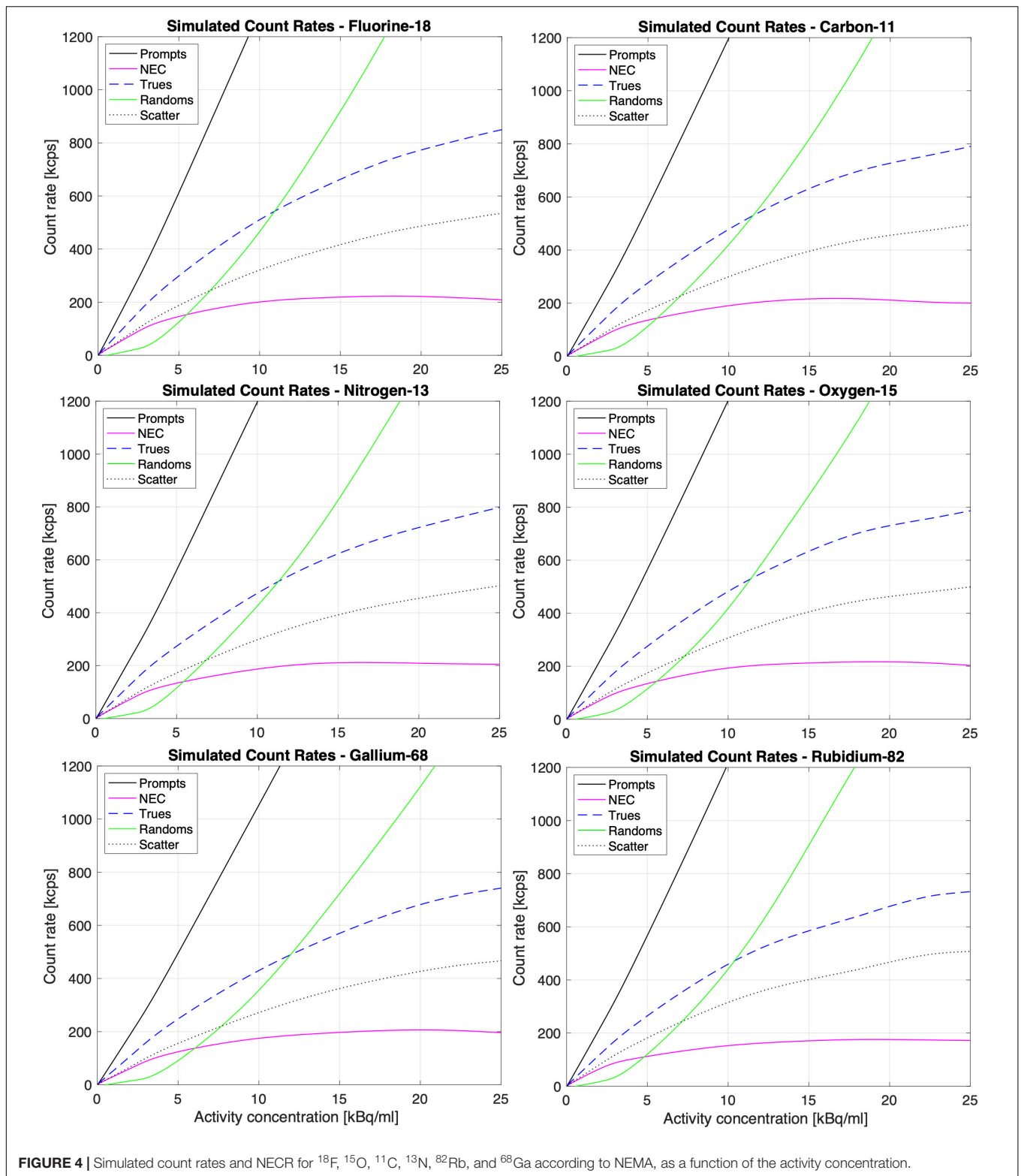
Positron Range Evaluation Using the GATE Model for the GE Signa PET/MR

Table 4 shows the comparison of the simulated positron range in soft tissue for different radioisotopes with and without 3T magnetic field with measured values taken from literature (Li et al., 2017; Soultanidis et al., 2011). The simulated mean positron range values for different isotopes in soft tissue, lung and bone are presented on Tables 5, 6 with and without the presence of a 3T magnetic field, with the mean positron range averaged over all directions (Table 5) and the mean positron range calculated for the transversal

TABLE 3 | Sensitivity for different isotopes in the presence of 3T magnetic field, presented as the average value of the sensitivity at the center of the FOV and the sensitivity at 10 cm off center.

	Branching ratio (%)	Measured (cps/kBq) (Caribé et al., 2019)	Simulated (cps/kBq)	Theoretical values (cps/kBq)	R^2 at the center values
^{18}F	96.76	21.5	21.2		1.00
^{15}O	99.89		20.9	22.20	1.00
^{13}N	99.82		21.5	22.18	1.00
^{11}C	99.75		21.1	22.16	1.00
^{82}Rb	95.45		19.9	21.21	0.91
^{68}Ga	87.90	19.9	19.2	19.53	1.00





plane perpendicular to the magnetic field and axial plane parallel to the magnetic field (Table 6). The impact of the magnetic field on the positron range is also visually shown in Figures 5, 6.

DISCUSSION

In this work we have developed and evaluated a model for the GE Signa PET/MR to run realistic Monte Carlo simulations

TABLE 4 | Comparison of positron range in soft tissue for different radioisotopes with and without 3T magnetic field.

Max energy (keV)		Mean 3D positron range (mm)					
		GATE		Ref. (Li et al., 2017)		Ref. (Soultanidis et al., 2011)	
		None	3T	None	3T	None	3T
¹⁸ F	633.5	0.50	0.52	0.64	0.45	0.56	0.54
¹⁵ O	1732.0	1.87	1.66	2.01	1.74	2.44	2.00
¹³ N	1198.5	1.08	1.01	1.32	1.26		
¹¹ C	960.2	1.02	0.96	1.03	0.82	1.05	0.96
⁸² Rb	3378.0	4.85	3.82	4.29	3.65	5.21	3.90
⁶⁸ Ga	1899.0	2.32	2.04	2.24	2.02	2.62	2.07

TABLE 5 | Mean 3D positron range for different tissues and radioisotopes with and without 3T magnetic field.

		Mean 3D positron range (mm)					
		Soft tissue		Lung		Bone	
		None	3T	None	3T	None	3T
¹⁸ F		0.50	0.52	2.23	1.70	0.34	0.34
¹⁵ O		1.87	1.66	7.74	4.28	1.22	1.17
¹³ N		1.08	1.01	4.30	2.63	0.71	0.69
¹¹ C		1.02	0.96	3.05	1.97	0.51	0.51
⁸² Rb		4.85	3.82	18.2	10.1	3.09	2.74
⁶⁸ Ga		2.32	2.04	8.09	4.59	1.33	1.26

TABLE 6 | Mean positron range in the transversal (perpendicular to the magnetic field) and axial direction (parallel to the magnetic field) for different tissue types and radioisotopes with and without 3T magnetic field.

		Mean transversal positron range (mm)						Mean axial positron range (mm)					
		Soft tissue		Lung		Bone		Soft tissue		Lung		Bone	
		None	3T	None	3T	None	3T	None	3T	None	3T	None	3T
¹⁸ F		0.27	0.26	0.95	0.73	0.17	0.17	0.27	0.27	0.95	1.08	0.17	0.17
¹⁵ O		0.93	0.77	3.74	0.97	0.61	0.57	0.93	0.93	3.75	3.74	0.61	0.61
¹³ N		0.54	0.49	2.15	0.74	0.35	0.34	0.54	0.54	2.15	2.15	0.35	0.35
¹¹ C		0.48	0.48	1.52	0.63	0.26	0.25	0.48	0.51	1.52	1.52	0.26	0.26
⁸² Rb		2.42	1.62	9.10	2.25	1.54	1.28	2.42	2.42	8.95	8.96	1.54	1.55
⁶⁸ Ga		1.01	0.95	4.04	1.00	0.66	0.61	1.01	1.16	4.05	4.04	0.66	0.66

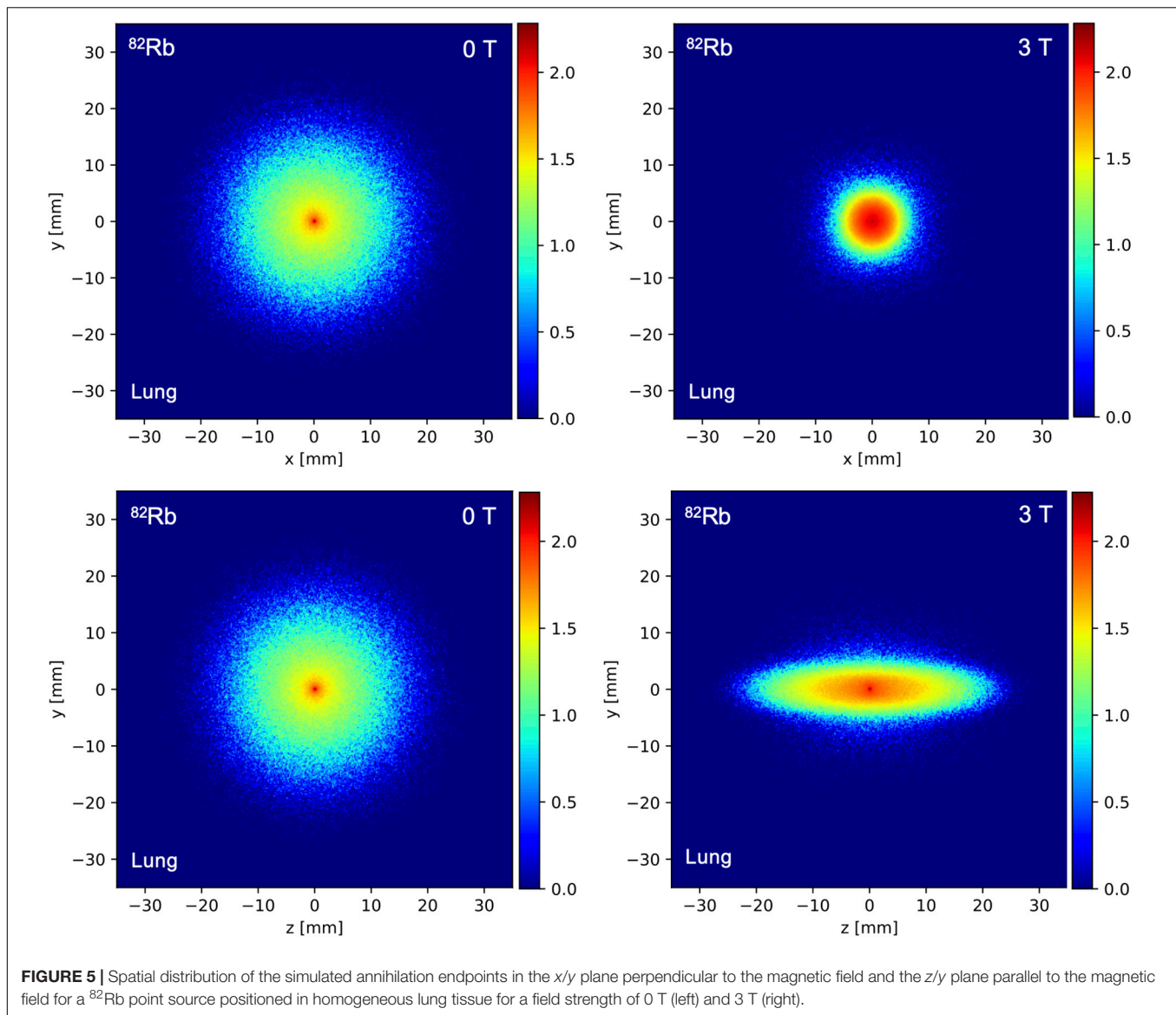
using GATE. The model was validated by comparing simulated sensitivity and NECR data ¹⁸F and ⁶⁸Ga with corresponding measurements performed on a GE Signa PET/MR system (Caribé et al., 2019). Once validated, these simulations allowed us to evaluate the system characteristics in terms of sensitivity and NECR for different, less conventional PET isotopes such as ¹⁵O, ¹³N, ¹¹C, and ⁸²Rb. In addition, the effect of the 3T magnetic field on positron range was investigated for different PET isotopes in different tissue types (lung tissue, soft tissue, and bone).

In terms of validating the GATE MC simulations, the simulated NEMA sensitivity values, presented in **Tables 1, 3**, were in line with the expected, theoretical values for all simulated PET radioisotopes. These theoretical values were based on the measured GE Signa PET/MR sensitivity for ¹⁸F while accounting for the differences in branching ratio between each isotope and ¹⁸F. These sensitivity values confirmed the higher count rate and increased sensitivity (Iagaru et al., 2019) of the GE Signa PET system due several design factors including Compton scatter recovery, longer axial FOV and reduced ring diameter (Lubberink and Herzog, 2011; Wagadarikar et al., 2014; Hsu et al., 2017).

For the pure β^+ emitters such as ¹¹C, ¹³N, and ¹⁵O, the sensitivity was comparable to that of ¹⁸F. However, ⁶⁸Ga and ⁸²Rb showed considerable differences. For ⁶⁸Ga, this was expected as literature data already reported a sensitivity of about 2 cps/kBq lower than ¹⁸F (Peng and Levin, 2012), which was confirmed by the simulations. However, for ⁸²Rb with a positron branching ratio very similar to ¹⁸F (less than 2% difference), the sensitivity is much lower than expected. This could be explained by the high energy of 3.381 MeV of the emitted positrons such that only one aluminum sleeve surrounding the line source is not adequate enough to generate sufficient annihilations. Therefore, sensitivity measurements with only one attenuating layer of aluminum surrounding the line source should be discarded for ⁸²Rb or material with a higher density than aluminum should be considered (see **Figure 3** and **Table 3**). In addition, and specifically for ⁸²Rb, a significant portion of the coincidences were detected outside of the scanner bore, which, in theory, is not possible since the LOR corresponding to two annihilation photons detected by the scanner can be positioned outside of the scanner. However, due to the additional 777 keV prompt-gamma emission, two gamma photons originating from a decaying ⁸²Rb source, can be registered as a pair of annihilation photons by the scanner, even when the source is situated outside of the scanner bore.

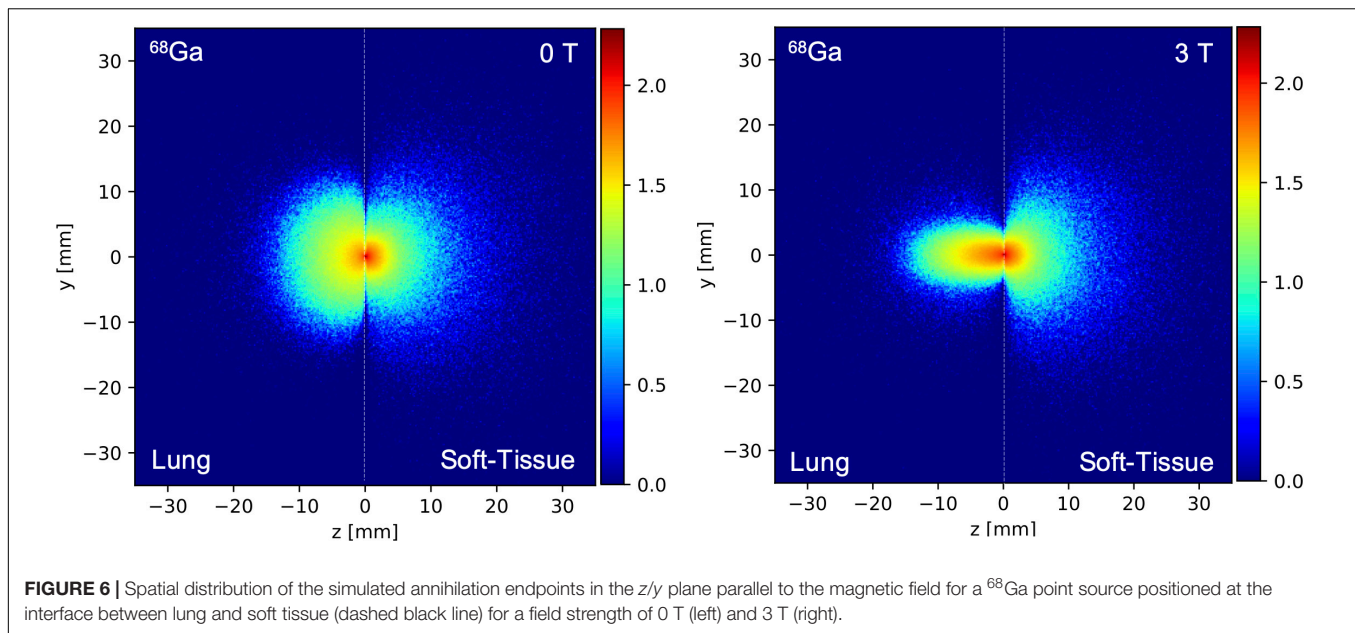
The results of the simulated NEMA count rate performance tests of the GE Signa PET/MR are summarized in **Figure 4** and **Table 2** and showed good agreement with previous count rate data for ¹⁸F (Levin et al., 2016a). These results confirmed that GATE MC simulations can be used to study the count rate performance of the GE Signa PET/MR. For positron emitters with high branching ratios for β^+ decay such as ¹¹C, ¹³N, and ¹⁵O, the simulation results confirmed a peak NECR similar to ¹⁸F with the corresponding activity concentration scaled by the inverse of the positron fraction.

For the higher energy positron emitters such as ⁶⁸Ga and ⁸²Rb, the simulated count rates were slightly lower than the measured values for ¹⁸F, as shown in **Figure 4** and **Table 2**. These lower values are primarily due to the respective 1.2% (1.883 MeV) and 13.1% (2.604 MeV) fraction of β^+ decay for ⁶⁸Ga and ⁸²Rb, which also results in prompt gamma emissions. These prompt gammas contaminate the PET signal by generating additional random, scattered and detection events which, in turn, increases the deadtime effects. The third gamma effect was also reported by different research groups (Martin et al., 1995; Converse et al., 2003).



In terms of the positron range, the 3T magnetic field clearly reduced the positron range by a factor up to 3–4 in the direction perpendicular to the magnetic field, especially for the higher energy positron emitters such as ^{15}O , ^{68}Ga , and ^{82}Rb and for low-density tissues such as lung tissue. While changes in positron range could clearly be observed in the perpendicular direction, the magnetic field does not have a clear impact on the positron range in the direction of the magnetic field, as was shown in **Figure 5** and **Tables 4–6**. The impact of the magnetic field on the positron range is highly dependent on the positron energy and tissue type as shown in **Tables 5, 6**. The latter is known to be related to the tissue electron density such that the mean free path of the positron is larger for tissues with lower electron density (Cal-González et al., 2013). This dependency is clearly demonstrated at the interface between different tissues as shown in **Figure 6**. These findings are in agreement with previous studies on the positron range (Rickey et al., 1992;

Cal-González et al., 2009; Shah et al., 2014; Alva-Sánchez et al., 2016; Huang et al., 2016; Caribé et al., 2017), and confirm a reduced positron range in the perpendicular direction of a magnetic field. Moreover, studies have also indicated (Iida et al., 1986; Wirtz et al., 1997; Soultanidis et al., 2011; Kraus et al., 2012) that a higher magnetic field will also induce a greater reduction of the positron range. However, it has to be noted that this effect was negligible for low energy positron emitters, such as ^{18}F . Moreover, the expected improvement of the PET image resolution, resulting from a reduced positron range by the presence of a 3T magnetic field, will only partially be observed in the resolution properties of the GE Signa PET/MR system due to the limited resolution of the PET detectors. Indeed, detector-dependent factors, such as crystal size and crystal penetration during detection, and inherent limitations such as the non-collinearity of the annihilation photons are also present and can explain why a reduced positron range with an increasing



magnetic field does not translate directly into improved image quality (Herzog et al., 2010; Bertolli et al., 2016; Caribé et al., 2019; Wadhwa et al., 2020). However, in a preclinical setting with small diameter detector rings and crystal sizes, the impact of a reduced positron range on the PET image quality is expected to be much higher while the use of monolithic crystals or recordings of the depth of interaction in clinical PET systems can further enhance the PET resolution such that it becomes more sensitive to positron range effects (Hammer et al., 1994; Stockhoff et al., 2019).

However, there are also limitations to be considered for this study. The dead time digitizer settings have a certain degree of uncertainty since these values were not provided by the manufacturer. This could affect the NEMA sensitivity estimates via the exponential regression of the simulated data (Khalif et al., 2016) and could explain the slightly lower simulated sensitivity values compared to theoretical values. Due to the uncertainty of the dead time digitizer settings, the deadtime was heuristically tuned to match measured data, and then applied to other simulations. These settings could also have lowered the scatter count rate (~ 500 kcps scatter at 20 kBq/ml as shown in Figure 4), compared to ~ 700 kcps (Levin et al., 2016a) and ~ 600 kcps (Caribé et al., 2019) scatter (at the same activity concentration) reported values for the Signa PET/MR with ^{18}F . Moreover, it should be noted that the count rates and NECRs for each simulation in this study were estimated using the NEMA approach which does not require an estimate for the number of random events (National Electrical Manufacturers Association [NEMA], 2012). This could explain the slight underestimation of the scatter fraction which was determined directly from the count events in the ROOT file. Indeed, for all of isotopes, the simulated scatter fractions were around 38 to 40%, which is slightly lower compared to reported, measured scatter fraction of 43.3% for ^{18}F . Finally, this study only evaluated the impact of a 3T magnetic field on the positron range, as this is a field strength

which is clinically relevant and in line with the magnetic field of GE Signa PET/MR.

CONCLUSION

GATE Monte-Carlo simulations were validated for simulating the GE Signa PET/MR system and used to predict sensitivity and NECR performance for ^{18}F , ^{15}O , ^{13}N , ^{11}C , ^{82}Rb , and ^{68}Ga . The GATE based predicted sensitivity and NECR data were in line with expected and previously published sensitivity and NECR values for all simulated PET isotopes and confirmed the impact of deadtime effects and increased random events on NECR for ^{68}Ga and ^{82}Rb because of the additional prompt gamma emissions. In addition, we have investigated the impact of the magnetic field on the positron range for different tissue types and PET isotopes. The improvement of image resolution resulting from a decreased positron range in the plane perpendicular to a 3T magnetic field, especially for high energy positron emitters, is only partially observed in the resolution properties of the GE Signa PET/MR system due to the limited spatial resolution of the PET detectors.

DATA AVAILABILITY STATEMENT

The datasets generated for this study are available on request to the corresponding author.

AUTHOR CONTRIBUTIONS

PC performed the conceptualization. PC, AD, NE, and CT contributed to the simulations of the study. PC and AD performed the data collection. PC, AD, and DP-B completed the

data analysis. All authors discussed the results and commented on the manuscript, contributed to the design of the study, and read and approved the final manuscript.

FUNDING

This present study was conducted with a grant support to the first author from CNPq, the National Council of

Technological and Scientific Development – Brazil (process number 235040/2014-2).

ACKNOWLEDGMENTS

This work was partially published at EANM'19 in Barcelona, Spain as a short 400-word abstract (Congress and October, 2019).

REFERENCES

- Afshar-Oromieh, A., Zechmann, C. M., Malcher, A., Eder, M., Eisenhut, M., and Linhart, H. G. (2014). Comparison of PET imaging with a ^{68}Ga -labelled PSMA ligand and ^{18}F -choline-based PET/CT for the diagnosis of recurrent prostate cancer. *Eur. J. Nucl. Med. Mol. Imaging* 41, 11–20. doi: 10.1007/s00259-013-2525-5
- Alva-Sánchez, H., Quintana-Bautista, C., Martínez-Dávalos, A., Ávila-Rodríguez, M. A., and Rodríguez-Villafuerte, A. (2016). Positron range in tissue-equivalent materials: experimental microPET studies. *Phys. Med. Biol.* 61, 6307–6321. doi: 10.1088/0031-9155/61/17/6307
- Banerjee, S. R., and Pomper, M. G. (2013). Clinical applications of Gallium-68. *Appl. Radiat. Isot.* 76, 2–13. doi: 10.1016/j.apradiso.2013.01.039
- Bertolli, O., Eleftheriou, A., Cecchetti, M., Camarlinghi, N., Belcari, N., and Tsoumpas, C. (2016). PET iterative reconstruction incorporating an efficient positron range correction method. *Phys. Med.* 32, 323–330. doi: 10.1016/j.ejpm.2015.11.005
- Cal-González, J., Herraiz, J. L., España, S., Desco, M., Vaquero, J. J., and Udías, J. M. (2009). “Positron range effects in high resolution 3D pet imaging,” in *Proceedings of the IEEE Nuclear Science Symposium Conference Record* (Orlando, FL: IEEE) 2788–2791.
- Cal-González, J., Herraiz, J. L., España, S., García Corzo, P. M., Vaquero, J. J., and Desco, M. (2013). Positron range estimations with PeneloPET. *Phys. Med. Biol.* 58, 5127–5152. doi: 10.1088/0031-9155/58/15/5127
- Caribé, P., Koole, M., Deller, T., Van Laere, K., and Vandenbergh, S. (2017). NEMA NU 2-2007 Performance Characteristics of GE Signa Integrated PET/MR: impact of using different PET Isotopes. *Eur. J. Nucl. Med. Mol. Imaging* 44, 119–956.
- Caribé, P., R. V., Koole, M. D., Asseler, Y., Deller, T. W., Van Laere, K., and Vandenbergh, S. (2019). NEMA NU 2-2007 performance characteristics of GE Signa integrated PET/MR for different PET isotopes. *EJNMMI Phys.* 6:11.
- Catana, C., van der Kouwe, A., Benner, T., Michel, C. J., Hamm, M., and Fenchel, M. (2010). Toward implementing an MRI-based PET attenuation-correction method for neurologic studies on the MR-PET brain prototype. *J. Nucl. Med.* 51, 1431–1438. doi: 10.2967/jnumed.109.069112
- Congress, A., and October, N. M. (2019). *Annual Congress of the European Association of Nuclear Medicine*, Vol. 46. Barcelona: Barcelona International Convention Centre.
- Conti, M., and Eriksson, L. (2016). Physics of pure and non-pure positron emitters for PET: a review and a discussion. *EJNMMI Phys.* 3:8.
- Converse, A. K., Nye, J., Barnhart, T. E., Dick, D. W., Avila-Rodríguez, M. A., and Sundaresan, R. (2003). MicroPET performance in the presence of the third gamma. *IEEE Nucl. Sci. Symp. Conf. Rec.* 3, 1797–1799.
- Efthimiou, N., Emond, E., Wadhwa, P., Cawthorne, C., Tsoumpas, C., and Thielemans, K. (2019). Implementation and validation of time-of-flight PET image reconstruction module for listmode and sinogram projection data in the STIR library. *Phys. Med. Biol.* 64:aa9b9.
- Eleftheriou, A., Tsoumpas, C., Bertolli, O., and Stiliaris, E. (2014). Effect of the magnetic field on positron range using GATE for PET-MR. *EJNMMI Phys.* 1, 49–50.
- Emond, E. C., Groves, A. M., Hutton, B. F., and Thielemans, K. (2019). Effect of positron range on PET quantification in diseased and normal lungs. *Phys. Med. Biol.* 64:205010. doi: 10.1088/1361-6560/ab469d
- Hammer, B. E., Christensen, N. L., and Heil, B. G. (1994). Use of a magnetic field to increase the spatial resolution of positron emission tomography. *Med. Phys.* 21, 1917–1920. doi: 10.1118/1.597178
- Herzog, H., Lida, H., Weirich, C., Tellmann, L., Kaffanke, J., and Spelleberg, S. (2010). “Influence from high and ultra-high magnetic field on positron range measured with a $^{9.4}\text{TMR-BrainPET}$,” in *Proceedings of the IEEE Nuclear Science Symposium & Medical Imaging Conference*, (Knoxville, TN: IEEE), 3410–3413.
- Hoffend, J., Mier, W., Schumacher, J., Schmidt, K., Dimitrakopoulou-Strauss, A., and Strauss, L. G. (2005). Gallium-68-DOTA-albumin as a PET blood-pool marker: experimental evaluation in vivo. *Nucl. Med. Biol.* 32, 287–292. doi: 10.1016/j.nucmedbio.2005.01.002
- Hsu, D. F. C., Ilan, E., Peterson, W. T., Uribe, J., Lubberink, M., and Levin, C. S. (2017). Studies of a next-generation silicon-photomultiplier-based time-of-flight PET/CT system. *J. Nucl. Med.* 58, 1511–1518. doi: 10.2967/jnumed.117.189514
- Huang, S. Y., Savic, D., Yang, J., Shrestha, U., and Seo, Y. (2016). “The effect of magnetic field on positron range and spatial resolution in an integrated whole-body time-of-flight PET/MRI system,” in *Proceedings of the 2014 IEEE Nuclear Science Symposium and Medical Imaging Conference* (Seattle, WA: IEEE), 3–6.
- Iagaru, A., Mittra, E., Minamimoto, R., Jamali, M., Levin, C., and Quon, A. (2019). Simultaneous whole-body time-of-flight ^{18}F -FDG PET/MRI. *Clin. Nucl. Med.* 40, 1–8. doi: 10.1097/rlu.0000000000000611
- Iida, H., Kanno, I., Miura, S., Murakami, M., Takahashi, K., and Uemura, K. (1986). A simulation study of a method to reduce positron annihilation spread distributions using a string magnetic field in positron emission tomography. *IEEE Trans. Nucl. Sci.* 33, 118–122.
- Jan, S., Santin, G., Strul, D., Staelens, K., Assié, K., and Autret, D. (2004). GATE: a simulation toolkit for PET and SPECT. *Phys. Med. Biol.* 49, 4543–4561.
- Jodal, L., Le Loirec, C., and Champion, C. (2012). Positron range in PET imaging: an alternative approach for assessing and correcting the blurring. *Phys. Med. Biol.* 57, 3931–3943. doi: 10.1088/0031-9155/57/12/3931
- Kemerink, G. J., Visser, M. G., Franssen, R., Beijer, E., Zamburlini, M., and Halders, S. G. (2011). Effect of the positron range of ^{18}F , ^{68}Ga and ^{124}I on PET/CT in lung-equivalent materials. *Eur. J. Nucl. Med. Mol. Imaging* 38, 940–948. doi: 10.1007/s00259-011-1732-1
- Khalif, M., Stute, S., Wagadarikar, A., and Comtat, C. (2016). “Modeling the GE Signa PET-MR with monte-carlo simulations using GATE,” in *Proceedings of the IEEE Nuclear Science Symposium and Medical Imaging Conference* (San Diego, CA: IEEE).
- Kolb, A., Sauter, A. W., Eriksson, L., Vandenbroucke, A., Liu, C. C., and Levin, C. (2015). Shine-through in PET/MR imaging: effects of the magnetic field on positron range and subsequent image artifacts. *J. Nucl. Med.* 56, 951–954. doi: 10.2967/jnumed.114.147637
- Kraus, R., Delso, G., and Ziegler, S. I. (2012). Simulation study of tissue-specific positron range correction for the new biograph mMR whole-body PET/MR system. *IEEE Trans. Nucl. Sci.* 59(5 Pt. 1), 1900–1909. doi: 10.1109/tns.2012.2207436
- Laforest, R., and Liu, X. (2008). Image quality with non-standard nuclides in PET. *Q. J. Nucl. Med. Mol. Imaging* 52, 151–158.
- Levin, C. S., Deller, T. W., Delso, G., Khalighi, M. M., Maramraju, S. H., and Grant, A. M. (2016a). NEMA NU 2-2012 performance studies for the SiPM-based ToF-PET component of the GE SIGNA PET/MR system. *Med. Phys.* 43, 2334–2343. doi: 10.1118/1.4945416
- Levin, C. S., and Hoffman, E. J. (1999). Calculation of positron range and its effect on the fundamental limit of positron emission tomography system spatial resolution. *Phys. Med. Biol.* 44, 781–799. doi: 10.1088/0031-9155/44/3/019

- Levin, C. S., Maramraju, S. H., Khalighi, M. M., Deller, T. W., Delso, G., and Jansen, F. (2016b). Design features and mutual compatibility studies of the time-of-flight PET capable GE SIGNA PET/MR system. *IEEE Trans. Med. Imaging* 35, 1907–1914. doi: 10.1109/tmi.2016.2537811
- Li, C., Cao, X., Liu, F., Tang, H., Zhang, Z., and Wang, B. (2017). Compressive effect of the magnetic field on the positron range in commonly used positron emitters simulated using Geant4. *Eur. Phys. J. Plus* 132:484.
- Lubberink, M., and Herzog, H. (2011). Quantitative imaging of 124I and 86Y with PET. *Eur. J. Nucl. Med. Mol. Imaging* 38(Suppl. 1), 10–18. doi: 10.1007/s00259-011-1768-2
- Marshall, R. C., Huang, S. C., Nash, W. W., and Phelps, M. E. (1983). Assessment of the [18F]fluorodeoxyglucose kinetic model in calculations of myocardial glucose metabolism during ischemia. *J. Nucl. Med.* 24, 1060–1064.
- Martin, C. C., Christian, B. T., Satter, M. R., Nickerson, L. D. H., and Nickles, R. J. (1995). Quantitative PET with positron emitters that emit prompt gamma rays. *IEEE Trans. Med. Imaging* 14, 681–687. doi: 10.1109/42.476109
- Mayerhoefer, M. E., Prosch, H., Beer, L., Tamandl, D., Beyer, T., and Hoeller, C. (2020). PET/MRI versus PET/CT in oncology: a prospective single-center study of 330 examinations focusing on implications for patient management and cost considerations. *Eur. J. Nucl. Med. Mol. Imaging* 47, 51–60. doi: 10.1007/s00259-019-04452-y
- Moses, W. W. (1994). Empirical observation of resolution degradation in positron emission tomographs utilizing block detectors. *J. Nucl. Med.* 34:101.
- Moses, W. W. (2011). Fundamental limits of spatial resolution in PET. *Nucl. Instrum. Methods Phys. Res. A* 648(Suppl. 1), 1–14.
- National Electrical Manufacturers Association [NEMA] (2012). *NEMA NU 2-2007: Performance Measurements of Positron Emission Tomographs*. Rosslyn, VA: National Electrical Manufacturers Association.
- Palmer, M. R., Zhu, X., and Parker, J. A. (2005). Modeling and simulation of positron range effects for high resolution PET imaging. *IEEE Trans. Nucl. Sci.* 52, 1391–1395. doi: 10.1109/tns.2005.858264
- Papp, L., Spielvogel, C. P., Rausch, I., Hacker, M., and Beyer, T. (2018). Personalizing medicine through hybrid imaging and medical big data analysis. *Front. Phys.* 6:19. doi: 10.3389/fphy.2018.00051
- Park, S. J., Rogers, W. L., and Clinthorne, N. H. (2007). Effects of positron range and annihilation photon acolinearity on image resolution of a Compton PET. *IEEE Trans. Nucl. Sci.* 54, 1543–1552. doi: 10.1109/tns.2007.902358
- Peng, H., and Levin, C. S. (2012). Study of PET intrinsic spatial resolution and contrast recovery improvement for PET/MRI systems. *Phys. Med. Biol.* 57, N101–N115.
- Phelps, M. E., Huang, S. C., Hoffman, E. J., Selin, C., Sokoloff, L., and Kuhl, D. E. (1979). Tomographic measurement of local cerebral glucose metabolic rate in humans with (F-18)2-fluoro-2-deoxy-D-glucose: validation of method. *Ann. Neurol.* 6, 371–388. doi: 10.1002/ana.410060502
- Rahmim, A., Tang, J., Lodge, M. A., Lashkari, S., Mohammad, R. A., and Bengel, F. M. (2008). “Resolution modeled PET image reconstruction incorporating space-variance of positron range: Rubidium-82 cardiac PET imaging,” in *Proceedings of the IEEE Nuclear Science Symposium Conference Record* (Dresden: IEEE), 3643–3650.
- Rickey, D. W., Gordon, R., and Huda, W. (1992). On lifting the inherent limitations of Positron Emission Tomography by using magnetic fields (MagPET). *Automedica* 14, 355–369.
- Shah, N. J., Herzog, H., Weirich, C., Tellmann, L., Kaffanke, J., and Caldeira, L. (2014). Effects of magnetic fields of up to 9.4 T on resolution and contrast of PET images as measured with an MR-BrainPET. *PLoS One* 9:e95250. doi: 10.1371/journal.pone.0095250
- Shao, Y., Cherry, S. R., Farahani, K., Meadors, K., Siegel, S., and Silverman, R. W. (1997). Simultaneous PET and MR imaging. *Phys. Med. Biol.* 42, 1965–1970.
- Soultanidis, G., Karakatsanis, N., Nikiforidis, G., and Loudos, G. (2011). Study of the effect of magnetic field in positron range using GATE simulation toolkit. *J. Phys. Conf. Ser.* 317:012021. doi: 10.1088/1742-6596/317/1/012021
- Stockhoff, M., Van Holen, R., and Vandenberghe, S. (2019). Optical simulation study on the spatial resolution of a thick monolithic PET detector. *Phys. Med. Biol.* 64:195003. doi: 10.1088/1361-6560/ab3b83
- Vallabhajosula, S., Solnes, L., and Vallabhajosula, B. (2011). A broad overview of positron emission tomography radiopharmaceuticals and clinical applications: what is new? *Semin. Nucl. Med.* 41, 246–264. doi: 10.1053/j.semnuclmed.2011.02.003
- Vandenberghe, S., Mikhaylova, E. D., Hoe, E., Mollet, P., and Karp, J. S. (2016). Recent developments in time-of-flight PET. *EJNMMI Physics* 3:3.
- Wadhwa, P., Thielemans, K., Efthimiou, N., Wangerin, K., Keat, N., and Emond, E. (2020). PET image reconstruction using physical and mathematical modelling for time of flight PET-MR scanners in the STIR library. *Methods* doi: 10.1016/j.ymeth.2020.01.005 [Epub ahead of print].
- Wagadarikar, A. A., Ivan, A., Dolinsky, S., and McDaniel, D. L. (2014). Sensitivity improvement of time-of-flight (ToF) PET detector through recovery of Compton scattered annihilation photons. *IEEE Trans. Nucl. Sci.* 61, 121–125. doi: 10.1109/tns.2013.2282119
- Wirrwar, A., Vosberg, H., Herzog, H., Halling, H., Weber, S., and Muller-Gartner, H.-W. (1997). 4.5 tesla magnetic field reduces range of high-energy positrons—potential implications for positron emission tomography. *IEEE Trans. Nucl. Sci.* 44, 184–189. doi: 10.1109/23.568801
- Yamamoto, S., Kuroda, K., and Senda, M. (2003). Scintillator selection for MR compatible gamma detectors. 2002 IEEE Nucl. Sci. Symp. Conf. Rec. 3, 1632–1635.

Conflict of Interest: The authors declare that the research was conducted in the absence of any commercial or financial relationships that could be construed as a potential conflict of interest.

Copyright © 2020 Caribé, Vandenberghe, Diogo, Pérez-Benito, Efthimiou, Thyssen, D'Asseler and Koole. This is an open-access article distributed under the terms of the Creative Commons Attribution License (CC BY). The use, distribution or reproduction in other forums is permitted, provided the original author(s) and the copyright owner(s) are credited and that the original publication in this journal is cited, in accordance with accepted academic practice. No use, distribution or reproduction is permitted which does not comply with these terms.



Influence of Multiple Animal Scanning on Image Quality for the Sedecal SuperArgus2R Preclinical PET Scanner

Nikos Efthimiou^{1,2*}, John D. Wright¹, Luke Clayton¹, Isaline Renard¹, Federico Zagni³, Paulo R.R.V. Caribé⁴, Stephen J. Archibald^{1,2} and Christopher J. Cawthorne^{1,2*}

¹Positron Emission Tomography Research Centre, University of Hull, Hull, United Kingdom, ²Department of Biomedical Sciences, University of Hull, Hull, United Kingdom, ³Medical Physics Department, University Hospital 'S. Orsola-Malpighi', Bologna, Italy, ⁴Medical Image and Signal Processing – MEDISIP, Ghent University, Gent, Belgium

OPEN ACCESS

Edited by:

Ivo Rausch,
Medical University of Vienna, Austria

Reviewed by:

Daniele De Paula Faria,
University of São Paulo, Brazil
Peter Homolka,
Medical University of Vienna, Austria

*Correspondence:

Christopher J. Cawthorne,
christopher.cawthorne@kuleuven.be
Nikos Efthimiou
nikos.efthimiou@ieee.org

Specialty section:

This article was submitted to
Medical Physics and Imaging,
a section of the journal
Frontiers in Physics

Received: 31 January 2020

Accepted: 26 November 2020

Published: 12 January 2021

Citation:

Efthimiou N, Wright JD, Clayton L,
Renard I, Zagni F, Caribé PRRV,
Archibald SJ and Cawthorne CJ (2021)
Influence of Multiple Animal Scanning
on Image Quality for the Sedecal
SuperArgus2R Preclinical
PET Scanner.
Front. Phys. 8:531662.
doi: 10.3389/fphy.2020.531662

Background: Increased throughput in small animal preclinical studies using positron emission tomography leads to reduced costs and improved efficiency of experimental design, however the presence of multiple off-centre subjects, as opposed to a single centered one, may affect image quality in several ways.

Methods: We evaluated the count rate performance using a NEMA scatter phantom. A Monte Carlo simulation of the system was validated against this dataset and used to simulate the count rate performance for dual scatter phantoms. NEMA NU4 image quality phantoms were then scanned in the central and offset positions, as well as in the offset position next to a uniform activity phantom. Uniformity, recovery coefficients and spillover ratios were then compared, as were two time frames for acquisition.

Results: Count rate performance assessed with a single NEMA scatter phantom was in line with previous literature, with simulated data in good agreement. Simulation of dual scatter phantoms showed an increase in scatter fraction. For the NEMA Image Quality phantom, uniformity and Recovery coefficients were degraded in the offset, and dual phantom cases, while spillover ratios were increased, notably when the chamber was placed nearest the gantry. Image quality metrics were comparable between the 20- and 10 min timeframes.

Conclusion: Dual animal scanning results in some loss of image quality on the Sedecal Argus PET scanner; however, this degradation is within acceptable limits.

Keywords: preclinical PET CT, dual phantom scanning, multiple animal scanning, Monte Carlo simulation, image quality, NEMA NU4, Sedecal Argus 2R

1 INTRODUCTION

Preclinical Positron Emission Tomography (PET) allows the longitudinal study of a range of biological processes in disease models, as well as being invaluable in the screening of novel diagnostic/theranostic PET probes. It is increasingly common for preclinical PET centers to scan multiple animals simultaneously in order to increase the cost-efficiency and throughput of studies,

especially with the use of short-lived PET isotopes such as [^{11}C], or where statistical requirements demand large study groups for the correct powering of experiments [1, 2].

Scanning multiple, radially displaced mice in the Field Of View (FOV) will increase attenuation and scatter, as well as the complexity of scatter correction. Additionally sensitivity and resolution will be reduced, while an increase in the overall activity in the FOV will increase dead time. As such, image quality is likely to degrade, and it is necessary to assess these effects on individual scanner/bed geometries as these vary considerably [3]. Although ultimately the effect on biological quantitation is of greatest importance, use of the NEMA NU4 image quality (IQ) phantom [4] allows direct comparison between systems.

Several groups have reported setups to achieve multiple animal imaging. Aide et al. [5] reported the use of a Siemens Biograph TrueV clinical PET-CT scanner and showed that tracer quantitation in the central and offset positions was highly correlated, albeit with lower system sensitivity and resolution (and higher injected activities) than commonly found in preclinical systems.

Aide et al. [1] went on to characterize a self-manufactured four-animal bed on the Siemens Inveon, demonstrating an increase in spillover ratios and a decrease in resolution for the NEMA IQ phantom; albeit with a high correlation between PET quantitation and biodistribution using this arrangement. Habte et al. [6] characterized a 3- and 4-bed setup for the R4 (Concorde Microsystems/Siemens) and Inveon (Siemens) scanners and demonstrated comparable *in vivo* quantitation between single and multiple animal scanning as long as attenuation correction was performed. Yagi et al. [7] reported another self-assembled multiple animal bed for the Inveon scanner, evaluating uniformity in mouse phantoms for four animals and demonstrating a comparable decrease to Habte et al. [6]. Seidel et al. [8] reported a dual mouse bed that enabled ECG-gated imaging to be carried out on the Argus PET-CT scanner but did not characterize effects on image quality.

Siepel et al. [9] studied the effects of scanning 2 and 4 animals, axially or radially displaced, in an Inveon scanner using the NEMA NU4 IQ phantom. They reported a decrease in uniformity, a reduction in Recovery Coefficient (RC) and an increase in Spill-Over ratio (SOR) for the 2 and 4 phantom radially-displaced cases, which could be improved by axial displacement. Rominger et al. [10] characterized an 8-mouse bed in the Inveon scanner, demonstrating that scatter correction and reduced overall activity in the field of view was necessary to achieve optimum quantitation in this setting. Using the PET-SORTEO simulation methodology, Reilhac et al. [11] assessed the signal degradation for dual animal scanning on the Inveon and the impact of this on the detection of biological variation. After demonstrating that their simulation gave comparable results to acquired phantom data, they went on to demonstrate that recovery coefficients and uniformity were decreased, while SOR (in this case peak-to-valley measure) were increased.

Most recently, Greenwood et al. [12] characterized a commercial four-chamber bed on a Mediso preclinical PET scanner, using NEMA phantoms and mice. As in previous

studies, they demonstrated a decrease in uniformity and recovery coefficients, and an increase in spillover ratios, in the multiple vs. single animal cases, though these increases were within the recently suggested limits for bias [13].

This study seeks to investigate the effect of dual animal scanning on the Sedecal SuperArgus2R preclinical scanner using the NEMA IQ phantom filled with a range of activities; also to assess the effects on IQ for common static scan frame lengths. Initially, we validate a Monte Carlo (MC) simulation of the scanner geometry and use it to compare the effect on count rate performance between single and dual NEMA scatter phantoms. We then go on to assess IQ metrics on phantoms placed either centrally, offset, or offset alongside a 20 mL syringe containing an equal activity, also comparing spillover ratios where air and water chambers are displaced toward the center of the field of view or the bore.

2 MATERIALS AND METHODS

2.1 SuperArgus2R Scanner

The Sedecal SuperArgus2R preclinical PET scanner (**Figure 1**) [14–16] features 18 phoswich detector blocks in an arrangement of 2 rings with diameter 118 mm and axial FOV 48.0 mm. In between the two rings there is gap of 8 mm. Each block has a two layers of 13×13 crystals of cerium-doped Lutetium Orthosilicate (LSO:Ce) (7 mm length) at the inner layer and cerium-doped Gadolinium Orthosilicate (GSO:Ce) (8 mm length) at the outer layer. Each crystal element has size mm^2 . The two crystals are joined back to back with an optically transparent method. From the 18 blocks, 7 are in coincidence. The coincidence window was 5 ns for all crystal combinations.

The phoswich detector arrangement provides Depth of Interaction (DOI) information, allowing for more uniform images and better radial spatial resolution [17]. As such, this detector configuration should also reduce spatial resolution degradation when scanning dual objects.

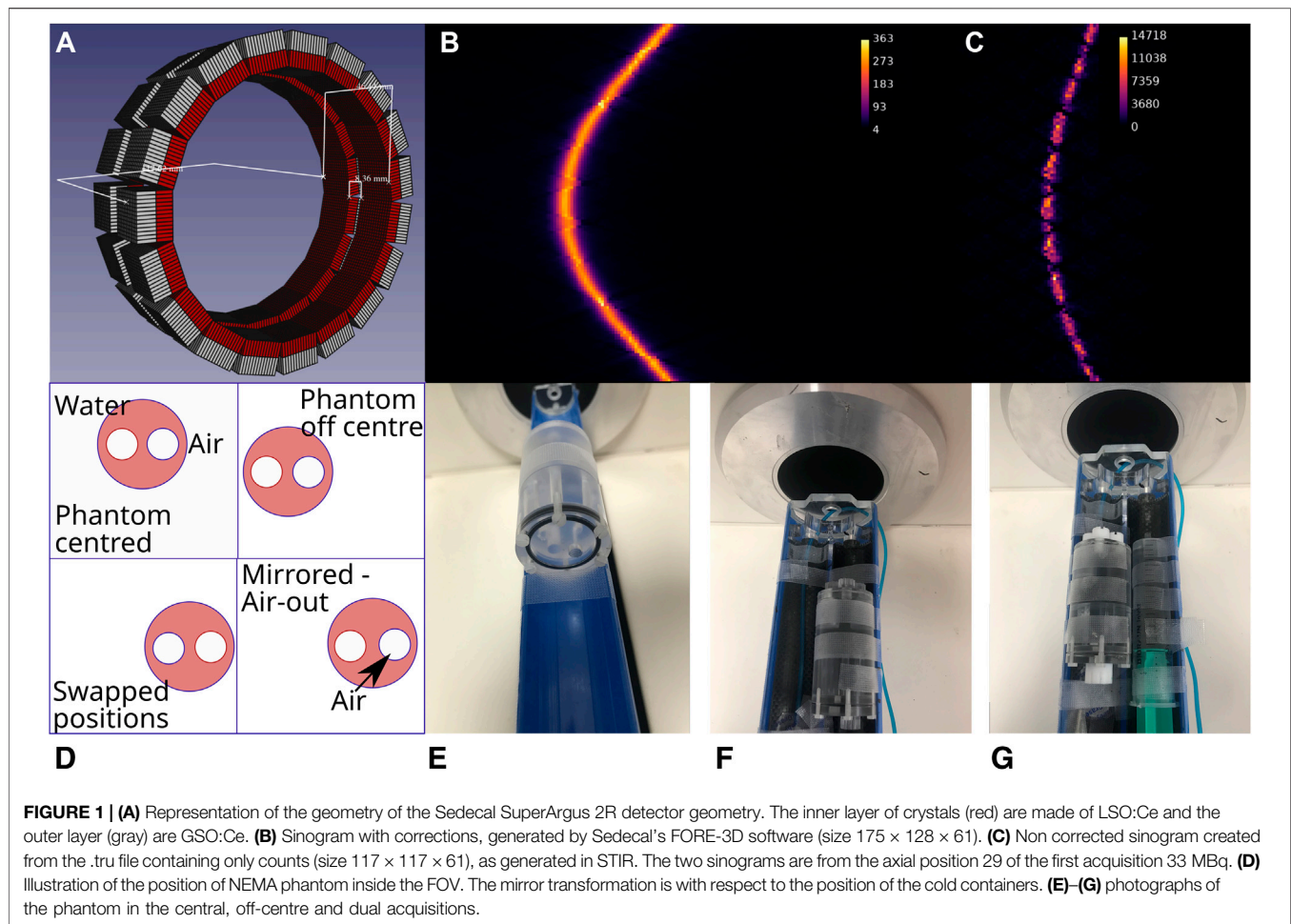
2.2 Monte Carlo Simulation Model

Due to the supplied animal bed on the scanner being too small to accommodate two scatter phantoms simultaneously, investigations on a single phantom in an offset bed position and dual phantom scatter fraction were performed in simulation only.

The MC simulation model was developed using the GATE (v.8.1) [18], simulation toolkit. The model was validated over the scanner's acceptance tests and measurements following the NEMA protocol [19]. The energy window was set to 250–700 keV, the same as the one used in the experiments. The coincidence window was set to 5.0 ns. The emstandard_opt3, physics model, was used without any variance reduction techniques or energy cuts.

2.2.1 Simulations for Count Losses, Scatter Fraction and NECR

A model of the NEMA scatter fraction phantom was simulated in order to compare the counting performance, scatter fraction and



Noise Equivalent Count Rate (NECR) for different placements in the FOV, using the validated GATE model. The model phantom matched the manufactured phantom that was used for the validation of the simulation model; a polyethylene cylindrical phantom 70 mm long and 25 mm in diameter (for details see Section 2.3).

The phantom was simulated solo in the center, offset (± 19.0 mm on the x axis, as defined in GATE) positions of the FOV [20, 21] as well as in combination with a second phantom. The model of the scanner included all parts of the physical scanner (plastic tubes, shielding etc).

2.3 NEMA Phantom Studies

All acquisitions were made using [^{18}F] produced using an ABT mini-cyclotron (ABT, United States).

2.3.1 Assessment of Scatter Fraction, Count Losses, Random Coincidences and NECR

The system was evaluated according to Section 4 of the NEMA NU4-2008 standard [4]. A polyethylene cylindrical phantom 70 mm long and 25 mm in diameter was manufactured and a 3.2 mm hole was drilled 10 mm off center to fit a capillary tube made of Borosilicate glass (World Precision Instruments, 1B200-4). The capillaries had an outer diameter 2.0 mm and inner 1.12 mm.

Phantom data were acquired with a starting activity of approximately 35 MBq of [^{18}F]. A series of 10 min scans followed by a 15 min of rest were acquired, lasting in total for more than 3 half-lives (6 h), using the 250–700 keV energy window.

2.3.2 Raw Data Processing

The NEMA NU4-2008 [4] protocol requires that uncorrected sinograms holding only number of coincidences are processed. However, direct extraction of such data from the scanner was not possible. By default, the scanner saves the recorded coincidences (after application of the energy window) in the proprietary .tru files which essentially are histograms holding counts per detector combination with detector pair coordinates. The scanner's software has the option to extract pre-corrected (for dead time and decay) FORE-3D sinograms [22] (Figure 1B), typically for Filtered Back-Projection reconstruction, which are not suitable for the execution of the NEMA protocol.

We addressed the issue by appropriately modifying the IO component of the STIR image reconstruction library [23] to read the .tru files and export projection data. Besides the new input function, the issue of the multiple detector layers, which are not currently supported by STIR, was addressed by means of simple

geometrical translations in order to assign the events on a single cylindrical model.

Finally, as suggested in the NEMA protocol, Single Slice Rebinning was performed on the projection data using the tool provided in STIR (**Figure 1A**). The sum of all bins in the sinograms we generated was equal to the sum of events in the .tru file.

2.3.3 Assessment of Image Quality

A NEMA NU4-2008 image quality phantom [4] containing 2.5 or 10 MBq of ^{18}F (representing low and high activity acquisitions in mice respectively) was scanned at the center and offset positions and alongside a (20 mL) syringe filled with the same activity as illustrated in (**Figure 1B**). The activity was within 2.5% of stated dose at acquisition start. PET acquisitions used the 250 – 700 keV energy window, with two bed positions to fully cover the phantom, over a period of 20 min (2×10 min) or 10 min (2×5 min) to assess the effect of different timeframes on image quality. CT acquisitions covered the entire PET field of view and were performed at 40 kV and 140 μA beam current, with 360 projections and 1 shot). Attenuation maps were generated from a segmented version of the CT image scaled to 511 keV, as part of the standard reconstruction process from the manufacturer.

Images were converted into DICOM format and loaded into a Mediso image analysis software (Mediso NEMA Tests, NEMA IQ) which automatically recognized the NEMA IQ phantom geometry and generated appropriate ROI's for uniformity (%Standard Deviation (%STD)), Spill-Over ratio (SOR) and Recovery Coefficient (RC). Generated ROIs were manually positioned over the respective regions of the phantom, according to the protocol's instructions, to return mean values and the percentage standard deviation.

In addition we sought to investigate whether the above figures of merit were consistent across the FOV. To assess this, we made acquisitions on single NEMA IQ phantoms positioned off-centre on the left- and right-hand side of the bore. For SOR assessments we also performed left- and right-sided offset acquisitions with the air chamber facing either toward or away from the scanner bore, in order to investigate any impact made through the inherent bias of the NEMA IQ phantom geometry. We also investigated the impact on dual phantom scanning when the NEMA IQ phantom is positioned on the left or right imaging bed.

Finally, we performed dynamic acquisitions at 10- and 20 min frames on centrally positioned NEMA IQ phantoms and dual offset positioned phantoms in order to assess the impact of reduced scan time on the same image quality metrics.

2.3.4 Image Reconstruction

PET image reconstruction was performed using Ordered Subsets-Expectation Maximization (OSEM) 2D, with 16 subsets after 2 full iterations. The 2D sinogram was generated using 3D Fourier Rebinning (FORE-3D) on the stored data files provided by the manufacturer. The stored sinograms were corrected for linearity and dead-time. In order to reduce the amount of blurring, the maximum ring difference was set to 16 rings and a span 3; the

default settings recommended by the manufacturer. No post-filtering was applied in the reconstructed images.

The reconstruction was performed with all available corrections applied (randoms, scatter and attenuation) and included normalization. The reconstructed images had 175×175 voxels, with 64 slices for acquisitions with a single bed position and 116 for two bed positions. The voxel size was $0.39 \times 0.39 \times 0.775 \text{ mm}^3$. CT reconstruction was performed using the manufacturer's filtered back-projection algorithm.

3 RESULTS

3.1 Validation of the Simulation Model

The count rates of prompt, true, random, scattered events and the NECR of the measured phantom acquisition are presented in **Figure 2A** as a function of activity in the FOV, and summarized in **Table 1**. At a starting activity of 10 MBq, reflecting a suggested maximal injected dose for a mouse, the count losses are approximately 3.3% which increases to 9.76% when the activity doubles to 20 MBq; representative of a dual scanning scenario. The ratio between random and true events remains below 21% up to activities of 20 MBq, and the NECR has a peak of 105 kcps at 26 MBq. Comparison between this measured data and its simulated counterpart (**Figure 2B**) shows good agreement, with the simulation data returning a 4.5% reduction in NECR peak. Scatter fractions were comparable at both 10- and 20 MBq (19.65 and 18.26% vs. 20.9 and 19.35% respectively).

Furthermore, the scatter rate steadily increases in the measured centrally positioned acquisition until around 25 MBq is reached, peaking at 45.6 kcps (**Figure 2A**). This closely correlates to the simulated counterpart where the scatter rate peaks at similar activity levels. The simulated data, however, show that 57.9% of scattered events occur within the phantom, and 28.4% of events take place in the Delrin (polyoxymethylene) tube, which resides in the scanner bore to protect the detector rings and electronics. 30% of scattered events occur on the gantry shielding and less than 1% on the animal bed.

3.2 Simulation of Dual Scatter Phantoms

Simulations of the single NEMA scatter phantom in the offset bed position shows count losses of 0.98% at 10 MBq, increasing to 13.3% at 20 MBq (**Figure 2C**). Likewise, the dual scatter phantom simulation returned count losses at 5.78% and 17.26% for both 10- and 20 MBq, respectively. The rate of random events occurring appears to almost double from 10 to 20 MBq yet remains below 20% (**Figure 2D**). In the case of simulated offset and dual phantom acquisitions, the scatter rate continues to increase until a peak of 53.22- and 58.23 kcps at 30 MBq, respectively. The dual phantom simulation increased in scatter rate by 17.4% compared to the centered phantom (**Table 2**).

3.3 NEMA NU4 Image Quality Phantom

3.3.1 Static Phantom Acquisition

3.3.1.1 Uniformity

The uniformity, (%STD) at the center of the FOV, offset position and dual scanning, for initial activities 2.5- and 10 MBq, is

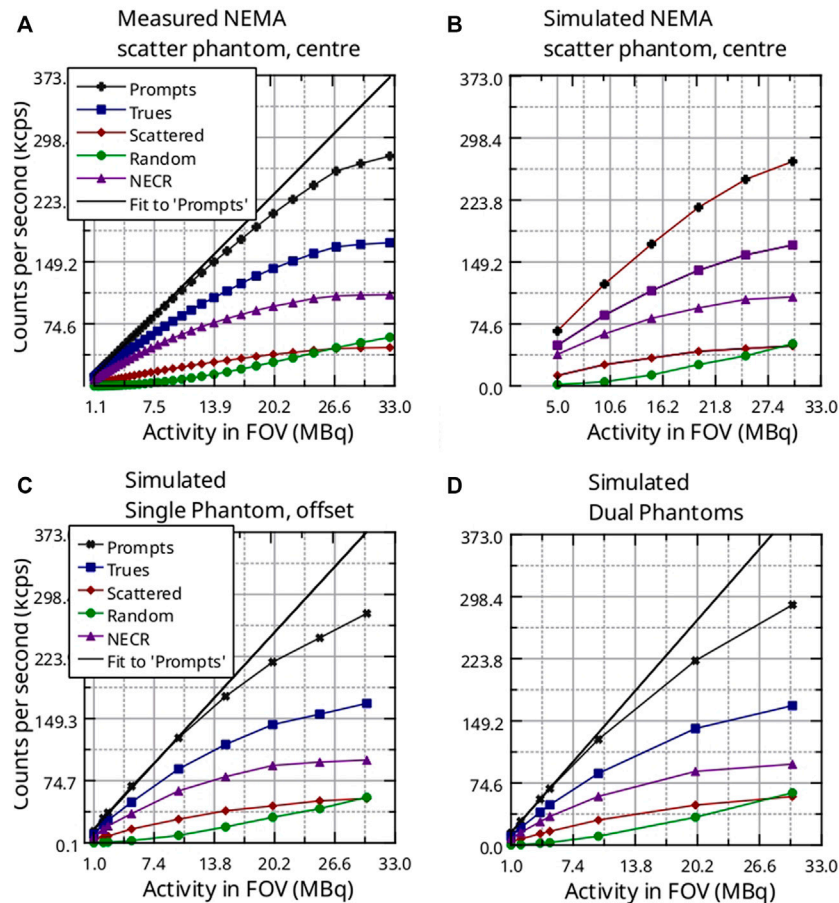


FIGURE 2 | Prompt, Trues, Random Scatter rates and NECR for the NEMA scatter phantom for (A) Experimental measurements at the central bed position. (B) Simulated central bed position. (C) Simulated off center, and (D) dual phantom scanning. The linear fit to the Prompts was performed for the first five points.

TABLE 1 | Measured and simulated trues, scattered and randoms fraction for two activities.

Activity (MBq)	Trues ratio		Scattered fraction		Random ratio		NECR	
	Sim (%)	Real (%)	Sim (%)	Real (%)	Sim (%)	Real (%)	Sim (%)	Real (%)
10	69.45	73.22	20.9	19.65	4.00	6.78	67.46	61.9
20	64.76	68.12	19.35	18.26	11.7	13.81	97.2	95.6

presented in **Figure 3A**. In **Figure 3J**, we present the corresponding CT images.

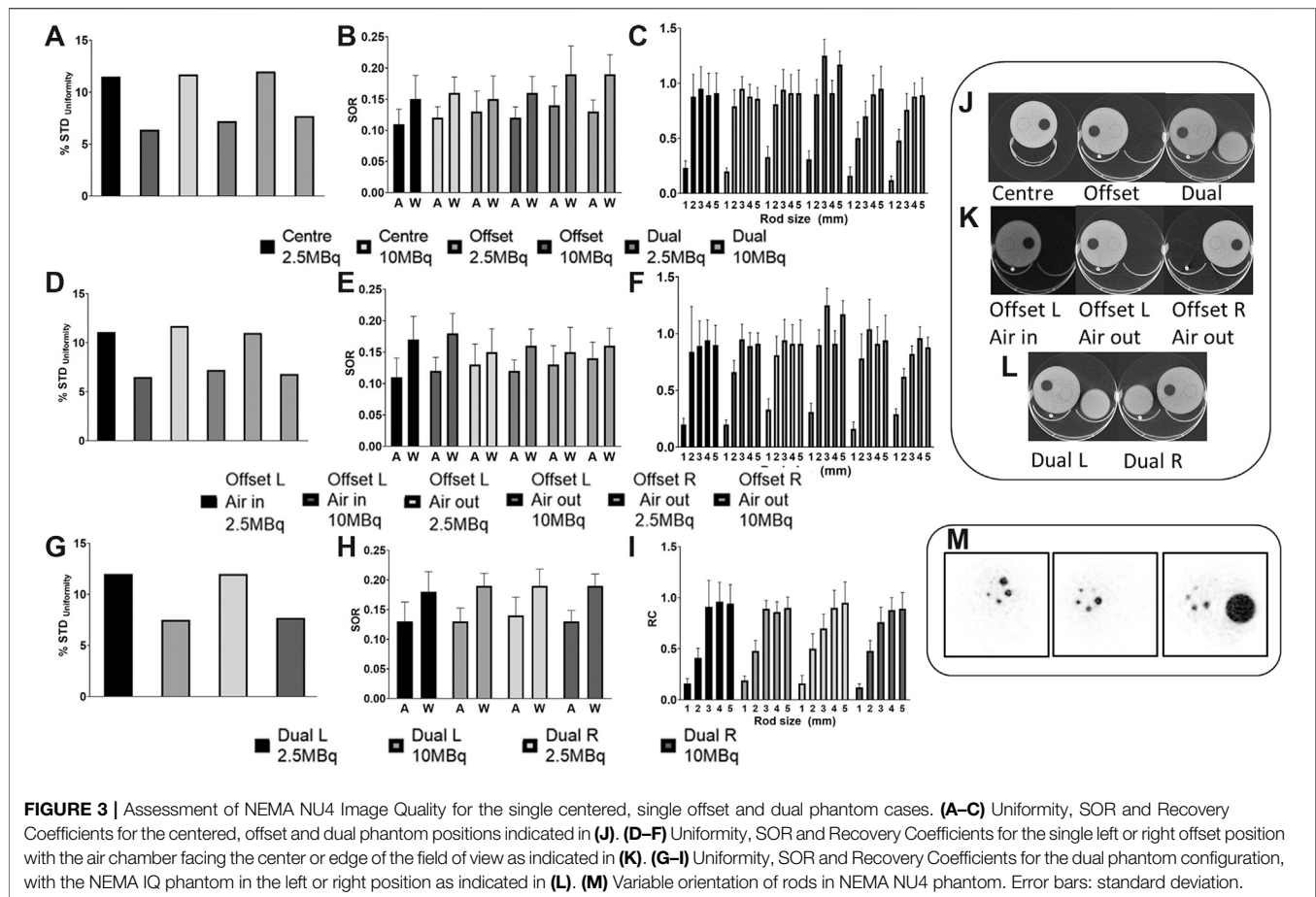
For both low (2.5 MBq) and high (10 MBq) acquisitions, the % STD increased when the phantom was placed at the offset position or when dual phantoms were scanned, compared to the single centered phantom case. Overall, %STD was higher for the low activity acquisitions (11–12%) vs those of higher activity (6–8%). Dual phantom acquisition returns 13% higher noise compared to single phantom acquisitions. We observe that line profiles placed over the uniform region of the NEMA IQ phantom and fitted with a polynomial (**Figure 4**) demonstrate asymmetrical fits for offset phantoms, with higher apparent activities closer to the scanner gantry. This phenomenon is not seen in the single centered phantom acquisitions and is

not as apparent in the dual phantom cases. Interestingly, when OSEM 3D reconstruction was employed, the artefact was more pronounced (see **Supplementary Data**).

Phantom positioning on the left- or right-hand side of the scanner had little impact on uniformity. Similarly, placement of the air chamber facing inwards or outwards had little effect (**Figure 3D**, corresponding images **Figure 3K**).

Likewise, uniformity is comparable between dual phantom acquisitions with the NEMA IQ phantom placed on the left or right side (**Figure 3G**).

Doubling the scan time from 10 to 20 min reduces %STD by 38.1 and 29.5% in single centered phantom acquisition for 2.5- and 10 MBq, respectively (**Figures 5A,D**). Increasing the scanning time from 10- to 20 min for dual phantom scanning



reduces the %STD of the uniformity by 34.4 and 26.0% for 2.5- and 10 MBq, respectively.

Adding a second activity source, as is the case for dual phantom scanning, increases the %STD 13.1 and 16.2% compared a single centered phantom at 2.5 MBq for both 10- and 20 min acquisition times, respectively. In the case of 10 MBq acquisitions, dual phantom scanning increases the %STD uniformity by 22.8 and 26.2% for 10- and 20 min acquisitions, respectively.

3.3.1.2 Recovery Coefficients

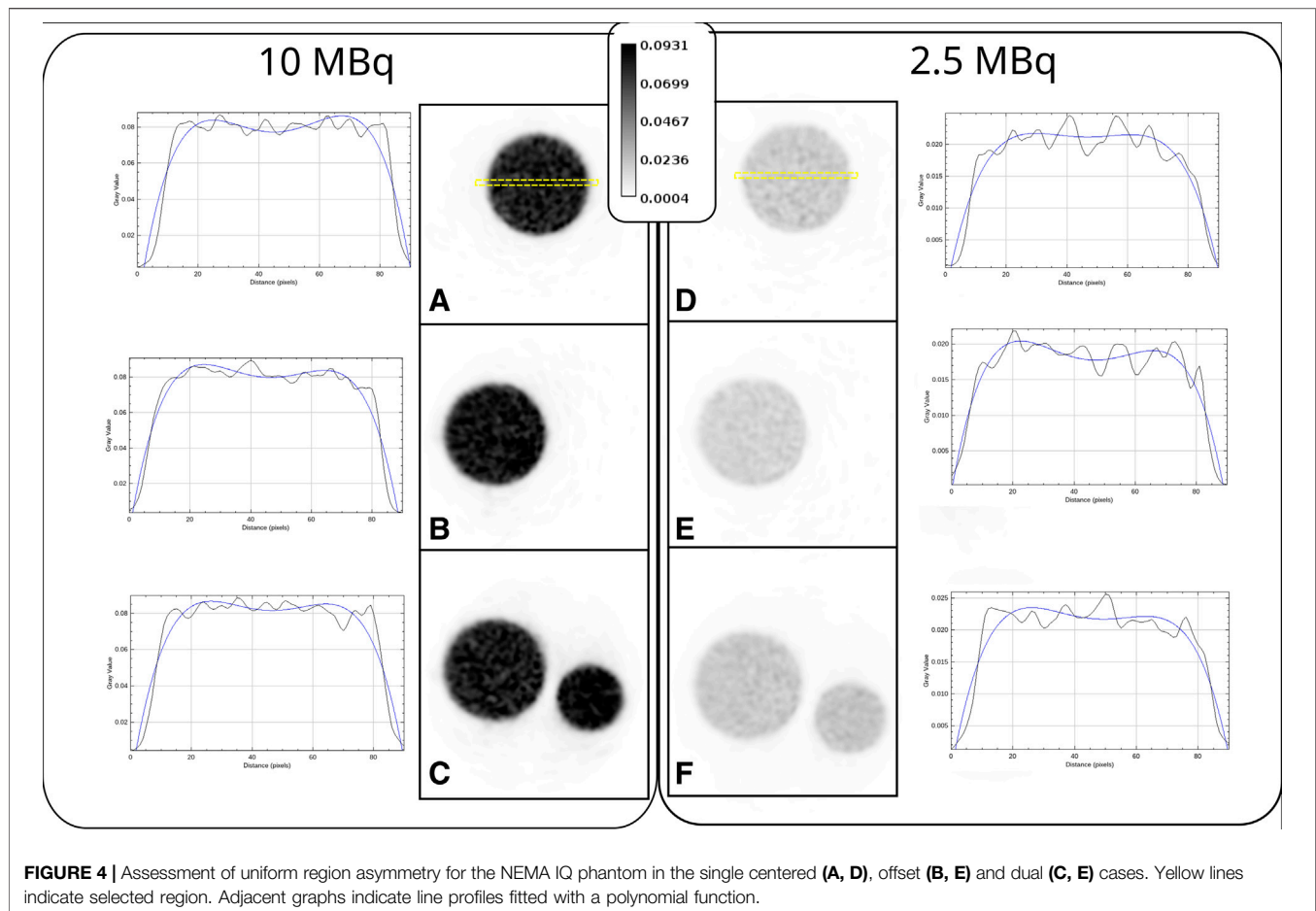
The mean values and %STD for the different phantom positions are presented in **Figure 3C**. The central slices of the rods taken from the 10 MBq acquisitions are shown in **Figure 3M**.

With the exception of the 10 MBq offset scan, acquisitions performed on phantoms positioned both centrally and offset return comparable data on recovery coefficients. In the case of the 10 MBq offset data, both the 3- and 5 mm diameter rods return recovery coefficients greater than 1. On the other hand, both offset acquisitions performed at 2.5- and 10 MBq show a more favourable recovery coefficient for the 1 mm compared to the centrally positioned scans. Finally, the dual phantom acquisitions show progressively poorer RCs with reducing rod size, with a reduction of 60 and 24% for the 2- and 1 mm rods, respectively, compared to the single offset acquisitions.

Recovery Coefficients remained generally consistent when the offset phantom was positioned on the left and right side of the scanner FOV (**Figure 3F**). Left side, air chamber facing outwards continued to show RC greater than 1.0 for 3- and 5 mm rods at 10 MBq, as did the 3 mm rod on the right side phantom, air chamber facing outwards at 2.5 MBq, but to a smaller extent. Interestingly, left side, air chamber facing inwards show a normal expected range of RC's at 10 MBq, albeit with a comparatively reduced 2 mm RC. No particular observations could be made between 2.5- and 10 MBq acquisitions, except that the 2 mm RC appeared to be poorer at 10 MBq, excluding the aforementioned left side, air out acquisitions. However, these observations could be equally explained by the variability in the exact positioning of the rods.

When the NEMA IQ phantom is positioned at the right-hand side for dual phantom scanning, the 3 mm rod's RC is poorer at both 2.5- and 10 MBq (**Figure 3I**). No other noteworthy difference can be seen between the RCs of the dual phantom acquisitions when the NEMA IQ phantom is position at either the left- or right-hand side.

Increasing the scan time from 10- to 20 min makes little difference to the overall mean values of the RC, with none of the mean values changing greater than 5.01% across all acquisitions, regardless of activity present and phantom orientation between single centered and dual phantom



(**Figures 5C,F**). The %STD of the RC, however, reduced by 46.4, 39.3, 50.7, 52.6 and 31.8% in the 20 min scan as compared to the 10 min scan for 1-, 2-, 3-, 4- and 5 mm rods, respectively.

3.3.1.3 Spill-Over Ratio

The spill-over ratios for the air and water chambers in the NEMA IQ phantoms positioned centrally, offset and offset in combination with a second phantom are presented in **Figure 3B**. At central positions, the SOR in the water chamber is 27% higher than the air chamber at both 2.5- and 10 MBq. The SOR for both chambers increases when dual phantom data is acquired. Compared to the centrally positioned phantom, the chamber orientation data from single offset scans show that the SOR in water increases by 15% when the water chamber is closest to the edge of the bore yet reduces by 5% when the water is closer to the center (**Figure 3E**). Whereas in the same data, the SOR in air remains largely unchanged regardless of orientation. When the same data is compared between the left- and right-hand side of the bore, we see that the air chamber has a slight increase in SOR on the right side than that of the left side, whereas the water chamber remains largely unchanged. It is noticeable from **Figures 3B,E** that the activity levels make little difference, with 10 MBq acquisitions increasing the SOR only slightly in each case.

4 DISCUSSION

4.1 Simulation of Multiple Phantoms

Both the measured and simulated prompt counts are in good agreement with Kehl et al. [24] and Zagni et al. [19] however, the latter study reports a marginally higher NECR. We suggest that this difference is due to the data processing method, as our results are produced by processing the raw sinograms, as suggested by the NEMA protocol. Other groups have reported the scanners' counting performance [14, 25], however those studies used non-standard phantoms, making direct comparison difficult.

The offset and dual phantom simulations do not result in a marked increase in randoms and NECR when compared to the single centred phantom for both 10 to 20 MBq (**Figure 2**). However, in the simulated studies the scatter fraction increases for both the off-centre and dual phantom compared to the single phantom case at both activity levels (**Figure 2; Table 2**). Scatter fractions for the single phantom (19.7%) were in line with literature values (21%), [3] and are relatively high, due to either the small size of the gantry or the increased within-detector scattering resulting from the phoswich design [26]. It is not possible to assess the effect of scatter on image quality directly as this will depend on the implemented corrections,

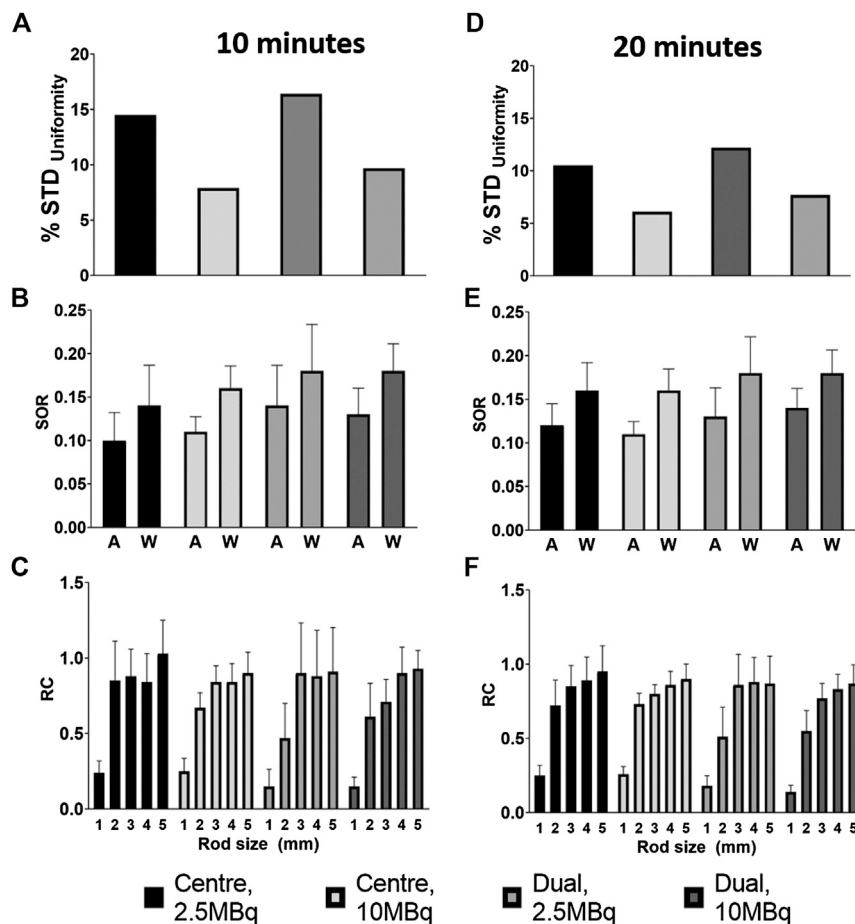


FIGURE 5 | Assessment of NEMA NU4 Image Quality for the 10 and 20 min summed frames for single centered and dual phantom cases. **(A–C)** Uniformity, SOR and Recovery Coefficients for the centered and dual phantom positions, 10 min summed frame. **(D–F)** Uniformity, SOR and Recovery Coefficients for the single or dual phantom positions, 20 min summed frame. Error bars = standard deviation.

though these could be assessed with simulation studies. Given the high density of the Delrin gantry cover (1.41 g/cm^3), our findings suggest that replacing the Delrin tube with a lower density material or removing altogether would significantly improve the scatter fraction. This simple modification could improve the NECR of the scanner and thereby provide better image quality at higher activity levels.

It has previously been proposed that the activity in the FOV at the time of acquisition should be approximately 90–95% of the NECR peak in order to improve image standardization [27]. In the case of the scanner being reviewed in this paper this corresponds to 18–20 MBq. Although, NECR has a valuable role in quantifying the statistical quality of the PET data, its value as a metric of image quality, with iterative reconstruction, is limited [28].

The image quality strongly depends on the many parameters of the reconstruction algorithm [29]. An increase in starting activity would allow for shorter imaging times, however this may result in an increase in absorbed dose to the animal above the threshold for biological effects [30], an issue for longitudinal

studies, although our reported modest increase in random events associated with higher activities suggests that imaging with higher activities would have a relatively small impact to image quality.

4.2 Uniformity

Our results indicate a higher level of noise for the single phantom case than previously reported [3]. However, this data was acquired using a single bed position and with a different activity (3.7 vs. 2.5 MBq). It has been previously reported that multiple bed positions increase variability [31].

When more than one or off-centre sources of activity are present in the scanner, our findings suggest that the Sedecal Super Argus 2R scanner performs favourably compared to similar studies using other scanners. Siepel et al. [9] reported an 18.4% rise in %STD of the uniformity from a single, centrally positioned phantom, to dual offset acquisition, similar to our study. However, a 50 mL centrifuge tube was used compared to our 20 mL syringe, which was chosen to more accurately reflect the volume of a mouse. Reilhac et al. [11] reported a higher increase of 43% in the %STD of the uniformity when scanning a Derenzo

TABLE 2 | Scatter fraction for simulated off-centre and dual phantom scanning.

MBq	Single centre (actual)	Single centre (simulated)	Scatter fraction	
			Single offset (simulated)	Dual (simulated)
10	19.65%	18.26%	22.52%	23.71% (21.36% @ 20 MBq total)
20	20.9%	19.35%	20.42%	21.36% (18.53% @ 40 MBq total)

phantom alongside a NEMA IQ phantom. Finally, Greenwood et al. [12] reported a decrease in uniformity (an increase of 55% in %STD) when assessing four phantoms simultaneously vs the single centered case. It may be expected to see such a significant increase in %STD when there are four sources of activity present, which was not assessed in our study.

4.3 Recovery Coefficients

Recovery coefficients generally decreased for the dual case, as reported previously. The variation that is sometimes seen in RCs (e.g., the 10 MBq offset case) may be explained by the placement of the 1 mm rod being geometrically closer to the center of the FOV in case of the offset acquisitions as the exact position of rod geometry was not factored in our acquisition protocol (see **Figure 3M**).

Similar behavior has been observed and reported on by Aide et al. [32] and Siepel et al. [9], who attributed this to the combined effect of ‘over-estimation of scatter correction plus the non-negativity constraint in the image reconstruction’. Furthermore, Greenwood et al. [12] showed that the smaller, 1 mm diameter rod was not discernible when scanning four phantoms simultaneously, which stands by our observations that RC diminishes as more sources of activity are introduced into the FOV.

It should also be noted that the NEMA protocol derives the %STD from the standard deviations of the line profiles along axial directions and the %STD_{uni} assuming Gaussian error propagation. However, this is not the correct standard deviation of the RC as the %STD of the maximum value of a randomly distributed value is not the standard deviation of the underlying distribution [33]. This results in an artificial increase of RC for smaller sources.

The phoswich detector arrangement inherently provides DOI information, allowing for an improved and more uniform spatial resolution in the images [17]. This detector configuration should naturally reduce the spatial resolution degradation when scanning dual objects, allowing for reconstruction methods without Point Spread Function (PSF) correction to perform well under these conditions. This is in contrast to the reported performance of OSEM 2D reconstruction for the Inveon [9, 32].

Our data shows that RC values do not significantly change between 10- and 20 min imaging frames. However, as expected, the %STD of the RCs is markedly higher on the shorter imaging time frames regardless of activity or scan orientation.

4.4 Spillover Ratios

Our data indicated a dependence of SOR on gantry proximity. The apparent increase on the water container in the offset case

could be a result either of limitations of the scatter correction algorithm, or by photons scattered by the Delrin tube, in close proximity at the edge of the gantry.

When scanning two subjects, the SOR increases by 17 and 12% for water and air, respectively. Siepel et al. [9] reported an approx. 32% increase in the SOR values for water and approx. 40% for air, albeit using a larger non-NEMA phantom in a scanner with a wider bore. The position dependency that we show for the single offset subject was not apparent in the dual case. As the SOR did not increase markedly between 2.5 and 10 MBq in the single centered case this suggests the effect is not due to the increased activity in the FOV.

No notable difference was observed in SOR between 10 and 20 min frames at both high and low activities, and between single centered and dual phantom scanning.

As Greenwood et al. [12] demonstrated, increasing the number of iterations during reconstruction may improve the SOR values. However, this may come at the expense of noise amplification, as shown by Gaitanis et al. [34]. The above, has not been assessed here.

When comparing simulated phantom data to NEMA IQ acquisition, it is worth noting that the SuperArgus2R has an axial FOV smaller than that of the NEMA phantom (47 vs. 50 mm), and thus NEMA IQ acquisitions used multiple bed positions. However, data on scatter fraction and NECR were acquired using effectively a single bed position as the NEMA protocol does not specify a similar setting for this case.

Image quality is also dependent on energy discrimination, and our studies used the 250–700 keV setting as used in other studies [3] and suggested to provide a good balance between counting performance and scatter rejection [35].

The primary application of preclinical PET at the University of Hull PET Research center is to assess the pharmacokinetics and biodistribution of novel imaging probes [36–39], for this application the degradation in image quality predicted for the two animal case is acceptable. For the application of existing tracers to provide physiological readouts in disease models, our data suggest that higher injected doses provide better image quality overall if dual animal scanning is warranted for logistical reasons [40].

5 CONCLUSION

In this study, we present the impact of dual subject scanning on the PET signal and image quality using the Sedecal SuperArgus 2R preclinical scanner. In brief, our experiments demonstrate a decrease in image quality between the single and dual phantom

cases, however of less magnitude than similar decreases reported for other scanners.

We conclude that the Sedecal AuperArgus 2R preclinical scanner is, therefore, suitable for dual animal scanning, particularly in biodistribution studies of novel radiotracers - as is a key operational objective of our facility. Regarding investigations looking into more subtle biological changes or smaller regions of interest, the scanning protocol and injected dose should be carefully considered to ensure that image quality is optimized throughout the field of view.

DATA AVAILABILITY STATEMENT

The datasets generated for this study are available upon reasonable request to the corresponding authors.

AUTHOR CONTRIBUTIONS

NE and JW contributed equally to this work and share first authorship. LC performed the scans of the NEMA scatter phantom for the characterisation of the scanner. NE and LC processed the raw data acquired from the scanner, and did the image analysis for the image quality phantom. NE and PC performed the GATE simulations, validated the simulations to the measured data, and performed the Monte Carlo

investigation. JW and IR performed the acquisition and analysis of the NEMA IQ phantom. FZ developed the original GATE Monte Carlo simulation model for the Argus scanner and advised in the processing of the data acquired from the scanner. CC contributed to the conception and design of the study. CC and SA are the grant holders and were involved in the organization and planning of the work and discussions on the results. All authors contributed in the drafting of the paper.

ACKNOWLEDGMENTS

We thank Assem Allam and his family for the generous donation to help found the PET Research Center at the University of Hull and for their continued support. We acknowledge the Viper High Performance Computing facility of the University of Hull and its support team. The authors would like to thank D. P. Roberts (PET Research Center, Univ. of Hull) for his valuable support and training.

SUPPLEMENTARY MATERIAL

The Supplementary Material for this article can be found online at: <https://www.frontiersin.org/articles/10.3389/fphy.2020.531662/full#supplementary-material>.

REFERENCES

- Aide N, Visser EP, Lheureux S, Heutte N, Szanda I, Hicks RJ. The motivations and methodology for high-throughput pet imaging of small animals in cancer research. *Eur J Nucl Med Mol Imag* (2012) 39:1497–509. doi:10.1007/s00259-012-2177-x
- Eckelman WC. Further discussions on choosing the number of animals for an experiment. *Nucl Med Biol* (2008) 35:1–2. doi:10.1016/j.nucmedbio.2007.10.002
- Goertzen AL, Bao QN, Bergeron M, Blankemeyer E, Blinder S, Canadas M, et al. Nema nu 4-2008 comparison of preclinical pet imaging systems. *J Nucl Med* (2012) 53:1300–9. doi:10.2967/jnumed.111.099382
- Weber S, Bruyndonckx P, Chatziioannou AF, Clark JC, Daube-Witherspoon ME, Di Domenico G, et al. Performance measurements of small animal positron emission tomographs. *J Nucl Med* (2002) 43:59p–59p.
- Aide N, Desmonts C, Beauregard JM, Beyer T, Kinross K, Roselt P, et al. High throughput static and dynamic small animal imaging using clinical pet/ct: potential preclinical applications. *Eur J Nucl Med Mol Imag* (2010a) 37:991–1001. doi:10.1007/s00259-009-1352-1
- Habte F, Ren G, Doyle TC, Liu HG, Cheng Z, Paik DS. Impact of a multiple mice holder on quantitation of high-throughput micropet imaging with and without ct attenuation correction. *Mol Imag Biol* (2013) 15:569–75. doi:10.1007/s11307-012-0602-y
- Yagi M, Arentsen L, Shanley RM, Hui SK. High-throughput multiple-mouse imaging with micro-pet/ct for whole-skeleton assessment. *Phys Med-Eur J Med Phys* (2014) 30:849–53. doi:10.1016/j.ejmp.2014.06.003
- Seidel J, Bernardo ML, Wong KJ, Xu BY, Williams MR, Kuo F, et al. Simultaneous ecg-gated pet imaging of multiple mice. *Nucl Med Biol* (2014) 41:582–6. doi:10.1016/j.nucmedbio.2014.03.015
- Siepel FJ, van Lier MgitbChen M, Disselhorst JA, Meeuwis APW, Oyen WJG, et al. Scanning multiple mice in a small-animal pet scanner: influence on image quality. *Nucl Instrum I& Methods Phys Res Sect A Accel Spectrom Detect Assoc Equip* (2010) 621:605–10. doi:10.1016/j.nima.2010.05.057
- Rominger A, Mille E, Zhang S, Boning G, Forster S, Nowak S, et al. Validation of the octamouse for simultaneous 18f-fallypride small-animal pet recordings from 8 mice. *J Nucl Med* (2010) 51:1576–83. doi:10.2967/jnumed.110.078451
- Reilhac A, Boisson F, Wimberley C, Parmar A, Zahra D, Hamze H, et al. Simultaneous scanning of two mice in a small-animal pet scanner: a simulation-based assessment of the signal degradation. *Phys Med Biol* (2016) 61:1371–88. doi:10.1088/0031-9155/61/3/1371
- Greenwood HE, Nyitrai Z, Mocsa G, Hobor S, Witney TH. High-throughput pet/ct imaging using a multiple-mouse imaging system. *J Nucl Med* (2020) 61:292–7. doi:10.2967/jnumed.119.228692
- McDougald W, Vanhove C, Lehnert A, Lewellen B, Wright J, Mingarelli M, et al. Standardization of preclinical pet/ct imaging to improve quantitative accuracy, precision, and reproducibility: a multicenter study. *J Nucl Med* (2020) 61:461–8. doi:10.2967/jnumed.119.231308
- Wang YC, Seidel J, Tsui BMW, Vaquero JJ, Pomper MG. Performance evaluation of the ge healthcare explore vista dual-ring small-animal pet scanner. *J Nucl Med* (2006) 47:1891–900.
- Green MV, Ostrow HG, Seidel J, Pomper MG. Experimental evaluation of depth-of-interaction correction in a small-animal positron emission tomography scanner. *Mol Imag* (2010) 9:311–8. doi:10.2310/7290.2010.00038
- Kastis GA, Gaitanis A, Fernandez Y, Kontaxakis G, Fokas AS. Evaluation of a spline reconstruction technique: comparison with FBP, MLEM and OSEM. Hawaii: *IEEE Nucl Sci Symp Conf Rec* (2007) 3187:3282–7. doi:10.1109/nssmic.2010.5874412
- Seidel J, Vaquero JJ, Siegel S, Gandler WR, Green MV. Depth identification accuracy of a three layer phoswich pet detector module. *IEEE Trans Nucl Sci* 46 (1999) 485–90. doi:10.1109/23.775567
- Jan S, Comtat C, Strul D, Santin G, Trebassen R. Monte Carlo simulation for the ecac exact hr+ system using gate. *IEEE Nucl Sci Symp Conf Rec* (2003) 1–5:2545–8. doi:10.1109/Nssmic.2003.1352409
- Zagni F, D'Ambrosio D, Spinelli AE, Cicoria G, Fanti S, Marengo M. Accurate modeling of a doi capable small animal pet scanner using gate. *Appl Radiat Isot* (2013) 75:105–14. doi:10.1016/j.apradiso.2013.02.003

20. Efthimiou N, Panayiotakis GS, Varvarigou A, Bouziotis P, Loudos G, Kandarakis I, et al. Small animal positron emission tomography using a dual head prototype based on pspmts and fpga readout. *IEEE Int Worksh Imaging Syst Techniq* (2008) 12:29–33. doi:10.1109/IST.2008.4659935
21. Efthimiou N, Maistros S, Tripolitis X, Samartzis A, Loudos G, Panayiotakis G. Tomographic evaluation of a dual-head positron emission tomography system. *Meas Sci Technol* (2011) 22:19. doi:10.1088/0957-0233/22/11/114010
22. Daube-Witherspoon ME, Muehllehner G. Treatment of axial data in three-dimensional PET. *J Nucl Med: Off Pub Soc Nucl Med* (1987) 28:1717–24.
23. Thielemans K, Tsoumpas C, Mustafovic S, Beisel T, Aguiar P, Dikaos N, et al. STIR: Software for tomographic image reconstruction release 2. *Phys Med Biol* (2012) 57:867–83. doi:10.1088/0031-9155/57/4/867
24. Kehl MI, Honer M, Schubiger PA, Ametamey SM. Small animal pet imaging: is strict standardization the key to more robust data? *Eur J Nucl Med Mol Imag* (2010) 37:S388.
25. Yang CC, Seidel J, Wang Y, Lee JS, Pomper MG, Tsui BMW. Validation of gate Monte Carlo simulation of the performance characteristics of a ge explore vista small animal pet system. *IEEE Nucl Sci Symp Conf Rec* (2007) 3187:1–11. doi:10.1109/Nssmic.2007.4436803
26. Goertzen AL. Coincidences originating from a single photon: an unrecognized and potentially significant source of scatter in small animal pet? *2009 IEEE Nucl Sci Symp Conf Rec* 1–5 (2009) 2888–91. doi:10.1109/Nssmic.2009.5401622
27. Watson CC, Casey ME, Bendriem B, Carney JP, Townsend DW, Eberl S, et al. Optimizing injected dose in clinical pet by accurately modeling the counting-rate response functions specific to individual patient scans. *J Nucl Med* (2005) 46:1825–34.
28. Chang T, Chang G, Clark JJ. Reliability of predicting image signal-to-noise ratio using noise equivalent count rate in pet imaging. *Med Phys* (2012) 39: 5891–900. doi:10.1118/1.4750053
29. Karakatsanis NA, Fokou E, Tsoumpas C. Dosage optimization in positron emission tomography: state-of-the-art methods and future prospects. *American journal of nuclear medicine and molecular imaging* (2015) 5:527–47.
30. Taschereau R, Chatziioannou AF. Monte Carlo simulations of absorbed dose in a mouse phantom from 18-fluorine compounds. *Med Phys* (2007) 34: 1026–36. doi:10.1118/1.2558115
31. Rahmim A, Lodge M, Karakatsanis N, Vladimir Y, Panin Y, Zhou Y, et al. Dynamic whole-body pet imaging: principles, potentials and applications. *Eur J Nucl Med Mol Imag* (2019) 46:501–18. doi:10.1007/s00259-018-4153-6
32. Aide N, Desmonts C, Briand M, Meryet-Figuere M, Poulain L. High-throughput small animal pet imaging in cancer research: evaluation of the capability of the inveon scanner to image four mice simultaneously. *Nucl Med Commun* (2010b) 31:851–8. doi:10.1097/MNM.0b013e32833dc61d
33. Hallen P, Schug D, Schulz V. Comments on the nema nu 4-2008 standard on performance measurement of small animal positron emission tomographs. *EJNMMI Phys* (2020) 7:27–35. doi:10.1186/s40658-020-0279-2
34. Gaitanis A, Kontaxakis G, Spyrou G, Panayiotakis G, Tzanakos G. Pet image reconstruction: a stopping rule for the mlem algorithm based on properties of the updating coefficients. *Comput Med Imag Graph* (2010) 34:131–41. doi:10.1016/j.compmedimag.2009.07.006
35. Kuntner C, Stout D. Quantitative preclinical pet imaging: opportunities and challenges. *Front Phys* (2014) 2:13–9. doi:10.3389/fphy.2014.00012
36. Burke BP, Baghdadi N, Kownacka AE, Nigam S, Clemente GS, Al-Yassiry MM, et al. Chelator free gallium-68 radiolabelling of silica coated iron oxide nanorods via surface interactions. *Nanoscale* (2015) 7:14889–96. doi:10.1039/c5nr02753e
37. Entract GM, Bryden F, Domarkas J, Savoie H, Allott L, Archibald SJ, et al. Development of pdt/pet theranostics: synthesis and biological evaluation of an (18)f-radiolabeled water-soluble porphyrin. *Mol Pharm* (2015) 12:4414–23. doi:10.1021/acs.molpharmaceut.5b00606
38. Burke BP, Miranda CS, Lee RE, Renard I, Nigam S, Clemente GS, et al. (64)cu pet imaging of the cxcr4 chemokine receptor using a cross-bridged cyclam bis-tetraazamacrocyclic antagonist. *J Nucl Med* (2020) 61:123–8. doi:10.2967/jnumed.118.218008
39. Allott L, Miranda C, Hayes A, Raynaud F, Cawthorne C, Smith G. Synthesis of a benzoxazinthione derivative of tanaproget and pharmacological evaluation for pet imaging of pr expression. *EJNMMI Radiopharm Chem* (2019) 4:1. doi:10.1186/s41181-018-0054-z
40. Gandhi R, Cawthorne C, Craggs LJL, Wright JD, Domarkas J, He P, et al. Cell proliferation detected using [(18)f]flt pet/ct as an early marker of abdominal aortic aneurysm. *J Nucl Cardiol* (2019) 7:17. doi:10.1007/s12350-019-01946-y

Conflict of Interest: The authors declare that the research was conducted in the absence of any commercial or financial relationships that could be construed as a potential conflict of interest.

Copyright © 2021 Efthimiou, Wright, Clayton, Renard, Zagni, Caribé, Archibald and Cawthorne. This is an open-access article distributed under the terms of the Creative Commons Attribution License (CC BY). The use, distribution or reproduction in other forums is permitted, provided the original author(s) and the copyright owner(s) are credited and that the original publication in this journal is cited, in accordance with accepted academic practice. No use, distribution or reproduction is permitted which does not comply with these terms.

Advantages of publishing in Frontiers



OPEN ACCESS

Articles are free to read
for greatest visibility
and readership



FAST PUBLICATION

Around 90 days
from submission
to decision



HIGH QUALITY PEER-REVIEW

Rigorous, collaborative,
and constructive
peer-review



TRANSPARENT PEER-REVIEW

Editors and reviewers
acknowledged by name
on published articles

Frontiers

Avenue du Tribunal-Fédéral 34
1005 Lausanne | Switzerland

Visit us: www.frontiersin.org

Contact us: frontiersin.org/about/contact



REPRODUCIBILITY OF RESEARCH

Support open data
and methods to enhance
research reproducibility



DIGITAL PUBLISHING

Articles designed
for optimal readership
across devices



FOLLOW US

@frontiersin



IMPACT METRICS

Advanced article metrics
track visibility across
digital media



EXTENSIVE PROMOTION

Marketing
and promotion
of impactful research



LOOP RESEARCH NETWORK

Our network
increases your
article's readership